PEM FUEL CELL MODELING AND CONVERTERS DESIGN FOR A 48 V DC POWER BUS

Carlos Alberto Restrepo Patiño

Dipòsit Legal: T. 1049-2012

PEM fuel cell modeling and converters design for a 48 V DC power bus

Doctoral Thesis

Carlos Alberto Restrepo Patiño

UNIVERSITAT ROVIRA I VIRGILI

Department of Electronics, Electric and Automatic Engineering

Tarragona

2012

Carlos Alberto Restrepo Patiño

PEM fuel cell modeling and converters design for a 48 V DC power bus

Doctoral Thesis

Supervised by
Dr. Roberto Giral and Dr. Javier Calvente

Department of Electronics, Electric and Automatic Engineering

UNIVERSITAT ROVIRA I VIRGILI

Tarragona
2012

UNIVERSITAT ROVIRA I VIRGILI

Departament d'Enginyeria Electrònica, Elèctrica i Automàtica
Escola Tècnica Superior d'Enginyeria
Edifici L-1, 3a planta despatx 331
Avda. Paisos Catalans, 26
Campus Sescelades
43007 Tarragona Spain
Tel.: + 34 977 559 610
Fax:+ 34 977 559 605

We, Roberto Giral and Javier Calvente, associate professors in the Department of Electronics, Electric and Automatic Engineering of the Rovira i Virgili University,

CERTIFY:

That the present study, entitled "PEM fuel cell modeling and converters design for a 48 V DC power bus", presented by Carlos Alberto Restrepo Patiño for the award of the degree of Doctor, has been carried out under our supervision at the Department of Electronics, Electric and Automatic Engineering of this university, and that it fulfils all the requirements to be eligible for the European Doctorate Label.

Tarragona, April the 20th, 2012.

.....	.....
Roberto Giral, PhD.	Javier Calvente, PhD.

To Nicole, for being my best friend, my companion, my love, for understanding and supporting me, and make my days happier.

To my mother and grandmother, for all the love, comprehension, for always being and still be an example to follow in my life, for the trust in me, and because I still am in debt with you.

To my little brother, for the sincere affection, the good times spend together, and because I know that my Ph.D represented a really hard separation for both of us, and for all the support you are still giving me, you turned into an example for me.

To Doris, Natalie, Klaus and Axel for the hospitality, support, also understanding, patience and for making me feel like another member of your family, and for being my adoptive family in Spain.

To Kiara, because you arrive at the end of a very important cycle of my life. You make me dream about the future.

A huge thank you to Paula, who selflessly supported me with this hard decision of doing my PhD in Spain, and whose friendship is very important to me right now.

And to all my family, and most of all to Cecilia, Sandra, Luz Adriana and Andrés Felipe for their love.

Acknowledgments

In a village of La Mancha, the name of which I have no desire to call to mind, I find myself today writing the most sincere acknowledgements to professor Luis Martínez Salamero for trusting me and for giving me the opportunity of making an PhD in the GAEI research group on Industrial Electronics and Automatic Control and for his enriching talks while being in conferences or during the trip to Toulouse.

I am also very thankful towards my supervisor professor Roberto Giral. His shared knowledge for the realization of the "functional models", his time spend for my research, the accompany during the writing of the different articles, which are part of my work now, have been very important for me. He encouraged me to write the PhD in English and allowed me to do what really makes me happy.

To the person who believed in me during the hardest times of my PhD, my Co-supervisor professor Javier Calvente. Also thank him for introducing me in the scope of DC-DC Power converters, for his teaching about modelling and design of realistic simulations of converters and whose objective critics helped me to do a better work.

I will be always grateful to the professors Abdelali El Aroudi, Enric Vidal, Angel Cid, Alfonso Romero, Luis Martínez Salamero, Roberto Giral , Javier Calvente, Miro Milanovič, Carlos Ramos and PhD student Tine Konjedic for their valuable contributions and collaboration in the realization of my publications.

A special thank you to professor Guillermo Ruiz and to PhD Julián Peláez, for their teaching and support with the DSP programming for the control of converters.

To the Faculty of Electrical Engineering and Computer Sciencie FERI of the University of Maribor for receiving me, for the provided assistance, for the patience with my English, for making me feel like a part of the team and for integrating me in the culture and traditions of Slovenia. I will never forget this experience, thank you all for it.

Thanks to PhD Mitja Truntič for sharing his valued knowledge about the control of converters using FPGA, and also for helping me with the design of the buck-boost bidirectional converter ant its control, and with whom I hope to make more researches.

I want to thank again the following professors: Luis Martínez Salamero, Enric Vidal and Javier

Calvente, who gave me the chance of one more year of research with this group, I will be always grateful for this.

To GAEI Laboratory, especially Josep María Bosque and Oriol Aviño for their collaboration on the functional models development. And to professor Hugo Valderrama, for his trust during my three years of teaching Regulación Automática.

Thanks to professor Germain Garcia at LAAS-CNRS. His kindness and collaboration during my short stay at his laboratory really helped and inspired me. I hope we can make more works together in future times.

Even if an ocean separates us, a special thanks to professor Alfonso Alzate and rector Luis Enrique Arango of the Universidad Tecnológica de Pereira, for all their collaboration and support before and while my thesis, and who encouraged me to catch this unique opportunity in life.

To PhD student Alejandro Garcés, for all his shown knowledge and for his friendship.

Thank you to all my workmates, especially to PhD student Carlos Torres, PhD Mauricio Muñoz and Ing. Natalia Cañas, for the good times.

For becoming my best friend, receiving me at his home and making me feel like one more of them, thank you to PhD student Tine Konjedic, and also a special thanks to my adoptive family in Slovenia. For the good times spend together, for the English teaching and for aaaall the needed patience to do so, for the good energy and all his help with the administrative paperwork, for the military-training and for bringing me my bike. And to PhD student Tijana Ristic for her friendship.

To Ph.D student Martin Petrun for his friendship, for opening the doors of his home to me, for the great times spend together, and his calm and diplomacy during lunch/debate, for the shared songs and for fixing my bike. Also a special thank you to the artist Katja Pavlic for her collaboration with my PhD cover design and all her selfless effort.

And a special thank you to all my friends, which where always there, sharing good and bad times.

PEM fuel cell modeling and converters design for a 48 V DC power bus

by

Carlos Alberto Restrepo Patiño

Department of Electronics, Electric and Automatic Engineering
Rovira i Virgily University
Tarragona, 2012

Abstract

Fuel cells (FC) are electrochemical devices that directly convert the chemical energy of a fuel into electricity. Power systems based on proton exchange membrane fuel cell (PEMFC) technology have been the object of increasing attention in recent years as they appear very promising in both stationary and mobile applications due to their high efficiency, low operating temperature allowing fast startup, high power density, solid electrolyte, long cell and stack life, low corrosion, excellent dynamic response with respect to the other FCs, and nonpolluting emissions to the environment if the hydrogen is obtained from renewable sources. The output-voltage characteristic in a PEMFC is limited by the mechanical devices which are used for regulating the air flow in its cathode, the hydrogen flow in its anode, its inner temperature, and the humidity of the air supplied to it. Usually, the FC time constants are dominated by the fuel delivery system, in particular by the slow dynamics of the compressor responsible for supplying the oxygen. As a consequence, a fast load transient demand could cause a high voltage drop in a short time known as oxygen starvation phenomenon that is harmful for the FC. Thus, FCs are considered as a slow dynamic response equipment with respect to the load transient requirements. Therefore, batteries, ultracapacitors or other auxiliary power sources are needed to support the operation of the FC in order to ensure a fast response to any load power transient. The resulting systems, known as FC hybrid systems, can limit the slope of the current or the power generated by the FC with the use of current-controlled dc-dc converters. In this way, the reactant gas starvation phenomena can be avoided and the system can operate with higher efficiency. The purpose of this thesis is the design of a DC-DC converter suitable to interconnect all the different elements in a PEMFC-hybrid 48-V DC bus. Since the converter could be placed between elements with very different voltage levels, a buck-boost structure has been selected. Especially to fulfill the low ripple requirements of the PEMFCs, but also those of the auxiliary storage elements and loads, our structure has inductors in series at both its input and its output. Magnetically coupling these inductors and adding a damping network to its intermediate capacitor we have designed an easily controllable converter with second-order-buck-like dominant dynamics. This new proposed topology has high efficiency and wide bandwidth acting either as a voltage or as a current regulator. The magnetic coupling allows to control with similar performances the input or the output inductor currents. This characteristic is very useful because the designed current-controlled converter is able to withstand shortcircuits at its output and, when connected to the FC, it facilitates to regulate the current extracted from the FC to avoid the oxygen starvation phenomenon. Testing in a safe way the converter connected to the FC required to build an FC simulator that was subsequently improved by developing an emulator that offered real-time processing and oxygen-starvation indication. To study the developed converters and emulators with different brands of PEMFCs it was necessary to reactivate long-time inactive Palcan FCs. Since the results provided by the manual reactivation procedure were unsatisfactory, an automatic reactivation system has been developed as a complementary study of the thesis.

Thesis Supervisors: Roberto Giral and Javier Calvente

Preface

This thesis reports the results of my Ph.D. study at the Departament dEnginyeria Electrònica, Elèctrica i Automàtica, Escola Tècnica Superior d'Enginyeria, Universitat Rovira i Virgili. It documents the work I carried out between December 2007 and December 2011, which was funded by the Universitat Rovira i Virgili in the first year and a half and subsequently by the Spanish Ministry of Education and Science, under FPU scholarship AP2008-03305. I made the study as a Ph.D student of the Automatic Control and Industrial Electronics Group, to which I have been affiliated since December 2007.

The thesis contains results that have been accepted or are to be submitted for publication as papers in international journals or conference proceedings, but the thesis format makes it easier for the reader to gain a better understanding of the overall work and of the improvements in the state of the art.

The thesis follows common publishing guidelines given by international journals. Therefore all the figures have been made in grayscale. Similarly, the bibliographical citations have been numbered in order of appearance, as have the equations, figures and tables. Finally, the simulations, the mathematical analysis, the simulator system, the real-time emulator, and the reactivation system presented in in each of the chapters have been carried out by using PSIM, Matlab/Simulink and LabVIEW softwares.

List of Figures

List of Tables

Contents

Dipòsit Legal: T. 1049-2012

Chapter 1

Introduction

Nowadays the world is clamoring for an energetic change to ensure a sustainability of natural resources for future generations. The increased use of fossil fuels since the industrial revolution is largely responsible for the globally increasing emissions of carbon dioxide, and consequently for the global warming and climate change. The economic growth of a nation is related to the control of energy resources and this has conducted to great social differences between developed and less developed countries. At present, there is no consensus among geologists about the oil reserves but many experts estimate that production will reach its maximum point in a few decades. The real oil reserves are not believable because the producing countries exaggerate their numbers to get loans from international institutions or private banks to be invested in commercial and infrastructure projects. The economic growth that is happening in developing countries like China and India require an increasingly important consume of oil making the reserves more disputed. Additionally the population is growing, especially in developing countries, therefore the required energy needs will increase and so will the oil prices. Compounding the oil situation, the large reserves are in politically unstable countries and this may worsen the situation even more. With this background, it is understandable that the great powers are making large investments to search for alternative energies to fossil fuels. In this context, the hydrogen is an energy carrier which is foreseen to play an important role in sustainable energy systems that is expected to replace fossil fuels. Hydrogen is the lightest, most basic and most abundant element in the universe. When it is used as an energy form, it becomes an inexhaustible fuel because the electrolytic production and the combustion are governed by the same chemical reaction in opposite directions. Another advantage is that the energy produced by hydrogen is clean, as long as it is obtained using renewable energy technologies, and free of carbon dioxide emissions.

1.1 Advantages and drawbacks of hydrogen as transportation fuel

Air pollution is a serious public health problem throughout the world, especially in industrialized and developing countries, and in this cases motor vehicle emissions are major contributors to urban air quality [3]. In this context, hydrogen can be used as a fuel applied directly in an internal combustion engine vehicle, not much different from the engines used with gasoline, but with the advantage of not emitting carbon dioxide to the atmosphere [3]. Nevertheless, the hydrogen internal combustion engine vehicle produces nitrogen oxides in small quantities, and researches has shown that nitrogen oxide is 310 times more harmful acting like a greenhouse gas than carbon dioxide [4]. An alternative to convert hydrogen energy into electric energy in an efficient manner is through a fuel cell which will be explained in more detail in another section. Nowadays, the consumers and government programs are demanding increased technical efficiency in new automobiles [5]. Therefore, the fuel cell vehicles have all the advantages to be an alternative to fossil fuel vehicles because it has more efficiency and is less polluting if the hydrogen is obtained by renewable energies. Nevertheless there are barriers to be overcome for hydrogen vehicles to become widely used. The following subsections will make a brief explanation of the main problems to be solved before hydrogen turns into a true alternative to fossil fuels in the automobile field.

1.1.1 Hydrogen storage

Hydrogen is the lightest and most abundant chemical element, constituting roughly 75% of the Universe's chemical elemental mass, and on Earth, it is the most abundant component of all flora and fauna, including the human body, with a 61%. Nevertheless, gaseous hydrogen is extremely strange to find on earth since its light weight allows it to escape from the Earth's gravity [6]. It only exists in nature in combination with other elements such as oxygen in the water, carbon and oxygen in the organic materials, and high proportion of carbon in the fossil fuels [7].

The hydrogen has physical and chemical properties that makes it a good candidate for a fuel, such as: odorless, stable, colorless, it does not react with oxygen until sufficient energy is supplied to begin an exothermic reaction that results in the production of water [6]. Furthermore, in comparison with other fuels the hydrogen has a wide range of flammability, a very low ignition energy, a higher ignition temperature, a fast flame speed, a very high diffusivity, and a wide detonation range in a confined state [3]. In addition, the hydrogen has the highest energy-to-weight ratio of any fuel since it is the lightest element and has no heavy carbon atoms like the hydrocarbons fuels. Therefore, the amount of energy liberated during the reaction of hydrogen, on a mass basis, is about

2.5 times the heat of combustion of common hydrocarbon fuels and this means that the mass of hydrogen required is only about a third of the mass of the needed hydrocarbon fuel [8]. Nevertheless, the hydrogens energy density, that denotes the amount of energy for a given volume of fuel, is the lowest in comparison with the common hydrocarbon fuels [9, 6]. Since the energy density is really a measure of how compactly hydrogen atoms are packed in a fuel, then the hydrocarbons of increasing complexity, with more and more hydrogen atoms per molecule, have increasing energy density [8]. The energy density of a fuel is also affected by whether the fuel is stored as a liquid or as a gas at specific pressure. To put it into perspective, the energy density of the liquid hydrogen is 8.5 MJ/litre, while the gasoline is 31.2 MJ/litre [8], therefore a hydrogen fuel tank would need to be at least three times larger than a gasoline tank with the same energy content.

On-board hydrogen storage for transportation applications continues to be one of the most technically challenging barriers to the widespread commercialization of hydrogen-fueled vehicles according to the U.S. Department of Energy. The hydrogen-storage-system mainly considered that a vehicle needs a minimum of 5 kg of hydrogen on board to allow a driving range of more than 500 km with a packaging, safety, cost, and performance competitive with current vehicles [10]. The hydrogen boiling point is -252.87 °C, which means that the storage temperature of liquid hydrogen (LH2) is -253 °C, known as cryogenic LH2, and at room temperature the hydrogen is in gas state. The hydrogen expansion ratio from the liquid to the gaseous state at atmospheric conditions is 1:848, therefore the most obvious solution should be to have liquid hydrogen (LH2) stored at or close to ambient pressure. However, there are disadvantages that make the LH2 storage in an impractical solution. The first one is that for the liquefaction of hydrogen a complex, multistage process requires a lot of energy is necessary, which makes this process expensive and not efficient [11, 6]. And the second one is that the LH2 tends to boil off because the tank can not be perfectly insulated and pressure build up has to be prevented by venting hydrogen because the pressures would very quickly become impossible to be contained safely [12, 6]. Therefore, typical boil off venting rates are 1 to 2% per day for automotive-sized cryogenic super-insulating tank [13] which means that it would lose up to a quarter part of a full tank per week [6].

Another possibility to store the hydrogen is by the metal hydride system that can absorb the hydrogen in gas state under high pressure and moderate temperature conditions [14]. This metal hydride system releases the hydrogen gas when a high temperature and low pressure is applied to them. This system has a high energy density by volume, a low operation pressure, and it is the safest of all possible methods of storing hydrogen [13]. Nevertheless, this method has a poor energy density by weight and therefore tends to be very heavy and expensive [13]. In addition, these technologies are not yet completely mature and therefore indications on energy requirements can be unreliable [7].

Finally, the high-pressure gas storage systems are the most common and most highly developed methods of storing hydrogen [13]. Now, researchers are focused on the design of cylinders that are able to support high pressure to minimize their size, cost and weight, to maximize the driving range and the security. Recent advances in carbon-fibre technology allow to design new cylinders, know as the QUANTUM TriShield, which are according with the standards of the European Integrated Hydrogen Project (EIHP) [15, 6]. Actually, the problems of hydrogen tank weight have two research directions: the first one uses cryo-compression tanks, which consists of a liquid-nitrogen filled jacket to cool the hydrogen down to -203 °C and increases its volumetric capacity by a factor of four [16, 6]. The second research direction is to integrate the tank as a part of the vehicle structure [6]. More details about the study of different methods of hydrogen storage on-board and off-board in vehicle applications can be found in [17].

Although the hydrogen storage is still an open research problem, and the expected improvements are not yet efficient enough, the currently used compressed gas storage has not hindered vehicle manufacturers to have commercial or concept vehicles as: Toyota FCV-R, Audi A2H2, Peugeot 207 EPure, Volkswagen Touran HyMotion, GM's Chevy Equinox Fuel Cell SUV, Daihatsu Tanto FCHV, Mercedes-Benz F-Cell, Ford Focus FCV, Kia Sportage FCEV SUV, and more. In addition, the BMW Hydrogen 7 is the first costumer car with a liquid hydrogen storage system [18] while the Honda FCX Clarity, which is the first fuel cell vehicle platform-exclusive in the world manufactured in series, works with hydrogen compressed gas [19]. The manner in which the cars convert hydrogen into electrical energy will be explained in next section. Actually, the commercial vehicles have improved technical efficiency by means of advantages of injection technologies, turbocharging, increased transmission efficiency, and overall vehicle technologies for aerodynamic, rolling resistance, and mass-reduction improvements [5]. However hybrid, electric and fuel cell vehicles exhibit superior performances than the internal combustion engine as presented in studies performed in [20, 5]. Despite its good efficiency, fuel cell vehicles can not be marketed on a global scale because it does not exist a hydrogen infrastructure to ensure the supply of fuel, and the reason for not being any infrastructure for transporting and distributing hydrogen is because there are no hydrogen vehicles.

1.1.2 Hydrogen transport and distribution

In order to supply a large demand for hydrogen in the future, it is necessary to design transport and distribution systems to ensure the supply of it to the users. There are many possibilities that can be used for the hydrogen distribution, depending on the quantity, and the place to be produced and consumed. A central production with a large scale production, independent of the manner in which

hydrogen is generated, and that requires hydrogen to be transported to the place of consumption, there are basically four alternatives. For short distances, a tube trailer to transport hydrogen compressed gas with a maximum of 400 kg per trunk can be used. While for short and medium distances, and up to 4000 kg, it is more recommended to transport it as a liquid in LH2 trailers. The third alternative is the use of pipelines for short, medium and large distance transfer of large and very large quantities in gas state, up to 100 tons/h. Finally, the last alternative is the international transport of LH2 via ships, that can transport up to 10000 tons per shipment, but so far there is no experience in this type of transport. For a more detailed study of the advantages and disadvantages of the different hydrogen transport alternatives refer to [21]. The main problems and potential solutions related to transport of hydrogen using tanks, either liquid or gas, have been studied in the previous section. Many projects are also evaluating the possibility of using the already existing natural-gas pipeline infrastructure for high pressure hydrogen transport [22]. The major risk of the pipeline transportation is the hydrogen embrittlement that is complicated to predict [23, 22]. This phenomenon happens when relatively small amounts of hydrogen are absorbed by the pipeline steel, but the expansion caused either by the presence of interstitial hydrogen atoms of the reformation of hydrogen molecules in the voids in the materials can lead to cracking and subsequent leaking from the pipeline [6]. References [6, 24, 23] offer more detailed information about this phenomenon. Another distribution possibility is to produce the hydrogen in small scales at places such as refueling stations using a electrolyzer which will be explained in the next section. With this strategy, the main drawbacks associated to the large scale hydrogen generation and transportation can be avoided [21]. The last distribution possibility is to produce the hydrogen using home energy stations that generates hydrogen for the car from natural gas and can also provide heat and electricity for the home at the same time [25]. This home energy station is designed by the same manufacturers of the Honda FCX Clarity described in the previous section.

An hydrogen infrastructure could be introduced quickly, but only if a sufficient government financial investment is provided [6]. A variety of economic studies to analyze the Market penetration of the hydrogen vehicles in different countries with different energy system models, mainly the MARKAL model, have been made [26, 27, 28, 29, 30]. In overall result of these studies is that the combination of tax-free hydrogen fuel, subsidies on hydrogen vehicles and sufficient hydrogen infrastructure supply will lead to quick market penetration of hydrogen vehicles in less than four decades.

1.1.3 Hydrogen Production

Every kind of energy source can be used in the hydrogen-producing process, and nowadays, the most common source for it is natural gas and other light hydrocarbons. Ironically, one of the reasons to use hydrogen as an energy source is to reduce the emissions of carbon dioxide, but right now, with

more or less 96% of the produced hydrogen coming from fossil fuels' conversion [3], the hydrogen-producing process has become a carbon dioxide producer itself, contributing to the greenhouse effect. This is where renewable energy sources come to play an important role: hydrogen could be produced from waste water, biomass (solid biomass, organic waste, etc.), solar, wind, geothermal, even nuclear energy, which would be a way of clean hydrogen production. At this moment, we have reached the highest carbon dioxide concentrations in at least 500.000 years. This situation makes it imperative to improve renewable sources, so that not only the use of hydrogen will be clean, but also the production process, and have, at the end, a globally environmental-friendly energy source.

1.1.4 Fuel Cell cost reduction

The fuel cell converts chemical energy into electricity, which is generated from the reaction between hydrogen and an oxidizing agent, usually the oxygen in the air. Over the past 170 years, many fuel cells have been developed, but only one seems to have a realistic possibility of being used as an energy source to drive a car: the polymer-electrolyte membrane fuel cells (PEMFCs). These have a low weight, require low gas pressure and operate at relatively low temperatures. Fuel cells working with hydrogen are a clean energy source, but here comes another problem associated with this kind of energy production, and concretely, this fuel cell: platinum, one of the most expensive metals on earth, is used as catalyst material in the polymer electrolyte membrane (PEM) of the PEMFCs, which makes it (at the moment) unsuitable for a sustainable way of energy source, because with this high costs, it is very difficult to compete with battery-based systems. And so researchers are working on decreasing the necessary amount of platinum (which some researchers have been able to reduce an 80%, from the years 2005 to 2010 [1]), or even trying to change the metal for cheaper ones. Researches at Alamos National Laboratory have found a way to produce platinum-free fuel cells, employing carbon, iron and cobalt on the cathod of the PEM-cell. Other researchers opted to replace the platinum with nickel and cobalt, even carbon nanotubes, but none could really archive the same results [6].

The chemistry of each different fuel cell type varies depending on the fuel, operating temperature, nature of the membrane and the composition of its electrolyte. Fuel Cell Today currently considers six main fuel cell types: PEMFC (including HT PEMFC), DMFC, MCFC, PAFC, SOFC and AFC. In terms of commercial success, the leader by far in terms of unit shipments is the PEMFC. This technology serves the biggest number of individual markets and is found throughout the portable, stationary and transport sectors. DMFC is the second most significant type by unit shipments and is mainly found in the portable sector, apart from some niche transport applications. Fuel Cell Today reports shipment numbers to the nearest 100 units, so while all fuel cell types are establishing markets for themselves, some unit shipments are currently too small to appear in our figures.

In megawatt terms the story is very different. The significance of MCFC, SOFC and PAFC in

the large stationary sector makes their contribution much more obvious. With PEMFC expected to be the electrolyte of choice for the automotive industry, its dominance in terms of shipments is likely to continue, but the contribution of other electrolytes to the megawatt total will undoubtedly grow as they are used in more prime power, micro-CHP, large CHP and UPS installations.

1.2 Fuel cell technology

Fuel cells (FC) are electrochemical devices that directly convert the chemical energy of a fuel into electricity. FCs can operate continuously as long as they are provided with sufficient amounts of reactant gases. FCs are generally classified according to the nature of the electrolyte as: proton exchange membrane FC (PEMFC), molten carbonate FC (MCFC), phosphoric acid FC (PAFC), solid oxide FC (SOFC), alkaline FC (AFC). An exception to this rule is the direct methanol FC (DMFC) which received its name for the ability to use methanol as a fuel. Table 1.1 summarizes the main characteristics of the most important FCs. For a detailed study of the historical evolution, principles, types, applications of FCs it can be found an extensive amount of literature [31, 19]. Power systems based on proton exchange membrane fuel cell (PEMFC) technology have been the object of increasing attention in the last years as they appear very promising both stationary and mobile applications, due to their high efficiency, low operating temperature allowing fast startup, high power density, solid electrolyte, long cell and stack life, low corrosion, excellent dynamic response with respect to the other FCs, and nonpolluting emissions to the environment if the hydrogen is obtain of renewable energies. [32, 33, 34]. This the reason because the PEMFCs is the most popular technology in terms of commercial success and megawatt terms as shown in Fig. 1-1

Table 1.1: Main characteristic of the different fuel cells type [1].

	PEMFC	**DMFC**	**MCFC**	**PAFC**	**SOFC**	**AFC**
Electrolyte	Ion exchange membrane (water-based)	Polymer membrane	Immobilised liquid molten carbonate	Immobilised liquid phosphoric acid	Ceramic	Potassium hydroxide
Operation temperature	80 °C	60-130 °C	650 °C	200 °C	1000 °C	60-90 °C
Electrical efficiency	40-60%	40%	45-60%	35-40%	50-65%	45-60%
Typical electrical power	$<$ 250 kW	$<$ 1 kW	$>$ 200 kW	$>$ 50 kW	$<$ 200 kW	$>$ 20 kW
Applications	vehicles, small stationary	Portable	Stationary	Stationary	Stationary	Submarines, spacecraft.

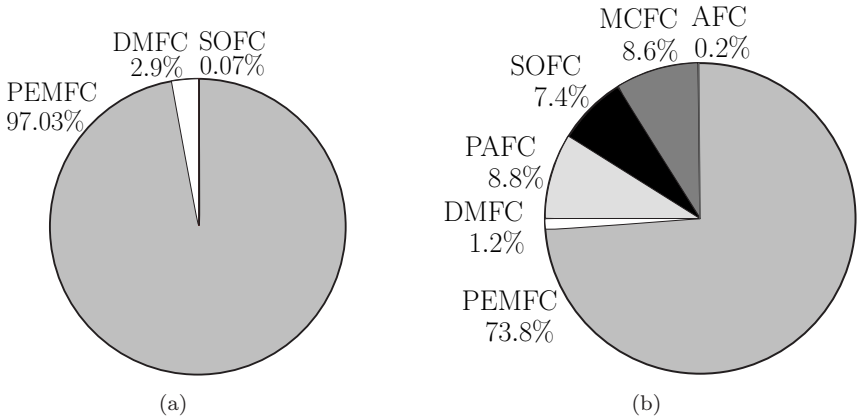

Figure 1-1: Fuel Cell Today reported in [1] (a) Shipments by Fuel Cell Type 2010 (b) MW by Fuel Cell Type 2010

1.2.1 PEMFC principle and structure

The reactant gases used by PEMFCs to produce electrical energy are hydrogen and oxygen. The basic structure and chemical reactions of a PEMFC are depicted in Fig.1-2. Hydrogen, in a gaseous state (H_2), enters into the fuel cell through the bipolar plates' channels on the anode side. These channels allow the distribution of gas uniformly through the entire surface of the gas diffusion layer. Then, the hydrogen molecule goes to the anode catalytic layer, where it is dissociated as electrons and protons

$$2H_2 \rightarrow 4H^+ + 4e^-. \tag{1.1}$$

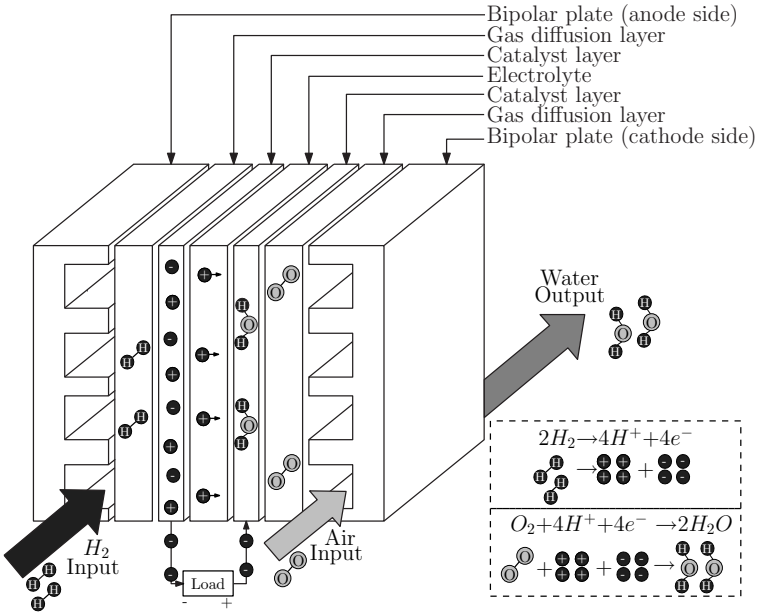

Figure 1-2: Basic structure and chemical reactions of a PEMFC.

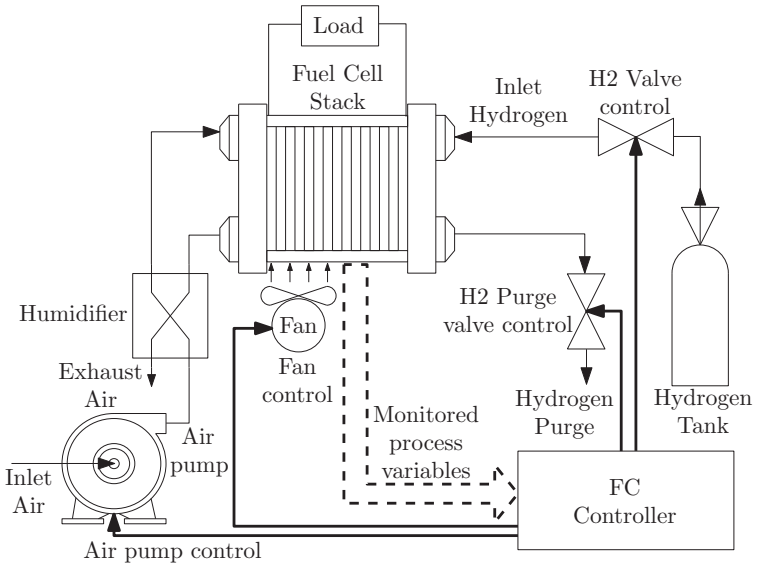

Figure 1-3: PEMFC system with main control subsystems.

The electrons flow through the electric load to the catalytic layer of the cathode, whilst the protons travel through the electrolyte membrane. The membrane blocks the flow of electrons to the catalyst layer on the cathode side. On the other side, the oxygen in a gaseous state (O_2), flows to the catalyst layer of the cathode from the bipolar plates channels within the cathode. Finally, the oxygen, the hydrogen protons and the electrons react to generate water onto the catalyst layer on the cathode side. The exothermic reaction is as follows

$$O_2 + 4H^+ + 4e^- \rightarrow 2H_2O + \ heat. \tag{1.2}$$

Each cell, as depicted in Fig. 1-2, generates a low dc voltage and a high dc current. In order to reach the power requirements of the load, as well as a sufficient level of dc voltage, it is necessary to connect individual FCs in series, what is known as a stack. The FC stack is a complex system that requires an auxiliary power-conditioning system to ensure safe, reliable and efficient operation under different operating conditions. In general, a PEMFC system includes four subsystems that manage the air, the hydrogen, the humidity, and the stack temperature, as shown in Fig. 1-3.

The output-voltage characteristics in the PEMFC are limited by the mechanical devices which are used for maintaining the air flow in the cathode by means of a compressor motor, the hydrogen flows in the anode through a controlled valve, the temperature is controlled using a cooling fan, and the humidity of the air in the cell by means of a humidity exchanger. Hence, the time constants are dominated by fuel delivery system. As a consequence, a fast load transient demand could cause a high voltage drop in a short time known as oxygen starvation phenomenon [35]. This condition of operation is harmful for the FC and for this reason it is considered as a slow dynamic response

equipment with respect to the load transient requirements. Therefore, batteries, ultracapacitors or other auxiliary power sources are needed to support the operation of the FC in order to ensure a fast response to any load power transient as shown in the Ragone plot of Fig. 1-4. The systems formed by a FC and an other auxiliary power source, known as FC hybrid systems, have been extensively researched over recent years [36, 37, 38, 39]. These hybrid systems can limit the slope of the current or the power generated by the FC with the use of current-controlled dc-dc converters. In this way, the reactant gas starvation phenomena can be avoided and the system can operate with higher efficiency [40, 41, 42, 43]. In this context, Chapter 2 is focused in the design of a DC-DC converter suitable to interconnect all the different elements in a PEMFC-hybrid 48-V DC bus. Since the converter could be placed between elements with very different voltage levels, a buck-boost structure has been selected. To fulfill the low ripple requirements of the PEMFCs our structure has inductors in series at its input and output. Magnetically coupling these inductors and adding a damping network to its intermediate capacitor we have designed an easily controllable converter. The Chapter 2 shows the high efficiency of the converter and the wide bandwidth of the voltage regulator initially tested. The current control of the converter is addressed in Chapter 3. The magnetic coupling allows to control either the input or the output inductor currents. This is very useful because the designer current-controlled converter is able to withstand shortcircuits at its output and when connected to the FC facilitates to regulate the current extracted from the FC to avoid the oxygen starvation phenomenon. To test in a safe way the converter connected to the FC it was decided to build the FC simulator presented in Chapter 4. The basic capabilities in simulating the FC behaviour were improved by the emulator developed in Chapter 5 that offers real-time processing and oxygen-starvation indication. To test the developed converters and emulators with different brands of PEMFC it was necessary to reactivate long-time inactive Palcan FCs. Since the results provided by the manual reactivation procedure were unsatisfactory, the automatic reactivation system presented in Chapter A has been developed.

1.3 List of publications

The main contributions in this project have been presented in the following publications and a submitted paper.

Journal papers:

I C. Restrepo, J. Calvente, A. Cid-Pastor, A.E. Aroudi, R. Giral, “A Noninverting BuckBoost DCDC Switching Converter With High Efficiency and Wide Bandwidth”, IEEE Transactions on Power Electronics, Vol. 26, No. 9, pp. 2490-2503, ISSN 0885-8993, Sept. 2011.

II C. Restrepo, J. Calvente, A. Romero, E. Vidal-Idiarte, R. Giral, “Current-Mode Control of

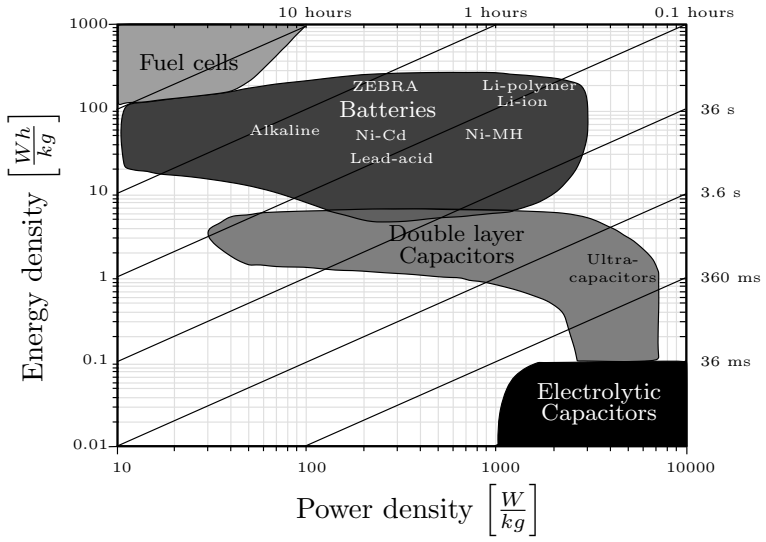

Figure 1-4: Ragone plot which describes the energy storage technologies in terms of energy density and power density. Diagonal lines represent different characteristic times obtained by dividing the energy density by the power density.

a Coupled-Inductor BuckBoost DCDC Switching Converter", IEEE Transactions on Power Electronics, Vol.27, No.5, pp. 2536-2549, ISSN 0885-8993, May 2012.

III C. Restrepo, C.A. Ramos-Paja, R. Giral, J. Calvente, A. Romero, "Fuel cell emulator for oxygen excess ratio estimation on power electronics applications", Computers & Electrical Engineering, Vol.38, No.4, pp. 926-937, ISSN 0045-7906, July 2012.

IV C. Restrepo, T. Konjedic, J. Calvente, R. Giral, "A review of the main power electronics' advances in order to ensure efficient operation and durability of PEMFCs", Automatika Journal for Control, Measurement, Electronics, Computing and Communications, Online ISSN 1848-3380, Print ISSN 0005-1144, Vol.2, No.53, pp. 184-198, April - June 2012.

V C. Restrepo, O. Aviño, J. Calvente, A. Romero, M. Milanovič, R. Giral, "Reactivation System for Proton-Exchange Membrane Fuel-Cells", Submitted to Energies, ISSN 1996-1073.

VI C. Restrepo, J. Calvente, R. Giral, A. Romero,"PEM fuel cell digital emulator based in a dynamic circuital model adjusted with an evolutionary algorithm (Spanish)", Submitted to Revista Iberoamericana de Automática e Informática Industrial, ISSN 1697-7912.

VII C. Restrepo, T. Konjedic, J. Calvente, M. Milanovič, R. Giral,"Fast Transitions Between Current Control Loops of the Coupled-Inductor Buck-Boost DC-DC Switching Converter", Submitted to Power Electronics Letters, ISSN 1540-7985.

Full papers in conferences with oral presentation:

I C. Restrepo, J. Calvente, R. Giral, M. Milanovič, "Virtual instrument for the characterization of inductors at different operation points", XIII International PhD Workshop OWD 2011, ISBN 83-922242-8-0, Wisla, Poland, 22-25 Oct. 2011.

II C. Restrepo, J. Calvente, R. Giral, A Gárces, A. Romero, "Algoritmo Evolutivo para la determinación de los parámetros de un modelo circuital en el análisis de la Espectroscopia de Impedancia Eléctrica (Spanish)", Seminario Anual de Automática, Electrónica e Instrumentación SAAEI 2010, The University of the Basque Country, ISBN 978-84-95809-75-9, Bilbao, Spain, 7-9 Jun. 2010.

III C. Restrepo, C. Torres, J. Calvente, R. Giral, R. Leyva, A. Romero, J. Molina, "Emulador digital de una pila de combustible PEM basado en un modelo dinámico (Spanish)", Seminario Anual de Automática, Electrónica e Instrumentación SAAEI 2009, Carlos III University of Madrid, ISBN 978-84-692-2596-7, Madrid, Spain, 1-3 Jul. 2009.

IV C. Torres, R. Leyva, C. Restrepo, J. Calvente, "Modelado de un convertidor Buck-Boost mediante la técnica difusa Takagi-Sugeno (Spanish)", Seminario Anual de Automática, Electrónica e Instrumentación SAAEI 2009, Carlos III University of Madrid, ISBN 978-84-692-2596-7, Madrid, Spain, 1-3 Jul. 2009.

V C. Restrepo, J. Calvente, R. Giral, "Instrumento virtual para obtener el modelo del inductor en diferentes puntos de operación (Spanish)", Seminario Anual de Automática, Electrónica e Instrumentación SAAEI 2008, Technical University of Cartagena, ISBN 978-84-969-9704-2, Cartagena, Spain, 9-11 Sep. 2008.

VI H. Ramírez, C. Restrepo, J. Calvente, A. Romero, R. Giral, "Sistemas de Arranque para un Convertidor Buck-Boost en un Bus DC (Spanish)", Accepted in the Seminario Anual de Automática, Electrónica e Instrumentación SAAEI 2012, University of Minho, Guimaraẽs, Portugal, 11-13 Jul. 2012.

VII Aviño, C. Restrepo, A. Romero, R. Giral, J. Calvente, E. Vidal-Idiarte, "Sistema de seguimiento de la tasa de exceso de oxígeno para pilas de combustible mediante cálculo simplificado (Spanish)", Accepted in the Seminario Anual de Automática, Electrónica e Instrumentación SAAEI 2012, University of Minho, Guimaraẽs, Portugal, 11-13 Jul. 2012.

Poster presentation:

I C. Restrepo, C. Torres, J. Calvente, R. Giral, R. Leyva, "Simulator of a PEM Fuel-Cell Stack based on a Dynamic Model", 35th Annual Conference of IEEE Industrial Electronics 2009 IECON'09, pp. 2796-2801, University of Porto, Porto, Portugal, 3-5 Nov. 2009.

Other publications:

I C. Torres, C. Restrepo, A. Alzate,"Static and dynamic design guidelines for dc-dc converters (Spanish)", Scientia et Technica, Vol.42, pp. 57-62, ISSN 0122-1701, Aug. 2009.

II C. Torres, D. Murillo, C. Restrepo, "Design and Construction of a Three-phase inverter (Spanish)", Scientia et Technica, Vol.40, pp. 37-42, ISSN 0122-1701, Dec. 2008.

III A. Alzate, C. Torres, C. Restrepo, "Design of a Power System Stability Fuzzy based in the technique LMI (Spanish)", Scientia et Technica, Vol.40, pp. 31-36, ISSN 0122-1701, Dec. 2008.

IV A. Alzate, C. Torres, C. Restrepo, "Control of a STATCOM on a Power System by Means of Pole Placement and LQR (Spanish)", Scientia et Technica, Vol.39, pp. 66-71, ISSN 0122-1701, Sep. 2008.

V A. Alzate, C. Torres, C. Restrepo, "Design of the Parameters based in Evolutionary Technique of a Power System Stability (Spanish)", Scientia et Technica, Vol.37, pp. 31-36, ISSN 0122-1701, Dec. 2007.

Chapter 2

A Non-Inverting Buck-Boost DC-DC Switching Converter with High Efficiency and Wide Bandwidth

2.1 Abstract

A novel DC-DC switching converter consisting of a boost stage cascaded with a buck converter with magnetically coupled coils is presented. The converter has the same step-up or step-down voltage conversion properties as the single inductor non-inverting buck-boost converter but exhibits non-pulsating input and output currents. The converter's control-to-output transfer function is continuous between operation modes if a particular magnetic coupling is selected. The addition of a damping network improves the dynamics and results in a control-to-output transfer function that, even in boost mode, has two dominant complex poles without right half plane zeroes. An example shows that an output voltage controller can be designed with the same well-known techniques usually applied to the second-order buck regulator. Details of a prototype and experimental results including efficiency, frequency and time domain responses are presented. The experimental results validate the theoretical expected advantages of the converter, namely, good efficiency, wide bandwidth and simplicity of control design.

2.2 Introduction

In such converter applications as battery charging and discharging, power factor correction, fuel cell regulation, and maximum power point tracking of solar panels, a DC-DC converter is used to obtain a regulated voltage from an unregulated source. When the regulated voltage is within the voltage range of the unregulated voltage source, a step-up/step-down DC-DC converter is required [44, 45, 46, 47, 48, 49, 50, 51, 52, 53, 54, 55, 56].

Step-up/step-down DC-DC converters with a single active switch, such as buck-boost, flyback, Sepic and Ćuk topologies, have high component stresses and low efficiencies at the same operating point as the boost or the buck converter if the output voltage is greater or smaller than the input voltage, respectively [57].

It is possible to combine a buck converter with a boost converter to obtain a two independently controllable switch buck-boost converter, the size and performance comparable to those of the simple buck or boost stages [58]. For example, the cascade combination of a buck and a boost stages results in a single inductor non-inverting buck-boost converter with high performance which is widely used in low voltage applications [47, 48, 49, 50, 51]. These converters do not operate in buck-boost mode, because it is more efficient to operate them in either buck mode if the output voltage is lower than the input one or in boost mode otherwise [45]. Some non-inverting buck-boost converters are high efficient at higher operational voltages [55, 56] but have the drawback that they have a complex control. In [55], the authors state that the detailed modelling of the plant and the controller is currently ongoing. In [56], the output voltage regulators required depend on whether the mode of operation is boost or buck.

The single inductor non-inverting buck-boost converter is used in applications in which it is important for the magnetic elements to be small and cheap. However, when the voltages are high, the size of the converter's capacitors is also important. In this case, it would be appropriate to use the cascade buck-boost power converter that has two inductors, one at the input and the other at the output [44, 46]. With these inductors, the input and output currents are non-pulsating, the noise level is lower, and the currents are easier to control and limit than in the pulsating case.

Most of the converters mentioned earlier, when operating in continuous conduction boost mode, have a right-half-plane (RHP) zero that difficults to design their controller, limits the bandwidth of the loop and penalizes the size of the output capacitor [49]. One possible solution to these problems is the topology called the KY buck-boost converter [59]. This converter has a very fast transient response, which is achieved by using switched capacitors for energy transfer, and it is recommended

for low-power applications. The tristate boost converter reported in [60] eliminates the RHP zero but is not very efficient; besides, this technique has never been applied to the buck-boost topology. In [54] a two-inductor boost superimposed with a buck converter satisfactorily solves the RHP zero problem but both active switches of the structure are floating, which requires complex drivers. Another solution to the problem of the RHP zeros adopted in the work reported here is to use magnetic coupling between inductors [61] combined with damping networks [62, 63]. This solution has made it possible to design high-power boost converters with high efficiency and wide bandwidth [64, 65, 66].

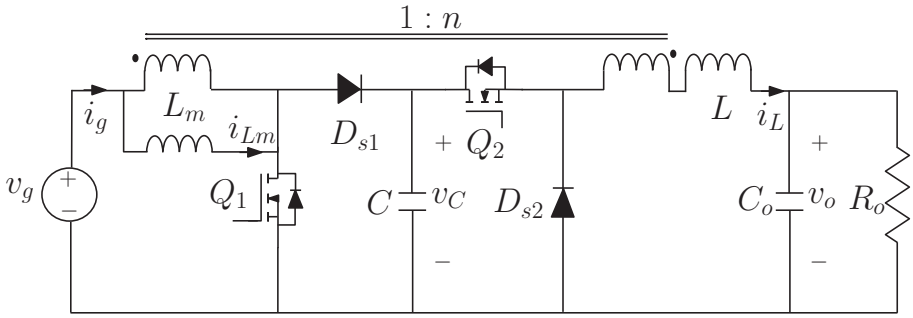

Figure 2-1: Schematic circuit diagram of the buck-boost converter with magnetic coupling between inductors.

The purpose of this chapter is to analyze the cascaded connection of a boost and buck converter, with magnetic coupling between inductors, shown in Fig. 2-1. This converter can operate in boost mode, as in Fig. 2-2(a), and buck mode, as in Fig. 2-2(b). Both topologies have non-minimum phase transfer functions under certain parametric conditions and have been proposed for battery charge/discharge regulators for satellites [67]. As will be seen, the proposed converter exhibits high efficiency in the desired range of operation in spite of using diodes instead of synchronous rectification. It also presents a wide bandwidth and low current ripples that reduce the size of the input capacitor and especially that of the output one. Finally, the converter control is simpler that the state-of-the-art, which could reduce design costs.

The remainder of this chapter is organized as follows. Section 2.3 presents the key waveforms of the converter and discusses the small-signal converter model. In the same section, the turns ratio n of the transformer is also determined, thus avoiding the need for two transfer functions, namely, one for the buck mode and another for the boost mode, is also determined. This means that the same transfer function can be used to describe the converter in both modes and simplifies the controller design. A damping network is added in Section 2.4 where analytical expressions are obtained to design a minimum phase transfer function. Section 2.5 focuses on a complete circuit design for the buck-boost converter and its control. Finally, the last two sections present simulated and experimental results, and the conclusions of this work.

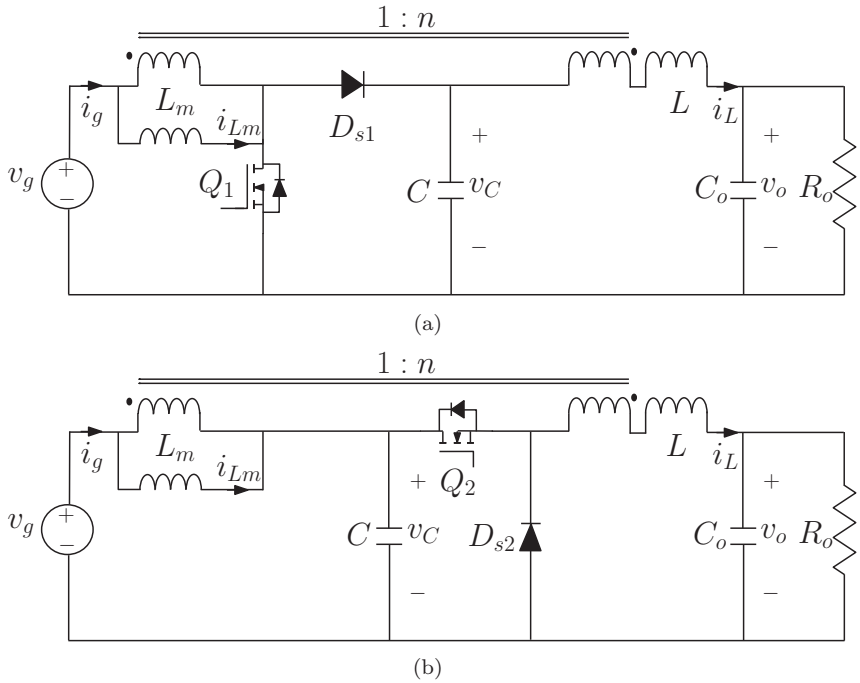

Figure 2-2: Operating modes of the buck-boost converter: (a) boost mode; (b) buck mode.

2.3 Analysis of the Buck-Boost Converter with magnetic coupling between inductors

Lets us consider the unidirectional buck-boost converter with magnetic coupling between the input and output inductors shown in Fig. 2-1. The typical current and voltage waveforms of this converter in steady state are depicted in Fig. 2-3. In boost mode, the currents are shown in Fig. 2-3 (a) and the corresponding voltages in Fig. 2-3 (b). Fig. 2-3 (c) and (d) represent current and voltage waveforms in buck mode. The bottom traces of each plot correspond to u_1 and u_2, which are, respectively, the logic activation signals of switches Q_1 and Q_2. In boost mode $u_2 = 1$ while u_1 switches whereas in buck mode $u_1 = 0$ while u_2 switches. The duty cycles of u_1 and u_2 have been adjusted to obtain a mean output voltage of 48 V. In a typical design, the ripple in the intermediate capacitor voltage v_C is bigger than that of the output voltage, which makes it possible to use a small intermediate capacitor. As can be observed in Fig. 2-3, a common characteristic of the two operation modes is that currents i_g and i_L are non-pulsating with a triangular-shaped ripple.

Assuming a continuous conduction mode (CCM) of operation, no parasitic effects and a switching frequency much higher than the converter natural frequencies, the use of the state-space averaging (SSA) method [68] to model the converter leads to the following set of differential equations

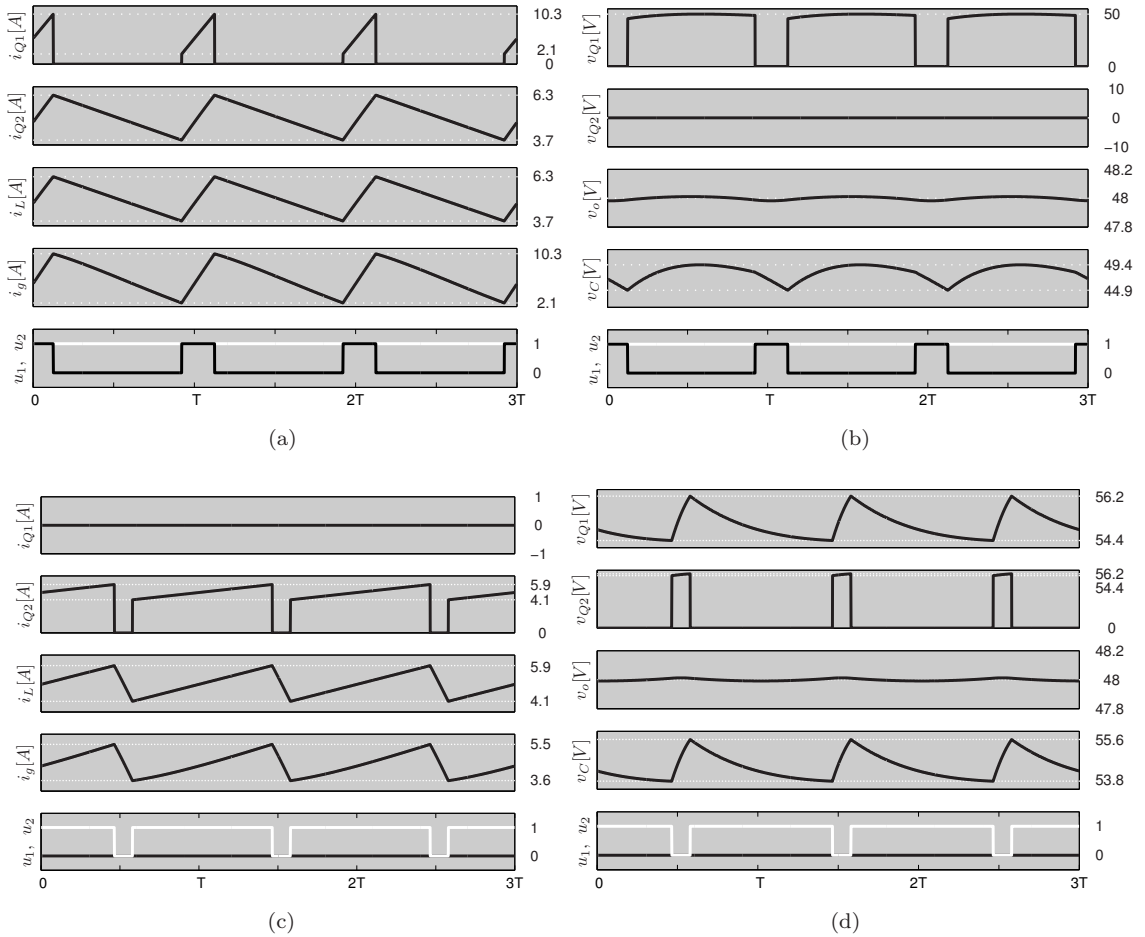

Figure 2-3: Typical waveforms of Fig 2-1 converter for $V_o = 48$ V: (a), (b) currents and voltages in boost mode with $V_g = 39$ V; (c), (d) currents and voltages in buck mode with $V_g = 55$ V. Logic signals u_1 (in black) and u_2 (in white) indicate switch Q_1 and Q_2 states, respectively.

$$\begin{aligned}
\frac{d\bar{i}_{L_m}(t)}{dt} &= \frac{v_g(t) - \overline{v}_C(t)(1 - d_1(t))}{L_m} \\
\frac{d\bar{i}_L(t)}{dt} &= \frac{\overline{v}_C(t)d_2(t) + n(v_g(t) - \overline{v}_C(t)(1 - d_1(t))) - \overline{v}_o(t)}{L} \\
\frac{d\overline{v}_C(t)}{dt} &= \frac{-\bar{i}_L(t)d_2(t) + (\bar{i}_{L_m}(t) + n\bar{i}_L(t))(1 - d_1(t))}{C} \\
\frac{d\overline{v}_o(t)}{dt} &= \frac{\bar{i}_L(t)}{C_o} - \frac{\overline{v}_o(t)}{R_o C_o}
\end{aligned} \tag{2.1}$$

where d_1 and d_2 are the duty cycles of the switches Q_1 and Q_2, respectively, and the overline stands for averaging during one switching period. To analyze the pulse-width-modulated (PWM) converters operating in CCM the PWM-switch modeling method presented in [69] can be used. This method describes the way in which the active switches, Q_1 and Q_2, and the passive switches, D_{s1} and D_{s2} can be replaced by current and voltage controlled sources. The controlled current source expression

corresponds to the product of the duty cycle and the current through the corresponding MOSFET switch when this is closed. Similarly, the controlled voltage source is the product of the duty cycle and the the voltage blocked by switch diode. Fig. 2-4(a) presents the converter shown in Fig. 2-1 with its respective controlled sources. This PWM-switch model gives exactly the same equations (2.1) as the SSA method. Assuming that the converter is in steady state with constant duty cycles, $d_1(t) = D_1$ and $d_2(t) = D_2$, and input voltage $v_g(t) = V_g$, and using the principles of inductor volt-second and capacitor charge balance [57], the steady-state expressions of the inductor currents and capacitor voltages are

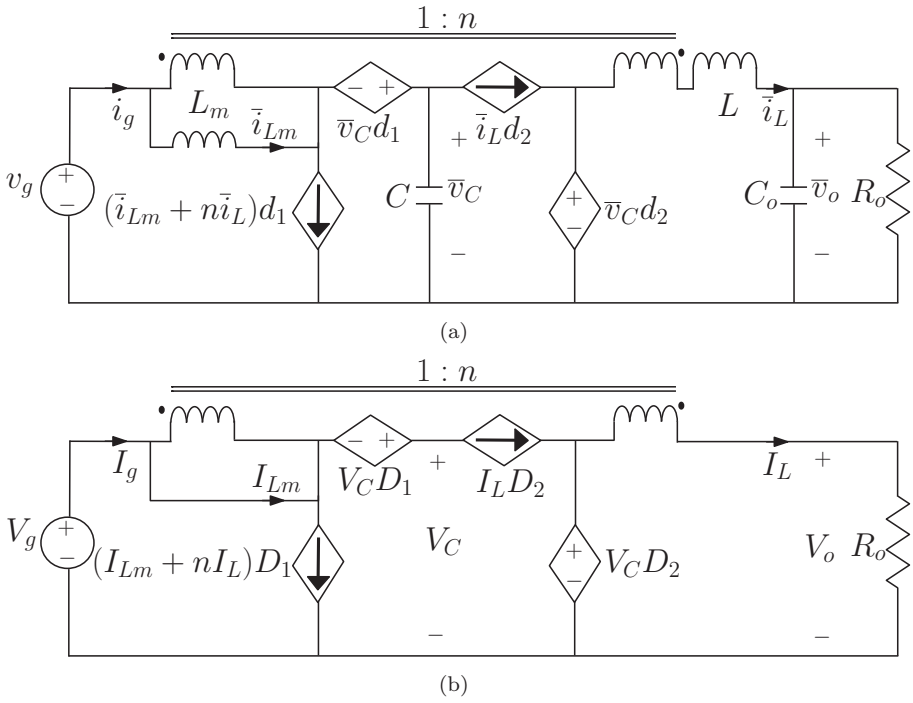

Figure 2-4: Schematic circuit diagrams of the buck-boost converter with magnetic coupling between inductors: (a) large-signal averaged model and (b) DC model.

$$\begin{aligned} I_{L_m} &= \frac{V_g D_2(D_2 - n + nD_1)}{R_o(1-D_1)^2} \\ I_L &= \frac{V_g D_2}{R_o(1-D_1)} \\ V_C &= \frac{V_g}{1-D_1} \\ V_o &= \frac{V_g D_2}{1-D_1}. \end{aligned} \tag{2.2}$$

These equations could also be derived from (2.1) by noting that, in steady-state, the derivatives are zero or, equivalently, from the DC circuit of Fig 2-4(b). It is worth noting that the DC values of

the state variables $\overline{v}_o$, $\overline{v}_C$ and $\overline{i}_L$ do not depend on the transformer turns ratio n. From the output capacitor voltage V_o in (2.2), the voltage conversion ratio $M(D_1, D_2)$ is given by

$$M(D_1, D_2) \equiv \frac{V_o}{V_g} = \frac{D_2}{1 - D_1}. \tag{2.3}$$

Our goal is for the converter operate either in boost mode ($0 < D_1 < 1$ and $D_2 = 1$) or buck mode ($0 < D_2 < 1$ and $D_1 = 0$), and switch smoothly from one mode to another. Let us define a single control variable u that can take the values between 0 and 2 ($0 < u < 2$). The duty cycles D_1 and D_2 are related to the new variable u as

$$\begin{aligned} D_1 &= \max(0, u - 1) \\ D_2 &= \min(1, u). \end{aligned} \tag{2.4}$$

The new voltage conversion ratio can be expressed as follows

$$M(u) = \frac{\min(1, u)}{1 - \max(0, u - 1)}. \tag{2.5}$$

With this control input, the DC voltage conversion ratio $M(u)$ is continuous between the boost and buck modes of operation, as depicted in Fig. 2-5(a). On the border between the two modes of operation $u = 1$, so $D_1 = 0$ and $D_2 = 1$. Fig. 2-5(b) shows how to generate the switch activation signals $u_1(t)$ and $u_2(t)$ from the control signal $u(t)$, and a symmetric triangular wave of amplitude $V_{ramp} = 1$ V.

To obtain a small-signal model around a steady-state operating point, we assume that the input voltage is constant and the duty cycles $d_1(t)$ and $d_2(t)$ are equal to D_1 and D_2 plus some superimposed small AC variations $\widehat{d}_1(t)$ and $\widehat{d}_2(t)$, respectively,

$$\begin{aligned} v_g(t) &= V_g \\ d_1(t) &= D_1 + \widehat{d}_1(t) \\ d_2(t) &= D_2 + \widehat{d}_2(t). \end{aligned} \tag{2.6}$$

After these inputs are considered, the averaged inductor currents and capacitor voltages can also be expressed in terms of their corresponding steady-state values plus some superimposed small AC variations

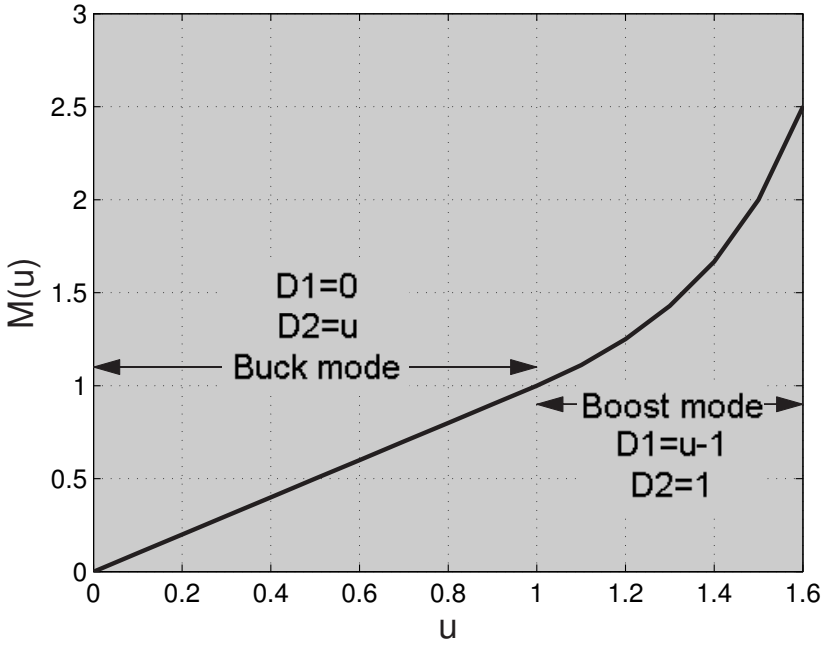

(a)

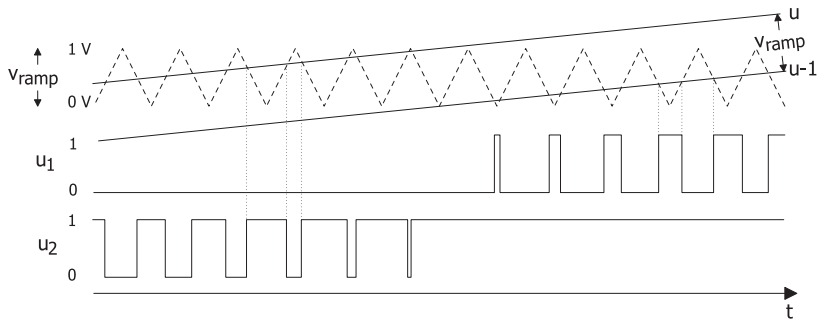

(b)

Figure 2-5: (a) DC conversion ratio $M(u)$ of the buck-boost converter.; (b) activation signal generation: comparison of control signals with a triangular signal to obtain the MOSFETs binary activation signals $u_1(t)$ and $u_2(t)$.

$$\begin{aligned} \overline{i}_{L_m}(t) &= I_{L_m} + \widehat{i}_{L_m}(t) \\ \overline{i}_L(t) &= I_L + \widehat{i}_L(t) \\ \overline{v}_C(t) &= V_C + \widehat{v}_C(t) \\ \overline{v}_o(t) &= V_o + \widehat{v}_o(t). \end{aligned} \tag{2.7}$$

Assuming that the AC variations are much smaller than the steady-state values, the set of differential equations (2.1) can be linearized. The small signal state-space vector $\widehat{x}$ is defined as

$$\widehat{x} = \begin{bmatrix} \widehat{i}_{L_m} & \widehat{i}_L & \widehat{v}_C & \widehat{v}_o \end{bmatrix}^T. \tag{2.8}$$

Linearizing (2.1) around the equilibrium point (2.2) and separating the dynamic AC small-signal terms from the DC steady-state component, the following dynamic model is obtained:

$$\frac{d\widehat{x}}{dt} = A\widehat{x} + B_1\widehat{d}_1 + B_2\widehat{d}_2 \tag{2.9}$$

where A is the state matrix and B_1 and B_2 are, respectively, the input vectors corresponding to d_1 and d_2

$$A = \begin{bmatrix} 0 & 0 & \frac{D_1-1}{L_m} & 0 \\ 0 & 0 & \frac{D_2+n(-1+D_1)}{L} & -\frac{1}{L} \\ \frac{1-D_1}{C} & \frac{n(1-D_1)-D_2}{C} & 0 & 0 \\ 0 & \frac{1}{C_o} & 0 & -\frac{1}{R_oC_o} \end{bmatrix}$$

$$B_1 = \begin{bmatrix} -\frac{V_g}{L_m(D_1-1)} & -\frac{nV_g}{L(D_1-1)} & -\frac{V_g{D_2}^2}{CR_o(D_1-1)^2} & 0 \end{bmatrix}^T$$

$$B_2 = \begin{bmatrix} 0 & -\frac{V_g}{L(D_1-1)} & \frac{V_gD_2}{CR_o(D_1-1)} & 0 \end{bmatrix}^T.$$

Hence, on the boundary between the two modes of operation, the small-signal control-to-output transfer function with respect to the duty cycle $\widehat{d}_1$ is

$$G_{vod_1}(s)\Big|_{u=1} \equiv \frac{\widehat{v}_o(s)}{\widehat{d}_1(s)}\Big|_{u=1} = \frac{\mathcal{N}_1(s)}{\mathcal{D}(s)} \tag{2.10}$$

where

$$\begin{aligned} \mathcal{N}_1(s) &= V_g(R_onCL_ms^2 + (L_mn - L_m)s + R_o) \\ \mathcal{D}(s) &= L_mCLR_oC_os^4 + L_mCLs^3 + (L_mR_oC_o - 2L_mnR_oC_o + L_mCR_o + LR_oC_o + L_mn^2R_oC_o)s^2 \\ &\quad + (L_m - 2L_mn + L_mn^2 + L)s + R_o. \end{aligned}$$

In the same way, the small-signal control-to-output transfer function with respect to the duty cycle $\widehat{d}_2$ is

$$G_{vod_2}(s)\Big|_{u=1} \equiv \frac{\widehat{v}_o(s)}{\widehat{d}_2(s)}\Big|_{u=1} = \frac{\mathcal{N}_2(s)}{\mathcal{D}(s)} \tag{2.11}$$

where

$$\mathcal{N}_2(s) = V_g(R_oCL_ms^2 + (L_mn - L_m)s + R_o).$$

If the turns ratio n is equal to 1, the transfer functions $G_{vod_1}(s)$ and $G_{vod_2}(s)$ are coincident, and

$$G_{vod_1}(s)\Big|_{u=1;\ \ n=1} = G_{vod_2}(s)\Big|_{u=1;\ \ n=1} = \frac{V_gR_o}{LR_oC_os^2 + Ls + R_o}. \tag{2.12}$$

A similar procedure can be used to determine the small-signal control-to-output transfer functions $G_{i_Ld_1}(s)$ and $G_{i_Ld_2}(s)$. These transfer functions are also identical between the two modes of operation if $n = 1$

$$G_{i_Ld_1}(s)\Big|_{u=1;\ \ n=1} = G_{i_Ld_2}(s)\Big|_{u=1;\ \ n=1} = \frac{V_g(R_oC_os + 1)}{LR_oC_os^2 + Ls + R_o}. \tag{2.13}$$

Selecting $n = 1$, the dynamic characteristics of the output voltage and output current are continuous between the boost and buck modes, as shown in (2.12) and (2.13), but there is a double zero-pole cancellation, which indicates an uncontrollable internal dynamics. On the other hand, the small-signal control-to-output transfer function $G_{vo_{d_1}}(s)$ in boost mode ($u > 1$) with $D_2 = 1$ and $n = 1$ is

$$G_{v_od_1}(s)\Big|_{D_2=1;n=1} = \frac{\mathcal{N}_3(s)}{\mathcal{D}_3(s)} \tag{2.14}$$

where

$$\mathcal{N}_3(s) = V_g[(L_mCR_o - L_mCR_oD_1)s^2 - L_mD_1s + (Ro + RoD_1{}^2 - 2R_oD_1)] \tag{2.15}$$

$$\begin{aligned}\mathcal{D}_3(s) \quad = \quad & (D_1 - 1)^2(L_mCLR_oC_os^4 + L_mCLs^3 + (L_mD_1{}^2R_oC_o + L_mCR_o + LR_oC_o - 2D_1LR_oC_o \\ & + D_1{}^2LR_oC_o)s^2) + (L_mD_1{}^2 + L - 2D_1L + D_1{}^2L)s + (R_o - 2R_oD_1 + R_oD_1{}^2)).\end{aligned} \tag{2.16}$$

According to (2.15), $G_{v_od_1}$ has two RHP zeroes. The presence of these RHP zeroes tends to destabilize wide bandwidth feedback loops and makes the converter prone to oscillation [58]. The dynamics of the zeroes is the inner behavior of the system when the control regulates the output without error, e.g., the poles are attracted by the zeroes in a high gain closed loop linear system. In a converter with an ideal regulation of the output voltage, the inner dynamics is usually associated to the input filter. Thanks to the magnetic coupling, the dynamics of the zeroes of our converter in boost mode is of second order, associated to the variables i_{Lm} and v_c. Note that the zeroes in (2.15) depend on the parameters L_m and C. Therefore, damping the dynamics of i_{Lm} and/or v_c by adding a passive network could transfer the RHP zeroes to the left-half-plane (LHP). Following a similar procedure to the one reported in [61]-[62], a passive network was connected to the intermediate capacitor. This damping network can be seen as a low frequency snubber. The modified procedure

for calculating the parameter values of the passive damping network will be given in the next section.

2.4 Analysis of the coupled inductors Buck-Boost Converter with damping network

In this section, the buck-boost converter with the damping network included, which is depicted in Fig. 2-6, will be analyzed. The damping network consists of a series connection of a resistor R_d and a capacitor C_d connected in parallel with the converter intermediate capacitor C. With this damping network included and doing $n = 1$, the SSA model in CCM is

$$\begin{aligned}
\frac{d\bar{i}_{L_m}(t)}{dt} &= \frac{v_g(t) - \overline{v}_C(t)(1 - d_1(t))}{L_m} \\
\frac{d\bar{i}_L(t)}{dt} &= \frac{\overline{v}_C(t)d_2(t) + v_g(t) - \overline{v}_C(t)(1 - d_1(t)) - \overline{v}_o(t)}{L} \\
\frac{d\overline{v}_C(t)}{dt} &= \frac{-\bar{i}_L(t)d_2(t) + (\bar{i}_{L_m}(t) + \bar{i}_L(t))(1 - d_1(t))}{C} - \frac{\overline{v}_C(t) - \overline{v}_{C_d}(t)}{CR_d} \\
\frac{d\overline{v}_{C_o}(t)}{dt} &= \frac{\bar{i}_L(t)}{C_o} - \frac{\overline{v}_o(t)}{CR_o} \\
\frac{d\overline{v}_{C_d}(t)}{dt} &= \frac{\overline{v}_C(t) - \overline{v}_{C_d}(t)}{C_dR_d}.
\end{aligned} \tag{2.17}$$

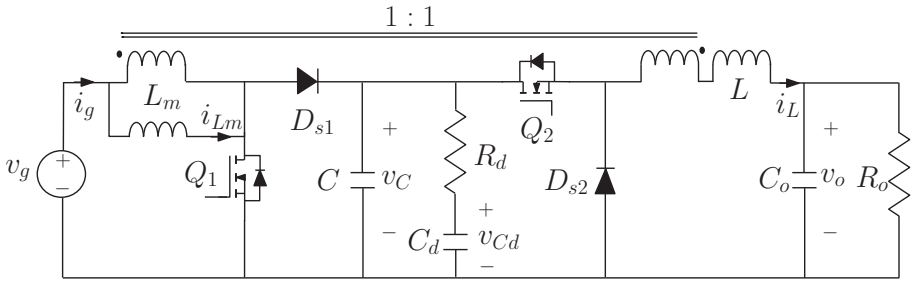

Figure 2-6: Coupled inductor buck-boost converter with RC type damping network and turns ratio 1:1 ($n = 1$).

As can be expected from (2.2), with $n = 1$ and the steady-state behavior of V_{C_d}, the converter operating point for constant duty cycles $d_1(t) = D_1$, $d_2(t) = D_2$, and input voltage $v_g(t) = V_g$ is

$$\begin{aligned} I_{L_m} &= \frac{V_g D_2 (D_2 + D_1 - 1)}{R_o (1 - D_1)^2} \\ I_L &= \frac{V_g D_2}{R_o (1 - D_1)} \\ V_C &= \frac{V_g}{1 - D_1} \\ V_{C_d} &= \frac{V_g}{1 - D_1} \\ V_o &= \frac{V_g D_2}{1 - D_1}. \end{aligned} \tag{2.18}$$

Linearizing the set of equations (2.17) around the operating point (2.18), we obtain the small-signal SSA model

$$\frac{d\widehat{x}}{dt} = A\widehat{x} + B_1\widehat{d}_1 + B_2\widehat{d}_2 \tag{2.19}$$

where the small signal state vector $\widehat{x}$, the state matrix A and the input vectors B_1 and B_2 of the system are now given by

$$\widehat{x} = \begin{bmatrix} \widehat{i}_{L_m} & \widehat{i}_L & \widehat{v}_C & \widehat{v}_{C_d} & \widehat{v}_o \end{bmatrix}^T$$

$$A = \begin{bmatrix} 0 & 0 & \frac{D_1-1}{L_m} & 0 & 0 \\ 0 & 0 & \frac{D_2+D_1-1}{L} & 0 & -\frac{1}{L} \\ \frac{1-D_1}{C} & \frac{1-D_2-D_1}{C} & -\frac{1}{R_d C} & \frac{1}{R_d C} & 0 \\ 0 & 0 & \frac{1}{R_d C_d} & -\frac{1}{R_d C_d} & 0 \\ 0 & \frac{1}{C_o} & 0 & 0 & -\frac{1}{R_o C_o} \end{bmatrix}$$

$$B_1 = \begin{bmatrix} -\frac{V_g}{L_m(D_1-1)} & -\frac{V_g}{L(D_1-1)} & -\frac{V_g {D_2}^2}{C R_o (D_1-1)^2} & 0 & 0 \end{bmatrix}^T$$

$$B_2 = \begin{bmatrix} 0 & -\frac{V_g}{L(D_1-1)} & \frac{V_g D_2}{C R_o (D_1-1)} & 0 & 0 \end{bmatrix}^T.$$

The transfer functions $G_{vod_1}(s)$ and $G_{vod_2}(s)$ now have a third-order numerator and a fifth-order denominator with two dominant complex poles. On the border between buck and boost operation modes, where $u = 1$, there is a triple zero-pole cancellation and the two transfers function correspond to expression (2.12). Since this control-to-output transfer function is identical to that of a second-order buck converter, it is possible to design its control loop compensator in the same well-known way if the internal dynamics corresponding to the cancelled poles is sufficiently damped. The poles of the internal dynamics are the roots of the cancelled polynomials in

$$G_{vod_1}(s)\Big|_{u=1} = G_{vod_2}(s)\Big|_{u=1} = \frac{p(s)(V_g R_o)}{p(s)(LR_oC_os^2 + Ls + R_o)} \tag{2.20}$$

where

$$p(s) = L_mR_dCC_ds^3 + (L_mC_d + L_mC)s^2 + R_dC_ds + 1. \tag{2.21}$$

The expression (2.21) can be expressed in a third degree polynomial factorized form as

$$p(s) = (\alpha\tau s + 1)(\tau^2 s^2 + 2\zeta\tau s + 1) \tag{2.22}$$

which leads to the following set of equations

$$\alpha\tau^3 = R_dC_dL_mC \tag{2.23}$$

$$\tau^2(2\alpha\zeta + 1) = L_m(C_d + C) \tag{2.24}$$

$$\tau(\alpha + 2\zeta) = R_dC_d. \tag{2.25}$$

Dividing (2.23) by (2.25) and isolating τ^2 yields

$$\tau^2 = \frac{L_mC(\alpha + 2\zeta)}{\alpha}. \tag{2.26}$$

Substituting (2.26) in (2.24) and isolating C_d provides the expression of the damping network capacitor

$$C_d = \frac{2\zeta C(1 + 2\alpha\zeta + \alpha^2)}{\alpha}. \tag{2.27}$$

From (2.25) and (2.26), it is straightforward that

$$R_d = \frac{\tau(\alpha + 2\zeta)}{C_d}. \tag{2.28}$$

Since the derivative of (2.27) with respect to α is

$$\frac{dC_d}{d\alpha} = \frac{2\zeta C(\alpha^2 - 1)}{\alpha^2} \tag{2.29}$$

C_d has a minimum for $\alpha = 1$. To minimize the size of the capacitor C_d, a value of $\alpha = 1$ is selected. With this choice, the expression of the damping resistance R_d is given by

$$R_d = \frac{(1+2\zeta)\sqrt{1+2\zeta}}{4\zeta(\zeta+1)}\sqrt{\frac{L_m}{C}}. \tag{2.30}$$

Finally, $\zeta = 1$ is selected as a trade-off between the size of the capacitor and a sufficient and robust damping of the internal dynamics. The resulting expressions of the damping network parameters are

$$\begin{aligned} C_d &= 8C \\ R_d &\approx 0.65\sqrt{\frac{L_m}{C}}. \end{aligned} \tag{2.31}$$

In the previous section, it was concluded that the small-signal control-to-output transfer functions $G_{vod_1}(s)$ and $G_{vod_2}(s)$ have the same expression at $u = 1$. Moreover, this expression corresponds to the small-signal control-to-output transfer function of a buck converter. To test the validity range of the small-signal model, a PSIM frequency response simulation was carried out using the switched model schematic circuit diagram shown in Fig. 2-7 and compared with the MATLAB calculated frequency response corresponding to the SSA model (2.12). In both cases, the parameters, whose selection will be explained in the next section, are $L_m = 14$ μH, $C = 2.6$ μF, $R_d = 1.5$ Ω, $C_d = 22$ μF, $L = 30$ μH, $C_o = 110$ μF, and $R_o = 9.6$ Ω. Three different input voltages $V_g = 39$ V (step-up, $u > 1$), $V_g = 48$ V (border, $u = 1$), and $V_g = 55$ V (step-down, $u < 1$) were considered. The duty cycles have been chosen to have a steady-state output voltage $V_o = 48$ V. The waveforms depicted in Fig. 2-3 were obtained for the previous list of component values.

The Bode plots of both frequency responses obtained from PSIM (switched) and MATLAB (small signal) are superimposed for the three different values of the input voltage and are depicted in Fig. 2-8. In this figure, the maximum frequency plotted corresponds to 50 kHz, which is half of the switching frequency. The frequency responses are very similar in shape to a second order system with two complex poles and no zeroes. We conclude that our buck-boost converter can be modelled and controlled as a buck converter for the input voltage range considered in the example.

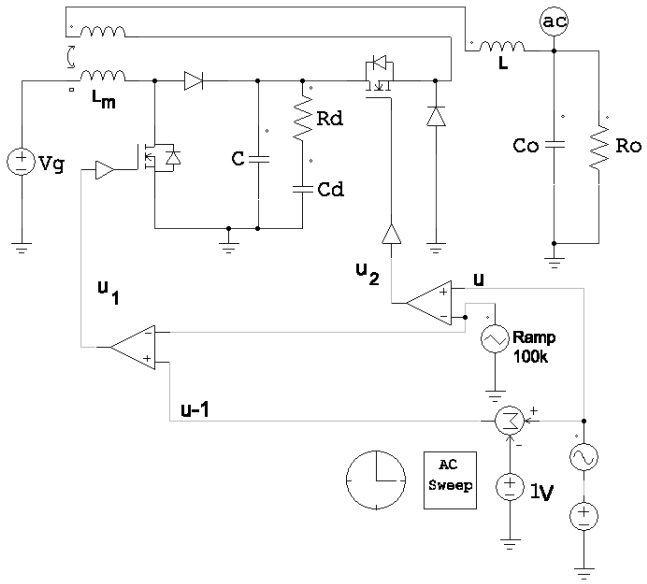

Figure 2-7: Circuit diagram corresponding to the PSIM simulation used to calculate the frequency response of the control-to-output transfer function.

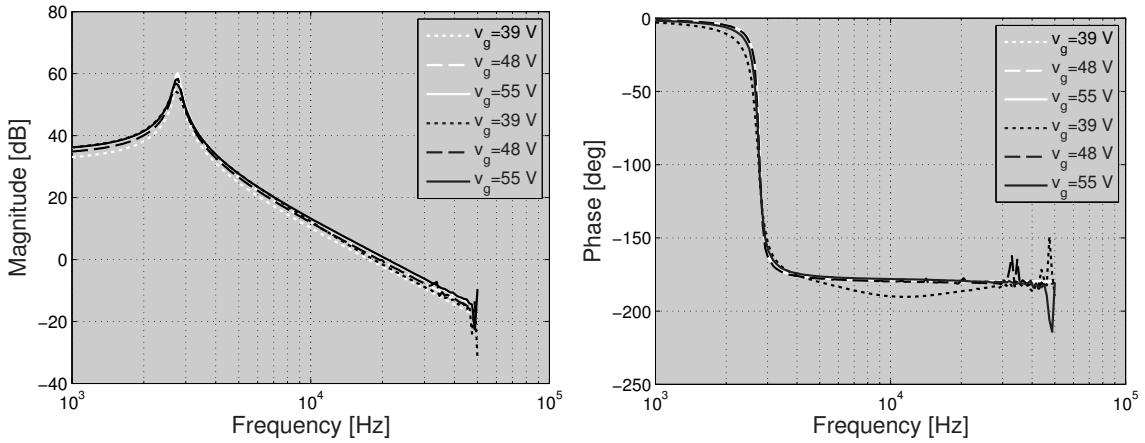

Figure 2-8: Frequency response of the small-signal control-to-output transfer function. The black lines correspond to the simulation of the switched model using PSIM (see Fig. 2-7) while the white lines correspond to MATLAB simulation of the linear small signal model (2.12).

To highlight the benefits of the magnetic coupling a frequency analysis comparison is performed between the converter in Fig. 2-7 and the equivalent converter without magnetic coupling in Fig. 2-9. The magnetic coupling is removed by converting the two coupled inductors in a single inductor which is located on the primary side and has the same number of turns and the same core as the coupled inductors. The magnetizing inductance used to calculate the coupled inductors is

$$L_m = \frac{\mu A N^2}{l} \tag{2.32}$$

where μ is the core permeability, A is the core area, l is the magnetic path length and, since $n = 1$, N is the number of turns in both primary and secondary windings. Therefore, assuming that the primary and secondary sides of the coupled inductor are connected in series in the same core, their equivalent inductance L_{eqv} is calculated as

$$L_{eqv} = \frac{\mu A (2N)^2}{l} = 4L_m. \tag{2.33}$$

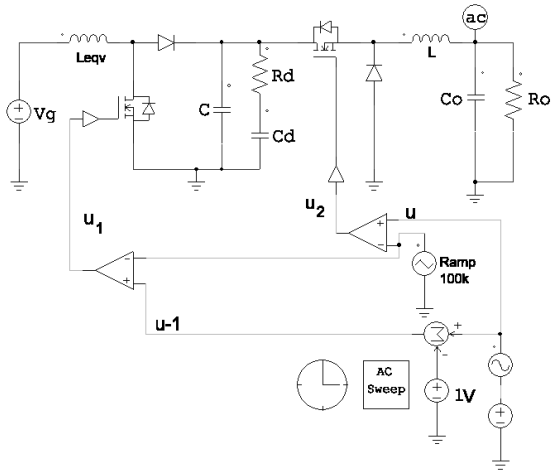

Figure 2-9: Circuit diagram corresponding to the PSIM simulation used to calculate the frequency response of the control-to-output transfer function without magnetic coupling.

Fig. 2-10 shows the transfer functions of the cascaded buck-boost converter without magnetic coupling superimposed on the transfer functions of the coupled inductor depicted in Fig. 2-8. All the traces in the figures correspond to PSIM simulations of the switched models of Fig. 2-7 and Fig. 2-9. The responses in black are those of the converter without magnetic coupling whereas the white responses are those of the system with magnetic coupling. The white traces are less scattered for all three voltages in both magnitude and phase. There are two resonant peaks in the black traces but only one peak in the white ones. At the frequencies of the second peak, the phases of the black traces present a change of -180^o that does not exist in the white cases. The response of the boost mode depicted in black is coherent with a system with two pairs of LHP complex poles and one RHP real zero. In the buck and buck-boost modes, the black responses are caused by two pairs of LHP complex poles and one pair of RHP complex zeroes.

The frequency responses mean that the controller design in the black cases is more difficult. It is very likely that any closed loop system designed on the basis of the black frequency responses will have a small bandwidth and a poor output regulation.

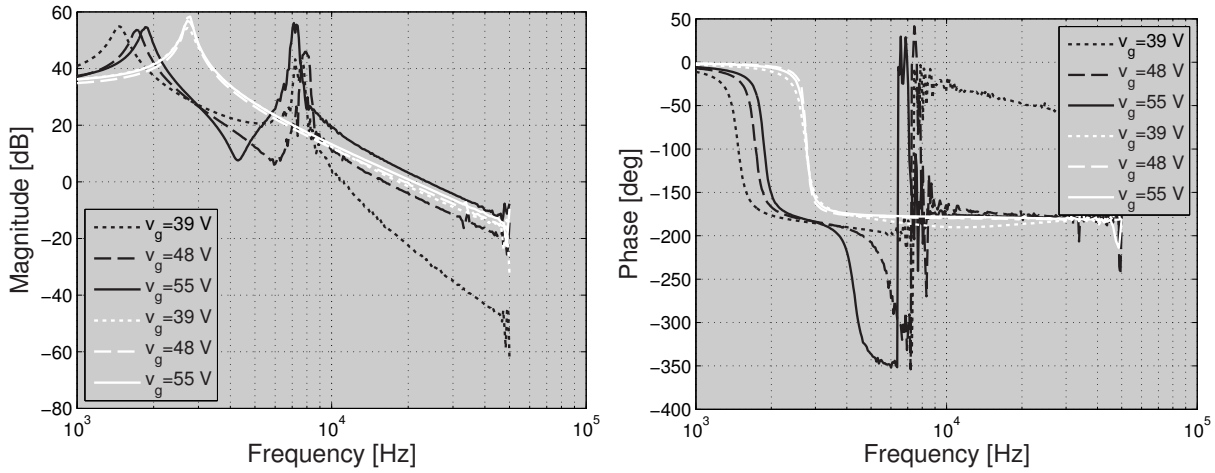

Figure 2-10: Frequency response of the small-signal control-to-output transfer functions provided by PSIM AC Sweep simulations. The white traces are those of the switched model with magnetic coupling (Fig. 2-7). The black traces are those of the switched model without magnetic coupling (Fig. 2-9).

2.5 Circuit design

2.5.1 Buck-boost converter power stage

The buck-boost converter is designed as a battery discharge regulator (BDR) of 13 in-series lithium-ion battery cells, so the input voltage V_g range from 39 V to 55 V. The output voltage V_o regulates a DC bus of 48 V. The maximum power output is 480 W for a load resistance $R_o = 9.6\ \Omega$ and the switching frequency is 100 kHz. The parameter values of the buck-boost converter in Fig. 2-6 were selected according to specifications of input and output peak to peak current ripples of $\triangle i_{gpp} = 12$ A and $\triangle i_{Lpp} = 4$ A; maximum output impedance of $Z_{omax} = 150\ \text{m}\Omega$; maximum power dissipation in the damping resistor $P_{R_d} = 4$ W, and also expression (2.31). The expressions used to calculate the ripples of i_L, i_g and v_c are listed in Table 2.1. If a triangular shaped v_c ripple is assumed, the power loss in R_d is

$$P_{R_d} = \frac{\triangle v_{Cpp}}{12R_d}. \tag{2.34}$$

The maximum output closed loop impedance can be calculated approximately as

$$Z_{omax} = \frac{1}{2\pi f_c C_o} \tag{2.35}$$

where f_c is the crossover frequency (CF) of the voltage loop.

After a worst case analysis was performed in both buck and boost modes to find the specifications at nominal power, the components that were finally selected for the buck-boost converter power stage are the ones listed in Table 2.2. To achieve good efficiency, N-channel MOSFETs with low

Table 2.1: Peak to peak ripple of the converter variables i_L, i_g and v_C in CCM

Ripple	**Buck mode**	**Boost mode**
$\triangle i_{Lpp}$	$\frac{(V_g - V_o)V_o T}{V_g L}$	$\frac{V_g(V_o - V_g)T}{V_o L}$
$\triangle i_{gpp}$	$\frac{(V_g - V_o)V_o T}{V_g L}$	$\frac{V_g(V_o - V_g)T(L + L_m)}{V_o L L_m}$
$\triangle v_{Cpp}$	$\frac{(V_g - V_o)V_o^2 T}{V_g^2 R_o C}$	$\frac{(V_o - V_g)T}{R_o C}$

on-resistance and fast Schottky diodes were selected. Kool Mμ core inductors were chosen because of their low cost and availability. Capacitors that must absorb high pulsed current are ceramic. The equivalent series resistance (ESR) of C_d is much smaller than R_d. All components are rated up to 100 V.

Table 2.2: Components of buck-boost converter

Component	**Description**	**Type**
Q_1, Q_2	Power MOSFET	IRFB4110PbF
D_{s_1}, D_{s_2}	Schottky Rectifier	40CPQ080GPbF
L_m	Coupled inductors	Core: 77083A7 Magnetics Wire size: 15 AWG[b] Number of turns: 13:13
C	Ceramic Capacitor	3 $\times$ 2.2 μF[a] X7R dielectric
C_o	MKT Capacitor	5 $\times$ 22 μF
L	Inductor	Core: 77083A7 Magnetics Wire size: 15 AWG[b] Number of turns: 20
R_d	Damping Resistor	1.5 Ω, 4 W
C_d	MKT Capacitor	22 μF

[a] The capacitance depends on the operating voltage. For V_c = 48 V the equivalent capacitance is 2.6 μF.

[b] Multifilar equivalent.

The capacitance value of the ceramic capacitor with X7R dielectric used in the experimental prototype varies with temperature and current as reported in the technical data sheet provided by the manufacturer. But it varies more strongly with the operation voltage as presented in the experimental measurements of Fig 2-11. In this experiment the capacitor is connected to a known value resistance R_{kn} in series as shown in Fig. 2-12. The time constant of this simple circuit is measured with the oscilloscope and thus the value of the capacitor can be calculated for the specific operation voltage. The equivalent capacitance presented in Table 2.2 is estimated from the

experimental voltage ripple v_c using the expression given in Table 2.1.

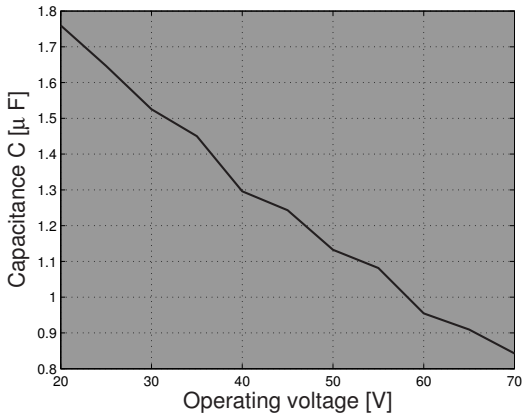

Figure 2-11: Capacitance-Voltage Characteristic for the ceramic capacitor with X7R dielectric and a nominal value of 2.2 μF used in the prototype.

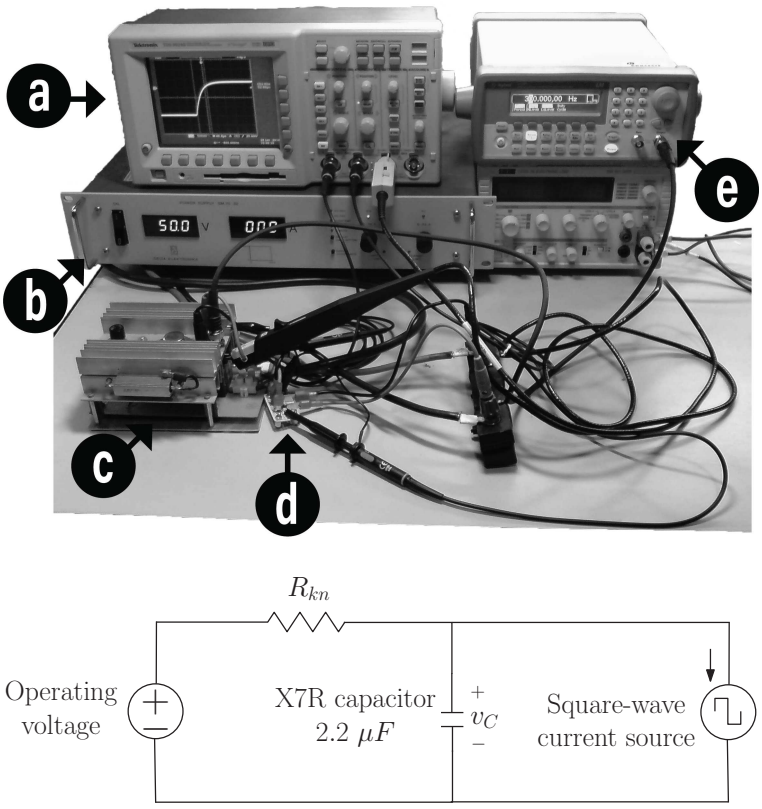

Figure 2-12: Experimental configuration of the measurement of the capacitance variation with the operation voltage by the ceramic capacitor with X7R dielectric and a nominal value of 2.2 μF: (a) oscilloscope, (b) DC power supply, (c) DC electronic load current with external reference, (d) RC network, (e) signal generator.

2.5.2 Buck-boost control circuit

Once the model (2.12) in the section above had been verified, the next step was to design the control loop compensator. A compensation network for the buck converter-like transfer function plotted in Fig. 2-8 was designed following classical rules [70]. The third-order compensator transfer function is

$$G_c = \frac{\widehat{u}}{\widehat{v}_o} = K\frac{(\tau_3 s+1)(\tau_4 s+1)}{s(\tau_1 s+1)(\tau_2 s+1)} \tag{2.36}$$

where the compensator parameters were selected as follow: $\tau_1 = 1\ \mu$s, $\tau_2 = 2\ \mu$s, $\tau_3 = \tau_4 = 1/(2\pi)$ ms, and $K = 210$ s/V.

The circuit diagram of the compensator and the pulse width modulation (PWM) implemented in PSIM is presented in Fig. 2-13(a), which includes an estimation of the switching delays. The fact that there are delays prevents extreme duty cycles and causes a nonlinearity in the transitions between boost and buck modes [71]. To mitigate these problems, a third mode of operation is permitted in an adjustable small vicinity zone between buck and boost modes [50, 71]. The new operation mode is called buck-boost mode because the previous two modes overlap in an interleaving-like manner, i.e., both MOSFETs can switch in the same period but their switching instants are almost π rad out of phase. The overlapping adjustment is achieved by reducing the displacement between the signals that, by their comparison with the triangular signals, generate u_1 and u_2.

The circuit schematic diagram of the buck-boost control experimental stage is shown in Fig. 2-13(b). The main component of the control system is the dual-PWM controller-integrated circuit TL1451A that generates the switch activation signals $u_1(t)$ and $u_2(t)$. This single monolithic chip has two error amplifiers, an adjustable oscillator, a reference voltage of 2.5 V, and dual-common-emitter output transistor circuits. The triangular signal oscillator was adjusted to have a frequency of 100 kHz, an amplitude of 0.7 V and a DC offset of 1.4 V. One of the error amplifiers is used to implement the compensator (2.36) to obtain the signal u, and the other one is used to get the signal ($u - 0.7$ + overlapping adjustment) in the manner presented in Fig. 2-13(c). This figure shows an example of the driving signals u_1 and u_2 generation.

2.5.3 Buck-boost driver with modified bootstrap

An IR2110 integrated driver has to switch the low side N-Channel MOSFET in the boost stage Q_1, and the high side N-Channel MOSFET of the buck stage Q_2. A bootstrap circuit is needed to supply the floating voltage to drive Q_2. In buck operation, Q_1 should always be OFF while Q_2 switches. In buck-boost mode both Q_1 and Q_2 are switched in the same period. In these latter two modes a classical bootstrap circuit would operate correctly. The driver operates most critically in pure boost mode because the bootstrap capacitor C_B must be sufficiently charged to keep Q_2 ON for as long as needed. In these circumstances, the capacitor of conventional bootstrap circuits could

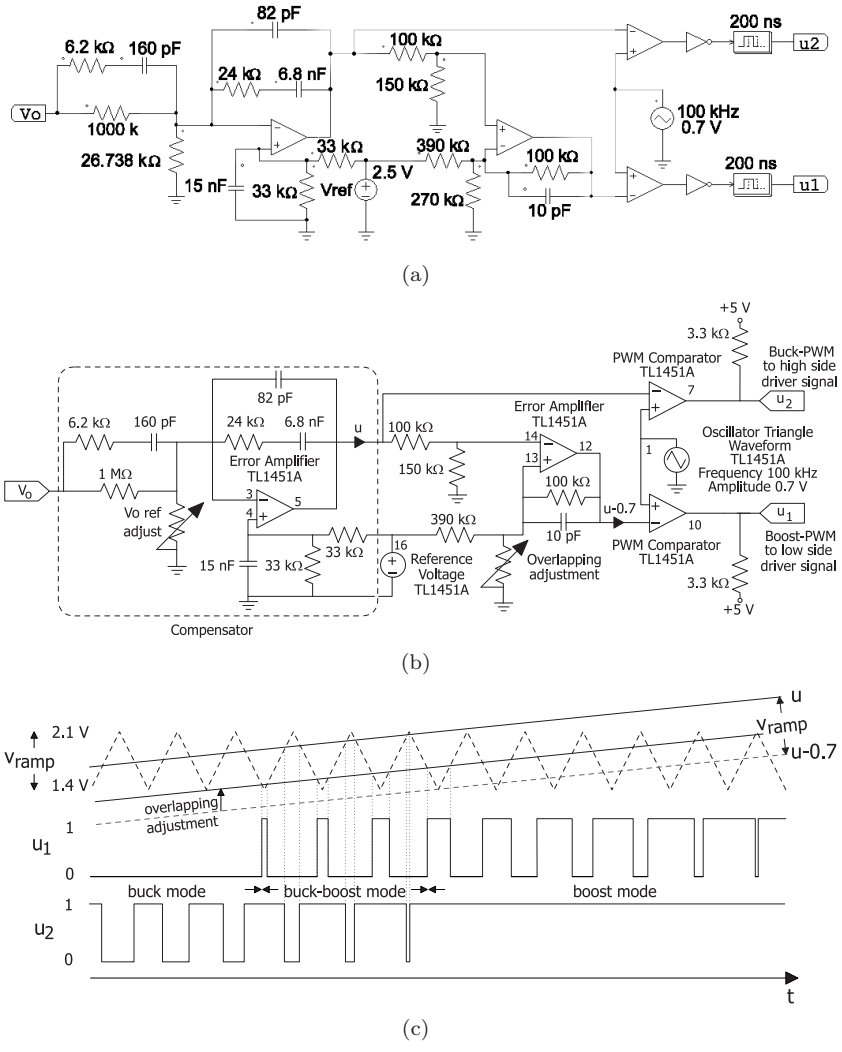

Figure 2-13: Schematic of: (a) the compensator G_c and the dual PWM simulated in PSIM, (b) buck-boost control circuit diagram, (c) an example of driving signals generation.

be insufficiently charged. To avoid the malfunction of the converter in boost mode, it is therefore necessary to refresh the capacitor charge. A solution to this problem is presented in [72], where a charge pump topology with an external clock signal is used. A similar charge pump driver that refreshes the bootstrap capacitor with the use of the boost control pulses is shown in Fig. 2-14. Since the source of Q_2 is always at a level higher than 15 V, the usual bootstrap path through diode D_A will be cut OFF, so an additional bootstrap circuit made of $C_{B_{aux}}$, D_B, D_C, T_C, T_D, and a couple of resistors, was added to recharge C_B. The boost pulses turn on the auxiliary Darlington transistor T_D, permitting $C_{B_{aux}}$ to charge to 15 V through D_A, D_C and T_D. The direct polarization of D_C keeps T_C OFF. When T_D turns OFF, T_C starts conducting and provides a current path to recharge C_B from $C_{B_{aux}}$ through D_B. Fig. 2-13(b) shows a variable resistor that permits the empirical overlapping adjustment that guarantees that the bootstrap capacitor will be properly charged by

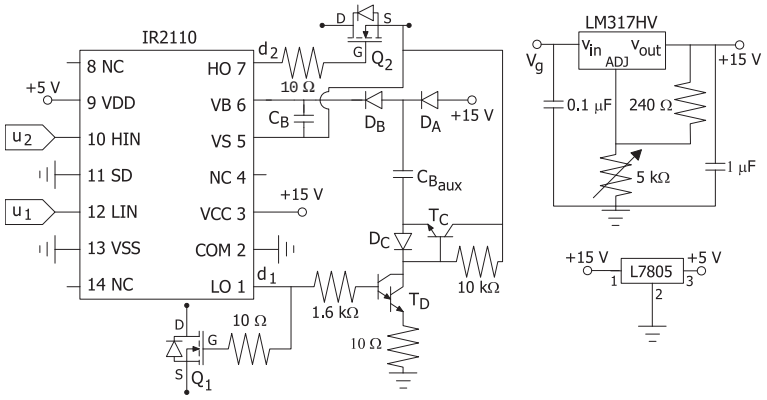

Figure 2-14: Scheme of the buck-boost driver with a modified bootstrap circuit and auxiliary supplies.

switching the high side MOSFET when the boost driving pulses are narrower than 2%. A couple of cascaded linear regulators provide the supply voltages (15 V and 5 V) of the driver circuit shown in Fig. 2-14 and the control circuit presented in Fig. 2-13(b) from the power stage input voltage V_g.

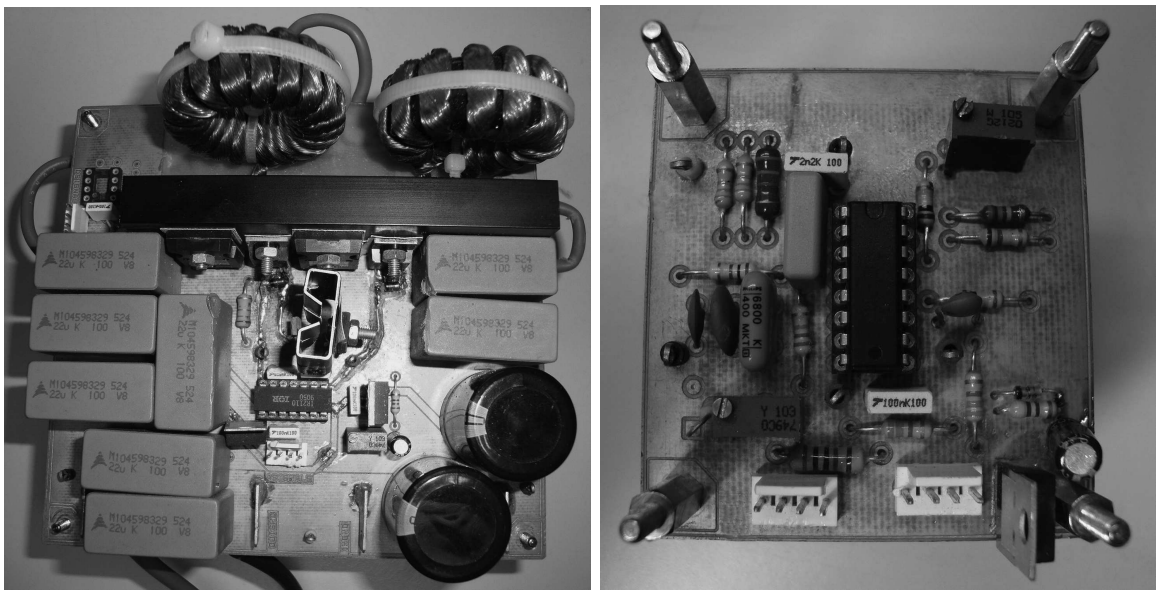

(a) (b)

Figure 2-15: Regulator prototype (a) buck-boost power stage, (b) dual PWM control stage.

2.6 Experimental results

Fig. 2-15 shows pictures of the power stage and the control circuit of the buck-boost regulator prototype. The experimental response of the buck-boost regulator to a low-frequency triangular input voltage going from 36.8 V to 55.8 V is depicted in Fig. 2-16 where the waveform of the output

voltage can be compared with its corresponding simulation. In addition to the input and output voltages, the simulated logic signals u_1 and u_2, ranging from 0 V to 1 V, are also depicted on the left. The oscillogram on the right shows the equivalent signals that correspond to the outputs of the dual PWM controller that are in the 0 V to 5 V range. The input voltage range ensures that in both simulation and experimental measurements the converter works in its three operation modes. The output voltage is well regulated and exhibits a smooth behavior in all the transitions between modes. These good results are due to the use of the same controller in all the operation modes. The sampling capabilities of the digital oscilloscope made it possible to capture the switching noise in the output voltage waveform. There is less switching noise in boost mode because it is attenuated at the output by a third order filter while the buck stage has only a second order filter between its switches and the output.

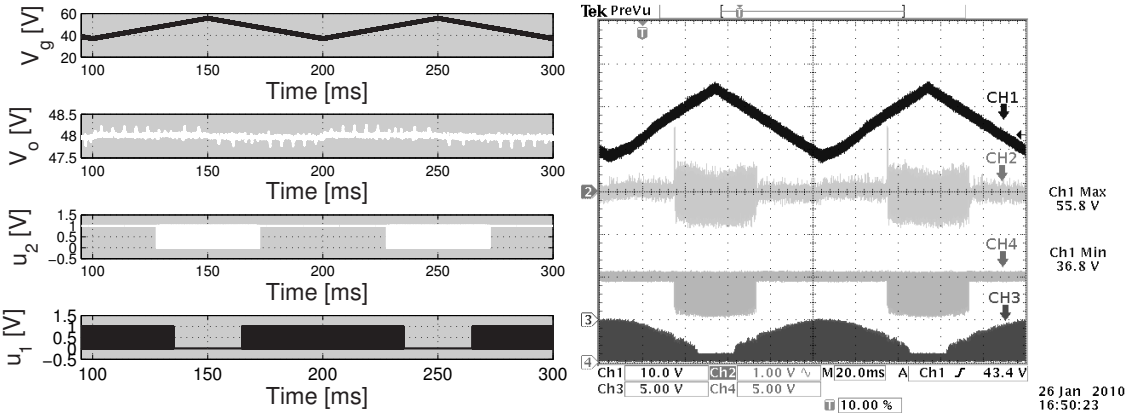

(a) (b)

Figure 2-16: Waveforms of input voltage V_g, output voltage V_o, boost pulses u_1 and buck pulses u_2 for changes in the input voltage. (a) PSIM simulation (b) Waveforms measured. CH1: V_g (10 V/div), CH2: V_o (1 V/div, AC coupling), CH3: u_1 (5 V/div), CH4: u_2 (5 V/div), timebase: 20 ms/div.

Fig. 2-17 shows the experimental setup for measuring the efficiency of the hard-switching buck-boost converter. The efficiency measurements take into account the consumption of the drivers and control stages. A Voltech PM6000 Power Analyzer with calibrated precision shunt resistors measures the input and output currents. The energy conversion are shown efficiencies as a function of the output current i_{R_o} for different input voltage v_g levels in Fig. 2-18(a), whereas in Fig. 2-18(b), the horizontal axis is the input voltage and the output current is the parameter of the set of curves. Since buck-boost mode there are some switching losses, for a given current the maximum efficiencies are attained in boost and buck modes when the input voltage is close to the desired output level. The maximum efficiency obtained of about 97% would be improved if the diodes could be substituted by synchronous rectifier MOSFETs [55, 56]. Other techniques like multiphase and zero voltage switching (ZVS) [55] or dynamic adjustment of the switching frequency [56] are also possible.

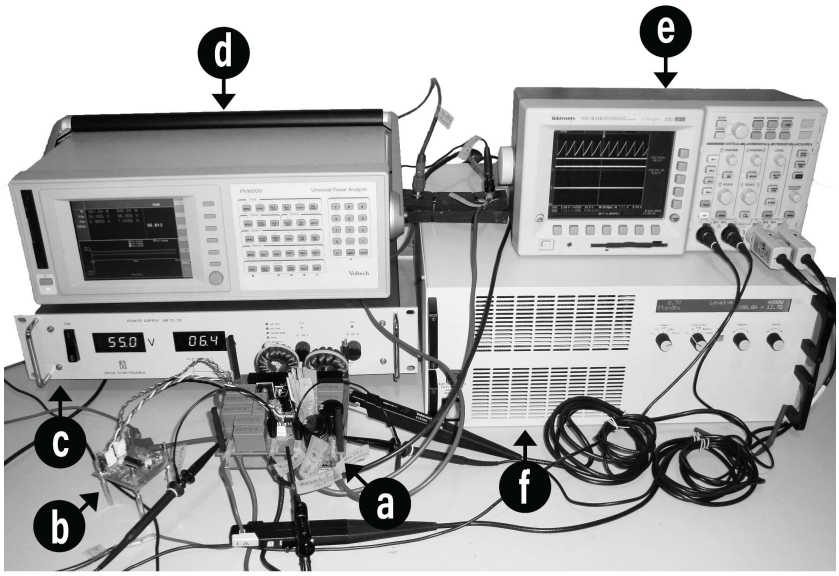

Figure 2-17: Experimental configuration of the measurement of efficiency: (a) buck-boost converter, (b) buck-boost control, (c) DC power supply, (d) power analyzer, (e) oscilloscope, (f) DC electronic load.

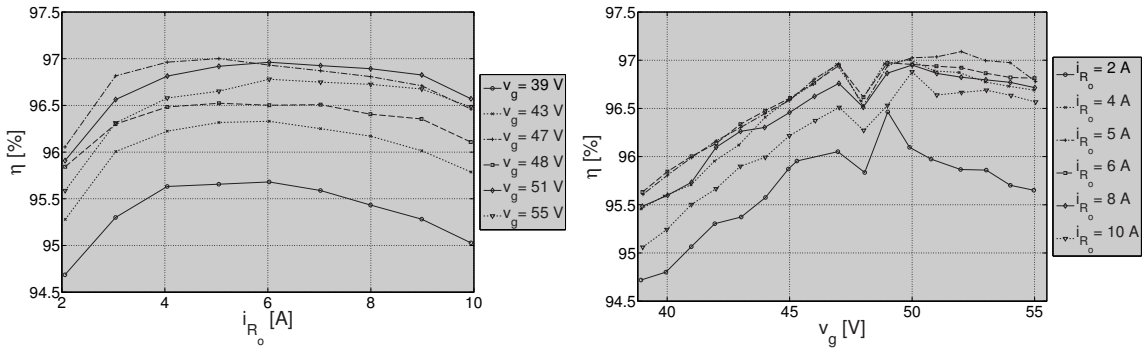

(a) (b)

Figure 2-18: Energy conversion efficiency for $V_o = 48$ V as: (a) function of the output current i_{R_o} for different input voltage v_g levels, (b) function of the input voltage v_g for different output current i_{R_o} levels.

PSIM-simulated and experimental Bode plots of the regulator loop gain are illustrated in Fig. 2-19. In the simulations, delays and losses were estimated. The frequency measurements were obtained using a frequency response analyzer (FRA) Venable 3120 as shown in Fig. 2-20. This frequency response has the three above mentioned modes of operation, which are achieved by varying the value of the input voltage v_g.

Some of the differences that can be observed between simulated and experimental loop-gain Bode plots for $v_g = 48$ V are attributed to the nonlinearities in the transitions between the modes mentioned above. Other differences are mainly due to nonlinearities in some passive components

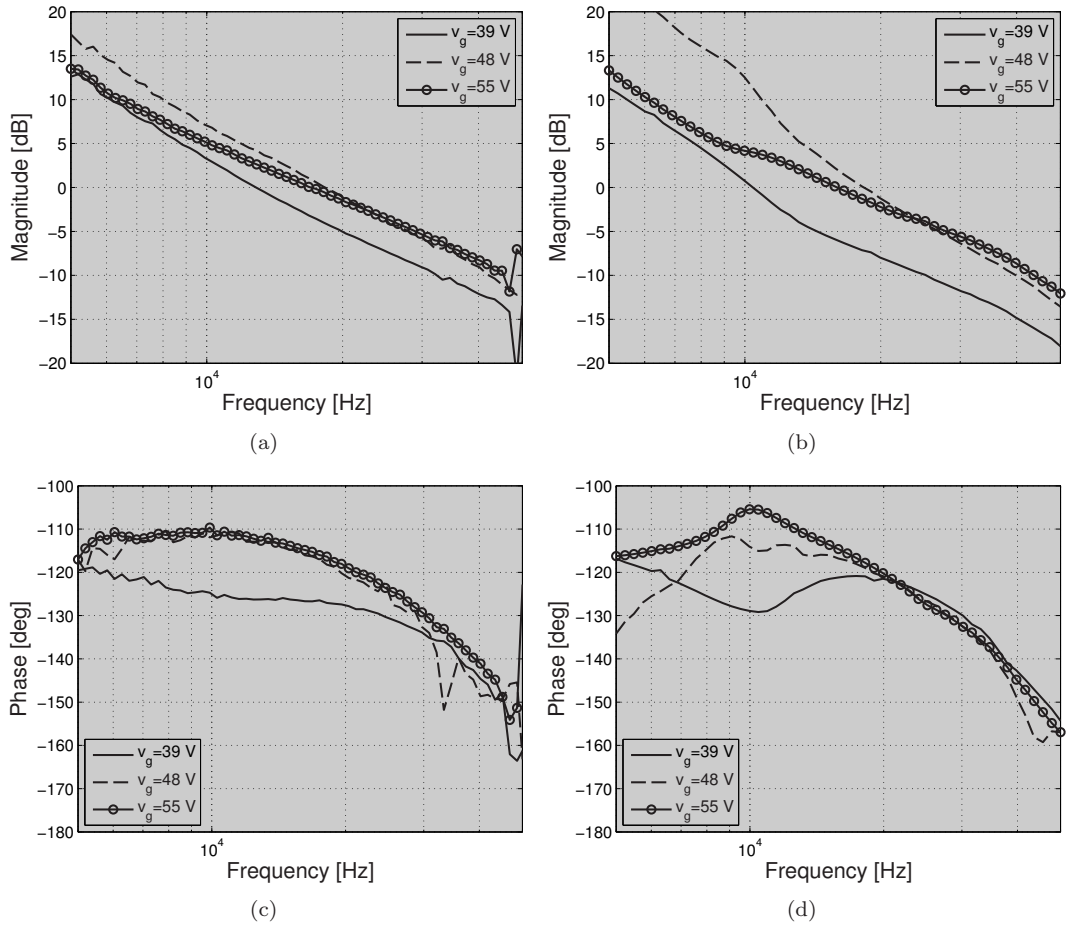

Figure 2-19: Loop-gain Bode plots of the buck-boost converter: boost mode for $v_g = 39$ V, buck-boost mode for $v_g = 48$ V and buck mode for $v_g = 55$ V. a) Simulated magnitude, b) Experimental magnitude, c) Simulated phase, d) Experimental phase.

of the experimental prototype. For instance, the capacitance of the intermediate capacitor exhibits a strong dependency on the applied voltage as has already been noted in Fig. 2-11. Also, the parameters of the magnetic components vary with the mean average current flowing through them. The crossover frequency and phase margin (PM) are calculated and listed in Table 2.3 for each input voltage value. In spite of the differences observed between the simulated and the experimental frequency responses, the table shows remarkably similar results in all cases. As in a buck regulator, the bandwidth is wide since the crossover frequency is between one tenth and one fifth of the switching frequency. Furthermore, the PMs indicate that the feedback system is stable for the desired input voltage range.

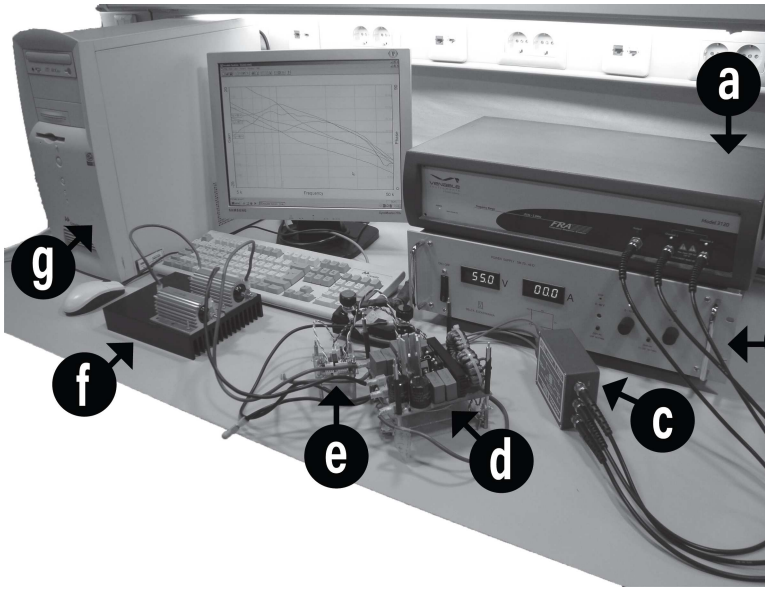

Figure 2-20: Experimental configuration of the measurement of frequency response: (a) frequency response analyzer, (b) DC power supply, (c) Bode box injection transformer, (d) buck-boost converter, (e) buck-boost control, (f) resistive load, (g) computer with Venable software.

Table 2.3: CF and PM for different input voltages

	Simulated		Experimental	
$\mathbf{V_g}$ [V]	**CF** [kHz]	**PM** [deg]	**CF** [kHz]	**PM** [deg]
39	13	54	11	51
48	18	62	18	61
55	17	65	16	65

Figs. 2-21 to 2-27 show simulated and experimental transient responses to load changes for various constant input voltages in to boost, lower buck-boost, buck-boost, upper buck-boost and buck modes. For each input voltage, the load current was changed from 10 A to 5 A in the top subplots (a) and (b) and from 5 A to 10 A in the bottom subplots (c) and (d). In all cases, the output voltage is well regulated and the transient deviations are within the desired boundaries. In addition to output voltage and current, the input current and the intermediate capacitor voltage are also depicted. The transient dynamics of these variables is damped as expected, and there is reasonable agreement between simulated and measured variables. The main discrepancy appears near and in the buck-boost mode, as is illustrated in Figs. 2-22, 2-23 and 2-24. Extreme duty cycles, close to zero or to one, are required to obtain a smooth transition between operation modes, but they cannot be achieved in practice because switching delays are unavoidable, the dual PWM controller integrated circuit TL1451A is not designed for this application and the integrated circuit

layout of the regulator prototype is an experimental prototype that is not optimized to avoid these problems. For this reason, when the input and output voltages are close, switching pulses can be skipped and the resulting ripple contains components at frequencies below the converter switching frequency [71]. The skipped pulses also appear in transients such as the one depicted in Fig. 2-22(d) in which a boost pulse is missed. In Figs. 2-23(b) and 2-24(b) during the transient some buck pulses are close to the zone where a missing one should have been and one unexpected boost pulse appears. In our prototype, this noise is attenuated by the output LC filter or rejected by the control loop and has little effect on the output voltage. Pulse skipped pulses do not hinder the operation of the buck-boost converter and have also been reported in the widely used non-inverting buck-boost converter. Therefore, we will focus on the current control of our converter, which we believe is more important, and leave the investigation of the skipped pulses for future study.

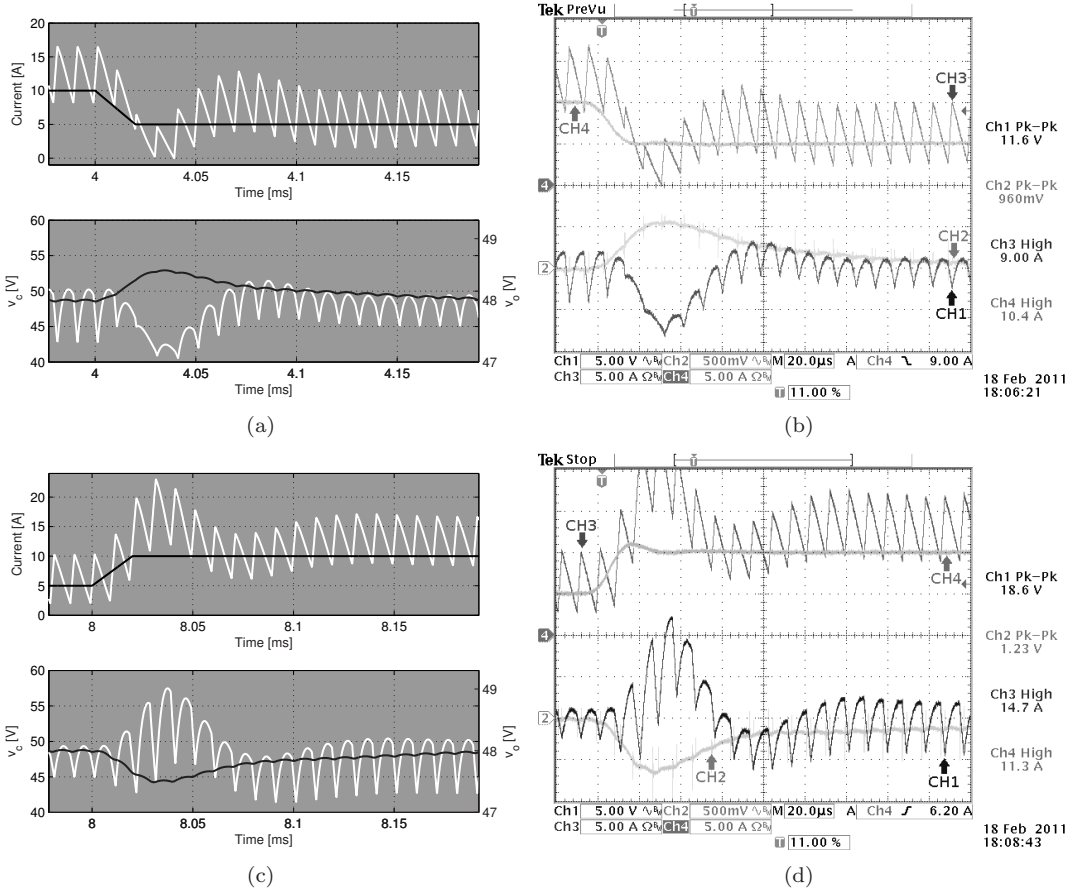

Figure 2-21: (a),(c) PSIM simulations and (b),(d) experimental measurements of the converter main variables when the load current changes from 10 A to 5 A and back to 10 A while the input voltage is $V_g = 39$ V. Black traces show the simulated output current i_{Ro} and output voltage v_o while the input current i_g and the intermediate capacitor voltage v_c are in white. CH1: v_c (5 V/div), CH2: v_o (500 mV/div, AC coupling), CH3: i_g (5 A/div) and CH4: i_{Ro} (5 A/div).

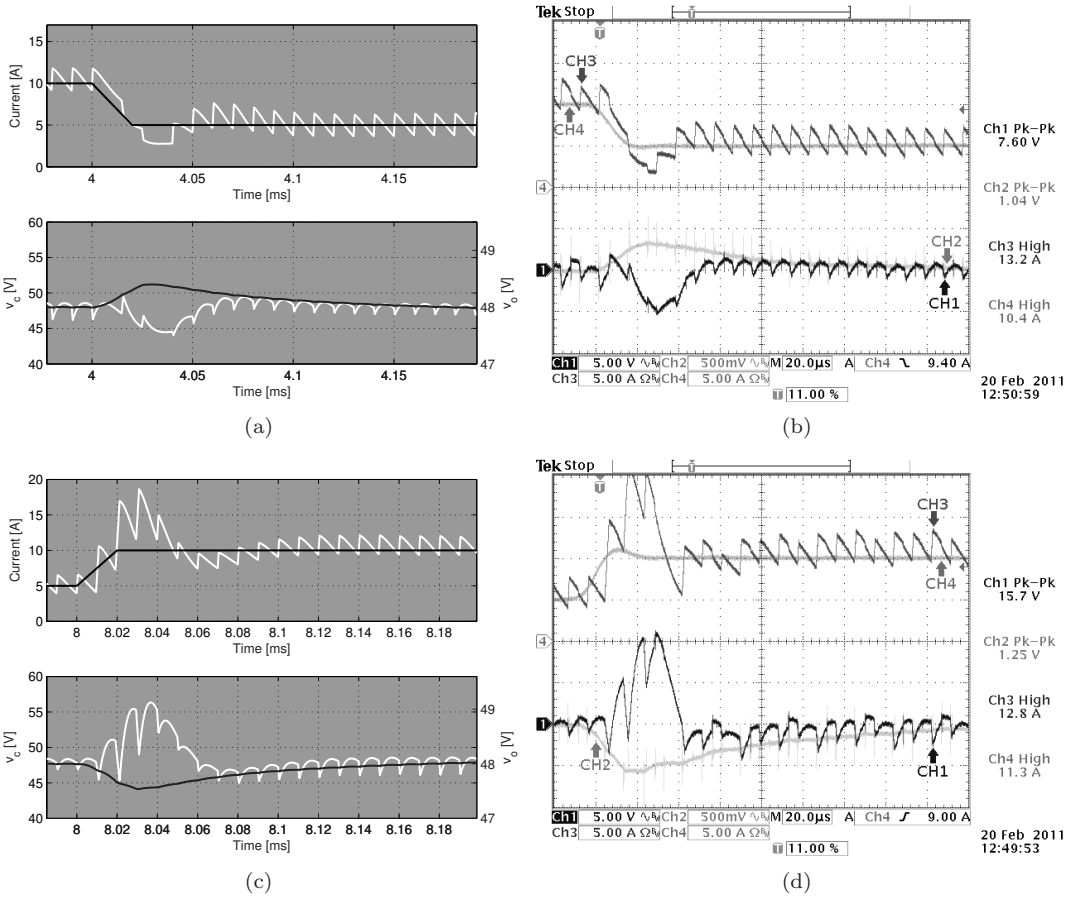

(a) (b)

(c) (d)

Figure 2-22: Simulated (a), (c) and measured (b), (d) converter main variables for the same load changes as Fig. 2-21 and $V_g = 46$ V.

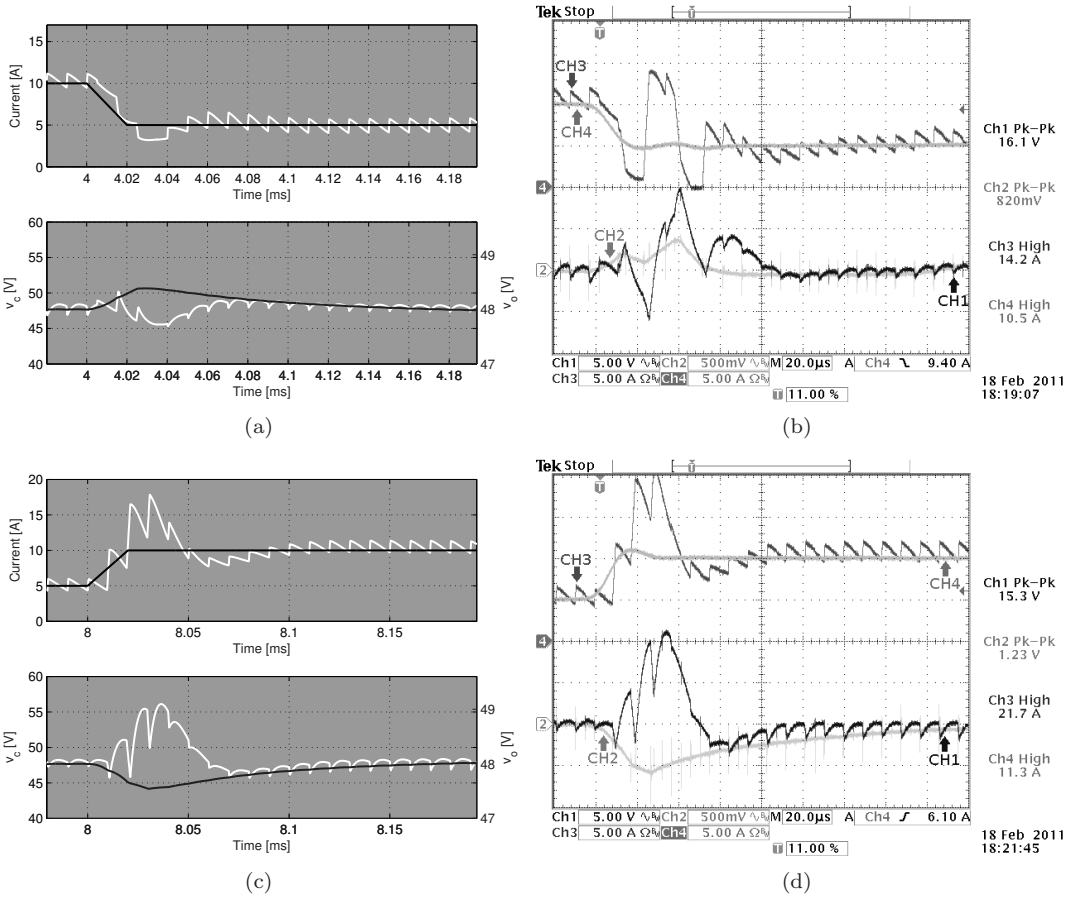

Figure 2-23: Simulated (a), (c) and measured (b), (d) converter main variables for the same load changes as Fig. 2-21 and $V_g = 47$ V.

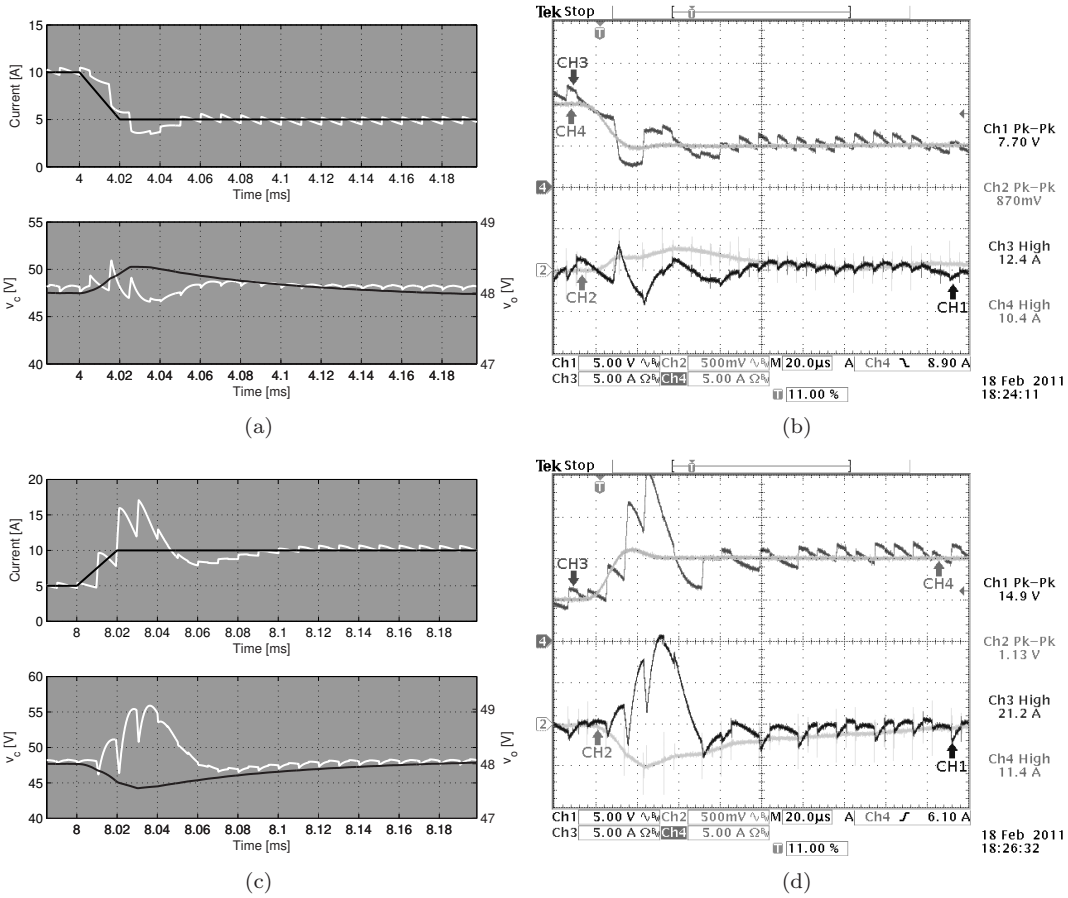

Figure 2-24: Simulated (a), (c) and measured (b), (d) converter main variables for the same load changes as Fig. 2-21 and $V_g = 48$ V.

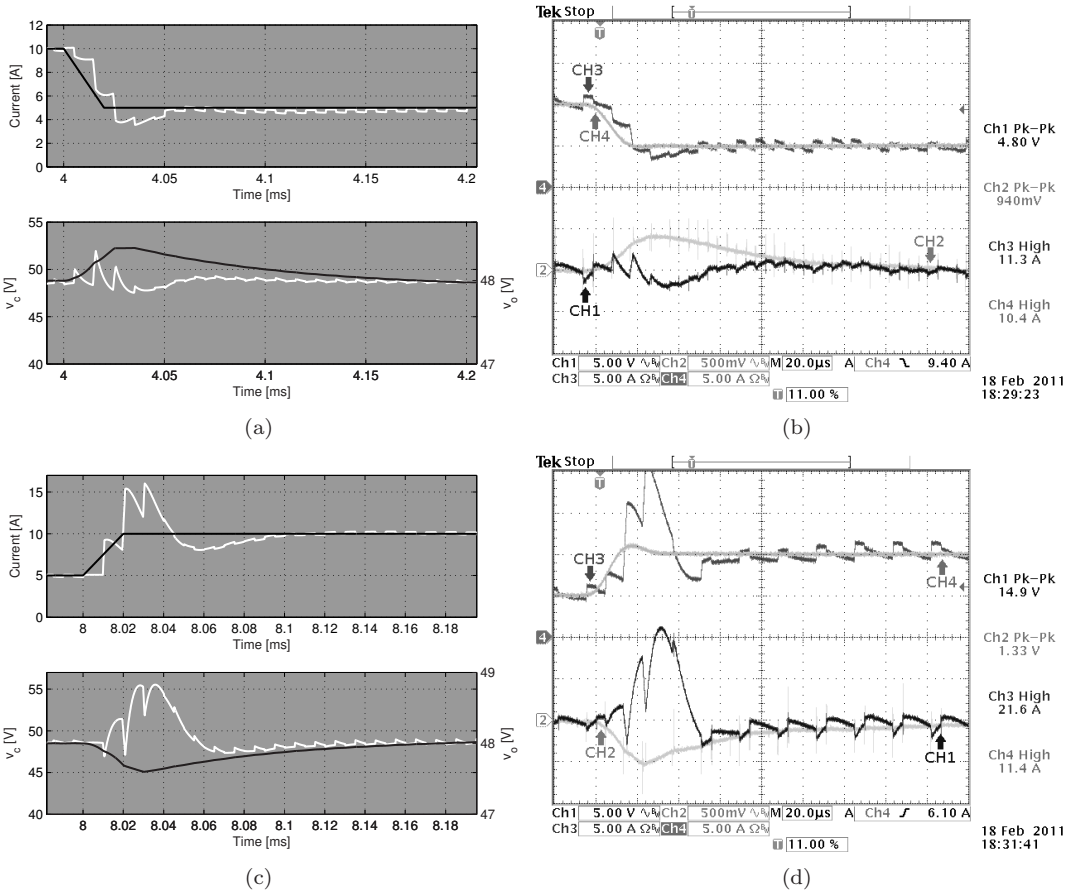

Figure 2-25: Simulated (a), (c) and measured (b), (d) converter main variables for the same load changes as Fig. 2-21 and $V_g = 49$ V.

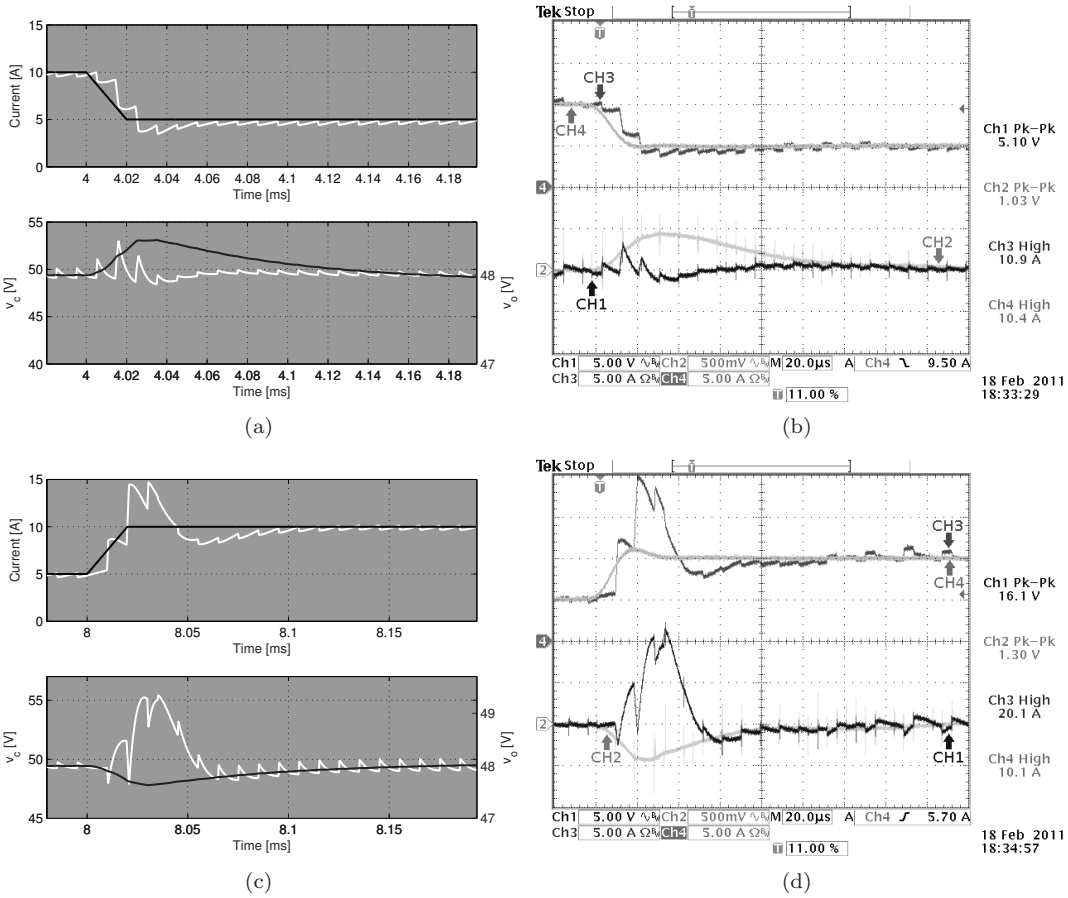

Figure 2-26: Simulated (a), (c) and measured (b), (d) converter main variables for the same load changes as Fig. 2-21 and $V_g = 50$ V.

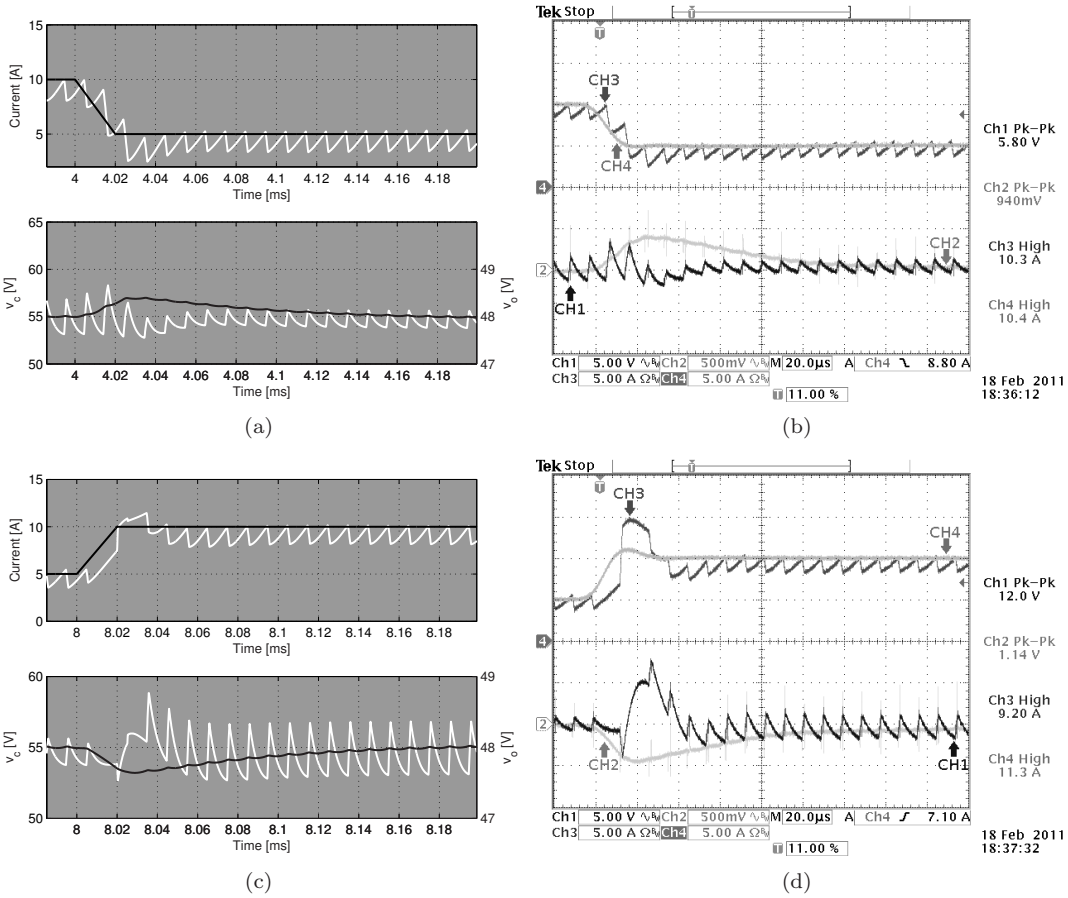

Figure 2-27: Simulated (a), (c) and measured (b), (d) converter main variables for the same load changes as Fig. 2-21 and $V_g = 55$ V.

2.7 Conclusions

A new non-inverting buck-boost DC-DC switching converter was obtained by magnetically coupling the input and output inductors of a cascade connection of the boost and buck stages. The combination of a coupling and a damping network at the intermediate capacitor provides a minimum-phase control-to-output transfer function with two dominant complex poles, simulation and experimental results of a prototype verify the predicted wide control bandwidth because there are no RHP zeroes. Efficiency is high when the converter switches are operated in three regions that depend on the input-output voltage ratio: boost, buck and buck-boost. In the buck-boost region both MOSFETs are allowed to switch in the same period. This overlapping is permitted only for a narrow range of nearly equal input and output voltages to improve the efficiency. The converter usually operates in the other more efficient modes in which there is only one periodically switching MOSFET. In buck mode, the MOSFET of the boost stage is always OFF, whereas in boost mode, the buck stage MOSFET is continuously ON, so a bootstrap driver had to be specially built for the buck stage high-side N channel MOSFET.

For a given specification of output impedance and voltage ripple, we believe that the proposed converter could offer a solution with larger magnetic components but smaller capacitors than other state-of-the-art topologies. Since both input and output currents are non pulsating there are two or more possible current control strategies. For this reason, controlling the converter in current mode is a work in progress. The input and/or output converter currents cycle-by-cycle limiting capability offers interesting possibilities to many applications like battery, supercapacitor, PV panel or fuel cell energy management. Future work will also consider a bidirectional implementation of the switches that could provide even higher conversion efficiencies. Another open problem is the converter operation at light loads where several discontinuous conduction modes can appear.

Chapter 3

Current Mode Control of a Coupled-Inductor Buck-Boost DC-DC Switching Converter

3.1 Abstract

This chapter makes an in-depth study of the coupled-inductor buck-boost converter described in chapter 2. The output voltage of this DC-DC converter can be regulated above and/or below its input voltage with high efficiency and wide bandwidth. The control of the input and/or output non-pulsating converter currents is addressed. The small-signal control-to-input/output current open-loop transfer functions makes it possible to design the average current-mode controllers. The combination of the input and output current controllers with an additional output voltage limiter loop is proposed as a method for regulating one of the currents while limiting the maximum values of the other two variables. The theoretical analyses have been validated by means of simulations and also experimentally on a 48-V 800-W purpose-built prototype. In particular, the frequency response measurements that have been carried out for a representative set of the converter operating points are in good agreement with the simulations.

3.2 Introduction

Many applications need either the input-current or the output-current of the power stage to be controlled. In photovoltaic power generation systems the input-current is controlled so that the maximum power point of the PV modules can be tracked [73, 74, 54, 75]. An input-current control

is also used in fuel cell applications such as [43], where fuel consumption is minimized and the loads are connected to a regulated DC bus voltage. In [38] and [76] the control minimizes the fuel cell input-current undulation rate, and in [36] it limits the slope of the fuel cell current to prevent the starvation phenomenon. The input-series-output-parallel connection [77], which consists of multiple modular DC-DC converters connected in series at the input and in parallel at the output, requires an output-current control to ensure that the load current is shared equally between the converters. Light-emitting diode (LED) technology typically requires power electronic drivers to regulate LED currents and obtain an optimum balance between the efficacy, color stability, and power factor correction [78, 79].

In distributed generation systems (DGS) [80] and satellite power systems [54, 67] different DC-DC converters need to be designed in which the input or output current control depends on their position in the system. PEM fuel cell-based DGS topologies are usually combined with auxiliary storage devices in such hybrid configurations as the series or the parallel ones [81], or the more efficient series-parallel hybrid (SPH) topology non-regenerative presented and analyzed in [80]. If SPH is to be implemented in practice, DC-DC switching converters with regulated input and/or output currents are required to interface between varying voltage-source-like elements such as fuel cells, batteries, supercapacitors, etc. One possible solution is to use Ćuk converters because they make it easy to control both input and output currents and they operate in voltage step-up or step-down modes. The main drawbacks of the non-isolated basic Ćuk stage are the reverse polarity of its input-output voltage transfer ratio and the fact that it is less efficient than structures using four switches [57]. Up to six battery charge/discharge DC-DC converter topologies whose input and output currents can be regulated with wide bandwidth are presented in [67]. However, none of them can offer simultaneous step-up and step-down voltage conversion capabilities.

In many other applications, such as uninterruptible power supplies [44], battery charging and discharging [47, 46, 49, 51, 55, 56, 48, 50], power factor correction [50, 45], fuel cell regulation [52, 50, 55], and maximum power point tracking of solar panels [53], a DC-DC converter is used to obtain a regulated output-voltage from an unregulated source. When the regulated voltage is within the voltage range of the unregulated voltage source, a step-up/step-down DC-DC converter is required. In continuous conduction step-up mode, most of the converters mentioned earlier [47, 46, 49, 51, 55, 56, 48, 50, 45, 52, 53] present a right-half-plane (RHP) zero that makes it difficult to design their controller, limits the bandwidth of the control loop and penalizes the size of the output capacitor [49].

One possible way of eliminating the boost converter RHP zero that can be used efficiently in low

and high power applications, and which does not have floating switches nor require complex drivers is to use magnetic coupling between inductors [61] combined with damping networks [62, 63]. This solution has made it possible to design high-power buck-boost converters with high efficiency and wide bandwidth [82]. This converter is the result of combining two of the topologies proposed in [67]: a) the coupled inductor boost converter with *RC* type damping network and output filter, and b) the coupled inductor buck converter with *RC* type damping network and input filter. The resulting coupled inductor buck-boost converter [82] has the same step-up or step-down voltage conversion properties as the single inductor non-inverting buck-boost converter but exhibits non-pulsating input and output currents, which makes several current control strategies possible. Since the converter structure is novel and it makes it possible to operate in several operation modes and to regulate the input or/and output current, many of its applications are still to be developed. The output-voltage compensator that was studied and implemented in [82] performed well for the various ranges of operation and it was proposed that current control strategies to regulate the input and the output currents of the novel non-inverting buck-boost converter could be studied and implemented in the future. This is what we are doing in this chapter. We predict that the system can be used to transfer energy between unregulated voltage sources limiting the input-power and the output-power with a single compact converter structure and relatively simple control.

The rest of this chapter is organized as follows: Section 3.3 discusses the small-signal converter model and presents the small-signal control-to-input-current and control-to-output-current transfer functions for the various operation modes. An average current-mode control of the input and output current is designed in Section 3.4. Experimental measurements and PSIM simulation Bode plots of the input and output current regulator loop-gains for the different operation modes are presented in Section 3.5. The energy conversion efficiencies of an 800-W coupled-inductor buck-boost experimental prototype, the experimental transient responses, and a capacitor-charging power supply application example are also provided. Finally, the main conclusions of this chapter are outlined in Section 3.6.

3.3 Analysis of the coupled inductors Buck-Boost Converter

Let us consider the unidirectional buck-boost converter with magnetic coupling between the input and output inductors, *RC* type damping network and coupled inductors turns ratio 1:1 shown in Fig. A-1. For the analysis of the converter it is assumed that the input-voltage v_g and the output-voltage v_o are voltage sources such as fuel cells, batteries, supercapacitors and regulated DC buses. Therefore, our primary focus in the converter analysis is the control of its input and/or output current. Assuming a continuous conduction mode (CCM) of operation, no parasitic effects and a

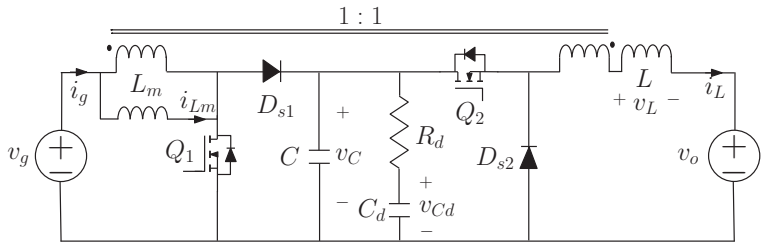

Figure 3-1: Schematic circuit diagram of the buck-boost converter with magnetic coupling between inductors and damping network R_dC_d.

switching frequency much higher than the converter natural frequency, the use of the state space averaging (SSA) method [68] to model the converter leads to the following set of differential equations

$$\begin{aligned}
\frac{d\bar{i}_{L_m}(t)}{dt} &= \frac{v_g(t) - \overline{v}_C(t)(1-d_1(t))}{L_m} \\
\frac{d\bar{i}_L(t)}{dt} &= \frac{\overline{v}_C(t)d_2(t) + v_g(t) - \overline{v}_C(t)(1-d_1(t)) - v_o(t)}{L} \\
\frac{d\overline{v}_C(t)}{dt} &= \frac{-\bar{i}_L(t)d_2(t) + (\bar{i}_{L_m}(t) + \bar{i}_L(t))(1-d_1(t))}{C} - \frac{\overline{v}_C(t) - \overline{v}_{C_d}(t)}{CR_d} \\
\frac{d\overline{v}_{C_d}(t)}{dt} &= \frac{\overline{v}_C(t) - \overline{v}_{C_d}(t)}{C_dR_d}
\end{aligned} \tag{3.1}$$

where d_1 and d_2 are the duty cycles of the switches Q_1 and Q_2, respectively, and the overline stands for averaging during one switching period. Assuming that the converter is in steady-state with constant duty cycles $d_1(t) = D_1$ and $d_2(t) = D_2$, input-voltage $v_g(t) = V_g$, and output-voltage $v_o(t) = V_o$, equating the right-hand side expressions in (3.1) to zero yields the steady-state conditions in the converter

$$0 = V_g - V_C(1-D_1) \tag{3.2}$$

$$0 = V_CD_2 + V_g - V_C(1-D_1) - V_o \tag{3.3}$$

$$0 = -I_LD_2 + (I_{L_m} + I_L)(1-D_1(t)) - \frac{V_C - V_{C_d}}{R_d} \tag{3.4}$$

$$0 = \frac{V_C - V_{C_d}}{R_d}. \tag{3.5}$$

Solving this system of equations for the DC components of the inductor currents and capacitor voltages leads to

$$
\begin{aligned}
I_{L_m} &= \frac{P_g(D_2 + D_1 - 1)}{V_g D_2} && (3.6)\\
I_L &= \frac{P_g(1 - D_1)}{V_g D_2} && (3.7)\\
V_C &= \frac{V_g}{1 - D_1} && (3.8)\\
V_{C_d} &= \frac{V_g}{1 - D_1} && (3.9)
\end{aligned}
$$

where P_g is the average input-power given by $P_g = V_g I_g = V_g(I_{Lm} + I_L)$.

Substituting the steady-state expression of the capacitor voltage V_C of (3.8) in (3.3) the following voltage conversion ratio $M(D_1, D_2)$ is obtained

$$M(D_1, D_2) \equiv \frac{V_o}{V_g} = \frac{D_2}{1 - D_1}. \tag{3.10}$$

Our goal is for the converter to operate in either boost or buck mode, switching smoothly between modes and reducing switching losses in all operation modes. Therefore, to generate the switch activation signals $u_1(t)$ and $u_2(t)$, let us define a single continuous control variable $0 \leq u(t) = d_1(t) + d_2(t) < 2$ so that in boost mode $d_2(t) = 1$ and $d_1(t) = u(t) - 1$, and in buck mode $d_1(t) = 0$ and $d_2(t) = u(t)$

$$u(t) = \begin{cases} 1 + d_1(t) & for \quad \text{boost mode} \\ \\ d_2(t) & for \quad \text{buck mode.} \end{cases} \tag{3.11}$$

In steady-state, the duty cycles D_1 and D_2 are related to the new variable $0 \leq U < 2$ as

$$
\begin{aligned}
D_1 &= \max(0, U - 1)\\
D_2 &= \min(1, U). && (3.12)
\end{aligned}
$$

The voltage conversion ratio $0 \leq M(U) < \infty$ can be obtained by substituting (3.12) in (3.10), which leads to

$$M(U) = -\frac{\min(1, U)}{\max(0, U - 1) - 1}. \tag{3.13}$$

With this control input, the DC voltage conversion ratio $M(U)$ is continuous between the boost and buck modes of operation. On the border between the two modes of operation $U = 1$, so $D_1 = 0$ and $D_2 = 1$. Fig. 3-2(a) shows the key waveforms in the generation of the switch activation signals $u_1(t)$

and $u_2(t)$ from the control signal $u(t)$, and a 50% duty cycle triangular waveform of $[0, 1]$ amplitude range. A schematic diagram of a dual pulse-width modulator circuit used to generate $u_1(t)$ and $u_2(t)$ is given in Fig. 3-2(b).

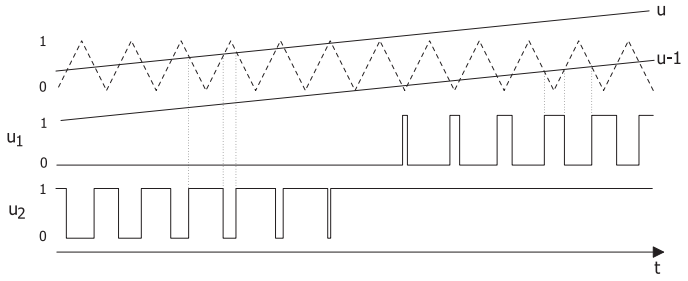

(a)

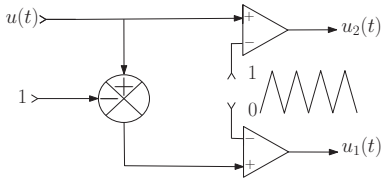

(b)

Figure 3-2: (a) activation signal generation: comparison of control signals with a triangular signal to obtain the MOSFET binary activation signals $u_1(t)$ and $u_2(t)$; (b) dual pulse-width modulator circuit used to obtain the MOSFET binary activation signals $u_1(t)$ and $u_2(t)$ from the signal control variable u.

To obtain a small-signal model around a steady-state operating point, we assume a constant input-voltage $v_g(t) = V_g$, a constant output-voltage $v_o(t) = V_o$, and duty cycles $d_1(t)$ and $d_2(t)$ that are equal to D_1 and D_2 plus some superimposed small AC variations $\widehat{d}_1(t)$ and $\widehat{d}_2(t)$ respectively

$$\begin{aligned} d_1(t) &= D_1 + \widehat{d}_1(t) \\ d_2(t) &= D_2 + \widehat{d}_2(t). \end{aligned} \tag{3.14}$$

Therefore, the single control variable $u(t)$ can be expressed as

$$u(t) = U + \widehat{u}(t). \tag{3.15}$$

In small-signal model, the duty cycles $\widehat{d}_1(t)$ and $\widehat{d}_2(t)$ are related to the single control variable $\widehat{u}(t)$ as

$$\widehat{d}_1(t) = \begin{cases} \widehat{u}(t) & for \quad \text{boost mode} \\ \\ 0 & for \quad \text{buck mode} \end{cases} \tag{3.16}$$

and

$$\widehat{d}_2(t) = \begin{cases} 0 & for \quad \text{boost mode} \\ \\ \widehat{u}(t) & for \quad \text{buck mode.} \end{cases} \tag{3.17}$$

The averaged inductor currents and capacitor voltages are also expressed in terms of their corresponding steady-state values plus superimposed small-signal AC variations in (3.18).

$$\begin{aligned} \overline{i}_{L_m}(t) &= I_{L_m} + \widehat{i}_{L_m}(t) \\ \overline{i}_L(t) &= I_L + \widehat{i}_L(t) \\ \overline{v}_C(t) &= V_C + \widehat{v}_C(t) \\ \overline{v}_{C_d} &= V_{C_d} + \widehat{v}_{C_d}(t). \end{aligned} \tag{3.18}$$

Assuming that the AC variations are much smaller than the steady-state values of (3.18) and (3.14), the set of differential equations (3.1) can be linearized around the operating point (3.6) to obtain the small-signal SSA model

$$\frac{d\widehat{x}}{dt} = A\widehat{x} + B_1\widehat{d}_1 + B_2\widehat{d}_2 \tag{3.19}$$

where the small-signal state vector $\widehat{x}$, the state matrix A and the input vectors B_1 and B_2 of the system are given by

$$\widehat{x} = \begin{bmatrix} \widehat{i}_{L_m} & \widehat{i}_L & \widehat{v}_C & \widehat{v}_{C_d} \end{bmatrix}^T$$

$$A = \begin{bmatrix} 0 & 0 & \frac{D_1-1}{L_m} & 0 \\ 0 & 0 & \frac{D_2+D_1-1}{L} & 0 \\ \frac{1-D_1}{C} & \frac{1-D_2-D_1}{C} & -\frac{1}{R_dC} & \frac{1}{R_dC} \\ 0 & 0 & \frac{1}{R_dC_d} & -\frac{1}{R_dC_d} \end{bmatrix}$$

$$B_1 = \begin{bmatrix} -\frac{V_g}{L_m(D_1-1)} & -\frac{V_g}{L(D_1-1)} & -\frac{P_g}{V_gC} & 0 \end{bmatrix}^T$$

$$B_2 = \begin{bmatrix} 0 & -\frac{V_g}{L(D_1-1)} & \frac{P_g(D_1-1)}{V_gD_2C} & 0 \end{bmatrix}^T.$$

In order to design their respective controllers, Laplace-domain control-to-input-current and control-to-output-current transfer functions are obtained for both duty cycles $\widehat{d}_1(s)$ and $\widehat{d}_2(s)$ from the

small-signal SSA model (3.19). The control-to-input-current small-signal transfer function in boost mode is obtained as

$$G_{i_g d_1}(s) \equiv \left.\frac{\widehat{i}_g(s)}{\widehat{d}_1(s)}\right|_{D_2=1} = -\frac{a_3 s^3 + a_2 s^2 + a_1 s + a_0}{k_1(b_4 s^4 + b_3 s^3 + b_2 s^2 + b_1 s)} \tag{3.20}$$

where

$$\begin{aligned}
a_3 &= {V_g}^2 R_d C C_d (L + L_m) \\
a_2 &= {V_g}^2 L C_d + L_m P_g {D_1}^2 R_d C_d + {V_g}^2 L_m C + L P_g R_d C_d - L_m P_g D_1 R_d C_d + L P_g {D_1}^2 R_d C_d \\
&\quad + {V_g}^2 L_m C_d - 2 L P_g D_1 R_d C_d + {V_g}^2 L C \\
a_1 &= -2 L P_g D_1 + L P_g {D_1}^2 + {V_g}^2 R_d C_d - L_m P_g D_1 + L_m P_g {D_1}^2 + L P_g \\
a_0 &= {V_g}^2 \\
b_4 &= L_m L R_d C C_d \\
b_3 &= L_m L (C + C_d) \\
b_2 &= R_d C_d (L + L_m {D_1}^2 + L {D_1}^2 - 2 L D_1) \\
b_1 &= L_m {D_1}^2 + L - 2 L D_1 + L {D_1}^2 \\
k_1 &= V_g (D_1 - 1).
\end{aligned}$$

In the same way, the control-to-input-current small-signal transfer function in buck mode is

$$G_{i_g d_2}(s) \equiv \left.\frac{\widehat{i}_g(s)}{\widehat{d}_2(s)}\right|_{D_1=0} = \frac{c_3 s^3 + c_2 s^2 + c_1 s + c_0}{k_2(e_4 s^4 + e_3 s^3 + e_2 s^2 + e_1 s)} \tag{3.21}$$

where

$$\begin{aligned}
c_3 &= {V_g}^2 D_2 L_m R_d C C_d \\
c_2 &= L_m P_g R_d C_d + L P_g R_d C_d + {V_g}^2 D_2 L_m C_d + {V_g}^2 D_2 L_m C - L_m P_g D_2 R_d C_d \\
c_1 &= L P_g + L_m P_g - L_m P_g D_2 + {V_g}^2 {D_2}^2 R_d C_d \\
c_0 &= {V_g}^2 {D_2}^2 \\
e_4 &= L_m L R_d C C_d \\
e_3 &= L_m L (C + C_d) \\
e_2 &= -2 L_m D_2 R_d C_d + L_m {D_2}^2 R_d C_d + L_m R_d C_d \\
&\quad + L R_d C_d \\
e_1 &= L_m {D_2}^2 - 2 L_m D_2 + L + L_m \\
k_2 &= V_g D_2.
\end{aligned}$$

Similarly, the control-to-output-current small-signal transfer function in boost mode can be written in the form

$$G_{i_L d_1}(s) \equiv \left.\frac{\widehat{i}_L(s)}{\widehat{d}_1(s)}\right|_{D_2=1} = -\frac{m_3 s^3 + m_2 s^2 + m_1 s + m_0}{k_1(b_4 s^4 + b_3 s^3 + b_2 s^2 + b_1 s)} \tag{3.22}$$

where

$$\begin{aligned} m_3 &= {V_g}^2 L_m R_d C C_d \\ m_2 &= {V_g}^2 L_m C_d + {V_g}^2 L_m C + L_m P_g {D_1}^2 R_d C_d - L_m P_g D_1 R_d C_d \\ m_1 &= -{V_g}^2 D_1 R_d C_d + {V_g}^2 R_d C_d - L_m P_g D_1 + L_m P_g {D_1}^2 \\ m_0 &= {V_g}^2 (1 - D_1) \end{aligned}$$

while the control-to-output-current small-signal transfer function in buck mode is

$$G_{i_L d_2}(s) \equiv \left.\frac{\widehat{i}_L(s)}{\widehat{d}_2(s)}\right|_{D_1=0} = \frac{n_3 s^3 + n_2 s^2 + n_1 s + n_0}{k_2(e_4 s^4 + e_3 s^3 + e_2 s^2 + e_1 s)} \tag{3.23}$$

where

$$\begin{aligned} n_3 &= {V_g}^2 D_2 L_m R_d C C_d \\ n_2 &= L_m P_g R_d C_d + {V_g}^2 D_2 L_m C_d + {V_g}^2 D_2 L_m C - L_m P_g D_2 R_d C_d \\ n_1 &= L_m P_g - L_m P_g D_2 + {V_g}^2 {D_2}^2 R_d C_d \\ n_0 &= {V_g}^2 {D_2}^2. \end{aligned}$$

In order to have a better understanding of the transfer functions (3.20) to (3.23), several numerical frequency responses are obtained for different power and voltage levels considering the following set of converter nominal parameters: $L_m = 35$ μH, $C = 7$ μF, $R_d = 1.5$ Ω, $C_d = 66$ μF and $L = 35$ μH. The voltages and power levels are determined by the following ranges: (15 V $\leq V_g \leq$ 55 V), (0 V $\leq v_o \leq$ 55 V), (0 A $\leq i_g \leq$ 16 A) and (0 A $\leq i_L \leq$ 16 A). While the choice of the power and voltage levels will be explained in Section 3.5, the parameter values of the coupled inductor buck-boost power stage are determined using the design criteria proposed in [82].

Each of the transfer functions (3.20) to (3.23) are studied in their respective mode and also at the border between the two modes of operation when $U = 1$. The Bode plots of frequency responses obtained from MATLAB simulation of the linear small-signal model are superimposed for the various operation modes in Figs. 3-3 and 3-4, where the maximum frequency plotted corresponds to 50 kHz, which is half of the switching frequency.

Although the small-signal transfer functions (3.20) to (3.23) correspond to a high order system, at high frequency, they present roughly first-order low-pass characteristics with magnitude slopes of about -20 dB per decade and phase angles approaching $-90°$ as is illustrated in Figs. 3-3 and 3-4. The presence of zeros in the right half-plane is discarded because they would have caused additional large falls in the phases that have not been detected in the figures. Therefore, using the design criteria proposed in [82], make it possible to design wide bandwidth and high phase margin current

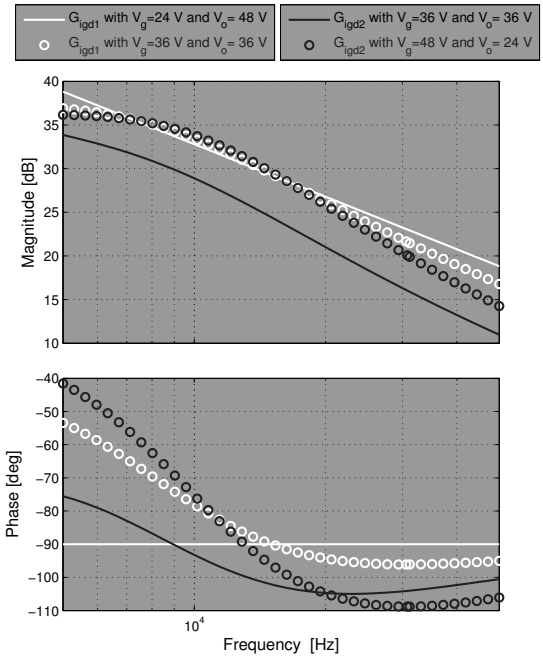

Figure 3-3: Frequency responses of the small-signal control-to-input-current transfer functions $G_{i_g d_1}(s)$ and $G_{i_g d_2}(s)$ for $P_g = 600$ W and operation voltages that correspond to boost, lower-border boost, upper-border buck and buck modes.

loops for the buck-boost converter that regulate the input or/and output current in all modes of operation.

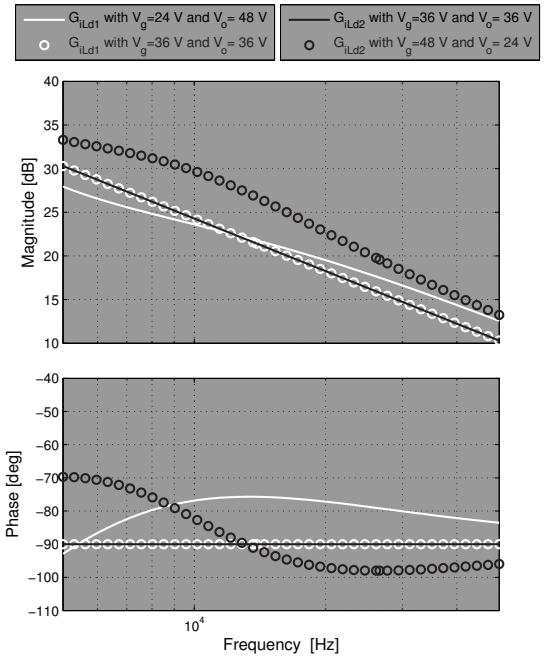

Figure 3-4: Frequency responses of the small-signal control-to-output-current transfer functions $G_{i_L d_1}(s)$ and $G_{i_L d_2}(s)$ for $P_g = 600$ W and operation voltages that correspond to boost, lower-border boost, upper-border buck and buck modes.

3.4 Average Current-Mode Control of a Coupled Inductor Buck-Boost DC-DC Switching Converter

In the section above, we obtained the small-signal transfer functions (3.20) to (3.23) that relate the converter's input and output currents to duty cycles $\widehat{d}_1(s)$ and $\widehat{d}_2(s)$ or, according to (3.16) and (3.17), the single control variable $\widehat{u}(s)$. Various control schemes can be implemented to regulate the input or the output current of the proposed buck-boost converter. We have selected the average current-mode control (ACC) because it offers excellent noise immunity, does not need a external compensation ramp enables the current of any circuit branch to be controlled [83, 84, 85, 86]. It has been extensively studied in the literature, and has been applied to a large number of systems with several final control objectives [87, 88]. In addition to the properties mentioned, the ACC is suitable for systems described by small-signal transfer functions such as the ones presented in the section above, in which the control variable $\widehat{u}$ corresponds explicitly to the duty cycle of the controlling signals. Furthermore, the ACC makes it possible to combine output and input current loops in a limiting manner, which will be explained in the next section. A small-signal SSA block diagram of the buck-boost converter with the ACC is illustrated in Fig. 3-5, where $\widehat{i}$ is the current to be controlled (the input or the output current), A_{cs} is the gain of the current sense amplifier, R_s is the current sense resistor, and F_m is the constant gain of the PWM modulator that is defined [89] by

$$F_m = \frac{1}{V_{pp}} \tag{3.24}$$

where V_{pp} is the peak to peak voltage of the triangle oscillator shown in Fig. 3-2(b).

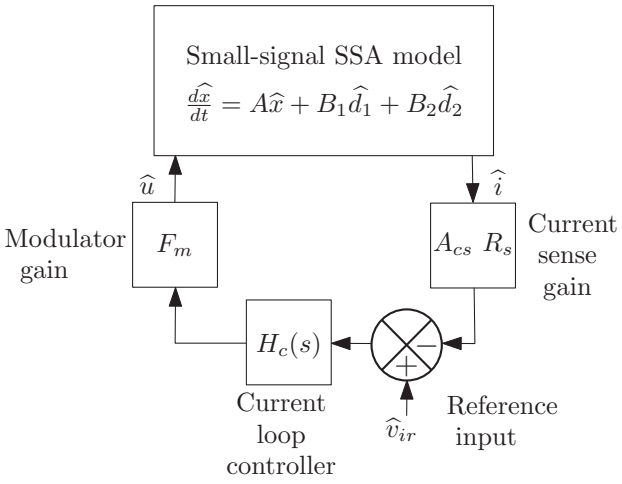

Figure 3-5: Small-signal block diagram of the converter system incorporating the ACC.

Now that the the small-signal transfer functions (3.20) to (3.23) have been presented, the next step is to design the control loop compensators. The current loop compensator $H_c(s)$ is designed using a lag network with a high frequency pole [90]. In [89], it is recommended to place the high frequency pole between one-third and one-half of the switching frequency to attenuate switching noise while in [86] it is recommended that this pole be located above half of the switching frequency. The intersection of both criteria requires the high frequency pole to be placed at half of the switching frequency. The low frequency pole of the compensator has been placed at the origin to eliminate the steady-state error [70]. The zero should be placed at least one decade below half the switching frequency according to the design guidelines proposed in [86]. Hence, the zero was placed at a tenth of the high frequency pole. Finally, the gains of both compensators were adjusted experimentally for the worst case of the frequency responses of the small-signal control-to-input/output current transfer functions of Figs. 3-3 and 3-4 to ensure wide bandwidth and a minimum phase margin of 45^o. The second order compensator transfer function of the input-current loop is

$$G_{cg}(s) = \frac{\widehat{u}(s)}{\widehat{i}_g(s)} = A_{cs}R_sF_mH_{cg}(s) = K_1\frac{(\tau_2 s + 1)}{s(\tau_1 s + 1)} \tag{3.25}$$

where the compensator parameters have been selected as follows: $\tau_1 = 3.3$ μs, $\tau_2 = 33$ μs, and $K_1 = 590$ s/A. The switching frequency is 100 kHz. The output-current loop compensator transfer function is

$$G_{cL}(s) = \frac{\widehat{u}(s)}{\widehat{i}_L(s)} = A_{cs}R_sF_mH_{cL}(s) = K_2\frac{(\tau_2 s+1)}{s(\tau_1 s+1)} \tag{3.26}$$

where $\tau_1 = 3.3\ \mu$s, $\tau_2 = 33\ \mu$s, and $K_2 = 1298$ s/A.

The small-signal SSA block diagram of the buck-boost converter and the ACC illustrated in Fig. 3-5 could have the practical realization shown in Fig. 3-6 for both current controllers. As can be seen in the practical realization scheme, both currents are measured on the high-side to allow converters in future applications to be connected in parallel.

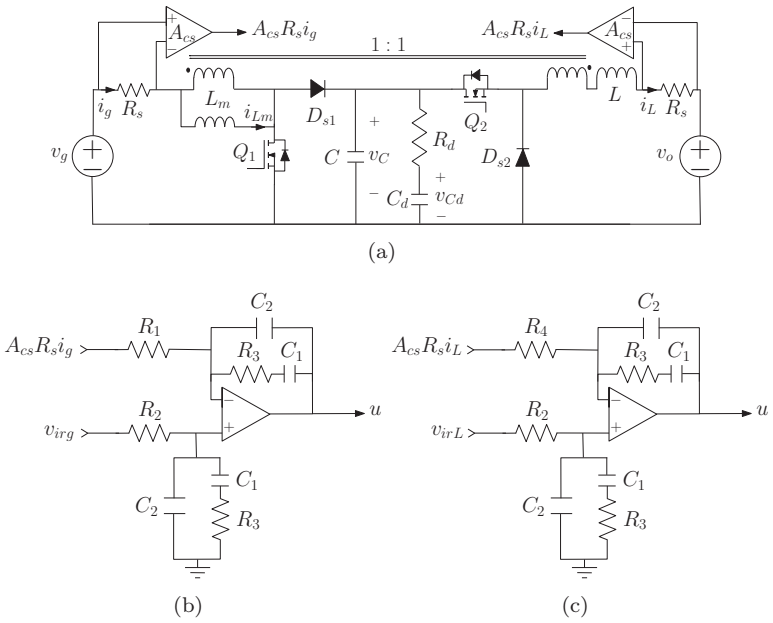

Figure 3-6: Average current-mode control of a buck-boost converter (a) buck-boost converter with the current sensors. Practical realization of the current loop compensation of the (b) output-current, (c) input-current

To verify the correct design of the controllers $G_{cg}(s)$ and $G_{cL}(s)$ we analyzed the loop-gain responses in all operation modes. According to the block diagram in Fig. 3-5 and the equation (3.25), the loop-gains of the system with input-current control evaluated in boost and buck modes are

$$T_g(s)\Big|_{boost} = G_{i_gd_1}(s)G_{cg}(s) \tag{3.27}$$

$$T_g(s)\Big|_{buck} = G_{i_gd_2}(s)G_{cg}(s). \tag{3.28}$$

The Bode plots of the loop-gain in (3.27) and (3.28) correspond to the black traces depicted in Fig. 3-7.

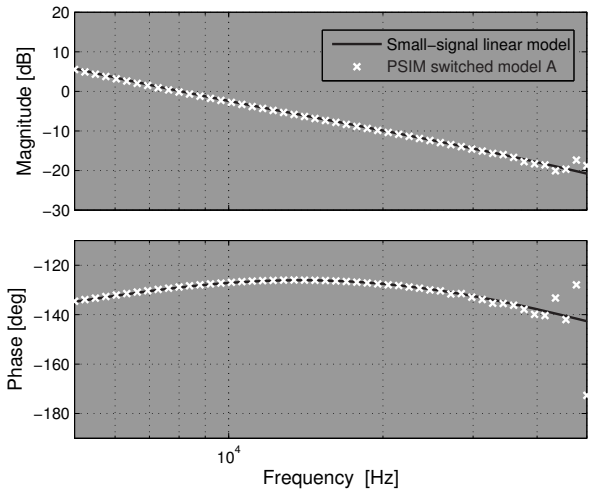

(a)

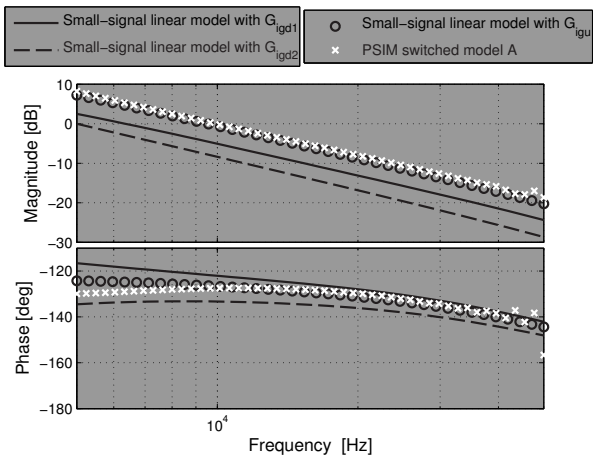

(b)

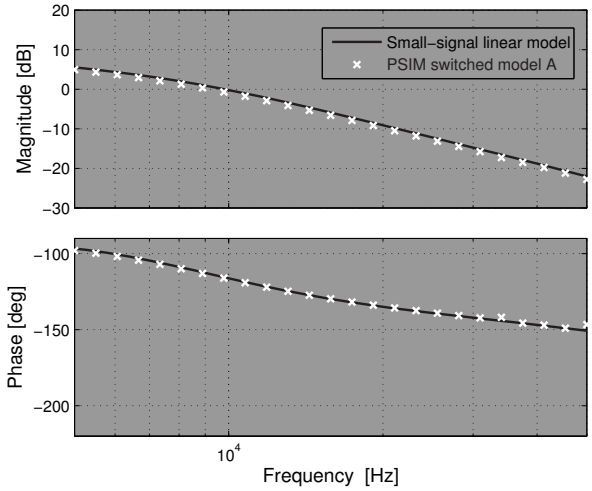

(c)

Figure 3-7: Loop-gain Bode plots of the buck-boost converter with input references that ensure input currents of: (a) 11 A in boost mode for $V_g = 36$ V and $V_o = 48$ V, (b) 12 A in lower-border boost and upper-border buck modes for $V_g = 32$ V and $V_o = 32$ V, (c) 8 A in buck mode for $V_g = 48$ V and $V_o = 24$ V. The black lines correspond to the small-signal linear model using MATLAB while the white x-marks correspond to the simulation of the switched model using PSIM.

To validate the small-signal linear model, a PSIM frequency response simulation was carried out using a switched model (called model A), as illustrated in Fig. 3-8, and plotted using white x-marks in the loop-gain responses of Fig. 3-7.

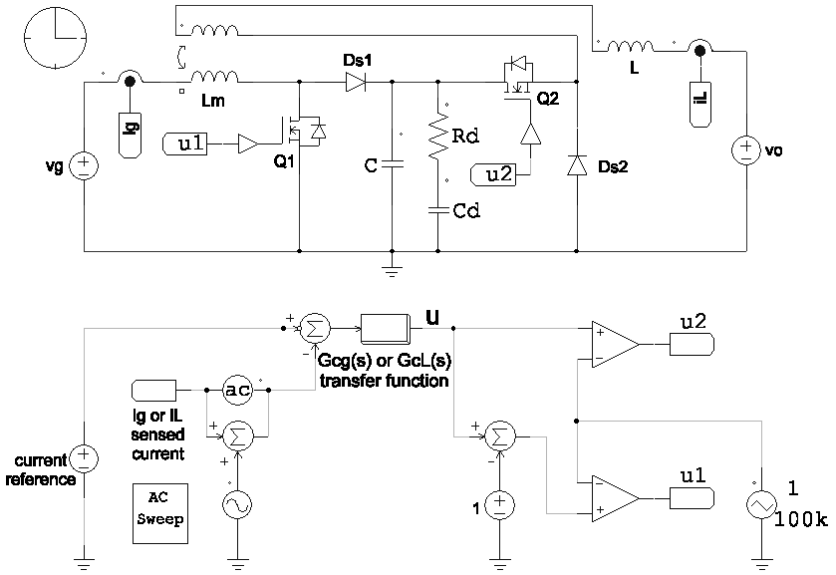

Figure 3-8: Circuit diagram corresponding to the PSIM simulation used to calculate the loop-gain Bode plots called PSIM switched model A.

The small differences in boost and buck mode between the two responses in Figs. 3-7(a) and (c) are due to the switching effects not included in the small-signal linear model. In lower-border boost and upper-border buck modes there are differences with the switched model A as can be seen in Fig. 3-7(b). Thus, neither of the two transfer functions, $G_{i_g d_1}(s)$ and $G_{i_g d_2}(s)$, is in a good agreement with the switched model on the border between the two modes of operation, $U = 1$. Consequently a model needs to be developed that fits better on the border between boost and buck operation modes. According to equations (3.16) and (3.17), in small-signal the duty cycles $\widehat{d}_1(t)$ and $\widehat{d}_2(t)$ are related in the border mode of operation $U = 1$ with the single control variable $\widehat{u}(t)$ as

$$\widehat{d}_1(t) = \begin{cases} 0 & if \quad U < 1 \\ \\ \widehat{u}(t) & if \quad U \geq 1 \end{cases} \qquad \widehat{d}_2(t) = \begin{cases} \widehat{u}(t) & if \quad U \leq 1 \\ \\ 0 & if \quad U > 1. \end{cases} \tag{3.29}$$

Therefore, on the border between the boost and the buck modes, the duty cycles are expressed as $\widehat{d}_1(t) = \widehat{d}_2(t) = \widehat{u}(t)$ and a new control-to-input-current small-signal transfer function is defined on the border as

$$G_{i_g u}(s) = G_{i_g d_1}(s)\Big|_{U=1} + G_{i_g d_2}(s)\Big|_{U=1} \tag{3.30}$$

All the operation modes of the buck-boost converter and its control can be generalized as is shown in the small-signal block diagram depicted in Fig. 3-9(a), where the dual PWM block is generated using the equation (3.29). According to the block diagram of Fig. 3-9(a), in boost mode the loop-gain of the system is (3.27) while in buck mode it is(3.28). On the border between boost and buck modes, the loop-gain is defined according to (3.30) as

$$T_g(s)\Big|_{U=1} = \left(G_{i_g d_1}(s)\Big|_{U=1} + G_{i_g d_2}(s)\Big|_{U=1} \right) G_{cg}(s). \tag{3.31}$$

This model is in good agreement with the switched model A even on the border of the boost and buck modes as shown in Fig. 3-7.

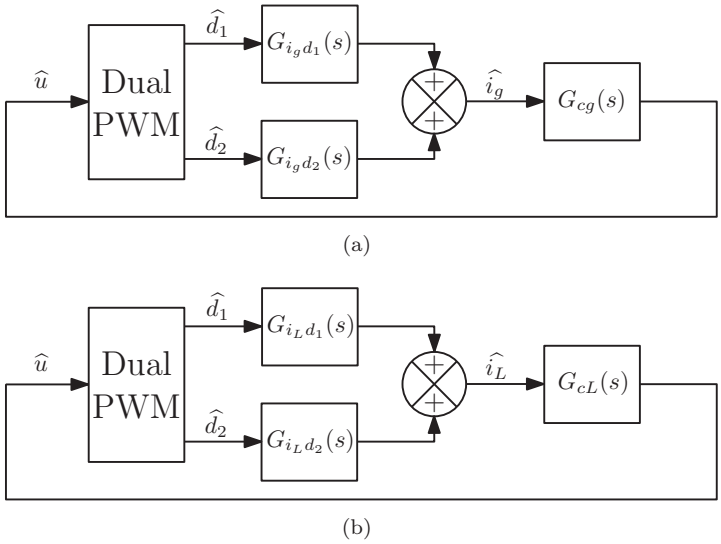

Figure 3-9: Small-signal block diagram of the converter used to calculate the different linear-model loop-gains of the: (a) input-current control, (b) output-current control.

Likewise, the loop-gain Bode plots in boost mode, buck mode and on the border between these modes with the output-current control

$$T_L(s)\Big|_{boost} = G_{i_L d_1}(s) G_{cL}(s) \tag{3.32}$$

$$T_L(s)\Big|_{buck} = G_{i_L d_2}(s) G_{cL}(s) \tag{3.33}$$

$$T_L(s)\Big|_{U=1} = \left(G_{i_L d_1}(s)\Big|_{U=1} + G_{i_L d_2}(s)\Big|_{U=1} \right) G_{cL}(s) \tag{3.34}$$

are constructed in Fig. 3-10 using the small-signal block diagram illustrated in Fig. 3-9(b).

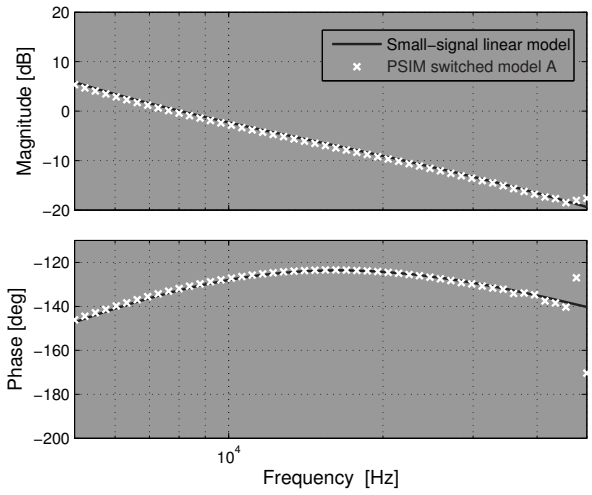

(a)

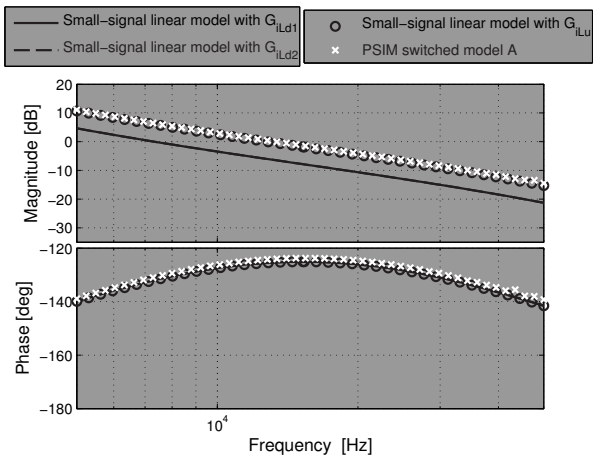

(b)

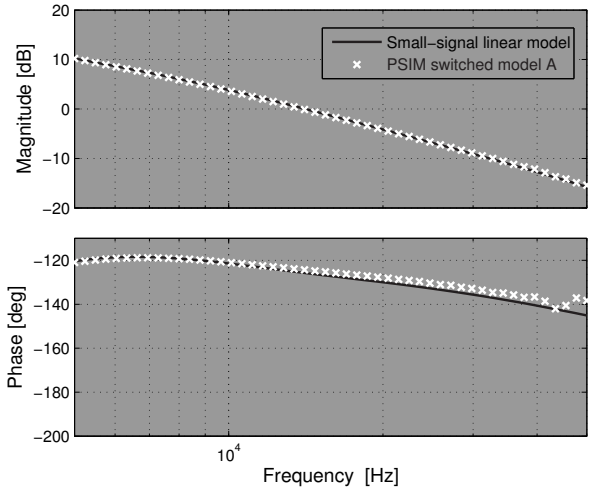

(c)

Figure 3-10: Loop-gain Bode plots of the buck-boost converter with input references that ensure input currents of: (a) 8 A in boost mode for $V_g = 36$ V and $V_o = 48$ V, (b) 11 A in lower-border boost and upper-border buck modes for $V_g = 36$ V and $V_o = 36$ V, (c) 15 A in buck mode for $V_g = 48$ V and $V_o = 24$ V. The black lines correspond to the small-signal linear model using MATLAB while the white x-marks correspond to the simulation of the switched model using PSIM.

According to Figs. 3-7 and 3-10, the small-signal linear models proposed for the closed loop buck-boost converter and the switching model are in good agreement. The theoretical crossover frequency of the response in Fig. 3-7 is about 10 kHz with a phase margin of 63^o in buck mode, 8 kHz with a phase margin of 51^o in boost mode, and 9 kHz with a phase margin of 53^o in the border. In Fig. 3-10, on the other hand, they are 13 kHz and 55^o in buck mode, 8 kHz with a phase margin of 47^o in boost mode, and 13 kHz with a phase margin of 56^o on the border between boost and buck modes. Consequently, we can ensure that the feedback system is stable at the operation point studied. As will be seen below, the controller gains have been refined by means of an experimental iteration in which some bandwidth has been traded-off for phase margin.

3.5 Experimental results

To validate the proposed converter and its analysis under ACC presented in the section above, a prototype of the coupled-inductor buck-boost converter depicted in Fig. 3-11(a) with the input and output current controller of Fig. 3-11(b) has been developed and tested. The buck-boost converter was been designed to transfer power between two voltage sources, such as batteries and supercapacitors, so that the input-voltage v_g and the output-voltage v_o ranged between 15 V and 55 V, 0 V to 55 V, respectively. The power supply for the analog control was obtained from the converter input-voltage v_g. A linear regulator was used to adjust the voltage supply to 15 V and determine the lower limit of v_g. The maximum converter input and output currents were limited to 16 A to prevent the saturation of the magnetic cores selected in the inductor design procedure, where the switching frequency of 100 kHz has been considered. The nominal values of the buck-boost power stage parameters, whose components are listed in Table 3.1, were selected according to the design criteria presented in detail in [82]. The main specifications are desired input and output peak-to-peak current and voltage ripples, the zeros damping factor, and power dissipation of the damping network. The ESR (Equivalent Series Resistance) of C_d is much smaller than R_d. All components are rated up to 100 V. Fig. 3-12 depicts a diagram of the coupled inductors structure with emphasis in the primary and secondary turns distribution in the selected toroidal core.

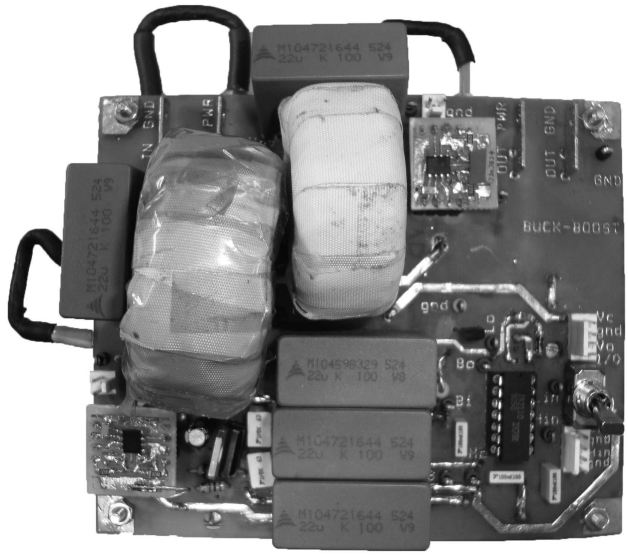

(a)

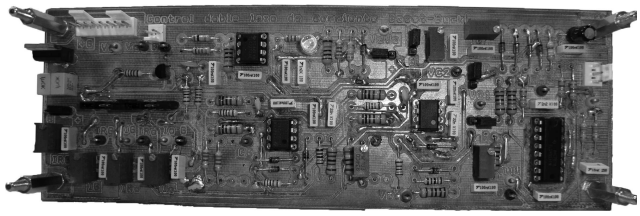

(b)

Figure 3-11: Regulator prototype (a) buck-boost power stage, (b) average current-mode control board.

Table 3.1: Components of buck-boost converter

Component	**Description**	**Type**
Q_1, Q_2	Power MOSFET	IRFB4110PbF
D_{s_1}, D_{s_2}	Schottky Rectifier	40CPQ080GPbF
L_m	Coupled inductors	Core: 77438A7 Magnetics Wire size: 12 AWG[b] Number of turns: 12:12 Inductance: 35 μH
C	Ceramic Capacitor	6 $\times$ 2.2 μF[a] X7R dielectric
L	Inductor	Core: 77083A7 Magnetics Wire size: 12 AWG[b] Number of turns: 29 Inductance: 35 μH
R_d	Damping Resistor	1.5 Ω, 4 W
C_d	MKT Capacitor	66 μF

[a] For $V_c = 48$ V the equivalent capacitance is 7 μF.

[b] Multifilar equivalent.

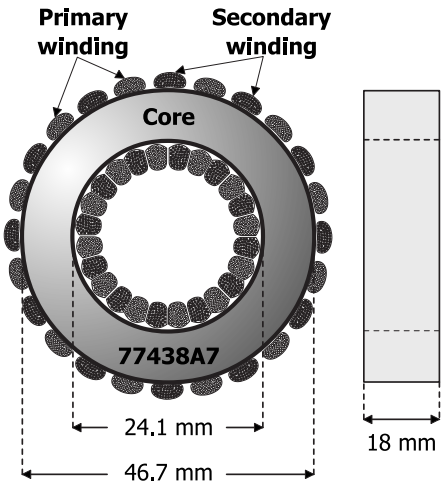

Figure 3-12: Longitudinal cut of the coupled-inductor.

The existence of delays means that duty cycles are not extreme and causes a nonlinearity in the transitions between boost and buck modes [71]. To mitigate these problems, a third mode of operation is permitted in an adjustable narrow transition zone between buck and boost modes [82, 71, 50]. In the new overlapping operation mode, called buck-boost mode, both switches are allowed to commutate within a switching period.

Experimental measurements and PSIM simulation Bode plots of the input-current regulator loop-gain are illustrated in Fig. 3-15 for the three different operation modes, achieved by selecting appropriate values for the input and output voltages, V_g and V_o. The input-current reference v_{iref} is adjusted in each mode to achieve a steady-state operation point corresponding approximately to 400 W, which is half of the maximum power of the converter. For the three operation modes, two switching models have been considered. The PSIM switching model A is the ideal model used in the previous section, whereas in the PSIM switching model B depicted in Fig. 3-13, estimations of delays, switching losses, a non-ideal current sensor model, and control stage operational amplifier models have been taken into account. In the circuit diagram of the PSIM switching model B the triangular-signal oscillator frequency has been adjusted to 100 kHz, an amplitude of 0.7 V and a DC offset of 1.4 V, which corresponds to the values that are used in the experiments and which will be explained in greater detail below. Moreover, since the voltage drop of diode D_1 is smaller than the amplitude of the triangular signal oscillator, model B considers an overlapping that ensures that the buck-boost region is narrow. The input-current loop compensator (3.25) and the output-current loop (3.26) transfer functions differ only in the gain. Therefore, the value of resistor RG in the simulation scheme presented in Fig. 3-13 is adjusted to 22 kΩ and 10 kΩ, the result is it provides $G_{cg}(s)$ and $G_{cL}(s)$, respectively. All simulations, for both switching models, have considered the nonlinearities in some passive components of the experimental prototype using their measured values instead of the theoretical nominal ones. For instance, the capacitance of the intermediate capacitor

exhibits a strong dependence on the applied voltage as has already been noted in Table 3.1 and in Fig. 2-11. Also, the parameters of the magnetic components vary with the mean average current flowing through them as shown in Fig. 3-14 (see Appendix B). The experimental frequency data have been obtained using a Venable 3120 frequency response analyzer (FRA). In the same way, experimentally measured and PSIM-simulated Bode plots of the output-current regulator loop-gain are illustrated in Fig. 3-16. Although not shown in these Bode plots, the theoretical small-signal frequency responses in buck and boost mode are in good agreement with the results obtained using the switched model A and could be used for a preliminary quick design of the controller parameters without having to develop more complex models [91]. In buck-boost overlapping mode the small-signal frequency response was not obtained theoretically but by using experimental measurements and simulations.

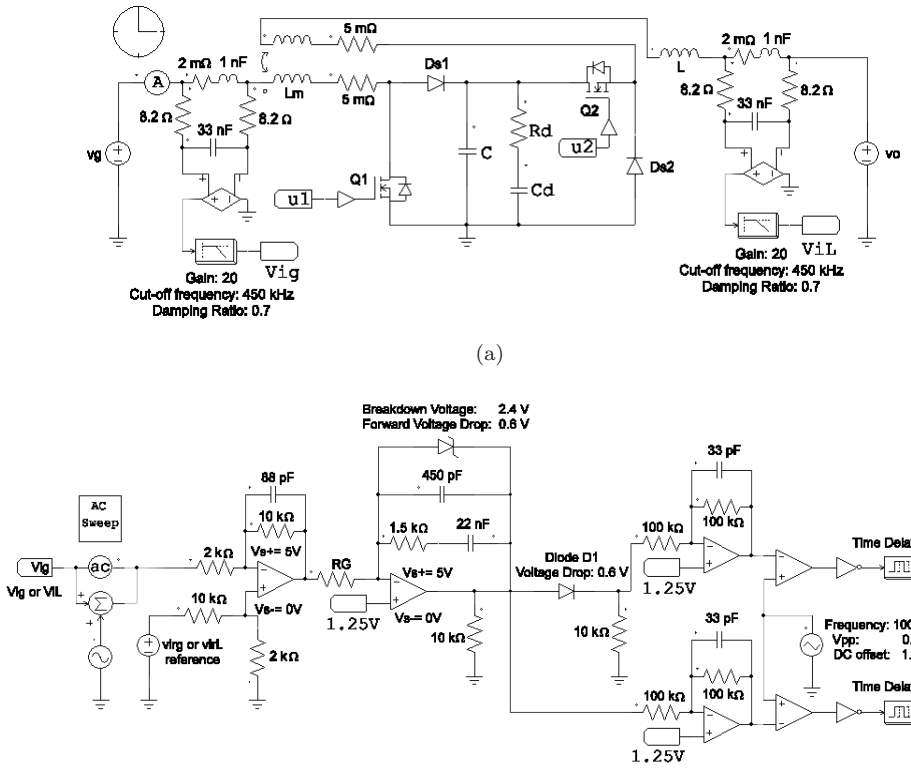

Figure 3-13: Circuit diagram corresponding to the PSIM simulation used to calculate the loop-gain Bode plots with the PSIM switched model B. (a)buck-boost power diagram, (b)buck-boost control circuit diagram.

The crossover frequencies (CF) and phase margins (PM) of the experimental frequency responses shown in Figs. 3-15 and 3-16 are measured and listed in Table 3.2 for each operation mode and current control. The stability margins are in agreement with the design criteria assumed in the previous section. The smallest measured phase margins are 44^o and, since the objective was 45^o, we conclude

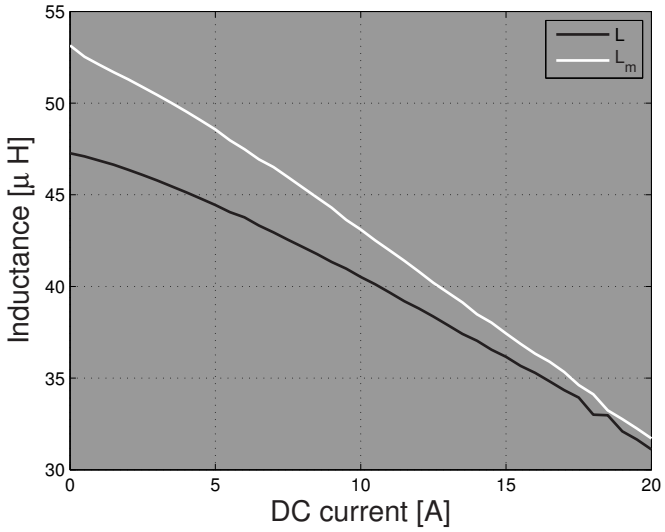

Figure 3-14: Inductance vs DC current characteristics. The black trace corresponds to the inductor L while the white trace corresponds to the magnetizing inductance L_m of the coupled inductor.

that the closed-loop system is stable for all the operation modes for both input and output current. The smallest crossover frequency is 8 kHz, which provides a reasonably wide bandwidth.

Table 3.2: Crossover frequency (CF) and phase margin (PM) for different operation modes

	Input-current control		**Output-current control**	
Operation mode	CF [kHz]	PM [deg]	CF [kHz]	PM [deg]
boost	8	47	8	44
buck-boost	11	45	17	46
buck	8	62	14	44

Three main factors explain the stability degradation: switching delays in the order of 200 ns, a small bandwidth of the current sensor circuit (one pole at about 300 kHz and another one close to 450 kHz), and the even more reduced bandwidth of the controller operational amplifiers (one pole of the voltage error amplifier at 230 kHz and a second one introduced by the current PI stage at 240 kHz). For instance, in the buck output-current case, the initial theoretical phase margin of 55^o has been reduced only to about 44^o. The first factor accounts for 1^o of the total 9^o phase margin reduction. The other two factors are responsible for 3^o and 5^o respectively. In the buck-boost mode the overlapping adjustment has a small influence on the system gain. Overall, the final experimental stability results are quite good in spite of the limiting factors mentioned. Future implementations could improve the bandwidth if better current sensors and operational amplifiers are selected.

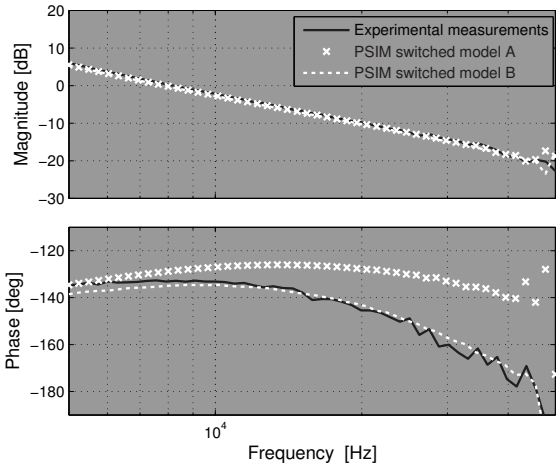

(a)

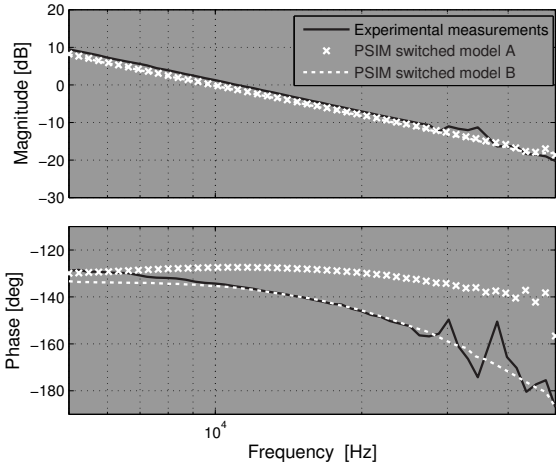

(b)

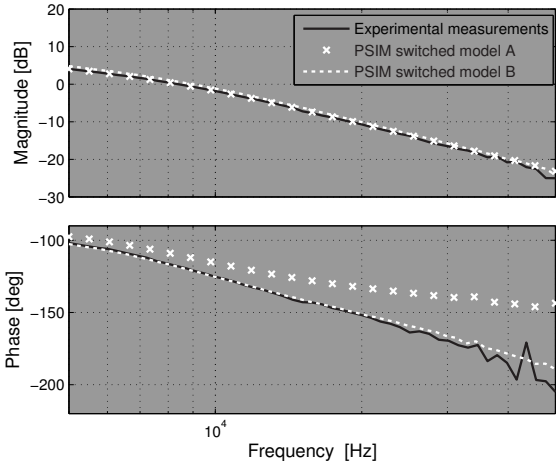

(c)

Figure 3-15: Loop-gain Bode plots of the buck-boost converter with input references that ensure input currents of: (a) 11 A in boost mode for $V_g = 36$ V and $V_o = 48$ V, (b) 12 A in buck-boost mode for $V_g = 32$ V and $V_o = 32$ V, (c) 8 A in buck mode for $V_g = 48$ V and $V_o = 24$ V.

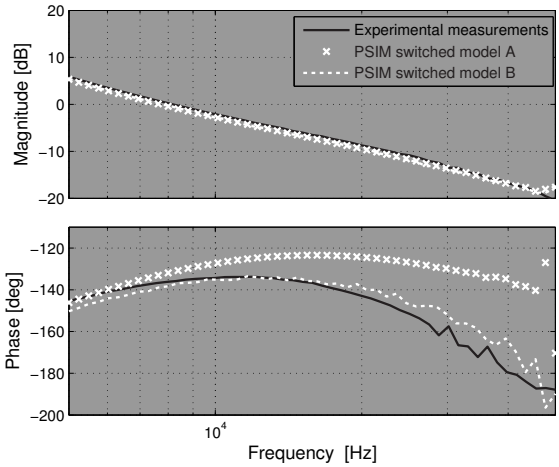

(a)

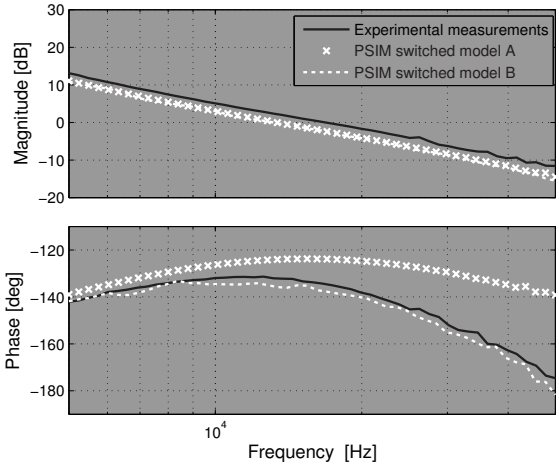

(b)

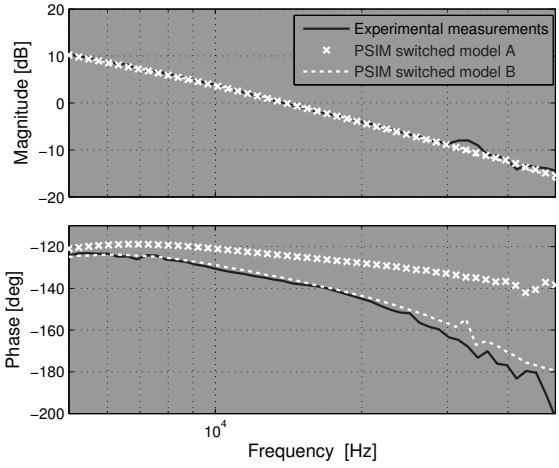

(c)

Figure 3-16: Loop-gain Bode plots of the buck-boost converter with input references that ensure output currents of: (a) 8 A in boost mode for $V_g = 36$ V and $V_o = 48$ V, (b) 11 A in buck-boost mode for $V_g = 36$ V and $V_o = 36$ V, (c) 15 A in buck mode for $V_g = 48$ V and $V_o = 24$ V.

The energy conversion efficiencies as a function of the output-current i_L and with output-current control are shown in Fig. 3-17 for the three different operation modes. In CCM, the converter efficiencies are in the range 93.5% to 96.5% including the power consumption of the control board of Fig. 3-11(b), the driver stage, and two current sensors with their conditioning circuits. These energy conversion efficiencies were experimentally measured using the Voltech PM6000 Power Analyzer. The buck-boost mode is the least efficient since in this mode both transistors are switching. Efficiencies will improve if the diodes are substituted by synchronous rectifier MOSFETs [55, 56]. Other efficiency improving techniques such as multiphase and ZVS [55] or the dynamic adjustment of the switching frequency [56] are also possible.

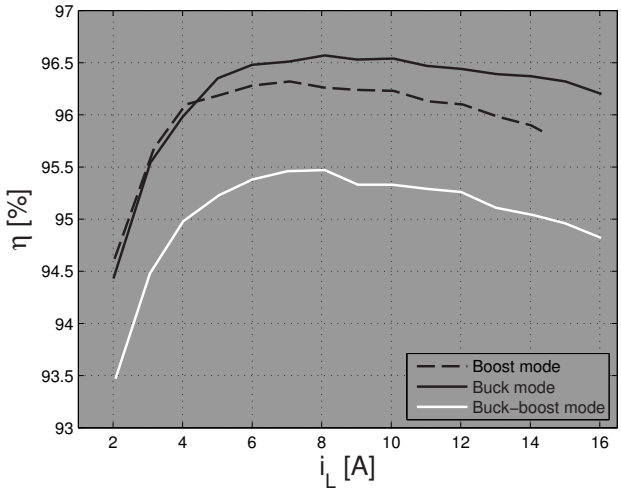

Figure 3-17: Energy conversion efficiency as a function of the output-current i_L in the three different modes of operation: boost mode with $V_g = 48$ V and $V_o = 55$ V, buck-boost mode with $V_g = 48$ V and $V_o = 48$ V and buck mode with $V_g = 55$ V and $V_o = 48$ V.

Fig. 3-18 depicts the main converter experimental waveforms when the input-current control reference is a high frequency triangular shaped signal. The input and output voltages have been adjusted to show the converter response in its three operation modes: (a) boost, (b) buck-boost, and (c) buck. The same waveform reference is also used to test the output-current control in the three different modes as is illustrated in Fig. 3-19. The four commutations per period that can be observed in a small zone of the input-current of Figs. 3-18(d) and 3-19(d) are caused by the overlapping in the buck-boost mode. In Fig. 3-18(c) it can be seen that the ripple in the simulation is smaller than the ripple obtained experimentally in Fig. 3-18(d) due to the nonlinearities of the PWM when the pulses are extreme. As can be observed in Figs. 3-18 and 3-19, the controlled current follows the fast 4 kHz triangular reference waveform in the three operation modes for both current control strategies. Therefore, these good transient responses validate the experimental wide bandwidths that are reported in Table 3.2.

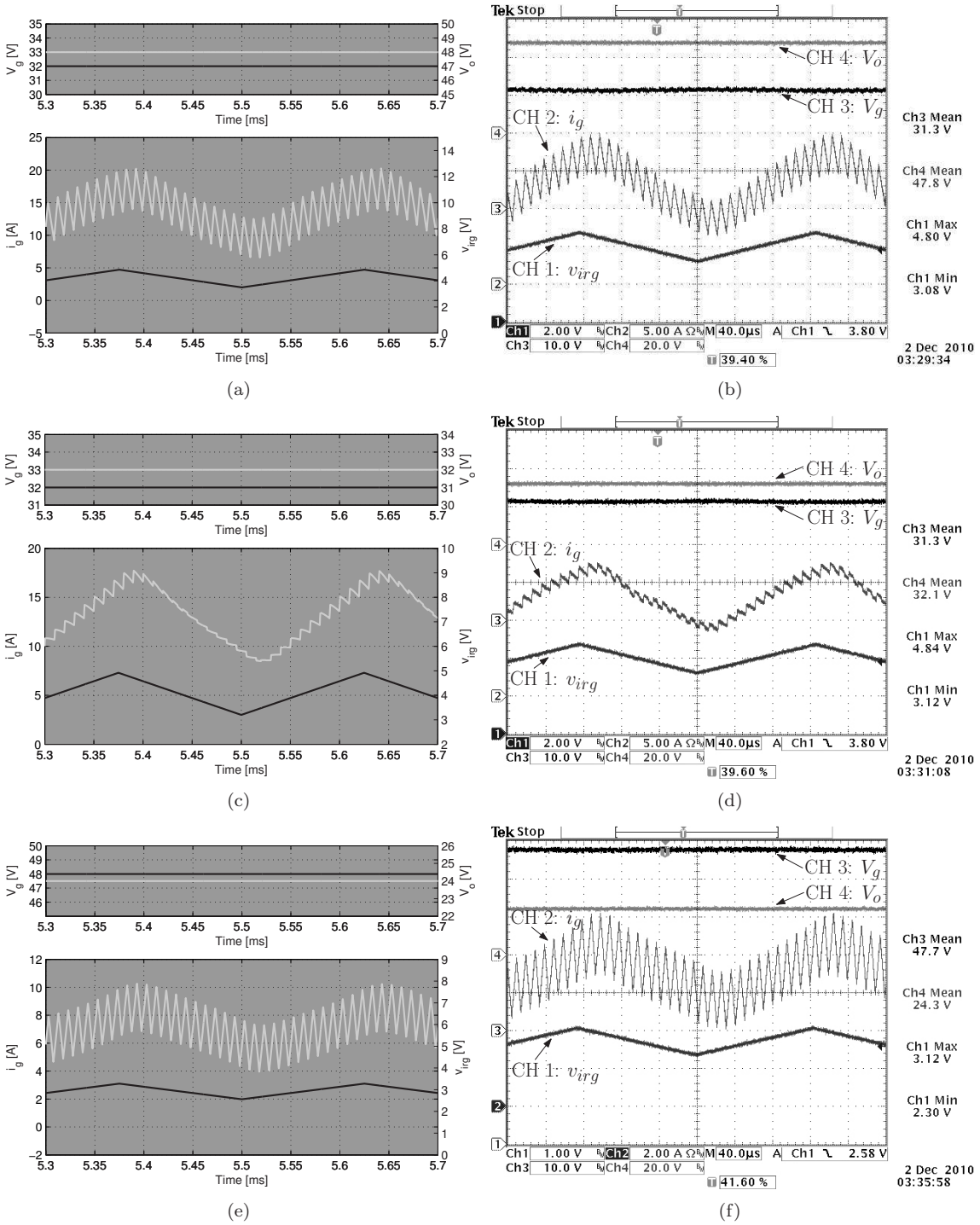

Figure 3-18: PSIM simulations (a), (c), (e) and experimental measurements (b), (d), (f) of the transient responses of the system under input-current control when the reference is a 4 kHz triangular waveform. Three operation modes are shown: (a),(b) boost mode with $V_g = 32$ V, $V_o = 48$ V, and $\bar{i}_g$ varies from 8 A to 16 A, (c),(d) buck-boost mode with $V_g = 32$ V, $V_o = 32$ V, and $\bar{i}_g$ varies from 8 A to 16 A, (e),(f) buck mode with $V_g = 48$ V, $V_o = 24$ V, and $\bar{i}_g$ varies from 4 A to 8 A. Black traces in the simulation show the input voltage V_g and the input reference v_{irg} while the output voltage V_o and the input current i_g are in white.

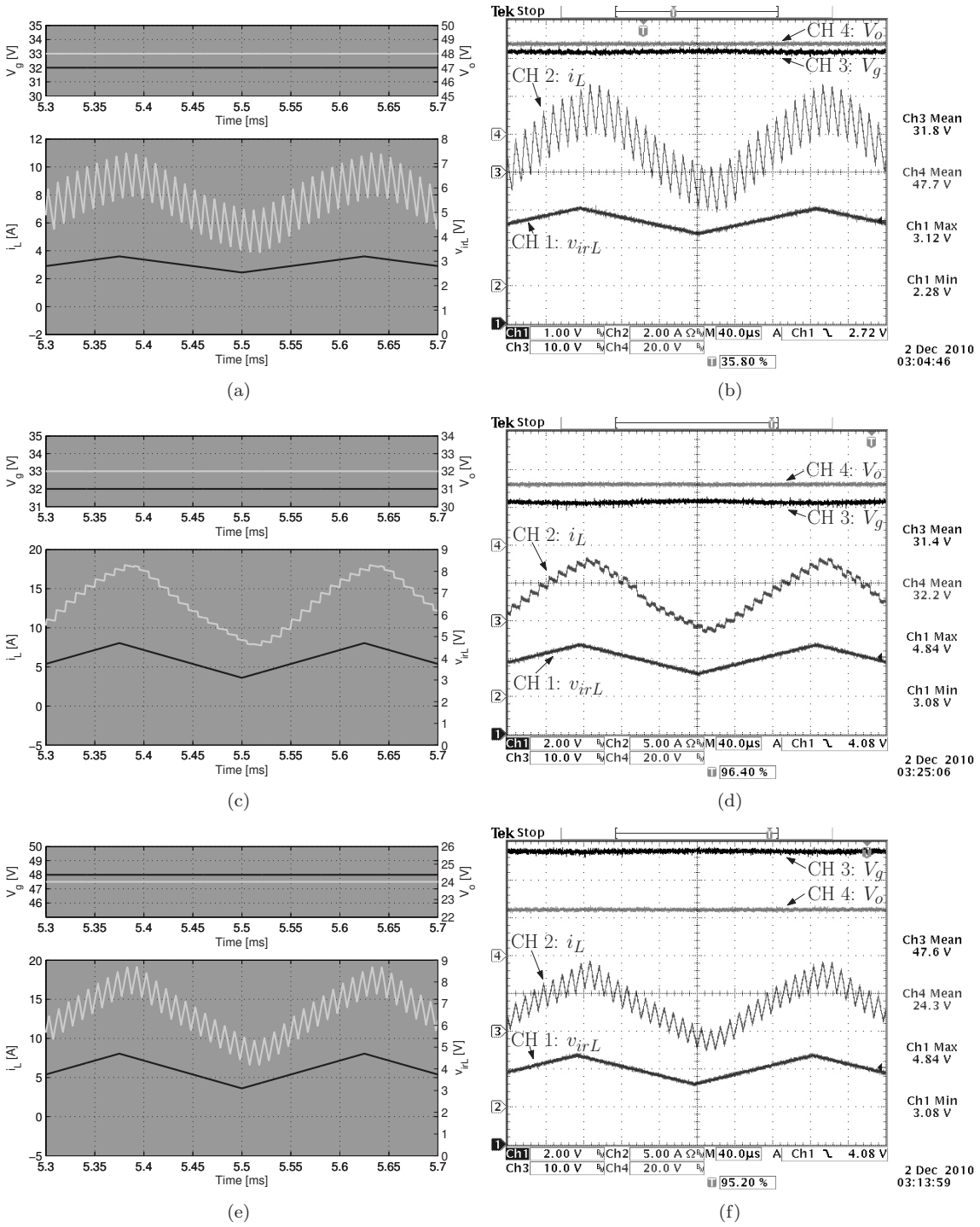

Figure 3-19: PSIM simulations (a), (c), (e) and experimental measurements (b), (d), (f) of the transient responses of the system under output-current control when the reference is a 4 kHz triangular waveform. Three operation modes are shown: (a),(b) boost mode with $V_g = 32$ V, $V_o = 48$ V, and $\bar{i}_L$ varies from 4 A to 8 A, (c),(d) buck-boost mode with $V_g = 32$ V, $V_o = 32$ V, and $\bar{i}_L$ varies from 8 A to 16 A, (e),(f) buck mode with $V_g = 48$ V, $V_o = 24$ V, and $\bar{i}_L$ varies from 4 A to 8 A. Black traces in the simulation show the input voltage V_g and the input reference v_{irL} while the output voltage V_o and the output current i_L are in white.

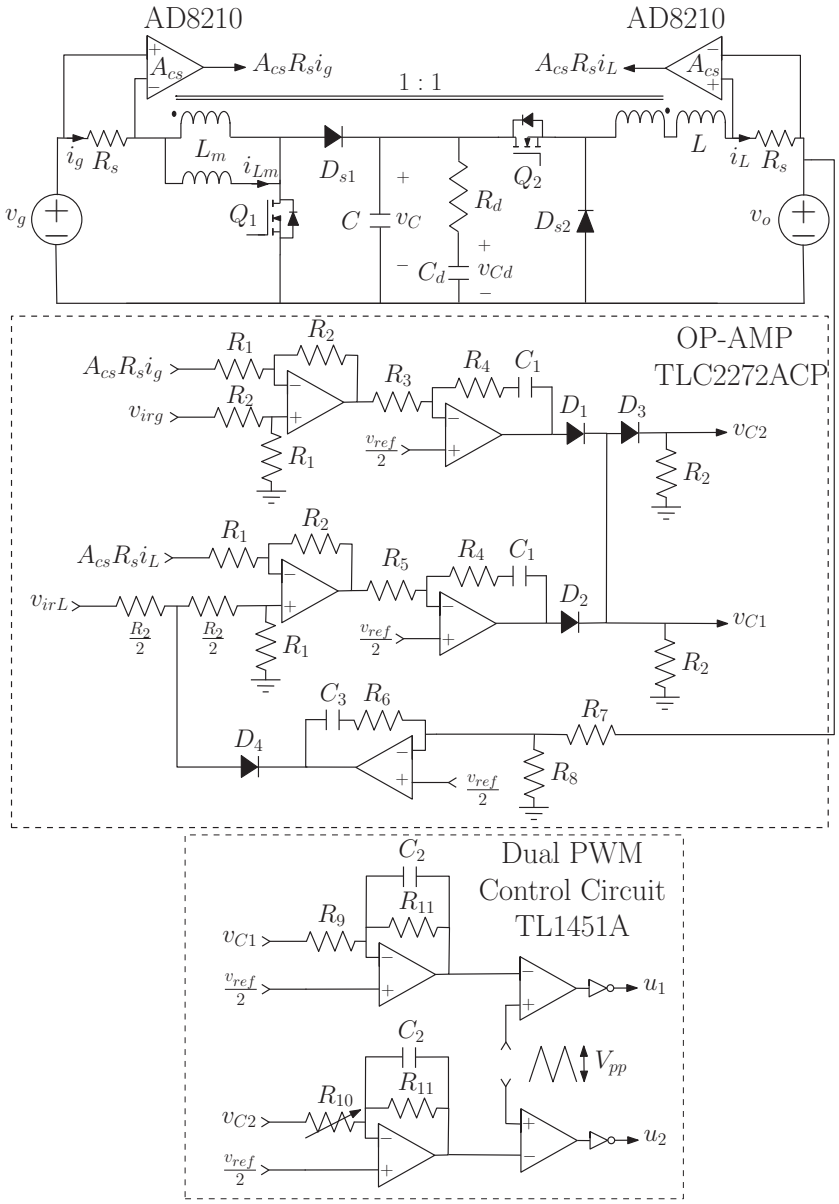

Figure 3-20: Proposed simplified scheme of the buck-boost converter prototype with input and output current loop compensators and output-voltage limiter.

Fig. 3-20 shows the final scheme of the buck-boost regulator that was implemented. In addition to the average input and output current-mode control loops, a new output-voltage control loop designed to limit the maximum voltage v_o has been included. The dual PWM controller integrated circuit TL1451A generates the switch activation signals $u_1(t)$ and $u_2(t)$.

Each separate current control loop has the small-signal behavior of the block diagram presented in Fig. 3-5 but split in three stages in cascade: an error amplifier block (TLC2272), a PI compensator (TLC2272), and high-frequency pole block (TL1451). This implementation makes it possible to use a unipolar 5 V supply for all the integrated circuits of the control board. The diodes D_1 and D_2

enable the two current loops to be combined so that, in steady-state, one of the currents is smaller than the input reference while the other, regulated by the active loop, is equal to the input reference. Thus, the maximum average value of each current is limited by its reference input. Combining both current loops in this way is a simple technique although if there is a transition between current control loops, it is slow because the PI for the loop not regulating the converter saturates, as is illustrated in Fig. 3-21. One technique that can be used to achieve fast transitions between control loops is pre-charging the capacitors of the current-control integrators [92].

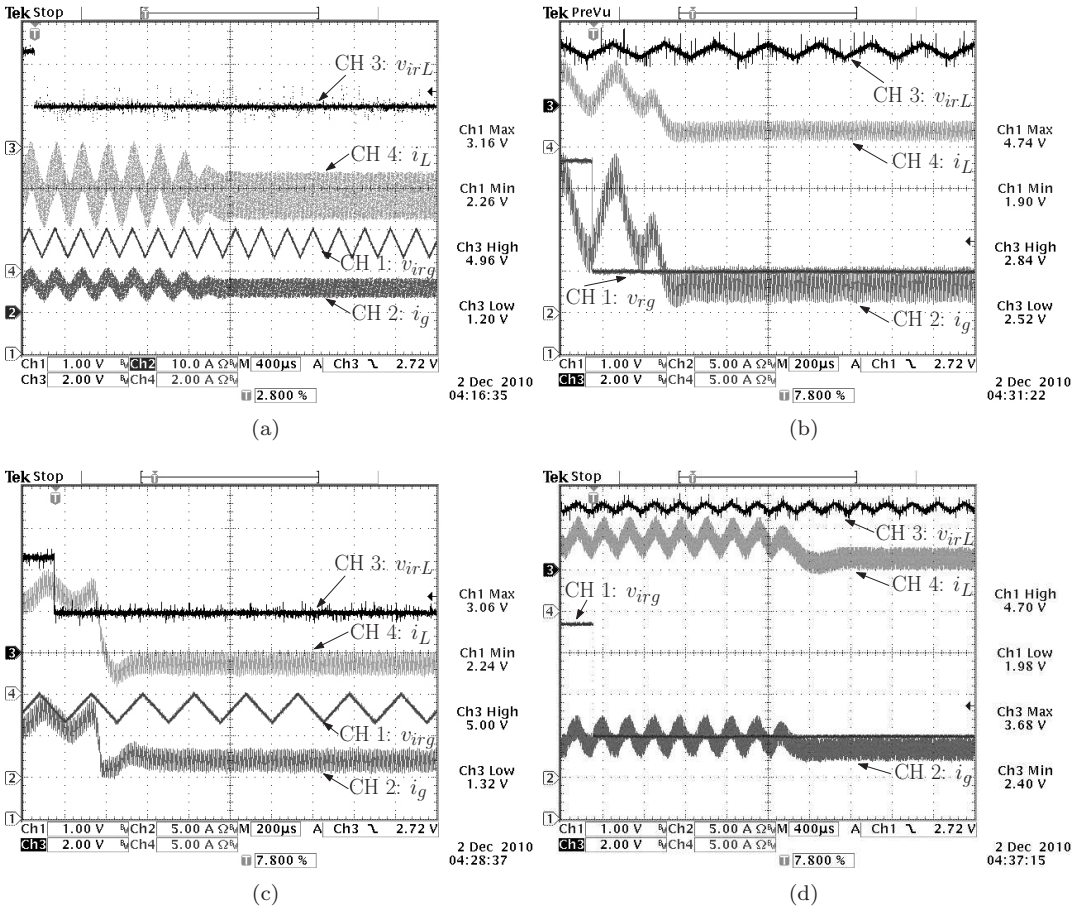

Figure 3-21: Transitions between control loops using two different input references. The first is a 4 kHz triangular waveform to ensure variations from 4 A to 8 A in the average current value and the second a 100 Hz square waveform that provides variations from 2 A to 16 A. Boost mode with $V_g = 32$ V, $V_o = 48$ V (a) triangular waveform in v_{irg} and square waveform in v_{irL}, (b) square waveform in v_{irg} and triangular waveform in v_{irL}. Buck mode with $V_g = 48$ V, $V_o = 24$ V (c) triangular waveform in v_{irg} and square waveform in v_{irL}, (d) square waveform in v_{irg} and triangular waveform in v_{irL}.

The TL1451A has two error amplifiers, an adjustable oscillator, a reference voltage of $V_{ref} = 2.5$ V, and dual common-emitter output transistor circuits. The triangular signal oscillator has been adjusted to a frequency of 100 kHz, an amplitude of $V_{pp} = 0.7$ V and a DC offset of 1.4 V. Therefore, the diode forward voltage drop of D_3 must be approximately V_{pp} to obtain the control signals v_{c1} and

v_{c2} as illustrated in Fig. 3-20. The variable resistor R_{10} makes it possible to adjust the overlapping zone in the buck-boost mode. Additionally, diode D_4 enables the reference of the output-current loop v_{irL} to be substituted by a limiting value provided by an outer PI loop when the output-voltage exceeds its maximum value. Fig. 3-22 depicts the PSIM control implementation of the input and output current loop compensators and the output-voltage limiter presented in Fig. 3-20.

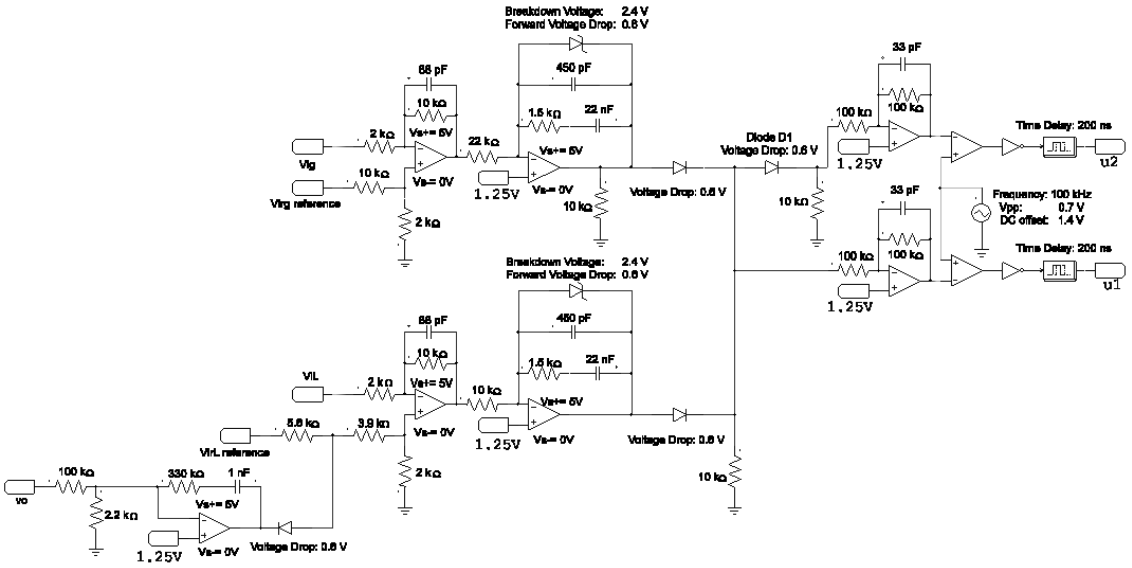

Figure 3-22: Circuit diagram of the buck-boost control circuit used in PSIM simulation in conjunction with the buck-boost power diagram of the Fig. 3-13(a) to simulate the final scheme proposed in Fig. 3-20.

To prove that the current sensors operated correctly the test box illustrated in Fig. 3-23 had to be developed. This box obtains a regulated power supply for the AD8210 from the input voltage and compares the current sensor output with the one obtained using a current probe of the oscilloscope as presented in Fig. 3-24. In addition, one variable load or two fixed ones can be connected and changes made with a switch to test the dynamics of the sensor. All these tests are performed in high common-mode voltage.

Figure 3-23: Different views of the current sensor test box.

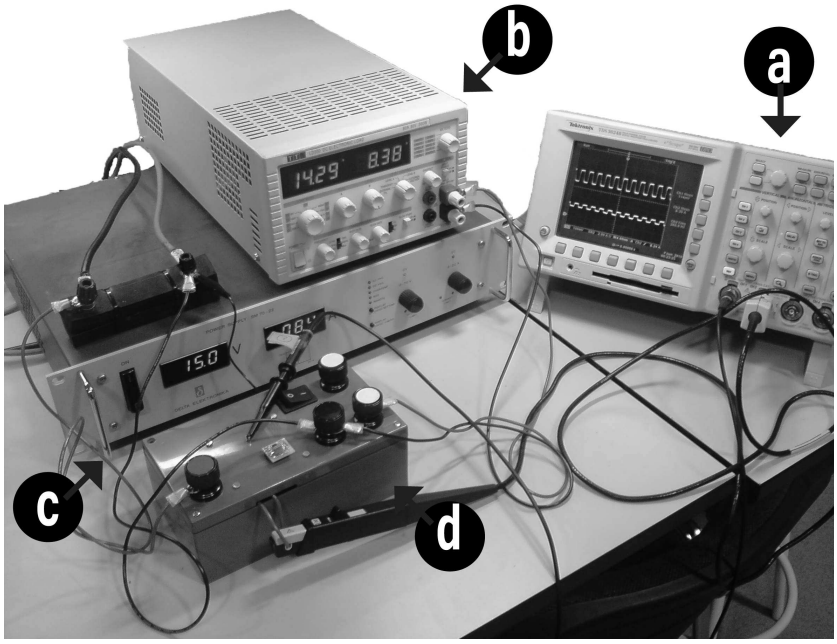

Figure 3-24: Experimental configuration to test the current sensor: (a) oscilloscope, (b) DC electronic load, (c) DC power supply, (d) test box.

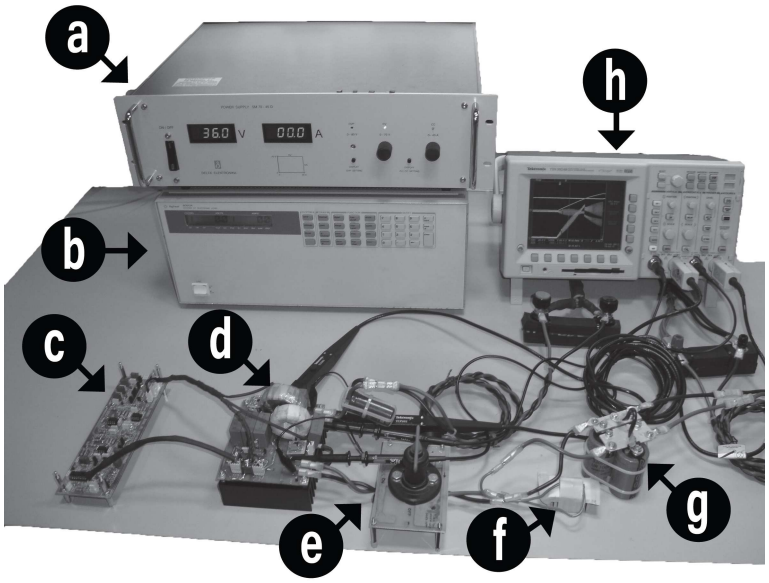

Figure 3-25: Experimental configuration of the capacitor charging system: (a) DC power supply, (b) DC electronic load in constant resistance mode of 48 Ω to ensure a minimum consumption, (c) buck-boost control, (d) buck-boost converter, (e) switch that minimizes electric arc formation, (f) Schottky rectifier in series with the load to prevent a reverse current, (g) Three electrolytic capacitor of 3.3 mF connected in parallel, (h) oscilloscope.

Finally, as already mentioned, one of the proposed applications of the buck-boost converter and its ACC are the charging-discharging of capacitors, supercapacitors and batteries. As an example to verify the operation of the current control loops and the voltage limitation, a capacitor-charging power supply was implemented using the experimental setup shown in Fig. 3-25. The experimental capacitor-charging waveforms are presented in Fig. 3-26. In this experiment, both current references are equal to 9.2 A, the maximum output-voltage adjusted by R_8 is equal to 49.2 V and the input-voltage V_g is equal to 36 V. Initially, there is a short circuit in the output voltage with a duration Δt_1, during which the active loop regulates the average output-current $\bar{i}_L$ to 9.2 A. At the beginning of Δt_2 the short circuit is removed and the capacitor voltage starts to increase with values lower than V_g. Therefore, in this time period the buck-boost power stage is in buck operation mode with an output-current control. During the small period Δt_3, the capacitor voltage and the input-voltage V_g are close, so the converter operates in buck-boost mode and the input current exceeds the current reference at the end of Δt_6, so that the new active loop is the input-current control. In the interval Δt_4, the capacitor voltage continues to increase and clearly shows a boost mode with an input-current control. At the beginning of Δt_5, the capacitor voltage exceeds the output-voltage limit of 49.2 V, so the new active loop is an output-current control limiting the output-voltage. One advantage of the ACC is that it regulates well even in discontinuous conduction mode (DCM)

as can be seen during the interval Δt_5 and in other experimental tests. The PSIM simulation of the controlled charge of the capacitor is presented in Fig. 3-27. The experimental result and the simulation are in good agreement as can be seen in Figs. 3-26 and 3-27. Since our model does not include the DCM operation the period Δt_5 does not appear in Fig. 3-27. Converter operation in DCM will be studied in a future work. The fast capacitor charging profile presented in Fig. 3-26 confirms the correct operation and interaction of the current control loops and the output voltage limiter for the three operation modes of the converter.

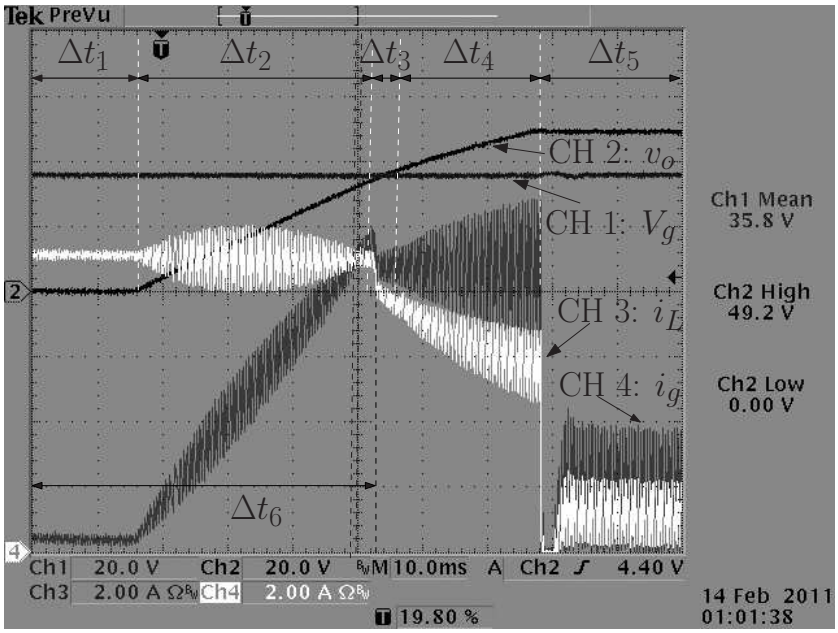

Figure 3-26: Experimental measurement of the controlled charging capacitor. CH1: input-voltage V_g (20 V/div), CH2: output-voltage v_o (20 V/div), CH3: output-current i_L (2 A/div), CH4: input-current i_g (2 A/div) and time base of 10 ms.

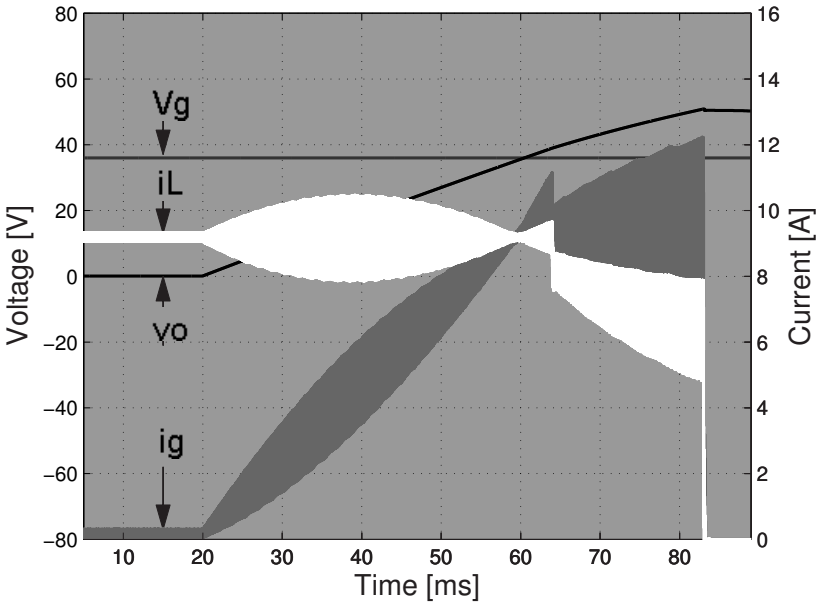

Figure 3-27: PSIM simulation of the controlled charging capacitor.

3.6 Conclusions

A recent study showed that the voltage-mode controlled coupled-inductor buck-boost converter is a high-efficient regulator with wide bandwidth and a continuous input-to-output voltage conversion ratio that makes it very useful in applications whose output voltages are above and/or below the input level. Since the converter has continuous input and output currents, the present contribution has studied the application of average current-mode control strategies that would also make the converter suitable for large voltage conversion ratio applications like battery/supercapacitor charging and discharging regulators or fuel-cell interfaces. Obtaining control-to-input/output current small-signal transfer functions in open-loop operation makes it possible to design fast input and output current controllers, as the switched mode ideal PSIM simulations have made clear. Experiments with a 800-W prototype have shown that delays and other implementation-related control limitations reduce the theoretical phase-margins and provide new adjustments for controller gains. Experiments with the prototype and simulations of an improved switched model that includes the main implementation non-idealities reveal that worst-case 45 degree phase-margins and 8 kHz wide-bandwidths are obtained for the two average current-mode controls considered.

The combination of the two current control strategies and an additional output voltage limiter loop is proposed as a simple method to control one of the currents and to impose limits on the maximum values of the other one and the output voltage. The advantages of this control have been revealed by using the prototype to charge a large capacitor from a short-circuit condition to a maximum voltage well above the input voltage of the buck-boost converter. In this experiment,

the input and output current references were selected so that a correct representative sequence of changes between active loops is evidenced. The use of the converter as a current regulator connected between variable voltage sources and loads is currently under investigation.

Future studies will also analyse the discontinuous conduction mode, the parallel connection of several stages, and the bidirectional implementation of the power stage and the current regulators.

Chapter 4

Simulator of a PEM Fuel-Cell Stack Based on a Dynamic Model

4.1 Abstract

This chapter presents a low cost, easy to use digital simulator for a Proton Exchange Membrane Fuel-Cell (PEMFC) stack. The PEMFC stack simulator is implemented by controlling the output voltage of a power source using LabVIEW. The simulator enables different models to be easily implemented and, simultaneously, makes it possible to study different FC types. The FC stack is represented by a circuital model that considers the capacitive effects of the electrodes and the internal thermodynamic characteristics. This model allows a simulator to be developed that reproduces the static and dynamic characteristics of a specific fuel cell. The program on the computer handles two main tasks: the first one is the evaluation of the model and the second one is the writing and reading of the experimental data. Each of these tasks is assigned to a different core of the computer and the communication between both processes is carried out using only local variables. The fact that the programming used specific tasks for each core allows for greater computational speed of the simulator. Experimental results are contrasted with the data model from a Relion SR-12 500-W PEMFC stack.

4.2 Introduction

Fuel cells (FC) are a highly promising source of distributed energy, because of their reliability and nonpolluting emissions to the environment [32]. FC simulators are needed in research since they make it possible to safely evaluate different control strategies and to test the performance of power transducers such as inverters and DC-DC converters. They also make it possible to carry out critical

tests that would otherwise involve a risk for the equipment. Moreover, different FC models and FC types can be studied using FC emulators.

The literature reports a PEMFC simulator that consists of a computer-controlled power rectifier controlled by LabVIEW software [93]. This simulator behaves like a PEMFC. The simulator calculates the theoretical V_{out} signal for a specific I current, I being the real current from the load connected to the rectifier. The V_{out} signal is compared with the real V_{dc} output that is measured from the rectifier, so the error between the theoretical signal and the real signal can be calculated. This error is used to manipulate the rectifier firing angle. One of the drawbacks detected in this simulator system is that the rectifier dynamic response is slower than a PEMFC response at fast load changes. Furthermore, the absence of a thermal model and the lack of parameter knowledge of the FC model mean that the real output voltage V_{out} cannot be accurately calculated for a given load current I.

The ohmic region of the static characteristic of the FC is represented by a linear function in [94]. The FC V-I characteristic is emulated by using a Digital Signal Processor (DSP), which controls a Buck converter delivering the desired V_{out} output signal. The main disadvantage of this proposal is that it requires three different linear functions to model the activation, the ohmic and the concentration regions without considering any of the associated dynamic effects of the FC.

The static characteristic of a Solid Oxide FC (SOFC) is presented in [95], by a third order polynomial of the I current. The voltage V_{out} is calculated from the I-current solution using the Newton-Raphson iterative method. The emulator was implemented using LabVIEW software. The main disadvantage of this application is that only the static characteristic is represented in the SOFC model.

The main advantage of the simulator of the Direct Methanol FC (DMFC) presented in [96] is that it does not require the use of a computer, acquisition cards or software licenses and replaces them all with a DSP based system. The main drawbacks of this system are the low mathematical complexity that the DSP can process, and the fact that it uses the the Nernst reversible voltage as a constant variable. A better approach presented in [97] uses a real single DMFC cell as a reference to determine the FC stack operation voltage. This approach is not applicable to all types of FC, since there are a limited number of single cell available. This emulator also has such disadvantages as fuel costs, and the need for a reformer and preheating equipment.

In [98], a simple emulator for a proton exchange membrane (PEM) fuel cell is presented. In

the study, the fuel cell emulator is developed by using the PEM electric circuit model proposed in [99]. The open circuit voltage E of the fuel cell is generated by a programmable DC power supply. The activation R_{act} and concentration R_{conc} resistances are represented by two of 330 $m\Omega$ resistors. The capacitor C is modeled by two 100 nF electrolytic capacitors connected in parallel. The ohmic resistance R_{ohm} is assumed to be equal to the internal resistance of the programmable power supply. The main advantage of this emulator is the simplicity of its implementation. Its main disadvantages are the absence of a temperature model, and the use of physical fixed value resistors that cannot show the dependence of the resistance on the temperature and current of the proposed model. Additionally, the hardware is specific for one type of fuel cell, and all the fixed components will have to be replaced to study another type of fuel cell. Finally, no resistor selection criteria are provided.

This chapter proposes a digital simulator based on the dynamic model of a Relion SR-12 500-W PEM FC stack, in the form of a circuital equivalent, proposed by Wang in [99]. The simulator uses a power supply controlled by a LabVIEW graphical interface. Due to the nature of the model it is necessary to use the LabVIEW control module, and simulation and multicore programming. The rest of this chapter is organized as follows: Section 4.3 provides a mathematical description of the dynamic model and details of the PEMFC simulator implementation in LabVIEW. A thermodynamic model based on heat balance equations and its corresponding LabVIEW development is presented in Section 4.4. Details of the experimental configuration and program development of the simulator are given in Sections 4.5 and 4.6, respectively. Experimental measurements and MATLAB simulations are presented in Section 4.7. Finally, the main conclusions of this chapter are outlined in Section 4.8.

4.3 Model of the Fuel Cell

This section provides a mathematical description for modeling the dynamics of a PEM FC stack. In order to simplify the analysis, the following assumptions are taken into account [100, 101, 32]:

1. One-dimensional treatment.

2. Ideal and uniformly distributed gases.

3. Constant pressures in the fuel-cell gas flow channels.

4. The fuel is humidified H_2 and the oxidant is humidified air. The effective anode water vapor pressure is 50% of the saturated vapor pressure while the effective cathode water pressure is 100%.

5. The fuel cell works under 100 °C and the reaction product is in liquid phase.

6. Thermodynamic properties are evaluated at the average stack temperature, temperature variations across the stack are neglected, and the overall specific heat capacity of the stack is assumed to be a constant.

7. Parameters for individual cells can be put together to represent a fuel-cell stack.

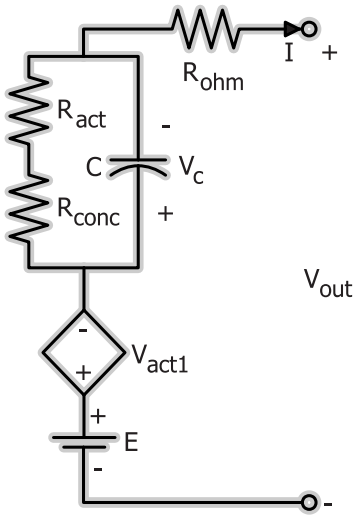

Figure 4-1: Electrical model of the PEMFC used to implement the simulator.

The circuital model of the PEMFC is represented in Fig. 4-1. The output voltage is given [102] by

$$V_{out} = E - V_{act1} - V_C - V_{ohm} \tag{4.1}$$

where the reversible potential [99] is calculated as follows

$$E = E_0^0 + \frac{RT}{2F} \ln \left[p_{H_2} (p_{O_2}^{0.5}) \right] - k_E (T - 298.15) - \lambda_e I(s) \frac{\tau_e s}{\tau_e s + 1} \tag{4.2}$$

where

E_0^0 is the standard reference potential [1.229 V].

T is the temperature of the FC [K].

R is the constant of ideal gases [8.3143 J/(mol K)].

F is the Faraday constant [96.487 kC/mol].

p_{H_2} is the partial pressure of hydrogen in the channel [Pa].

p_{O_2} is the partial pressure of oxygen in the channel [Pa].

k_E is an empirical constant [85 mV/K].

τ_e is the constant time delay of the flow for a load transient [80 s].

λ_e is a constant factor [69.4 $\mu\Omega$].

Fig. 4-2 shows the built-in LabVIEW sub-function which calculates the reversible potential and also shows the value of the constants used for this calculation. The model of the FC is developed in National Instruments' LabVIEW with the Control Design and Simulation module. This module enables the differential equation to be solved by different mathematical methods. In this case, the simulator uses the step variable third-order Runge-Kutta method to solve the afore mentioned differential equation (4.7) of the circuit in Fig. 4-1.

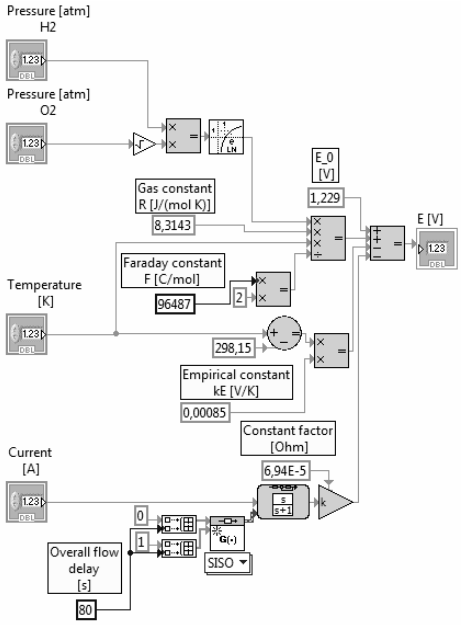

Figure 4-2: Block diagram used to calculate the reversible potential.

The activation voltage in a fuel cell is given according to the Tafel equation [103]

$$V_{act} = \frac{RT}{\alpha z F} \ln\left(\frac{I}{I_0}\right) = T[a + b\ln(I)] \tag{4.3}$$

where α is the electron transfer coefficient, I_0 is the exchange current and z is the number of electrons participating in the electrode reaction. Unfortunately, not all of the parameters of this equation are directly available. Therefore, it is necessary to use empirical means to estimate these unknown terms. An empirical equation is proposed in [100], to which a constant has been added. It can be written as

$$V_{act} = \eta_0 + a\ (T - 298.15) + Tb\ln(I) = V_{act1} + V_{act2}. \tag{4.4}$$

The voltage activation V_{act1}, which depends only on the temperature of the FC, is calculated as follows

$$V_{act1} = \eta_0 + a\ (T - 298.15) \tag{4.5}$$

where η_0 is the temperature invariant part and a is a constant term in the Tafel equation [103]. The subfunction to calculate the activation voltage is shown in Fig. 4-3.

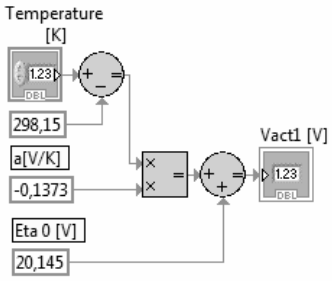

Figure 4-3: Activation voltage drop affected only by the internal temperature.

The ohmic losses can be expressed [99] as

$$V_{ohm} \quad = \quad I\ R_{ohm} = I\ [0.2793 + 0.001872\ \cdot I - 0.0023712\ (T - 298.15)]. \tag{4.6}$$

In Fig. 4-4 the subfunction for the calculation of the ohmic voltage is described.

Fig. 4-1 shows the voltage at the model capacitor which can be calculated as

$$V_C = \left(I - C\frac{dV_C}{dt}\right) \cdot (R_{act} + R_{conc}) \tag{4.7}$$

where R_{act} is the resistance that varies with the temperature and the current of the FC and which is expressed [99] as

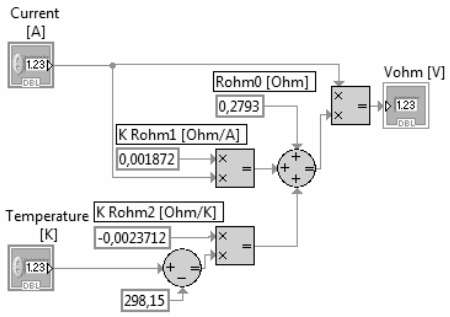

Figure 4-4: Block diagram used to calculate the ohmic voltage drop.

$$\begin{aligned} R_{act} &= 1.2581 + 0.00112\,(T - 298.15) - 1.6777 \times 10^{-6} \cdot I^5 + 1.2232 \times 10^{-4} \cdot I^4 \\ &\quad -3.3998 \times 10^{-3} \cdot I^3 + 0.045452 \cdot I^2 - 0.31163 \cdot I \end{aligned} \tag{4.8}$$

R_{conc} also depends on the current and the temperature [99] and its expression is

$$\begin{aligned} R_{conc} &= 0.080312 + 0.0002747\,(T - 298.15) + 5.2311 \times 10^{-8} I^6 - 3.4578 \times 10^{-6} I^5 \\ &\quad +8.6437 \times 10^{-5} I^4 - 1.0089 \times 10^{-3} I^3 + 5.554 \times 10^{-3} I^2 - 0.010542 I \end{aligned} \tag{4.9}$$

The final block diagram represented in LabVIEW for the electrical model of the PEMFC is shown in Fig. 4-5.

4.4 Thermal model

The thermodynamic model of the PEM fuel cell is based on heat balance equations. This model calculates the net heat generated by the chemical reaction inside the fuel cell, as shown in the following equation

$$\dot{q_{net}} = \dot{q_{chem}} - \dot{q_{elec}} - \dot{q_{s+l}} - \dot{q_{loss}} \tag{4.10}$$

where q_{chem} represents the calorific or chemical energy, q_{elec} is the electrical energy, q_{s+l} corresponds to latent and sensible calorific energy, also called heat of transformation and potential energy in the form of heat energy, and q_{loss} represents heat losses. They are all expressed in joules [104, 105]. The calorific energy is given by

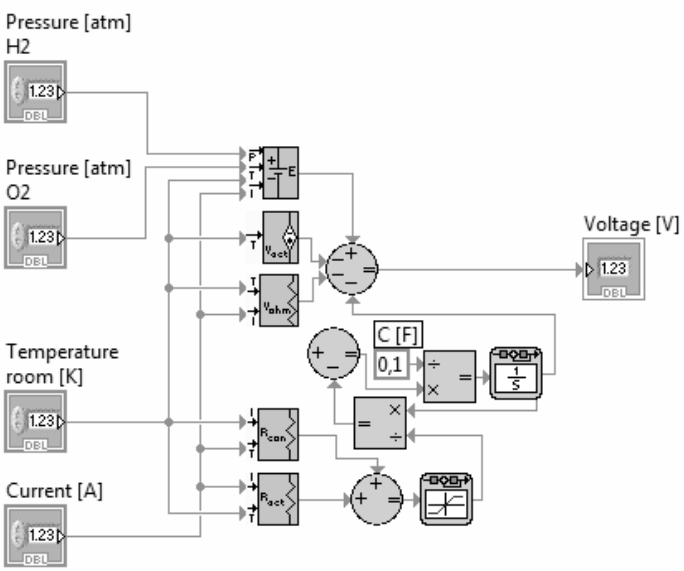

Figure 4-5: Block diagram of the electrical model of the PEMFC shown in Fig. 4-1 implemented in LabVIEW.

$$\dot{q_{chem}} = \dot{\eta}_{H_2,c}\Delta G \tag{4.11}$$

with $\dot{\eta}_{H_2,c}$ as the consumed molar flow of H_2. This can be calculated as

$$\dot{\eta}_{H_2,c} = \frac{I}{2F}N_{cell} \tag{4.12}$$

where N_{cell} is the number of cells in the stack. The second factor of the calorific energy, ΔG, represents the free Gibbs energy or free enthalpy, and is calculated [106] as

$$\Delta G = \Delta G_o - RTln\left[p_{H_2}(p_{O_2^{0.5}})\right] \tag{4.13}$$

where ΔG_o is the free energy in standard conditions given in $[\frac{J}{mol}]$.

The electrical energy is calculated as

$$\dot{q_{elec}} = V_{out}I. \tag{4.14}$$

The sensible and latent heat energy is determined as

$$\dot{q_{s+l}} = \left(\dot{\eta}_{H_2,c}.C_{H_2} + \dot{\eta}_{O_2,c}.C_{O_2} + \dot{\eta}_{H_2O,g}.C_{H_2O,l}\right).\Delta T + \dot{\eta}_{H_2O,g}.H_V \tag{4.15}$$

where the temperature variation ΔT is equal to $T - T_{room}$, $C_{H_2}, C_{O_2}, C_{H_2O,l}$ are specific heat capacities in $[\frac{J}{mol.K}]$, H_V is the heat vaporization of H_2O in $[\frac{J}{mol}]$, $\dot{\eta}_{H_2O,g}$ is the generated mole flow of H_2O in $[\frac{mol}{s}]$, and $\dot{\eta}_{O_2,c}$ is the consumed mole flow of O_2, which is given by

$$\dot{\eta}_{O_2,c} = \frac{I}{4F}.N_{cell}$$

Finally, heat losses are calculated in

$$\dot{q_{loss}} = h_{cell}.\Delta T.N_{cell}.A_{cell}. \tag{4.16}$$

where h_{cell} is the coefficient of connectivity heat transference in $[\frac{W}{m^2.K}]$ [104] and A_{cell} the area of each cell in $[\frac{W}{m^2.K}]$.

In steady state, $\dot{q_{net}} = 0$, the fuel cell operates at constant temperature. During transients, the temperature in the fuel cell varies according to the following expression [104]

$$\dot{T} = \frac{\dot{q_{loss}}}{M_{FC}.C_{FC}}$$

where M_{FC} is the total mass of the fuel cell $[kg]$ and C_{FC} is the specific heat capacity of the stack $[F]$. The diagram in Fig. 4-6 represents the implementation in LabVIEW of the fuel cell temperature model.

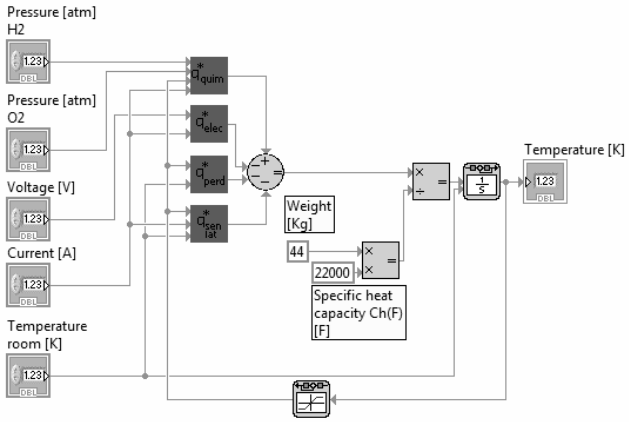

Figure 4-6: Block diagram of thermodynamic properties in the PEMFC.

Therefore, the block diagram of the thermo-electric model of the fuel cell is obtained by joining the circuital model presented in Fig. 4-6 and the thermal model presented in Fig. 4-5, which results in the model in Fig 4-7.

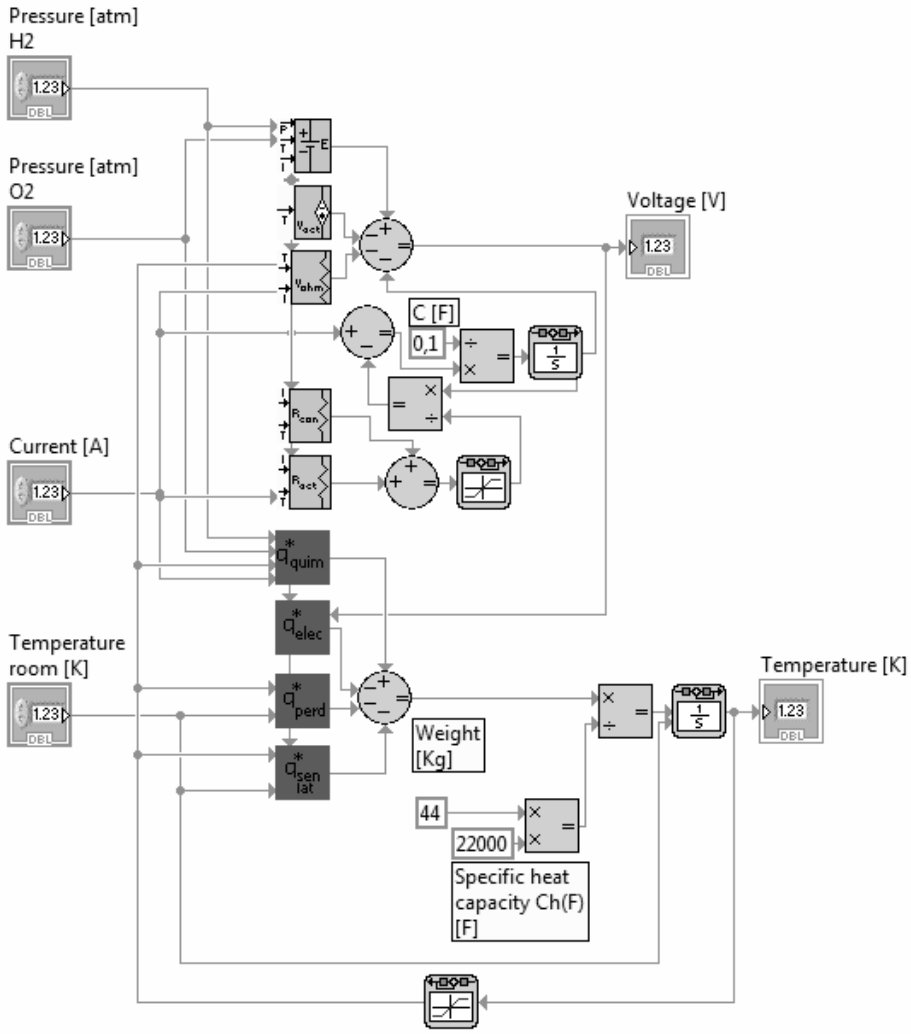

Figure 4-7: Block diagram of the thermo-electric model of the PEMFC used by the simulator.

4.5 Experimental configuration

The experimental setup configuration used to validate the mathematical model implemented in LabVIEW is shown in Fig. 4-10. The acquisition card NI USB-6008 inputs are the current given by the source of power and the room temperature. The value of the current is given by the power source *Electronika Delta SM 1500* through its programming analog port. The source provides a voltage in the [0 to 5]V range, which is proportional to the value of this current. The temperature value is measured by an LM35 sensor. This integrated-circuit provides a linearly proportional output proportional to the temperature, in Celsius degrees, that is amplified by an AD620 instrumentation amplifier. The current and temperature values are delivered to the built-in LabVIEW model, which gives an output voltage reference for the power source. This value is scaled in the [0 to 5]V range proportional to the maximum voltage source output and is sent to the acquisition card by the analog

port of the programmable source. Connected to the voltage source to provide load changes there is a 6050a HP programmable electronic load whose parameters are programmed from the PC by using the National Instruments GPIB-USB-HS connector.

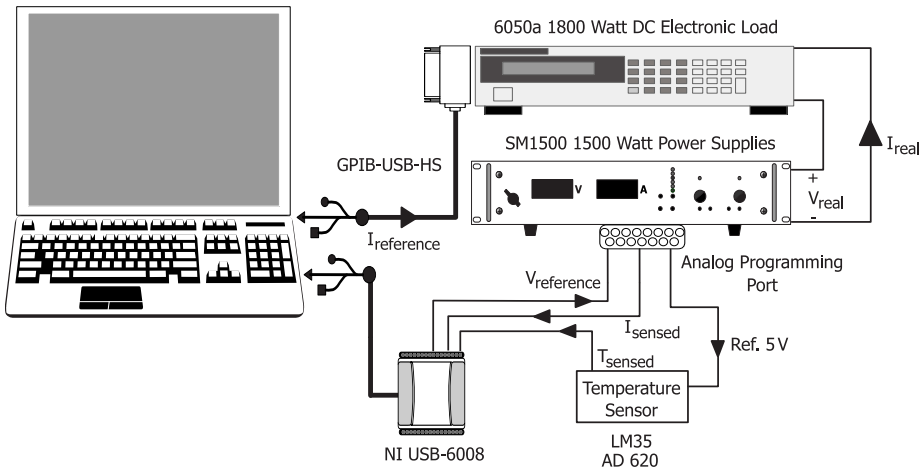

Figure 4-8: Experimental configuration of the PEMFC simulator.

Tables 4.1, 4.2 and 4.3 summarize the main characteristics of the elements of the experimental setup of the simulator presented in Fig. 4-10.

Table 4.1: Main features of the NI USB-6008 data acquisition device.

Analog Input	
Converter type	Successive approximation
Analog inputs	8 single-ended or 4 differential
Input resolution	12-bits differential or 11-bits single-ended
Maximum sampling rate	10 kS/s
Input impedance	144 kΩ
Single-ended input range	±10 V
Differential input range	±20 V, ±10 V, ±5 V, ±4 V, ±2.5 V, ±2 V, ±1.25 V, ±1 V
Analog Output	
Analog Output	2
Output resolution	12 bits
Maximum update rate	150 Hz
Output impedance	50 Ω
Output current drive	5 mA
Slew rate	1 V/μs
Short circuit current	50 mA

Table 4.2: Main features of the GPIB Controller for Hi-Speed USB.

Specifications	
Hi-speed USB signaling	480 Mb/s
IEEE 488 Compatibility	IEEE 488.1 and IEEE 488.2
IEEE 488 interlocked handshake	1.8 MB/s
IEEE 488 noninterlocked handshake (HS488)	7.2 MB/s
GPIB connector	IEEE 488 standard 24-pin
USB connector	USB standard series A plug

Table 4.3: Main features of the SM 70-22 Delta Elektronika BV power supply in voltage control mode.

Output	
Voltage	0 - 70 V
Current	0 - 22 A
Regulation	
Load 0 - 100%	2.5 mV
Line 120 - 265 V AC	1 mV
Ripple + noise	
rms (BW = 300 kHz)	3 mV
p-p (BW = 50 kHz)	15 mV
Analog programming inputs	
Input Range	0 - 5 V
Accuracy	±0.2%
Offset	0 - 5 V
Input impedance	$> 1\ M\Omega$
Reference voltage	
V_{ref}	5.114 V ± 15 mV
Rise time (10-90 %) for a voltage step of 0-70 V	
100 % load	13.2 ms
10 % load	4.4 ms
Fall time (90-10 %) for a voltage step of 70-0 V	
100 % load	12.9 ms
10 % load	129 ms
Programming connector	
Type	15 pole D-connector at rear panel (Female)

4.6 Multicore Processors

Fig. 4-9 shows the block diagram of the simulator, which has two main tasks. The simulation block in the top part gets the model inputs, current, hydrogen and oxygen partial pressures, and room temperature, from the time block depicted in the bottom part. The simulation block outputs are the voltage and inner temperature of the FC. The time block is responsible for acquiring the signals, controlling the electronic load, storing the time signals, generating the steady-state characteristics of the FC and sending to the power supply the voltage value to be placed in its terminal. Both blocks are executed in parallel, each one using a different processor to carry out its task, thereby ensuring a multicore process. The communication between the two blocks is carried out using local variables. The benefit of moving from a single- to dual-core computer is that performance increases twofold [107].

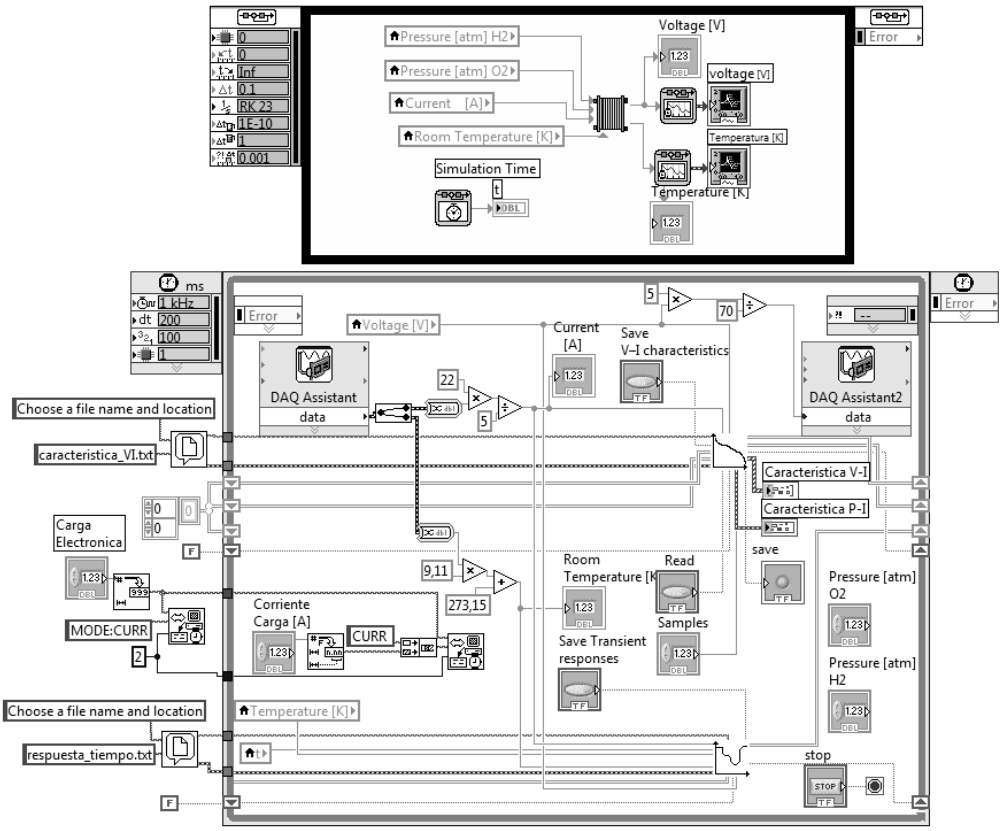

Figure 4-9: Block diagram of the simulator.

4.7 Experimental results

Fig. 4-10 shows the experimental setup for testing the PEMFC simulator and Fig. 4-11 illustrates the graphical user interface that controls the simulator developed in LabVIEW.

The steady state characteristics of the SR-12 FC were obtained by increasing the load current from 0 A to 21.6 A every 40 seconds, as shown in Fig. 4-12. The same figure shows the response of the Wang's model evaluated with the currents and temperatures acquired during the experimental test. The response of the simulator agrees very well with that of Wang's model.

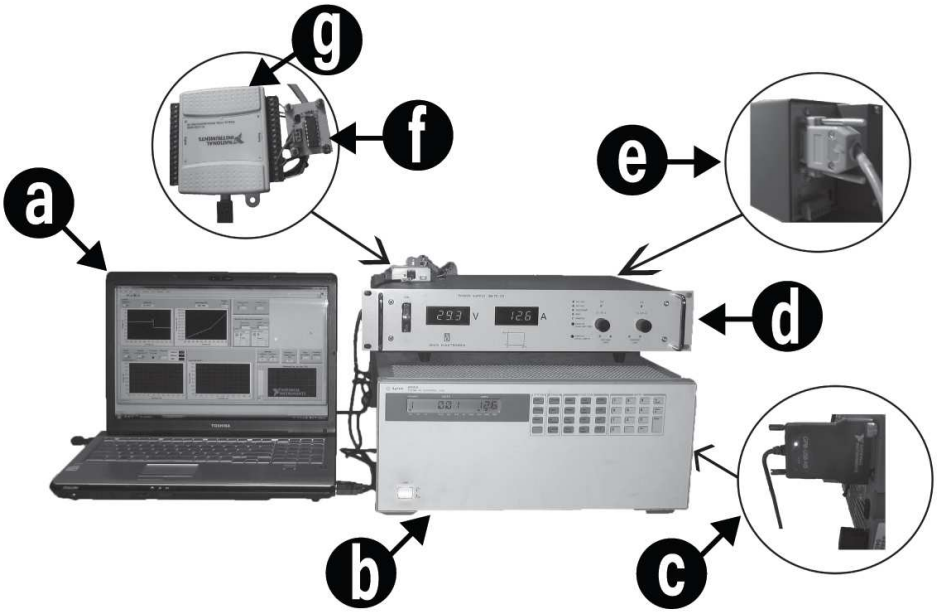

Figure 4-10: Experimental configuration of the PEMFC simulator: (a) Laptop with Intel core 2 duo processor, (b) DC electronic load, (c) GPIB-USB-HS connector, (d) DC power supply, (e) analog programming port, (f) temperature acquisition system, (g) NI USB-6008.

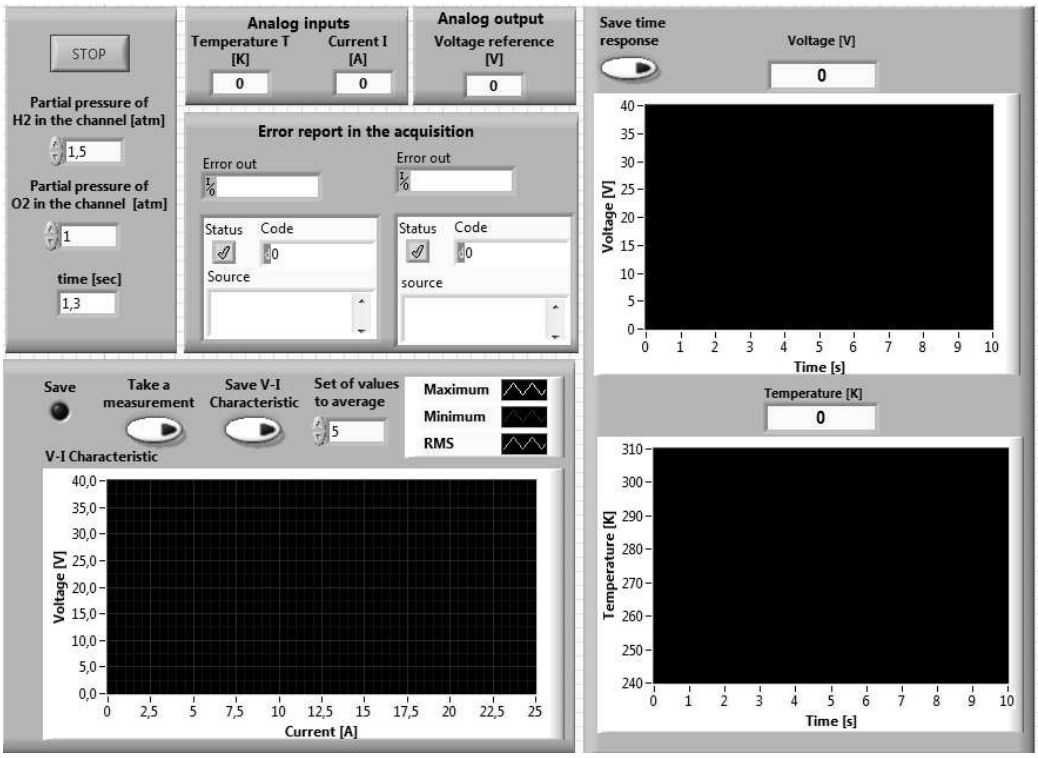

Figure 4-11: Graphical user interface of the simulator.

Fig. 4-12 shows three regions with different mechanisms loss that explain the voltage drop from the maximum ideal voltage. In the beginning of the curve the activation losses that are due to the slow reactions that occur at the electrode surface. In the middle of the curve the conduction losses that are caused by ohmic resistance opposed to the ionic flow in the electrolyte and the flow of electrons in the stack. This voltage drop is essentially proportional to the current density, so this area can be considered to be linear. Finally, the losses of concentration or mass transport are the result of the reduced concentration of the reactives on the surface of the electrodes. At the maximum current value that can produce electricity, the concentration on the catalyst surface is practically zero, since the reactives are consumed as soon as they are supplied to the surface. This zone corresponds to the right corner of the polarization curve in Fig. 4-12.

Fig. 4-13 shows the behavior of the output power versus current changes, where the behavior of the simulator and the model of Wang can be compared. The peak power of 500 W corresponds to the nominal power of the SR-12 FC.

The dynamic properties of the PEMFC depend mainly on the double-layer charging effects, fuel and oxidant flow delays, and thermodynamic characteristics inside the FC. Although the capacitance caused by the double-layer charging effect is large, in the order of several Farads for each cell, the

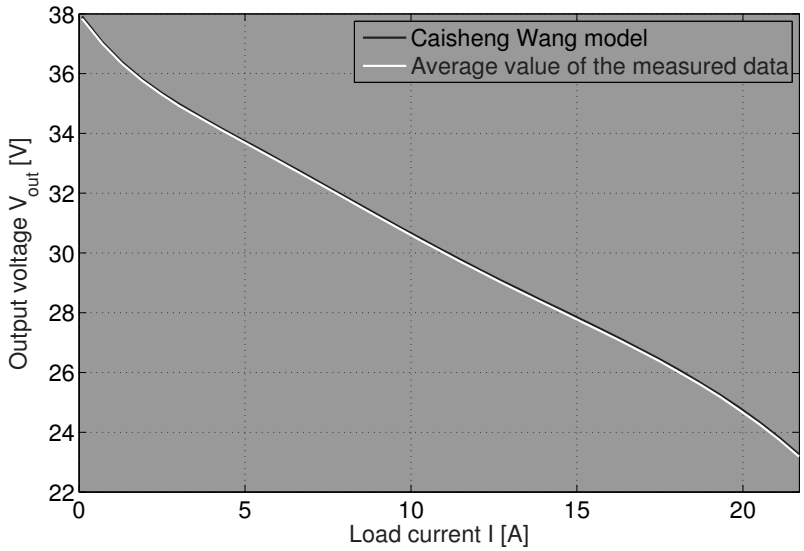

Figure 4-12: VI characteristics of Wang model and the simulator of the SR-12 fuel cell.

τ time constant is normally small because the activation resistances and concentrations are small when the FC works in the linear zone. Therefore, this capacitance will affect the transient response of the PEM fuel cell in the short time range. The transient responses of the model to the fast step load changes depicted in Fig. 4-14 are given in Fig. 4-15. The measured room temperature is shown in Fig. 4-16.

Fig. 4-15 shows that when the load current steps up, the voltage drops simultaneously due to the voltage drop across R_{ohm}, and then decays exponentially to its steady state value due to the capacitance of the double layer charging effect.

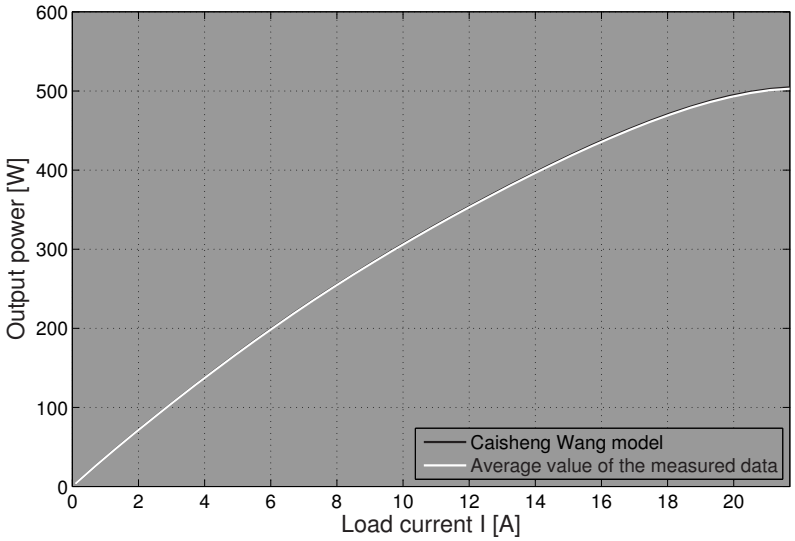

Figure 4-13: PI characteristics of Wang's theoretical model and the simulator.

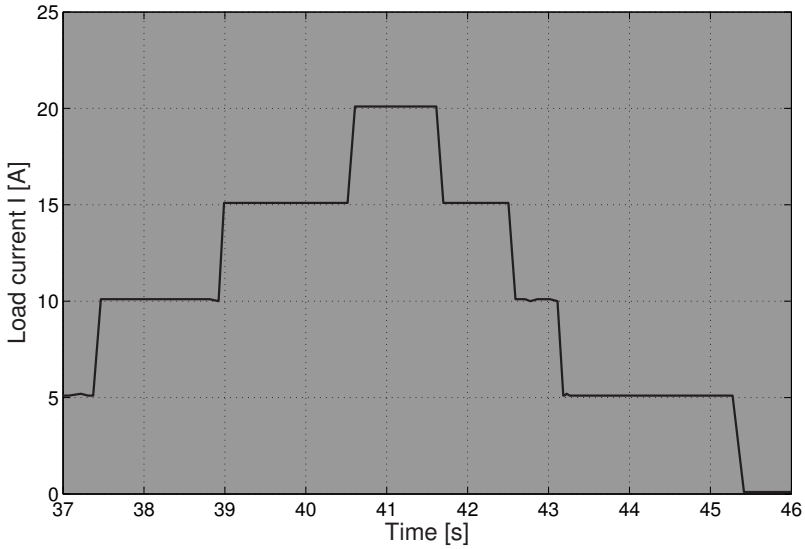

Figure 4-14: Variation in the load.

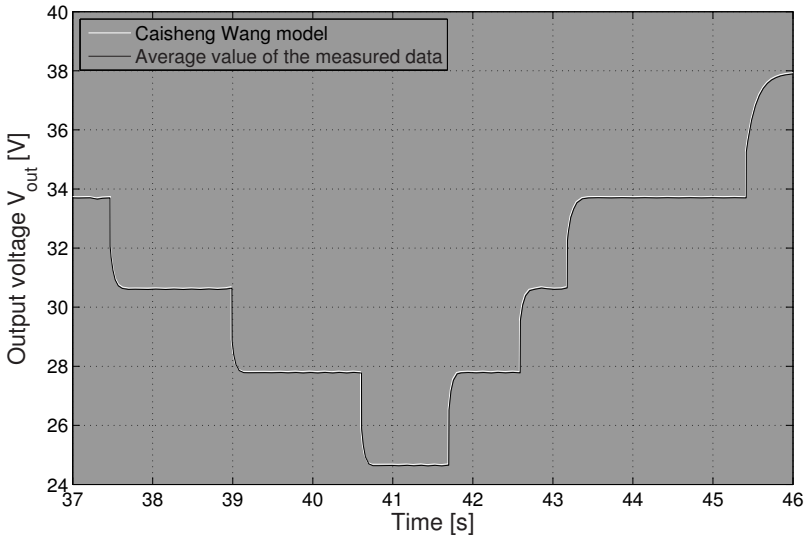

Figure 4-15: Dynamic response of the FC simulator in comparison with Wang's model.

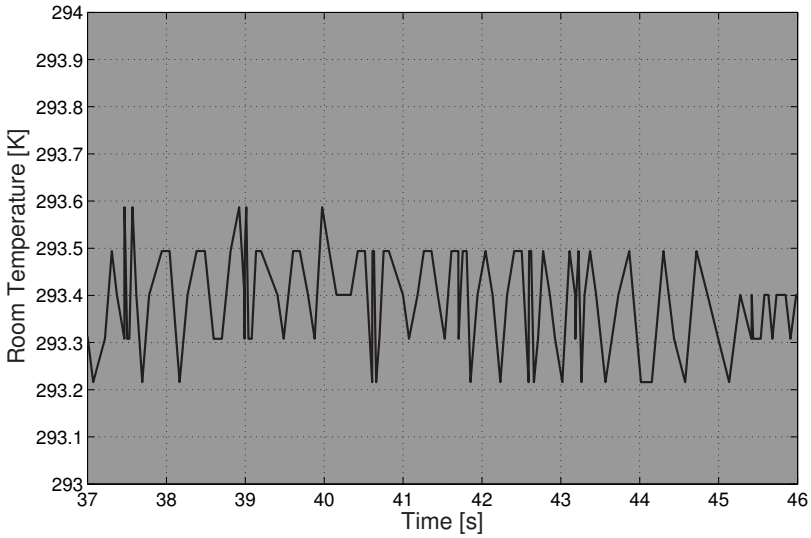

Figure 4-16: Measured room temperature.

In order to estimate how accurate the simulator is with respect to Wang's theoretical model, an error analysis was carried out using the Mean Relative Error (MRE) criterion [108] given in (4.17), where m_j and f_j represent the theory and experimental data sets, respectively, and N is the number of samples.

$$MRE(\%) = 100 \times \frac{1}{N} \sum_{j=1}^{N} \left| \frac{m_j - f_j}{m_j} \right| \tag{4.17}$$

Table 4.4: Dynamic validation error analysis (MRE) of the simulator

Curve	MRE [%]
VI characteristics	0.0865
PI characteristics	0.0855
Dynamic response	0.3704

The MRE criterion applied to the polarization curve data depicted in Fig. 4-12 gives a relative mean error equal to 0.00865%. The application of the same criterion to the power curves depicted in Fig. 4-13 gives a value equal to 0.0855% as shown in Table 4.4. Finally, the MRE of the dynamic responses gives an error equal to 0.3704%. These results confirm the accuracy of the simulator.

4.8 Conclusions

In this chapter a digital PEMFC simulator has been presented. The simulator is based on a dynamic mathematical model that considers the electrode double layer effect and the fuel cell internal thermodynamics. A LabVIEW software is used for the simulator hardware implementation. Experimental results are contrasted with the data model from a Relion SR-12 500-W PEM FC stack and validated with the theoretical model proposed by Wang in [99]. The accuracy of the simulator for both the polarization curve and the dynamic response is confirmed by the low MRE values obtained. The fuel cell chosen to test the simulator was the Relion SR-12 500-W PEM FC stack because the parameters of this stack model are available in the literature and also because the power source available in our research laboratory has a range of voltages and currents that fits well with those of the Relion stack. Since our laboratory has a Ballard NEXA 1.2 kW fuel cell, developing a simulator for this fuel cell is a task for the future that can be divided into three main sections. The first is to adjust the parameters of the thermal-electric model presented in this study for the Nexa fuel cell. The second is to find a power supply that has a range of voltages and currents that make it possible to simulate the Nexa fuel cell and find another model already tested for this stack. And the last is to find out more about instrumentation systems to ensure real-time development of FC emulators.

Once these tasks have been completed a Hardware-in-the-loop (HIL) system of the Nexa FC can be developed for testing different configurations, topologies and control strategies of the different equipment connected to it.

Chapter 5

PEM fuel cell emulator for oxygen excess ratio estimation in power electronics applications

5.1 Abstract

This chapter proposes a real-time emulator of a Proton Exchange Membrane Fuel-Cell (PEMFC) implemented by means of a power source controlled using the Matlab^{TM} real-time toolbox. The FC is represented by a polarization model that reproduces both static and dynamic behaviors. The emulator estimates the oxygen excess ratio behavior and interacts with electrical loads connected to the fuel cell terminals, such as motor drivers or switching converters. Consequently, the proposed emulator can be used to design and test devices, before they are connected to the fuel cell, to avoid the oxygen starvation effect and/or minimize the fuel consumption. The emulator has been adjusted to a real Ballard NEXA 1.2 kW fuel cell. The proposed PEMFC emulator has made it possible to implement and experimentally test a hardware-in-the-loop system in which the fuel cell load is a step-up switching converter. The controller has been designed and adjusted to avoid the oxygen starvation effect in the converter dynamics.

5.2 Introduction

Fuel cells (FC) are a highly promising source of distributed energy because of their reliability and nonpolluting emissions to the environment [32]. FC emulators, then, are needed in research, since they enable control strategies to be evaluated safely and the performance of power stages such as

inverters and dc/dc converters to be tested. They also make it possible to carry out critical tests that would otherwise a risk for the equipment [109], and different FC models and FC types can be studied using FC emulators.

Several FC simulators and emulators have been reported in the literature. For example, a PEMFC simulator consisting of a power rectifier controlled by a computer using LabVIEW software is reported in [93]. The simulator calculated the PEM theoretical output voltage V_{out} for a specific load current I. The error between the theoretical V_{out} signal and the measured rectifier output V_{dc} is minimized by controlling the rectifier firing angle. One drawback of this simulator system is that the rectifier dynamic response is slower than the PEMFC response at quick load changes. In [94], the ohmic region from the static characteristic of an FC is represented by a linear function. The linearized V-I curve, without considering dynamic effects, is emulated by using a Digital Signal Processor (DSP) which controls a Buck converter that delivers the desired V_{out} output signal. A similar simple approach is proposed in [95], where the V-I static characteristic of a Solid Oxide FC (SOFC) stack is modeled by a three order polynomial. The simulator was implemented using a laboratory power source controlled with LabVIEW. A real-time simulator or emulator of a Direct Methanol FC (DMFC) is presented in [96], where a DSP-based system replaces a computer, acquisition cards and costly licensed software. Since the selected DSP can process relatively low complexity mathematical equations, the Nernst reversible voltage is considered to be constant. The improved approach presented in [97] uses a real DMFC single cell as the reference to determine the FC stack operation voltage. However, this emulator requires additional equipment to reform and preheat the fuel that the reference cell consumes.

The FC emulator is a useful tool for evaluating dangerous operating conditions imposed by the load, where the most critical phenomenon is fuel or oxygen starvation [110]. The FC stack has a time constant of several hundredths of a millisecond. This constant is mainly determined by the compressor and the membrane hydration level [111]. Therefore, a high change in the load connected to the FC could produce a large voltage drop in a short time. This behavior is described by the authors as fuel or oxygen starvation. Fuel starvation describes the operation condition of the FC at sub-stoichiometric reaction conditions [110]. Several factors can cause reactant starvation: poor heat management during sub-zero temperatures and cold start-ups with ice in the cell can block the pores of the gas diffusion layers, poor stack design or assembly with uneven flux distribution between cells, poor cell design or machining with uneven mass distribution in flow fields and poor water management with channel block by flooding. When starved of fuel or oxygen, the FC performance degrades and the cell-voltage drops [112]. This operation condition is evidently dangerous for the FC stack [111]. Therefore, an accurate FC emulator is desirable so that dangerous operating

situations can be analyzed, and regulation strategies, and test devices intended to interact with real FC prototypes evaluated.

The emulator proposed in this dissertation is an improved version of the one presented in [113] which was a simulator without real-time execution capability adjusted to reproduce the output voltage characteristic of a Relion SR-12 500-W PEM FC stack. The main characteristics of the new emulator, adjusted to the 1.2 kW NEXA Power Module [114] shown in Fig. 5-1(a), are that it reproduces the dynamics of the FC, predicts the oxygen excess ratio and can be connected to real power electronics devices. Hence, the emulator proposed is a good candidate for testing power electronic devices for FC applications [115, 116, 117, 118, 119] and for determining their impact on the oxygen excess ratio (λ_{O_2}) so that potential sources of oxygen starvation can be avoided and/or detected. The emulator takes the thermal effects into account so that it can reproduce the general behavior better. The emulator accuracy has been validated by means of the experimental data presented in [114].

The rest of this chapter is organized as follows. Section 5.3 outlines the model used in the emulator. Section 5.4 proposes the implementation of the emulator using a PC-based kernel. Section 5.5 presents the validation of the emulator by means of experimental data. Section 5.6 gives an application example of the emulator connected to a step-up dc/dc converter to test its impact on the FC operation. Finally, the conclusions are given in Section 5.7.

5.3 Fuel cell system description and modeling approach

The model used to reproduce the behavior of the fuel cell system has been developed by using experimentally measurable inputs and outputs to adjust it to the real prototype [114, 120]. It allows real-time calculation of the model outputs. The model considers the thermal effects on the stack voltage and predicts the oxygen excess ratio λ_{O_2}, which is an important parameter in FC operation, and control and safety procedures that impact on FC durability [121].

The experimental system used in the modeling procedure is based on the Ballard 1.2 kW NEXA Power Module shown in Fig. 5-1(a), which is composed of a stack of 46 cells with 110 cm^2 area membranes. In this system the anode-cathode pressure ratio is regulated to prevent membrane damage, and also the stack temperature is limited. The Nexa system includes a control board that implements regulation strategies for the anode purge valve and the air compressor voltage to prevent undesired phenomena like flooding and oxygen starvation. Flooding occurs when the water generated and the inert gases supplied with the hydrogen get stuck in the anode and decrease the stack voltage and power [122]. Oxygen starvation occurs when not enough oxygen is supplied to

the fuel cell and cannot respond to the demand of the stack current. This degrades the FC, and frequently requires the FC to be shut down [123]. It decreases the stack power and increases the probability of hot spots or even burn-through on the surface of a membrane. To prevent this, the cathode oxygen excess ratio (λ_{O_2}) must be regulated by controlling the compressor motor voltage according to changes in current drawn from the stack [124, 125], where one of the main difficulties is to measure/estimate the oxygen excess ratio value.

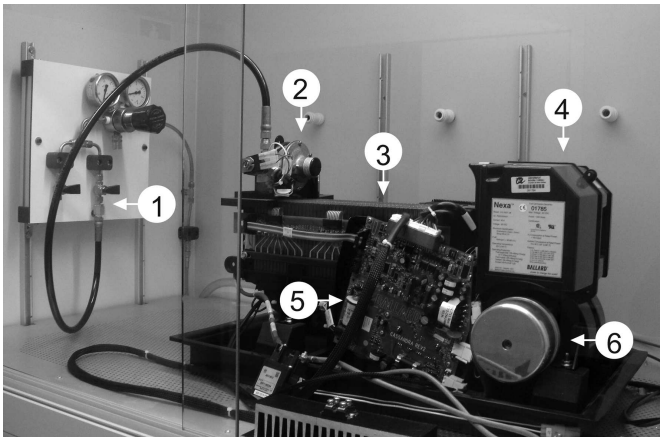

(a)

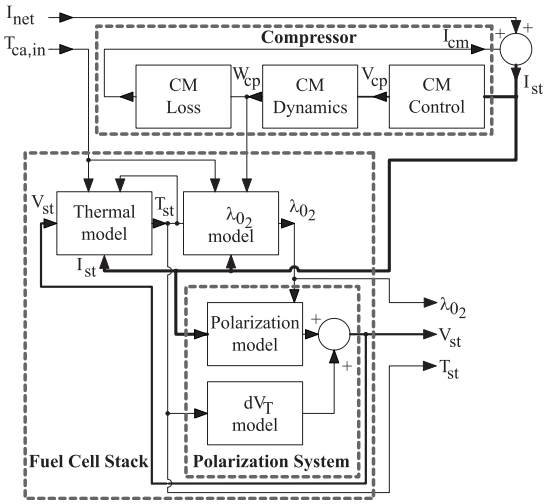

(b)

Figure 5-1: Ballard 1.2 kW Nexa power module. (a) Nexa power module (1. Hydrogen supply, 2. Hydrogen control valve, 3. Fuel cell stack, 4. Air compressor, 5. Control board, 6. Cooling fan.), (b) Fuel cell model structure.

The emulator inputs must be measurable variables, so the load current I_{net} and the ambient temperature $T_{ca,in}$ were selected as inputs. The model calculates the stack temperature T_{st} in order to take into account the thermal effects. The model outputs are the oxygen excess ratio λ_{O_2} and the stack voltage V_{st}.

The Nexa system uses the stack power to supply the compressor, and therefore the compressor is a closed loop system as depicted in Fig. 5-1(b). The air flow generated by the compressor W_{cp}, the net current requested by the stack I_{st}, and stack T_{st} and ambient $T_{ca,in}$ temperatures are used to process the oxygen excess ratio electrochemical equations. The stack power ($I_{st} \cdot V_{st}$) affects the thermal model that impacts on the stack voltage (V_{st}) and the oxygen excess ratio as described in the model structure.

The subsections below describe the main dynamics and relations of the fuel cell system used to process the model in a real-time environment. A more detailed description of the modeling approach is given in [114, 120].

5.3.1 Air-compressor model

The compressor model is composed of three main subsystems as depicted in Fig. 5-1(b): the compressor controller, the compressor dynamics, and the compressor consumption and losses. The first subsystem is the compressor controller of the Nexa system. It is a feedforward network that depends on the stack current to generate the compressor control signal. This controller has been identified from its experimental behavior as

$$V_{cp}(z) = 0.9987 \cdot I_{st}(z) + 46.02 \tag{5.1}$$

where $V_{cp}(z)$ is the compressor control signal [0%,100%] [114].

The main subsystem is the dynamics in the air flow, which has been identified from the experimental behavior of the Nexa system [114] following the Reaction Curve Method (RCM) [126], as

$$W_{cp}(z) = \frac{10^{-4}\left(1.446z^2 - 2.869z + 1.423\right)}{z^3 - 2.997z^2 + 2.993z - 0.9966} V_{cp}(z) - 45.00 \tag{5.2}$$

In (5.2), $W_{cp}(z)$ is the discrete representation of the air mass flow supplied to the cathode of the stack, and the discretization was performed by considering a sampling time $T_s = 1$ ms.

Finally, the electric power consumed by the FC system ancillaries, and mainly by the air compressor, are modeled by the compressor current I_{cm}, which perturbs the stack current I_{st} that also

depends on the net current I_{net} requested by the load as $I_{st} = I_{net} + I_{cm}$. The consumption and losses of the ancillaries have been identified experimentally from the prototype as a function of the air mass flow W_{cp} as follows [120, 114]

$$I_{cm} = -3.231 \times 10^{-5} \cdot W_{cp}^2 + 1.8 \times 10^{-2} \cdot W_{cp} + 0.616 \tag{5.3}$$

5.3.2 Thermal model

The thermal model can be obtained by an energy balance (5.5), where $\dot{H}_{reac}$ is the energy produced in the chemical reaction of water formation, P_{elec} is the electric power supplied and $\dot{Q}_{rad,B2amb}$ and $\dot{Q}_{conv,B2amb}$ are the amount of heat evacuated by radiation, and by natural and forced convection [127], respectively [120, 114]. This energy balance has been modeled by using the trapezoidal approximation and bilinear transform with a sampling time T_s, which leads to

$$T_{st}(z) = \frac{T_s}{2 \cdot m_{st} \cdot C_{st}} \cdot \frac{z+1}{z-1} \cdot \Delta H_{T_{st}} \tag{5.4}$$

$$\Delta H_{T_{st}} = \dot{H}_{reac} - P_{elec} - \dot{Q}_{rad,B2amb} - \dot{Q}_{conv,B2amb} \tag{5.5}$$

$$P_{elec} = P_{st} = V_{st} \cdot I_{st} \tag{5.6}$$

These thermal dynamics are modified by the air flow W_{cool} supplied by the cooling fan to limit the stack temperature in the Nexa prototype. This system has been identified [120, 127] as

$$W_{cool}(z) = 36 \cdot u_{cool}(z) \tag{5.7}$$

where $u_{cool}(z)$ is the control signal of the fan.

5.3.3 Electrochemical model: oxygen excess ratio

A PEM FC stack generates electricity from the chemical reaction between hydrogen (H_2) and oxygen (O_2) [128]. In order to prevent membrane stress and damages, the anode-cathode pressure ratio is regulated in a safe relation by modifying the hydrogen control valve, which regulates the anode pressure following the cathode pressure [129]. In this way, the main control variable is the oxygen flow, while the hydrogen flow is a consequence of the anode-cathode pressure ratio control.

The oxygen and hydrogen flows ($W_{O_2,reac}$ and $W_{H_2,reac}$, respectively) consumed in the reaction

depend on the stack current and are defined by electrochemistry principles [121, 127], as

$$W_{O_2,reac} = \mathsf{M}_{\mathsf{O}_2}\frac{\mathsf{n}\cdot I_{st}}{4\mathsf{F}} \quad , \quad W_{H_2,reac} = 2\mathsf{M}_{\mathsf{H}_2}\frac{\mathsf{n}\cdot I_{st}}{4\mathsf{F}} \tag{5.8}$$

where $\mathsf{M}_{\mathsf{H}_2}$, $\mathsf{M}_{\mathsf{O}_2}$, n and F are the hydrogen molar mass, the oxygen molar mass, the number of cells in the stack and the Faraday constant, respectively.

The ratio between the oxygen flow provided to the stack, generated by the air compressor, and the oxygen consumed in the electrochemical reaction is expressed by the oxygen excess ratio λ_{O_2} [121]

$$\lambda_{O_2} = \frac{W_{O_2,ca,in}}{W_{O_2,reac}} \tag{5.9}$$

The oxygen excess ratio must be regulated to $\lambda_{O_2} \geq 1$ in order to prevent starvation [123]. A high oxygen excess ratio, and thus high oxygen partial pressure, increases the stack power. However, after an optimum value is reached, further increments in λ_{O_2} cause an excessive air compressor consumption that decreases the efficiency of the overall system [120, 125].

5.3.4 Electrochemical model: polarization system

The polarization model of the stack is defined by the interaction of three effects at any time t: the activation of both electrodes, the charge transfer from electrode to electrode, and the voltage drop v_R introduced by the Ohm law applied to all resistive parts of the cell. These effects interact according to (5.10) as described in [114], where ΔE^0 is the open circuit voltage, (i.e. the difference of the standard potentials of the electrodes).

$$v(i,t) = \Delta E^0 + v_A(i,t) + v_D(i,t) + v_R(i,t) \tag{5.10}$$

The explicit equation of the stack polarization model [114] is given in (5.11), where A_D and A_A are parameters that model the open circuit voltage ΔE^0, i_{RA} and i_{RD} are parameters that define the saturation currents of the electrodes, and m is the number of cells that make up the stack. In the model, k is the Boltzmann constant, q is the electron charge, T is the reference temperature of 35 ^{o}C expressed in Kelvin and $R_C = m \cdot r_C$ is the overall stack resistance. Finally, I_{sc} is the short circuit current of the fuel cell.

$$V_{st} = m \cdot \frac{A_D \mathsf{k} T}{\mathsf{q}} \cdot \ln\left(1 + \frac{I_{sc} - I_{st}}{i_{RD}}\right) - m \cdot \frac{A_A \mathsf{k} T}{\mathsf{q}} \cdot \ln\left(1 + \frac{I_{st}}{i_{RA}}\right) - R_C \cdot I_{st} \tag{5.11}$$

The polarization model was parameterized by using experimental measurements from the Nexa prototype [114], and the stack temperature was regulated to the reference temperature $T_o = 35\ ^oC$. The λ_{O_2} was adjusted to between 3.0 and 6.5, and the relation given in (5.12) was obtained with the following parameters: $A_D kT/q = 199.9$ mV, $A_A kT/q = 6.9$ mV, $i_{RA} = 3.9$ mA, $i_{RD} = 790.8$ mA, and $R_C = 92.6\ m\Omega$.

$$I_{sc} = -0.45 \cdot \lambda_{O_2}^2 + 8.5 \cdot \lambda_{O_2} + 35 \tag{5.12}$$

In the experimental setup, the stack current was limited to the desired operating range of $I_{st} \geq 6.63$ A in which the compressor dynamics are linear. The fitting was performed using a new current axis $(I_{st} - 6.63)$ to reproduce the behavior of the non-linear polarization system.

The stack voltage predicted by the system of equations (5.11)-(5.12) is valid for the modeling reference temperature T_o. This means that a thermal correction factor needs to be introduced, which calculates the deviation of the polarization curve dV_T by using the changes in the stack temperature. The deviation law [127] has been experimentally identified as

$$dV_T = k_{dV} \cdot (T_{st} - T_0), \quad k_{dV} = \begin{cases} T_{st} > T_0 \rightarrow k_{dV} = 0.138 \\ T_{st} \leq T_0 \rightarrow k_{dV} = 0.250 \end{cases} \tag{5.13}$$

Finally, this model accurately reproduces the behavior of a commercial fuel cell system, and enables it to be emulated in realistic operating conditions. In the following sections the real-time implementation of this model is described.

5.4 Real-time simulation using a PC-based kernel

Real-time simulator applications are increasing because they allow rapid prototyping, low-cost experimental testing without the risk of damaging expensive equipment, and the design of different control system and signal processing algorithms. The PC-based real-time simulation has been used, for example, to develop a solar array voltage estimator [130], to measure a variable as complex as the torque in a switched reluctance motor [131], and to produce hardware-in-the-loop applications like the one presented in this disertation. Real-Time Windows Target™ is a rapid prototyping software by MathWorks™ that makes it possible to execute a complex system model in real-time with *Simulink*® external mode [132] [133]. Real-Time Windows Target™ uses a real-time kernel that runs at CPU ring zero and intercepts the interruption from the PC clock before the *Windows*® operating system receives it. This kernel, then, uses the interruption to trigger the execution of the compiled model in *Real-Time Workshop*®. Therefore, the kernel can give the highest priority

available to the real-time application. Real-Time Windows Target™ provides a connection between the real-time model and the model in *Simulink*® external mode. The real-time model can be connected to physical devices through an I/O board. Fig. 5-2 shows the block diagram of the emulator including the offline code generation sequence.

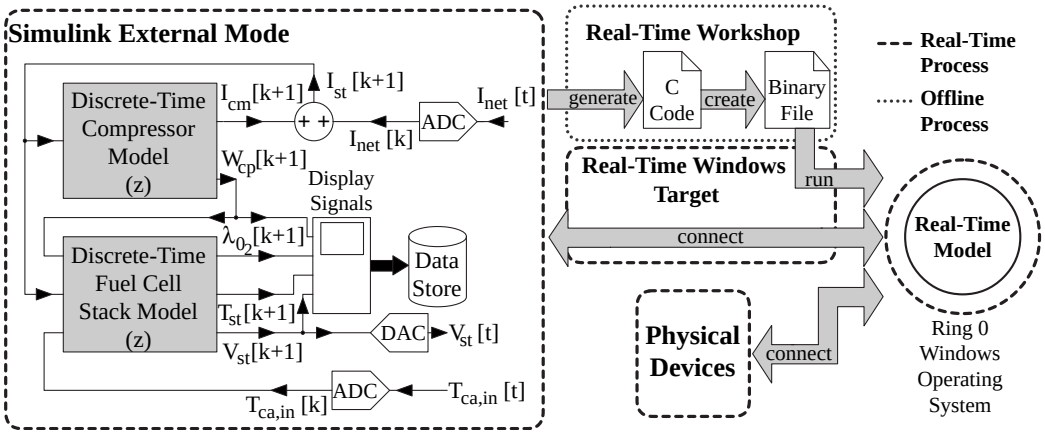

Figure 5-2: Block diagram of the emulator.

The system's real-time processing capability was validated by reading an analog input in a channel of the data acquisition (DAQ) card and writing the acquired value in an analog output channel. The *Simulink*® discrete simulation was configured to use the fourth order Runge-Kutta (RK4) integration technique with a step size of 1 ms. Microsoft Visual C++ 6.0© was used for the offline C compiling procedure. Fig. 5-3 shows that the delay between the input and output signals in the experiment is in the order of a few tenths of microseconds. This value is considered to be acceptable for the emulator model that operates in the millisecond range, two orders of magnitude greater than the delay.

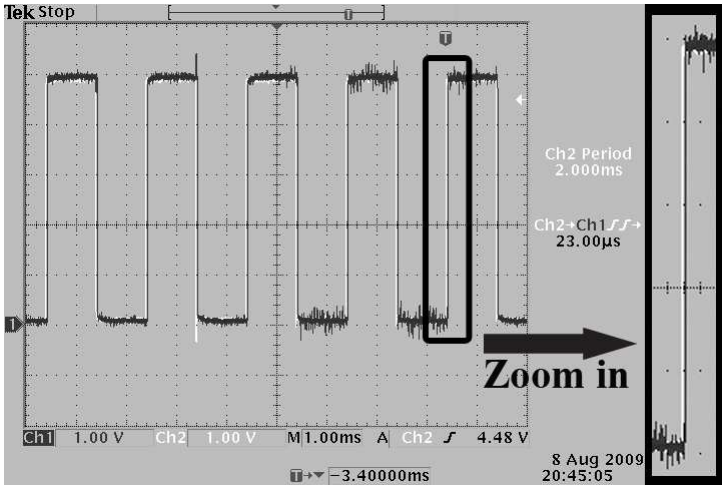

Figure 5-3: Delay between the input and output signals in the real-time implementation (23 μs).

Fig. 5-4 shows the experimental setup used to validate the mathematical models implemented in *Simulink*®. Although other solutions for implementing the emulator power stage are possible [109], we have selected a programmable power supply source *Electronika Delta SM 3000* because it is robust and versatile, and it is straightforward to interface with it. The acquisition card NI PCI6024E inputs are the current supplied by the power source to the load and the ambient temperature. The value of the current is given by the power source through its programming analog port. This power source provides a signal in the [0 to 5] V range that is proportional to the output current. The ambient temperature value is sensed by an LM35. This integrated circuit provides a voltage output linearly proportional to the temperature in Celsius degrees. This signal is amplified by an LM324 operational amplifier. The current and temperature values are delivered to the built-in *Simulink*® model that gives the reference for the output voltage of the power source. The output voltage reference is scaled between [0 to 5] V and drives the voltage source output proportionally. It is sent to the analog port of the programmable source through the acquisition card.

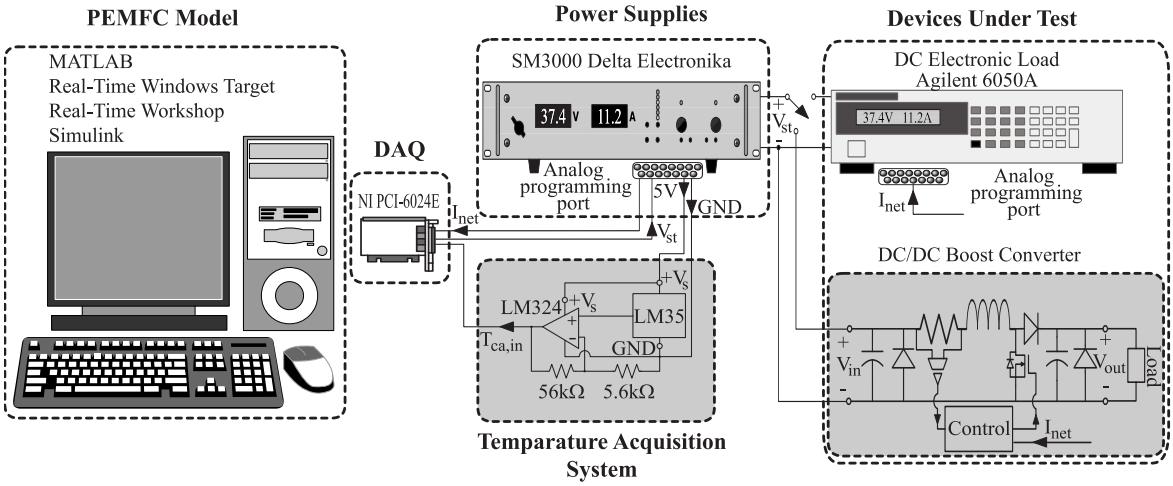

Figure 5-4: Experimental setup configuration of the Hardware-in-the-loop (HIL) fuel cell system.

Fig. 5-5 shows the real-time fuel cell model interface developed in Simulink. The DAQ input/output blocks, the scopes used to visualize and store the emulation data, and the switches adopted to choose between real-time data acquisition or reproduction of a pre-loaded current and/or temperature profile can also be observed. Finally, to operate the emulator turn on both Simulink and the *Electronika Delta SM 1500* power source, load the real-time model in Fig. 5-5, connect the load or device to be tested, and start the real-time simulation.

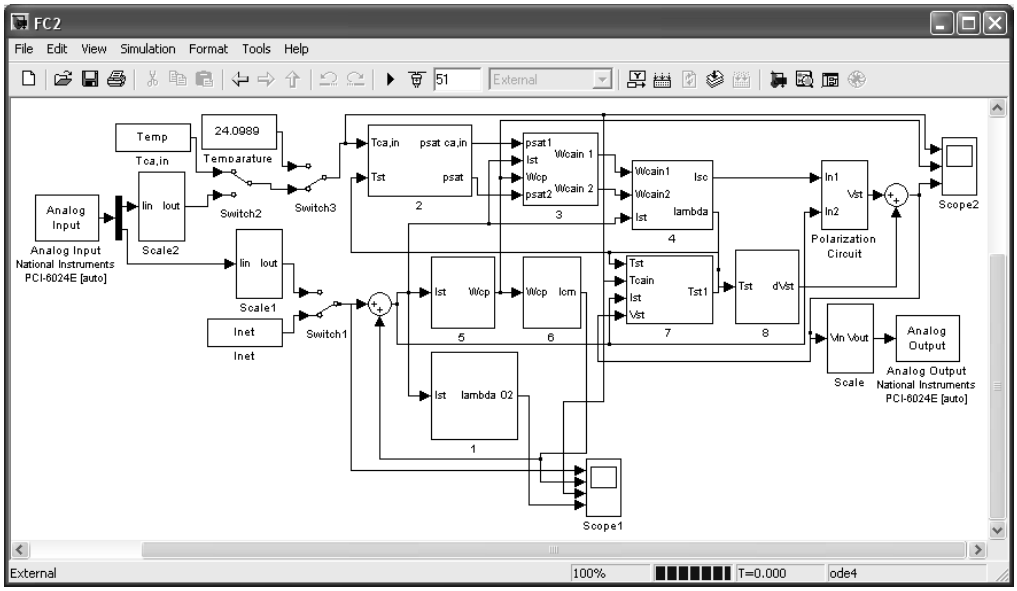

Figure 5-5: Simulink-based real-time FC model interface.

5.5 Experimental validation

The numerical results obtained with the emulator validated by means of experimental measurements on a 1.2 kW Ballard Nexa FC system as shown in Fig. 5-6. The parameters of the emulator model used in the validation procedure are given in Table 5.1.

Table 5.1: Emulator model parameters

Parameter		Value	Parameter		Value
m_{st}	[kg]	5	q	[C]	1.602176×10^{-19}
$m,\ n$	[–]	46	k	$[\mathrm{J \cdot kg^{-1}}]$	1.380650×10^{-23}
$\mathsf{M}_{\mathsf{H}_2}$	$[\mathrm{kg \cdot mol^{-1}}]$	0.002	C_{st}	$[\mathrm{J \cdot kg^{-1} \cdot K^{-1}}]$	1100
$\mathsf{M}_{\mathsf{O}_2}$	$[\mathrm{kg \cdot mol^{-1}}]$	0.032	F	$[\mathrm{C \cdot mol^{-1}}]$	96485

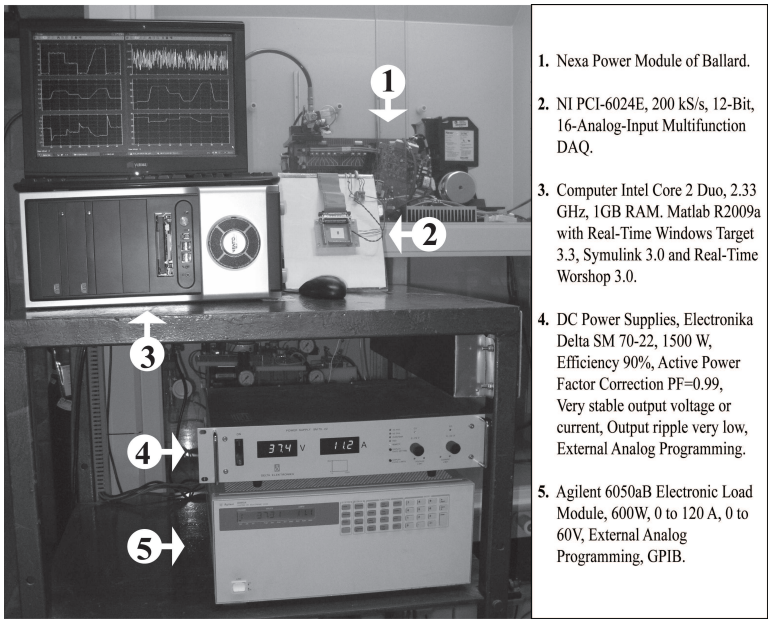

Figure 5-6: Experimental configuration of the PEM fuel cell emulator.

The steady-state characteristics of the Ballard NEXA power system that were obtained in a previous study [114] are compared with the emulator data as shown in Fig. 5-7. The emulator prediction is in good agreement with the experimental measurements for all the λ_{O_2} values in the 3 to 6.5 range considered.

The comparison between the experimental data from [114] and the emulator dynamic response is

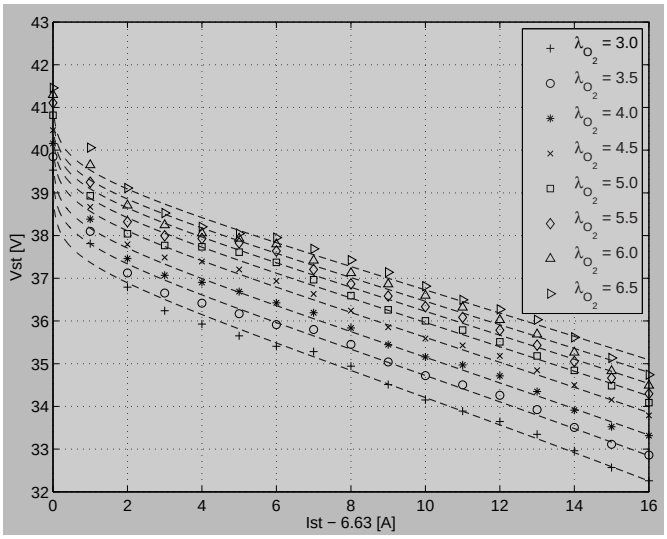

Figure 5-7: Polarization curves for different λ_{O_2} values provided by the emulator (continuous trace) with superimposed experimental data (discrete symbols).

presented in Fig. 5-8. The physical variables externally imposed on the real system and the emulator were the load current I_{net} and the ambient temperature $T_{ca,in}$. The applied I_{net} profile shown in Fig. 5-8(a) exhibits high and low frequency transients that permits a realistic validation of the model. The $T_{ca,in}$ behavior measured during the experiments is depicted in Fig. 5-8(b). The good agreement between the model and the experimental results also holds for the oxygen excess ratio λ_{O_2} (Fig. 5-8(c)). Experimental data made it possible to identify the λ_{O_2} static profile regulated by the control law implemented in the NEXA proprietary control board (5.14), which presents a static relation between the desired $\lambda_{O_2,Nexa}$ and the stack current I_{st}. This relation gives a safe λ_{O_2} reference against oxygen starvation only in steady state conditions but not during transients. The NEXA board controller parameters are $a_0 = 402.4$, $a_1 = 8.509 \times 10^{-5}$ $[1/A]$, $a_2 = -0.8387$ $[1/A^2]$, $a_3 = 0.027$ $[1/A^3]$, $b_0 = 61.4$ $[1/A]$ and $b_1 = 1.0$.

$$\lambda_{O_2,Nexa} = \frac{a_3 \cdot I_{st}^3 + a_2 \cdot I_{st}^2 + a_1 \cdot I_{st} + a_0}{b_1 \cdot I_{st} + b_0} \tag{5.14}$$

Similarly, Fig. 5-8(d) shows the comparison between the stack voltage experimental values and the experimental measurements from the emulator, where a satisfactory fitting of the results is evident.

The consumption and dynamics of the emulator air compressor were also compared with the experimental measurements. Fig. 5-8(e) compares the losses estimated by the emulator and the measured current consumption of the auxiliary systems, with the emulator reproducing the mean

consumption. Fig. 5-8(f) shows that the compressor dynamic model satisfactorily reproduces the experimental air mass flow.

The MRE criterion 4 applied to the data for the polarization curves depicted in Fig. 5-7 gives a relative mean error equal to 0.34 %. The application of the same criterion to the dynamic responses depicted in Fig. 5-8 gives the relative mean errors shown in Table 5.2. These results confirm the accuracy of the emulator. The errors in the ancillary systems, consumption and losses, compressor air flow, oxygen excess ratio and stack voltage are believed to be mainly due to the non-modeled ripple component affecting these signals.

Table 5.2: Dynamic validation error analysis (MRE) of the emulator

Variable	I_{cm}	W_{cp}	λ_{O_2}	V_{st}
MRE [%]	8.768	2.377	2.363	0.497

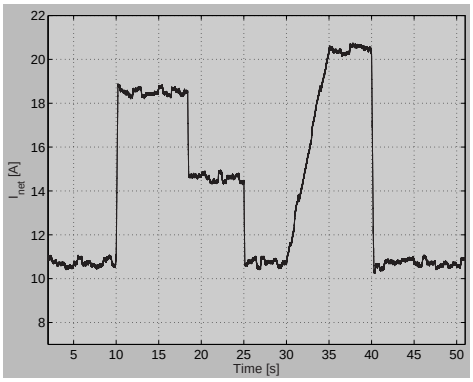

(a) Load current profile.

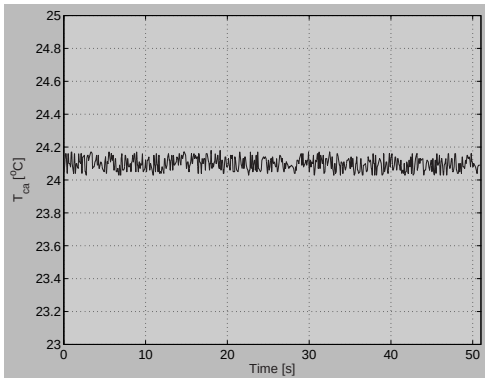

(b) Ambient temperature.

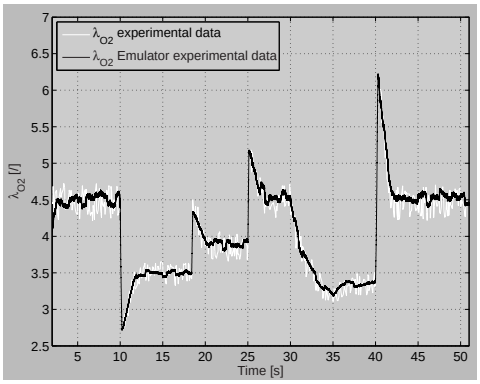

(c) λ_{O2} profile.

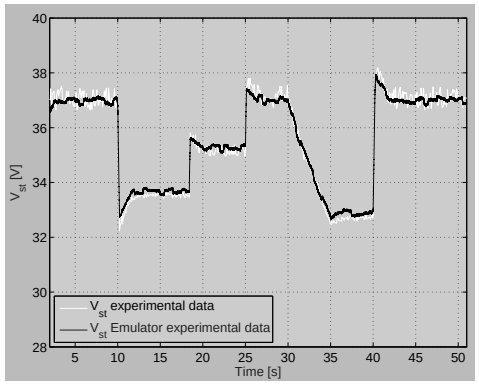

(d) Stack voltage profile.

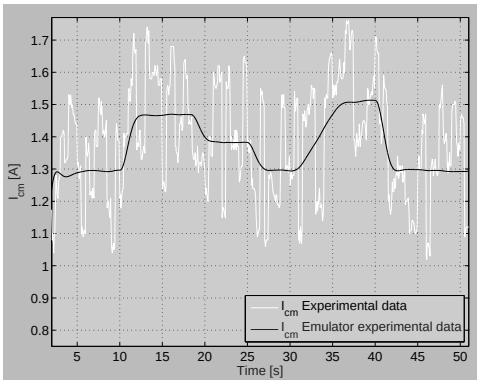

(e) Parasitic losses.

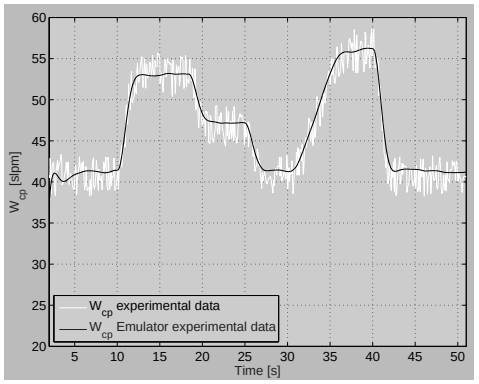

(f) Air mass flow profile.

Figure 5-8: PEMFC emulator experimental validation.

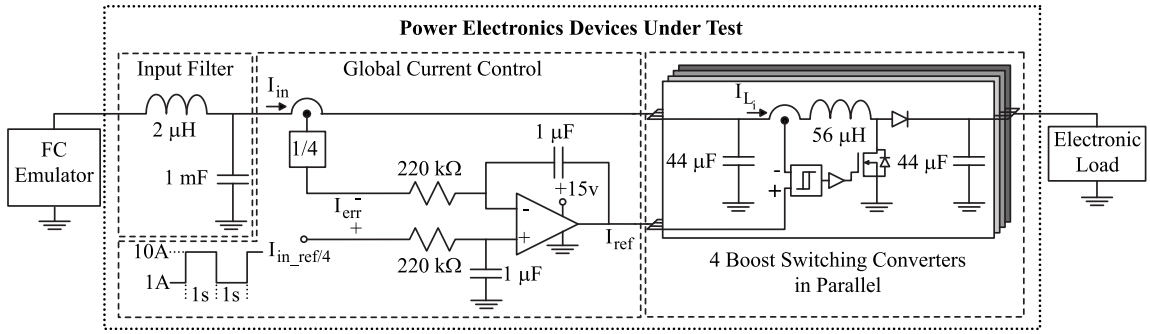

Figure 5-9: Diagram of the hardware-in-the-loop system.

5.6 Application Example

The emulator proposed in this disertation permits a safe a priori testing of several devices which, if connected to the FC, could cause oxygen starvation. To illustrate this, a design example of the control of a step-up dc/dc converter is presented. The converter has a second-order low pass input LC filter ($L = 2 \ \ \mu H$; $C = 1 \ \ mF$) to reduce the high frequency components that can degrade the operation of the FC [134]. The *1.2 kW* switching converter is implemented using four *300 W* boost converter modules in parallel [135], each one of which has a local inner sliding-mode current control. The reference of all inner loops is regulated by a global input current controller to obtain null steady-state error in the current supplied by to the FC. The parameters of the individual boost modules are $L = 56 \ \ \mu H$, $C_i = 44 \ \ \mu F$ and $C_o = 44 \ \ \mu F$, where C_i and C_o are the input and output high frequency capacitors, respectively. Fig. 5-9 shows a scheme of the hardware-in-the-loop system made up of the cascade connection of a real-time FC emulator, a power step-up converter (four boost converters in parallel) with its input filter and current control, and a programmable electronic load. A more detailed explanation on the circuit implementation is given in [136].

In Fig. 5-10, the experimental behavior of the λ_{O_2} for different changes in the system input current is shown. Different current transients with the same 96 A/s rise and fall slopes can be seen in Fig. 5-10(a). Fig. 5-10(b) depicts the λ_{O_2} profile for each current transient. A magnification of the 6 ms to 8 ms time interval shows that oxygen starvation ($\lambda_{O_2} < 1$) is predicted by the emulator. A 46 A current step with different slopes and their corresponding λ_{O_2} profiles are depicted in Fig. 5-10(c) and Fig. 5-10(d). The emulator predicts $\lambda_{O_2} < 1$ only for positive high fast transients, which indicates that controlling the current slew-rate can prevent oxygen starvation. One way of controlling the slew rate may be to include a slope limiter in the current loop. However, this method considers the slope but not the amplitude of the current step. If the amplitude and slew-rate effects have to be addressed simultaneously, other methods using fuzzy logic controllers [137] could be used.

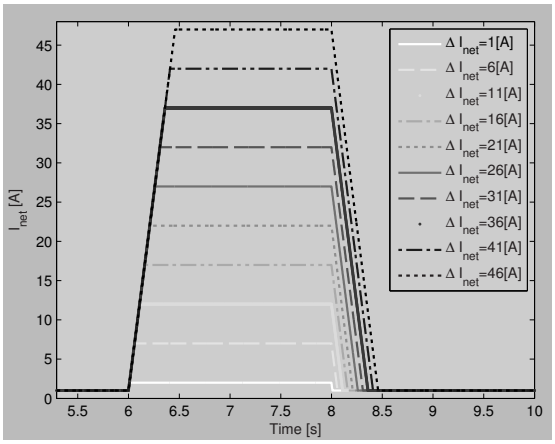

(a) Different current transient for a constant slope.

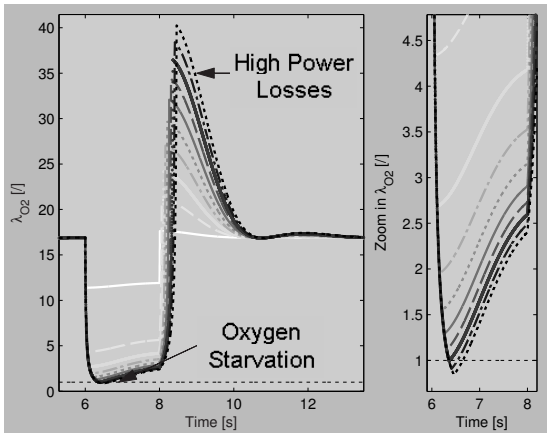

(b) λ_{O_2} by 5-10(a).

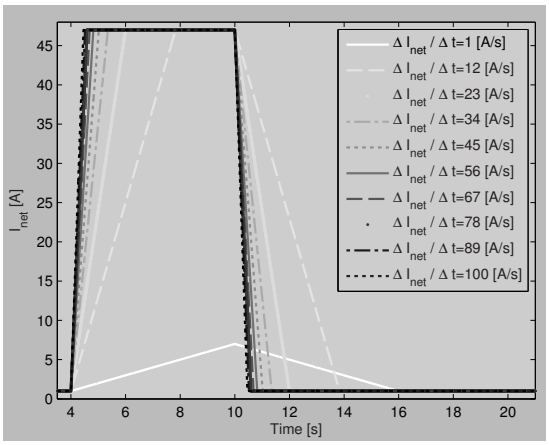

(c) Different slopes for a constant step current.

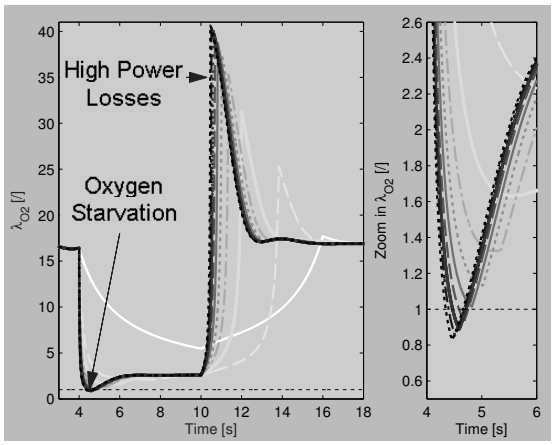

(d) λ_{O_2} by 5-10(c).

Figure 5-10: λ_{O_2} for different input current transients.

The experimental configuration of the emulator and the dc/dc converter is presented in Fig. 5-11. According to Fig. 5-10(d) a current slew-rate of 34 A/s ensures a λ_{O_2} higher than 1.3 for the 46 A step change. To limit the input current slope to around 34 A/s, the global current controller integrates the input current error (I_{err}) with a time constant of 220 ms yielding a $\lambda_{O_2} \geq 1.9$ condition for a 40 A step transient. This can be seen in Fig. 5-12(b), which depicts the emulator λ_{O_2} signal for the current transient shown in Fig. 5-12(a). The white trace in Fig. 5-12(a) corresponds to a step change of the emulator current from 4 A to 40 A, which is represented by a change in the converter's current reference signal from 1 V to 10 V. The black trace shows the measured current of one of the four 300 W modules using a current sensor with a 1 V/A gain. A peak-to-peak ripple of 2 A corresponding to a switching frequency of approximately 100 kHz can be observed in the boost converter current trace.

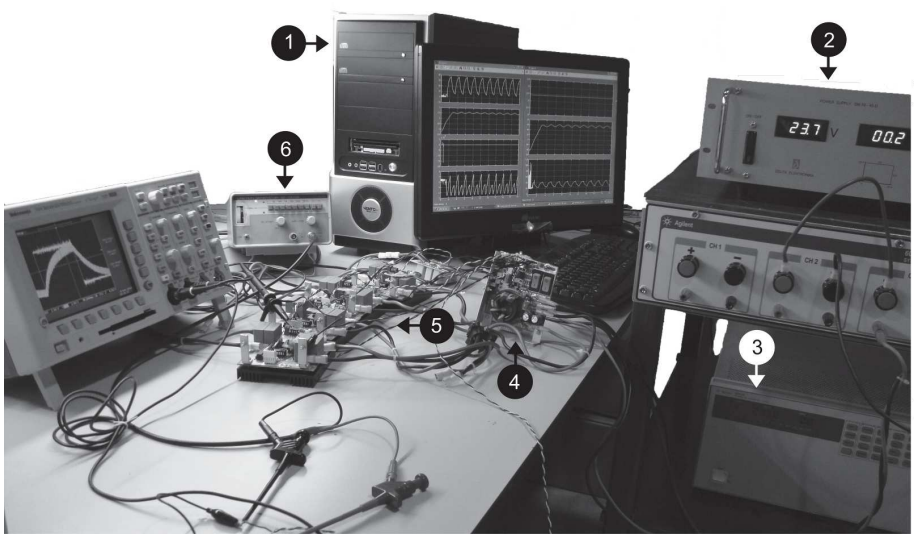

1. Computer Intel Core 2 Duo, 2.33 GHz, 1GB RAM, Matlab R2009a with Symulink 3.0, Real-Time Windows Target 3.3, Real-Time Workshop 3.0 and NI PCI-6024E.

2. DC Power Supplie, Electronika Delta SM 70-45, 3000 W and High Speed External Analog Programming.

3. Agilent 6050aB Electronic Load Module, 1800W, 0 to 120 A, 0 to 60V, External Analog Programming and GPIB.

4. Input Filter and Control Circuit.

5. DC/DC converters, 4 modules, 1200 W.

6. Input current reference.

Figure 5-11: Experimental configuration of the emulator and dc/dc converter.

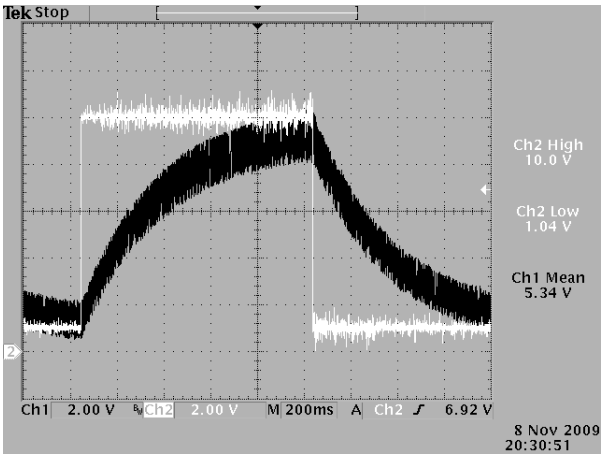

(a)

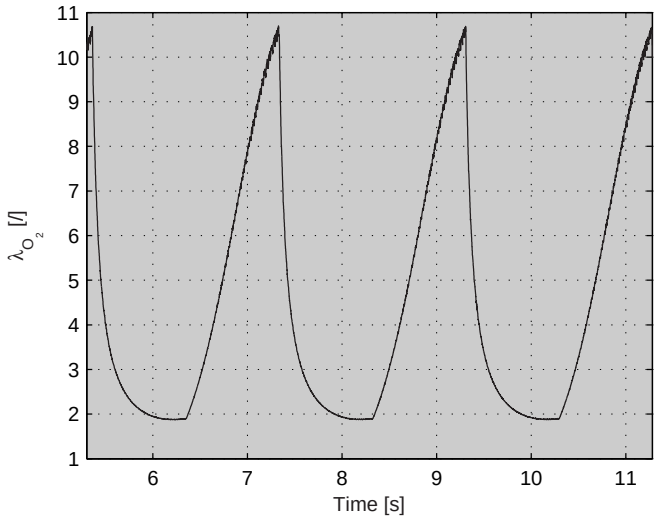

(b)

Figure 5-12: Experimental results of the emulator and dc/dc converter. (a) Current reference and current approximately limited by the slew-rate. (b) λ_{O_2} in the emulator.

5.7 Conclusions

Using an experimentally validated model of a 1.2 kW PEM fuel cell, a real-time emulator of the FC has been parameterized and its static and dynamic behaviors successfully tested. The emulator explicitly estimates the oxygen excess factor λ_{O_2} which when smaller than one, indicates the occurrence of the dangerous phenomenon of oxygen starvation.

The experiments revealed that oxygen starvation depends strongly on both the level and the slew-rate of the current extracted from the fuel cell. The emulator has been used to test different step-like current profiles and to identify the specific conditions that cause the oxygen starvation. It has been determined that, for a positive current transition from idle to a maximum level of 46 A, a slew-rate of 34 A/s does not cause oxygen starvation with a reasonable safety margin. Smaller current steps without oxygen starvation can be supplied even when slew rates are larger. The real-time emulator was used to build a hardware-in-the-loop system containing a step-up converter whose integral control loop was adjusted to prevent oxygen starvation. The experiments confirmed that a time constant of 220 ms results in an average slew-rate of 36 A/s and a minimum oxygen excess factor of about 1.9.

The emulator developed is a valuable tool that enables the power systems that are to be connected to the real fuel cell to be safely tested and adjusted. Work is still being carried out on the design of a DC bus using a new type of DC converter that will be connected to the fuel cell [82].

Chapter 6

Reactivation System for Proton-Exchange Membrane Fuel-Cells

6.1 Abstract

In recent years, Proton-Exchange Membrane Fuel Cells (PEMFCs) have been the focus of very intensive researches. Manufacturers of these alternative power sources propose a rejuvenation sequence after the FC has been operating at high power for a certain period of time. These rejuvenation methods could be not appropriate for the reactivation of the FC when it has been out of operation for a long period of time or after it has been repaired. Since the developed reactivation system monitors temperature, current, and the cell voltages of the stack, it could be also useful for the diagnostic and repairing processes. The limited number of published contributions suggests that systems developing reactivation techniques are an open research field. In this disertation, an automated system for reactivating PEMFCs and results of experimental testing are presented.

6.2 Introduction

Power systems based on proton-exchange membrane fuel cell technology have been the object of increasing attention over recent years. This is because they appear very promising for both stationary and mobile applications due to their high-efficiency, low-operating temperatures allowing fast start-up, high-power density, solid electrolytes, long cell and stack lives, low corrosion, and non-polluting emissions into the environment [32, 33, 34].

One of the areas addressed by researchers has been FC modelling. In the literature, there are several models that describe polymer electrolyte membrane fuel cell (PEMFC), ranging from static, dynamics, frequencial, impedance spectroscopy, empirical, electrochemical, electrical circuit, artificial neural network, and real-time simulation models. In addition, models that analyze and/or design air flow controllers that protect the FC from oxygen starvation during load transients, estimate the oxygen excess ratio, , analyzes the behavior of transient flooding in the cathode, permit studding of interactions between the different elements that can be connected to the FC, among many others, are also found in the literature [33, 34, 138, 139, 140, 141, 114, 142, 143, 144, 145, 146]. The estimation of parameters by a specific FC model is also an area of interest for researchers as evidenced by the number of publications that can be found on this topic [147, 146, 148].

Another recent area attracting research is the design of power converters for being connected to the FC [149, 150, 151, 152, 153, 38, 39, 154, 146, 155, 125, 156]. These power converters allow to manage the energy delivered by the stack to be used over wide-range of applications to be done in a safe and efficient manner. The studies focus primarily on the design of dc/dc converters, inverters and filters with high-efficiency, reliability, low-ripple input currents and isolated structures that ensure the correct and safe operation of the FC under all load conditions. The use of an FC emulator is the most suitable way of testing these power converters and other different devices before being connected to the FC. Advances in computing technologies, such as microprocessors, field-programmable gate arrays (FPGAs), digital signal controllers (DSP), multi-core processors and stream processors, have driven the development of increasingly complex, fast, versatile, and economical FC emulators into becoming another area of research. These, then, are needed in research, since they enable control strategies to be evaluated, in a safe, economical, realistic, real-time and repetitive manner, and the performances of power stages to be tested. They also make it possible to carry out critical tests that would otherwise be a risk for the equipment, and different FC models and FC types to be studied using FC emulators [139, 157, 143, 158, 93, 159]. The systems formed by the emulator and the devices to be connected to the FC is known as hardware-in-the-loop (HIL) simulation and it is one of more recently studied research areas [143, 158, 157, 159].

The output characteristics in the PEMFC are limited by the mechanical devices that are used to maintain the air-flow in the cathode by means of a compressor-motor, hydrogen-flow in the anode through an adjustable valve command, temperature control using a cooling-fan, and the humidity of the air in the cell by means of a humidity-exchanger. Hence, the time constants are dominated by a fuel delivery system. As a consequence, a load transient demand will cause a high-voltage drop after a short time, well-known as the oxygen starvation phenomena [35]. This operational condition

is evidently harmful for the FC and for this reason the FC is considered as slow dynamic-response equipment with respect to the transient load's requirement. Therefore, batteries, ultracapacitors or other auxiliary power sources are needed to work together with the FC, in order to ensure a fast response to any load power changes. Consequently, the systems formed by FC and other auxiliary power sources, known as FC hybrid systems, have been one of the more studied areas over recent years [36, 37, 38, 39].

As mentioned above, oxygen starvation is a complicated phenomenon that reduces an FC's life. This phenomenon entails a rapid decrease in cell-voltage, which in severe cases can cause a hot spot, or even burn-through on a membrane's surface [34]. Therefore, in the literature it is possible to find many studies on the oxygen starvation phenomenon, and it has become another area of research regarding FCs. In [125] controlling the FC air-pump voltage and regulating the FC-current through a dc/dc switching converter provides FC protection against the oxygen starvation phenomenon. In [160] the test station of fuel cell is built, equipped with versatile control systems that regulate the fuel-flow, the air-flow, and the temperature, for studying the behaviour of a PEMFC under different air stoichiometric conditions. The design of a high-speed three phase switch reluctance machine (SRM) presented in [160] is needed for driving a compressor regarding the air management of an automotive application FC, since this kind of compressor-motor is widely-used in high-speed applications. The two models of predictive control loops proposed and compared in [161] are aimed at satisfying the oxygen starvation avoidance criterion, and the maximum efficiency criterion in the FC. A very similar goal is addressed in [162], which analyzes the performance limitations and trade-offs associated with compressor-driven air supply and discusses different feed-forward and feed-back architecture controllers for avoiding oxygen starvation during load changes. A PEMFC dynamic electrical-circuit model that can estimate the oxygen excess ratio is presented in [114], and its model is used in [139] to implement a real-time simulation system. In [163] a simplified model of the permanent-magnet synchronous motor is used to feed the FC with air. This control ensures less excursions away from the motor-equilibrium operation point, and thus reduces the risk of oxygen starvation, and reacts quickly to load changes.

During shipping or idleness for a long period of time, the FC stack could lose its performance and it is necessary to reactivate it. The Nexa FC, of the manufacturer Ballard, has a rejuvenation sequence process that is performed prior to normal shutdown if the FC has been running for between 10-30 minutes at an average gross stack power of 200 W or greater, measured over the last 10 minutes of operation [164]. This automated rejuvenation process lasts approximately 3 minutes and restores any FC stack performance that may have been degraded by certain contaminants, by repeatedly cycling stack voltage under the presence of internal parasitic loads. The drawback of the

Nexa system is that a separate software has never been designated for the rejuvenation cycle and, depending on the severity of the performance degradation, the short duration of its rejuvenation process might be insufficient for obtaining the FC reactivation after a long inactivity period. Also, taking into account that the Nexa is a self-humidified closed system FC, triggering the Nexa's rejuvenation cycle with relatively high power levels without a previous reactivation cycle could endanger the FC. Additionally, not all FC's have the internal system of rejuvenation that Nexa has. Systems that achieve a rejuvenation of the FC stack can be found within two groups of patents, as described below. The performance of the stack may gradually decrease due to the accumulation of water in the stack, thus producing a blockage of those channels through which gases circulate. A technique that includes applying a vacuum to the manifold of a FC stack in order to remove at least some of the accumulated water, is presented in [165]. The performance of FC can also be affected by impurities known as electrocatalyst poisons, either from the reactant streams or generated from within the FC as intermediate species during FC reactions, which may be absorbed or deposited on the surface of the anode, and the cathode electrocatalysts [166]. The patents [166, 167, 168] show a system for removing electrocatalyst poisons and obtaining an improvement in FC performance. All the processes described are used to rejuvenate a healthy FC but none can be applied for achieving reactivation of a long time stored or repaired FC. Some user guides [169] recommend manual activation procedures to ensure a progressive humidification of the stack while performing frequent voltage measurements on each of the stack cells to ensure that they are always above a safe value. This process is slow, wastes a lot of hydrogen, and is manpower intensive. The study of the technical literature on the different FC power electronics application research areas, that has been resumed previously, has shown that there is not any automated system that can perform the reactivation of a PEMFC. This means that an automated reactivation system using a combination of software and hardware can be of great interest. This work opens the door to the reactivation of fuel cells a new area of research that will be vital to ensure a better positioning of PEMFCs as practical electrical generators and will promote their use.

The rest of this chapter is organized as follows: Section 6.3 describes the PEMFC system to reactivate, and Section 6.4 performs a detailed description of the hardware and software that comprises the proposed reactivation system. Finally, the last two sections present respectively experimental results and the conclusions of this work.

6.3 Description of the PEMFC system to reactivate

The air-cooled proton exchange membrane (PEM) fuel-cell stack comprising 40 membrane electrode assemblies (MEA) is the PC3F40 of the Palcan Fuel Cell Co Ltd as shown in Fig. 6-1 and its main

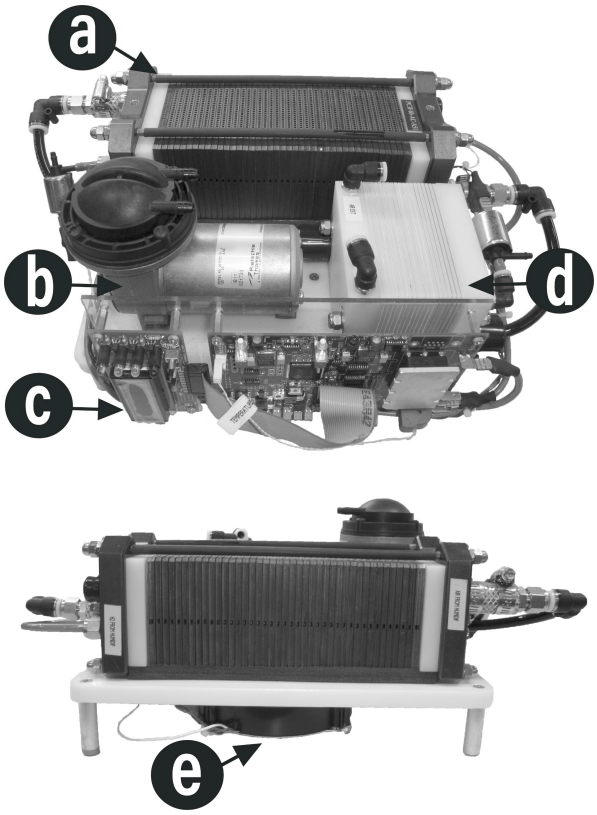

Figure 6-1: Top and back views of the PC3F40 fuel cell system: (a) PC3F40-AC-AXX stack, (b) air pump, (c) fuel cell controller, (d) humidifier, (e) fan.

characteristics are presented in Table 6.1. The PC3F40 fuel-cell power model includes the stack, air pump, humidifier, valves, relay, DC-DC converter, digital-signal processing (DSP) controller and displays, as shown in Fig. 6-2. The DSP-controller gets the feedback signal, such as fuel-cell voltage, current, and temperature, from the stack and sends the control signal to the air-pump, fan, valves and relay. The manufacturer recommends shutting-down the system immediately by turning the key to the off-position, if the following situations should occur: stack is over-heating, that is, the fuel cell temperature is over 75 °C, stack voltage is under 18 V, stack current is over 20 A, and the system connection is incorrect. In addition, the manufacturer delivers a list of warnings to be considered for obtaining good functioning of the fuel-cell. Many of these warnings are easy to perform, such as: never bring the inlets of air and hydrogen pressures be above 8 psig, never use pure oxygen in the stack, never use the stack when cooling air is not flowing along the cooling channels, never use a stack without proper cooling. One of the warnings determines the optimal point of operation as: monitor the temperature at the core outlet and never let it be above 75 °C, the stack is performs at its best between 50 and 65 °C. Finally, the last warning is a little more complex to perform as explained in the next session, this is: for better operation, a cell-voltage monitor is required, and

never allow a cell to go below 0.45 V.

Table 6.1: PC3F40-AC-AXX Palcan PEM FC stack specifications

Specifications	
Electrical voltage	20 - 40 V DC unregulated
Nominal power rating	400 W
Stack efficiency @ 400W	$> 40\%$
Dimension	
Width	11.7 cm
Height	11.3 cm
Depth	30 cm
Width	2.70 kg
Operating conditions	
Nominal Reactant Air	
Flow rate	24 SLPM
Inlet dew point temperature	55 °C
Inlet pressure	1.2 psig
Reactant Hydrogen	
H2 grade	Industrial grade
Consumption	4.4 SLPM
Inlet dew point temperature	55 °C
Inlet pressure	3 psig
Cooling requirement	
Coolant type	Air
Flow rate	As required
Stack temperature	60 °C
Range Reactant Air	
Flow rate	1 to 30 SLPM
Inlet dew point temperature	Stack temperature up to 60 °C
Inlet pressure	0.5 to 5 psig
Reactant Hydrogen	
H2 grade	Industrial grade, reformate
Inlet dew point temperature	Stack temperature up to 60 °C
Pressure	0.5 to 5 psig
Cooling	
Coolant type	Air
Flow rate	As required
Stack temperature	4 to 60 °C

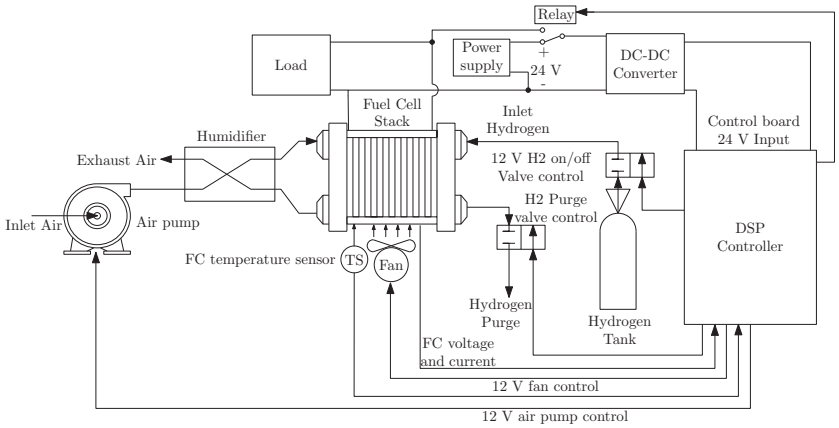

Figure 6-2: Block diagram of the PC3F40 fuel cell system.

6.4 Description of the PEMFC embedded and automated reactivation system

In the previous section, the main features of the PEMFC system required for reactivation, were described in detail. The complexity of the system for reactivating, and the reactivation process itself become crucial for the development of an embedded and automated reactivation system. The main functions of this system are: sensing the cells' voltages in the FC, sensing and controlling the temperature, sensing the current generated by the stack in order to determine the power-operation point, keeping the FC within those security conditions recommended by the manufacturer, and optionally allowing communication for the monitoring of key FC variables from an external system, such as a computer. This section presents the main characteristics of the hardware and software that make the PEMFC reactivation system.

6.4.1 Hardware of the fuel cell reactivation system

Cell voltage sensing and multiplexing stage

In general, fuel cells are systems with a large number of cells in series, thus making monitoring of the cell-voltage a complex task. This difficulty is due to the need of the data acquisition (DAQ) with 40 differential analog input channels to monitor 40 cell voltages in the specific case of the PC3F40 FC of Palcan and 47 differential analog input channels, in the case where it is necessary to reactivate the Nexa FC of Ballard. Although the market may get a few cards with a large number of differential analog input channels, such as the NI USB-6255, the PXI-6255, the NI PXI-6225, and the NI PCI-6255 of National Instruments, the USB-AI12-128A of Acces I/O Products, the DaqLab/2000 and DaqScan/2000 series of the Measurement Computing Corporation, their high-cost is the main disadvantage for their use. Therefore, it is necessary to build a system for monitoring

those voltages in a stack that can be extended to other possible cells requiring reactivation. The sensing voltage cells system consists of precision resistive dividers, as illustrated in Fig. 6-3, that convert the differential analog signals of the cells into referenced single-ended (RSE) signals, with a range of voltages of 0 V to 5 V, corresponding to the digital analog converter (DAC) range that will be used. The reading accuracy of the cell-voltages depends primarily on ADC resolution, the accuracies of the resistors, and the final voltage ranges of the resistive dividers. The manner in which the resistors are connected to the bipolar plates of the FC, follows the standard RJ45 for the connectors and their wiring. A capacitor is placed at each output of the resistive divider in order to stabilize and filter the acquired signal, as shown in Fig. 6-3. The acquired signals pass through a stage of multiplexing which allows for up to 48 differential signals to be sensored with only 6 analog inputs for the signal multiplexed, 3 digital outputs for the address decoders of all the multiplexers using the truth Table 6.2, and 3 digital-outputs for enable each of the multiplexers as depicted in Fig. 6-3. The high-performance CMOS analog multiplexer used is the DG407 Vishay Siliconix and its main characteristics are its fast transition time of 200 ns, higher accuracy, and high-speed data acquisition is included between their applications. The solution for acquiring the differential voltage proposed in this work is simple, low-cost, and provides high-speed acquisition with good accuracy.

Table 6.2: Truth table of the multiplexer stage

Position (k)	A_2 A_2	A_1 A_1	A_0 A_0
1	0	0	0
2	0	0	1
3	0	1	0
4	0	1	1
5	1	0	0
6	1	0	1
7	1	1	0
8	1	1	1

Fig. 6-4 shows the multiplexing circuit prototype presented schematically in Fig. 6-3. On either side of each multiplexer can be observed a 8P8C connector that allows an easy connection and disconnection of the signals coming from the fuel cell. The solution to acquire the differential voltage proposed in this work is a simple, low-cost, high speed acquisition and with good accuracy.

PWM FC fan Driver control and FC current and temperature sensing stage

Since, the FC performs better between 50 °C and 65 °C, it is important to control the temperature of the stack to obtain a reactivation in less time, and thus ensure lower consumption of hydrogen during the test. This required designing a stage that could control the FC fan using pulse-width modulation (PWM) and it is also required for characterizing the temperature sensor that has the FC, for proper control. Fig. 6-5 presents the circuit schematic of the stage responsible for FC

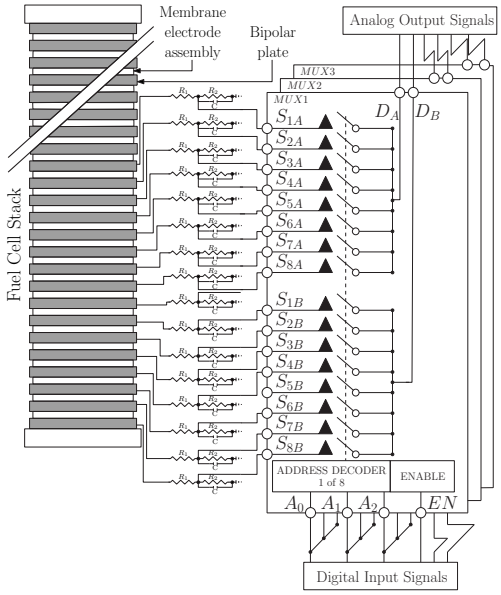

Figure 6-3: Circuit schematic of the multiplexing stage.

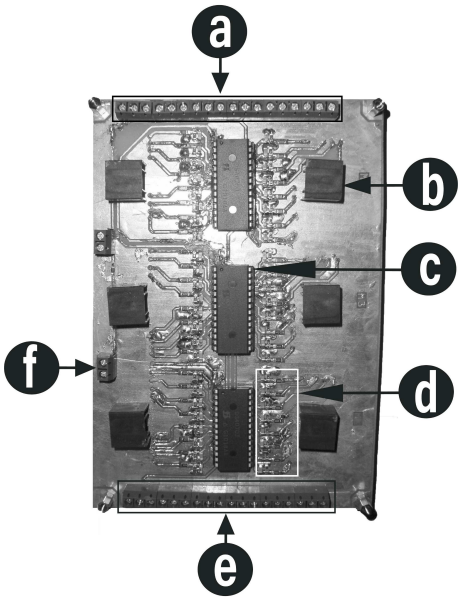

Figure 6-4: Circuit prototype of the multiplexing stage: (a) analog output signals, (b) 8P8C connector, (c) DG407 multiplexer, (d) resistive dividers, (e) digital input signals, (f) input power of 5 V.

temperature control. The PWM fan motor driver is implemented using a totem-pole output and the positive voltage regulator L78XX is selected according to the voltage that is powering the fan, and in the case of the PC3F40 FC is 12 V. This design allows to use the reactivation system for any kind of PEMFCs. In order to allow operation with high currents the IRFP150N MOSFET and the BYV79E diode are oversized. The FC thermistor is connected to a conditioning circuit that consist

of a resistance divider with a precise 5 V voltage source, as shown in Fig. 6-5. The thermistor is characterized for all the temperature ranges of the FC, using the experimental setup detailed in Fig. 6-6 and the FC thermistor characteristic as plotted in Fig. 6-7. Using a curve-fitting toolbox, the software of MATLAB adjusts the coefficients of the cubic polynomial of thermistor resistance, as a function of the temperature in °C as

$$\begin{aligned} Rt(Temp) &= -0.07108 \cdot Temp^3 + 16.37 \cdot Temp^2 \\ &\quad -1350 \cdot Temp + 4.186 \times 10^4. \end{aligned} \tag{6.1}$$

Therefore, the FC temperature as a function of voltage obtained by the conditioning circuit V_{temp} presented in Fig. 6-5 is:

$$\begin{aligned} Temp(V_{temp}) &= 1.914 \cdot V_{temp}^3 - 13.96 \cdot V_{temp}^2 \\ &\quad +54.04 \cdot V_{temp} - 38.74. \end{aligned} \tag{6.2}$$

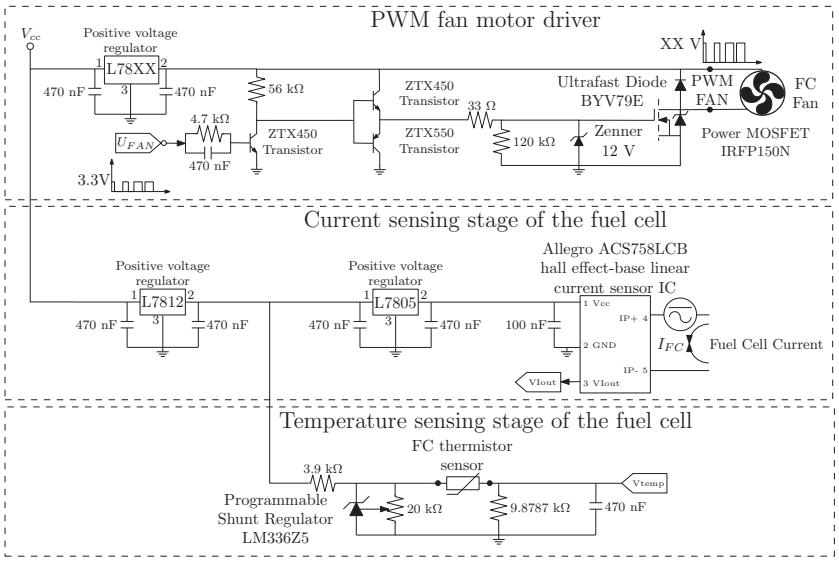

Figure 6-5: Circuit schematic of the PWM fan driver, current and temperature sensing of the PEMFC.

Finally, a current sensor is installed at this stage to measure the current generated by the cell, and thus determines its power output at all times. The Allegro ACS758xCB hall effect-base linear current sensor used can measure currents up to 50 A and can be used with other kinds of FC's. Additionally, this bidirectional sensor has a sensitivity of 40 mV/A, with internal resistance of only 100 $\mu\Omega$, thus providing a low-power loss. The circuit prototype of the temperature control and

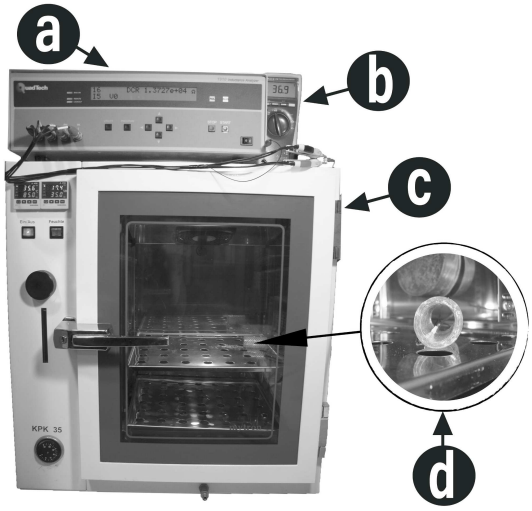

Figure 6-6: Experimental configuration to obtain the characteristic of the fuel cell thermistor: (a) 1910 inductance analyzer of the QuadTech manufacturer used to accurately measure the resistance, (b) the Fluke 179 digital multimeter to verify the measurement of temperature inside the oven, (c) KPK 35 oven of the Mytron manufacturer, (d) thermistor to characterize.

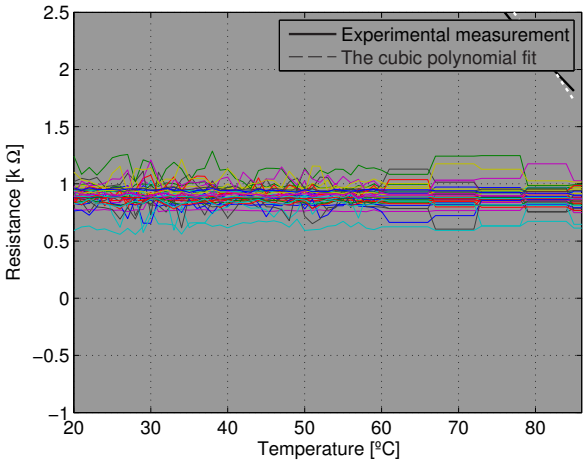

Figure 6-7: Fuel cell thermistor characteristic. In black line is depicted the experimental measurement using the configuration of Fig. 6-6 and in white line is represented the cubic polynomial fit of (6.1)

current sensing of the reactivation system is shown in Fig. 6-8.

Embedded control system

The selected system for the management of the systems presented above is the NI Single-Board RIO sbRIO-9631, which is cost-optimized with an embedded real-time processor, reconfigurable FPGA, and analog and digital inputs/outputs on one printed circuit board (PCB) [170]. The open design

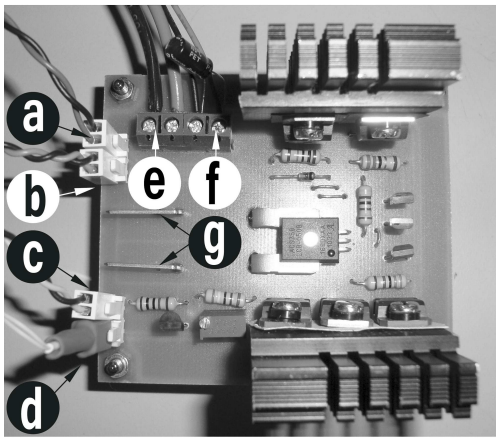

Figure 6-8: Circuit prototype of the temperature control and current sensing of the reactivation system: (a) PWM control input signal U_{FAN}, (b) analog output signal of the current measurement V_{Iout}, (c) analog output signal of the temperature measurement V_{temp}, (d) FC thermistor input, (e) input power V_{cc} of 15 V, (f) PWM control output signal PWM_{Fan}, (g) terminals for current being sample.

decreases cost and provides flexibility for designing a customized enclosure. NI Single-Board RIO devices are designed for acquisition applications that require high performance and reliability. The main characteristics of the sbRIO-9631 are described in the caption of Fig. 6-9.

PEM fuel cell reactivation system

Fig. 6-10 shows the configuration for all the hardware described above including the FC, the electronic load, and the computer for the monitoring and storage of the main variables. The difference in the sub-FC system presented in Fig. 6-10, with respect to that described in Fig. 6-2, is that the DSP does not control the temperature of the FC, but still controls the hydrogen supply and the air pump. It was necessary to design an additional stage of power conversion due to the different voltages of each stage comprising the reactivation system. The input voltage of this power conversion stage is the same power supply used by the FC control system, as shown in Fig. 6-10. During a test before starting, the reactivation of the FC was controlled by the Agilent 6050A DC electronic load through of its analog programming port in current mode, using an analog output signal of the sbRIO-9631. However, large fluctuations were present in the electronic load in the current mode that it threatened the FC. These fluctuations are due to the need of an input filter design for the electronic load, but since spectroscopic models for this kind of fuel-cell are unknown and our fuel cell was damaged to make this model, therefore it was impossible to create a proper filter design. The electronic load behaved stably in the resistance mode, but this mode can not be programmed using the analog programming port for this type of electronic load. The only forms that the electronic

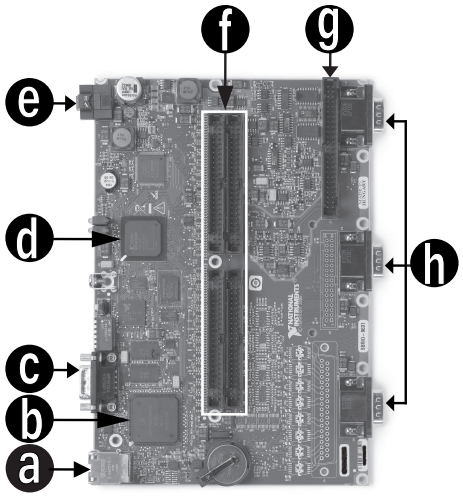

Figure 6-9: Top view of the sbRIO-9631: (a) RJ-45 ethernet port, (b) 266 MHz processor with 128 MB nonvolatile storage and 64 MB DRAM for deterministic control and analysis, (c) RS-232 serial port, (d) Xilinx Spartan-3 Reconfigurable with 1M gate FPGA by for custom timing, inline processing, and control, (e) 1930 V DC power supply connector, (f) 110 digital inputs or outputs of 3.3 V and TTL tolerant, (g) 32 single-ended or 16 differential analog input channels (16 bits of analog to digital converter (ADC) resolution and conversion time of 250 kS/s) and 4 analog output channels (16 bits of digital to analog converter (DAC) resolution), (h) connectors to expand the built-in analog and digital input/output.

load resistance mode is programmed for are manual or by using the GPIB port [171]. Therefore, the value of the electronic load current is sent through the ethernet port to the computer, together with the monitoring data and in the computer transformed into a resistance value that is sent using the GPIB port as shown in Fig. 6-10. Additionally, an analog output of the sbRIO-9631 was left, thus enabling its for use in other types of FC that allow for controlling the electronic load in current mode.

All hardware elements described and presented in this section 6.4 for the reactivation of the PEMFC and which are presented in Fig. 6-10 with a dashed line rectangle named PEM fuel cell reactivation system are developed experimentally using a methacrylate enclosures shown in Fig. 6-11. The methacrylate enclosures provides all the hardware development benefits such as strength, protection, security and easy operation, facility of connection and transportation, a compact system with overcurrent protection and a cooling system to operate for long hours without overheating. The reactivation system presented in Fig. 6-11 also has the possibility to reactivate other types of FC with more cells or more current levels, to control the temperature to reactivate the FC if this is necessary, to communicate with advanced protocols for monitoring the main variables, besides if not connected to the computer or if there is a failure in the computer during its execution the system is able to continue with the recovery of the FC despite the faults.

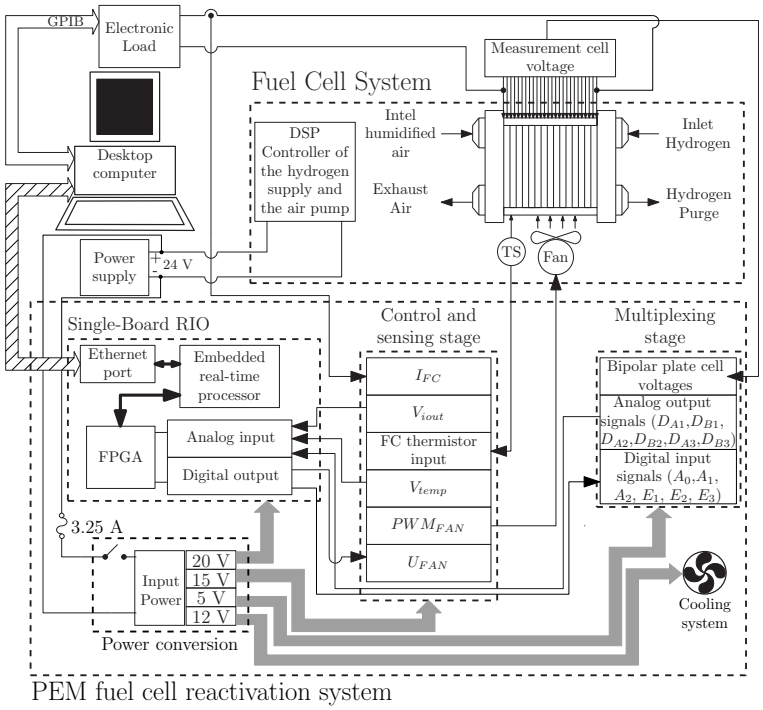

Figure 6-10: Hardware configuration using to the reactivation of PEMFC.

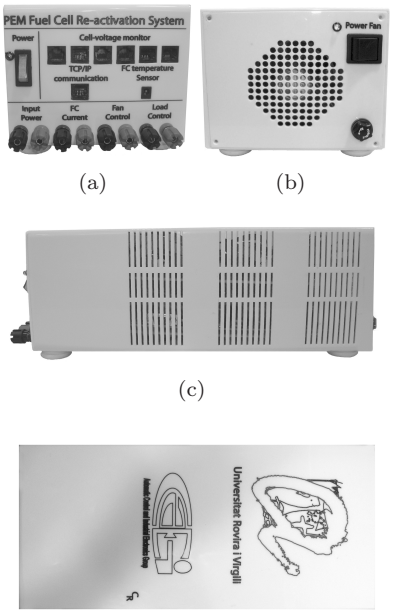

(a) (b)

(c)

(d)

Figure 6-11: Different views of the real-time automated system development for the reactivation of the PEMFC: (a) front view, (b) back view), (c) side view, (d) top view.

6.4.2 Software architecture of the fuel cell reactivation system

According to the hardware configuration shown in Fig. 6-10, it is necessary to develop programs for the desktop computer and for the Single-Board RIO. This latter device contains the design programs

for the real-time processor and for the reconfigurable FPGA. The software architecture diagram that controls the entire hardware described in the last section, is illustrated in Fig. 6-12. This subsection explains, in detail, all those programs implemented to ensure reactivation of the FC.

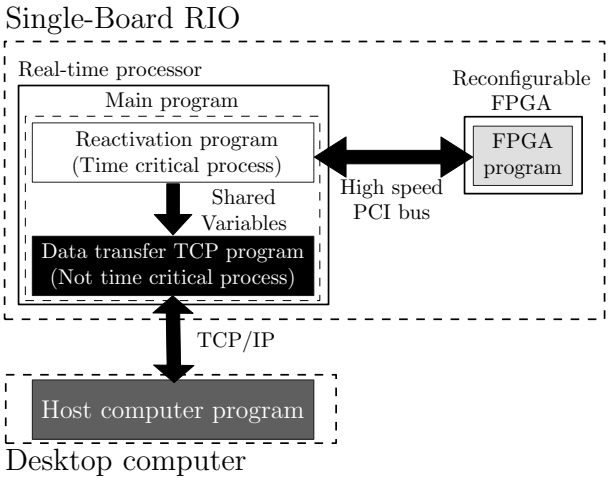

Figure 6-12: Software architecture diagram of the FC reactivation system.

As depicted in Fig. 6-12, the main program runs within a real-time processor and is basically responsible for executing in parallel the FC reactivation program and the transmission control protocol (TCP) communication program, as illustrated in the flowchart of the Fig. 6-13. This flowchart diagram has four process in parallel, the first one being responsible for FC reactivation, the second controls the FC temperature using a digital PID, the third write and read all signals connected to the reactivation system as can be seen in gray rectangles, and the fourth transmits the data to the host computer using TCP communication as can be seen in black rectangles in the Fig. 6-13. The reactivation and the temperature control processes use the reconfigurable FPGA in order to acquire or control the different signals required for FC reactivation as presented in gray rectangles in the Fig. 6-13. All input and output signals are connected directly to the FPGA, providing low-level customization of timing, and input and output signal processing. The FPGA is connected to the embedded real-time processor via a high-speed PCI bus, as shown in Fig. 6-12. The program of the FPGA presented in Fig. 6-13 uses the advantage of parallel computing offered by the reconfigurable FPGA in order to acquire the analog signals, D_{A1}, D_{B1}, D_{A2}, D_{B2}, D_{A3}, D_{B3}, V_{iout}, and V_{temp}, and to control each of the digital signals, A_0, A_1, A_2, E_1, E_2, E_3 and U_{FAN}.

The reactivation program process presented in Fig. 6-13 has the most important function of all regarding designed software. The design of this function is based on the methodology proposed by the fuel-cell manufacturer in order to obtain reactivation of the stack [169], but also adapting it to all the instrumentation systems designed for this purpose, and with the objective of it being valid for other types of FC. During the first part of this flowchart, the number of multiplexers necessary

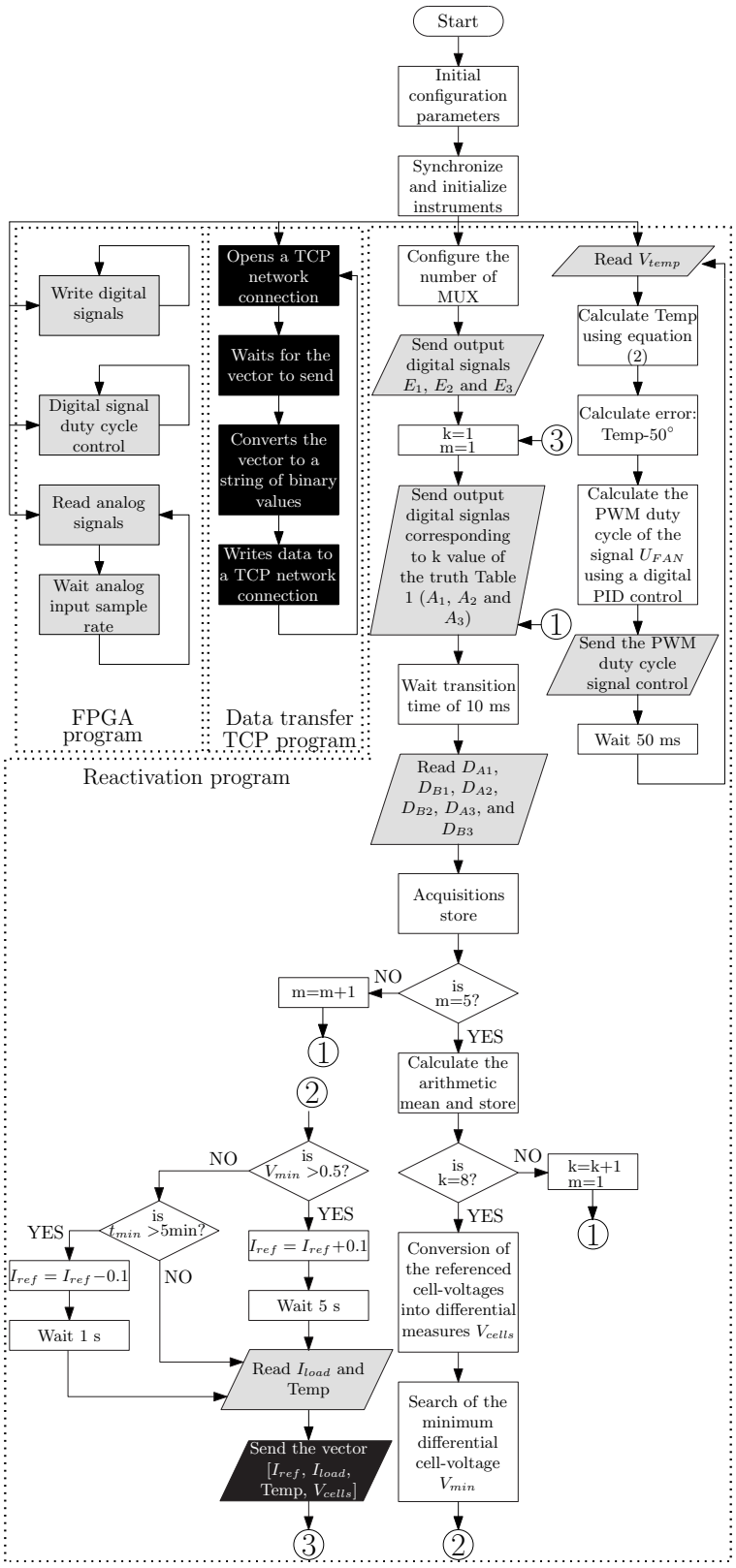

Figure 6-13: Flowchart of the reactivation process in the Single-Board RIO.

to sense the differential cell voltages within the FC, according to its number of MEA's are configured using the digital output enabling signals E_1,E_2, and E_3. The second part of the reactivation function presents a timed loop sequence with a period of 200 ms running in real time within the processor of the sbRIO. Inside the time-loop sequence, the truth table of the multiplexer stage, A_0,A_1,A_2, is controlled using a repetition structure. In order to reduce the noise from the acquired signals, an arithmetic mean is calculated. Each cell-voltages is sampled five times at a frequency of 100 Hz before calculating its mean value. The next step inside of the timed-loop sequence presented in Fig. 6-13, is to convert the referenced cell-voltages into differential cell-voltages and, thus, determine the voltage per cell. This is achieved by subtracting the voltage of each cell from the cell-voltage above and then multiplying it by the gain from the resistive divider. In those cases where all the voltage cells have a voltage greater than 0.5 V, this increases the load current by 0.1 A, and waits 5 seconds to ensure stabilization of the FC to the change of current. In the event that any of the cells voltages are less than 0.5 V, they should be expected to exceed this minimum value. During each iteration of the timed-loop sequence, the FC current I_{FC}, the FC temperature T_{emp} and the cell voltages are stored and sent to the Host computer program through an ethernet port using the TCP/IP. This program successfully ensures the sending of large amounts of data, 43 variables every 200 ms. If after 5 minutes the stack appears to have reached its limit, because the minimum cell-voltage does not exceed the value of 0.5 V, it is necessary to remove the load slowly as, 0.1 A with 1 second between changes, and the start again.

Finally, the host program running on the desktop computer and shown as a flowchart in Fig. 6-14, is responsible for receiving data using TCP/IP communication. This allow the user to view and store all the reactivation information by a graphical user interface and, additionally, an electronic load control through the GPIB port. As mentioned previously, the electronic load is controlled in resistive mode, therefore it was designed as a continuous function for converting the current sent by the reactivation program into a resistance value. This function is presented in (6.3) and its characteristic curve is illustrated in Fig. 6-15.

$$R_{load}(I_{load}) = \begin{cases} 600 - 1038\ I_{load} & for \quad I_{load} < 0.5A \\ \\ 38.62\ {I_{load}}^{-1.072} & for \quad I_{load} \geq 0.5A. \end{cases} \tag{6.3}$$

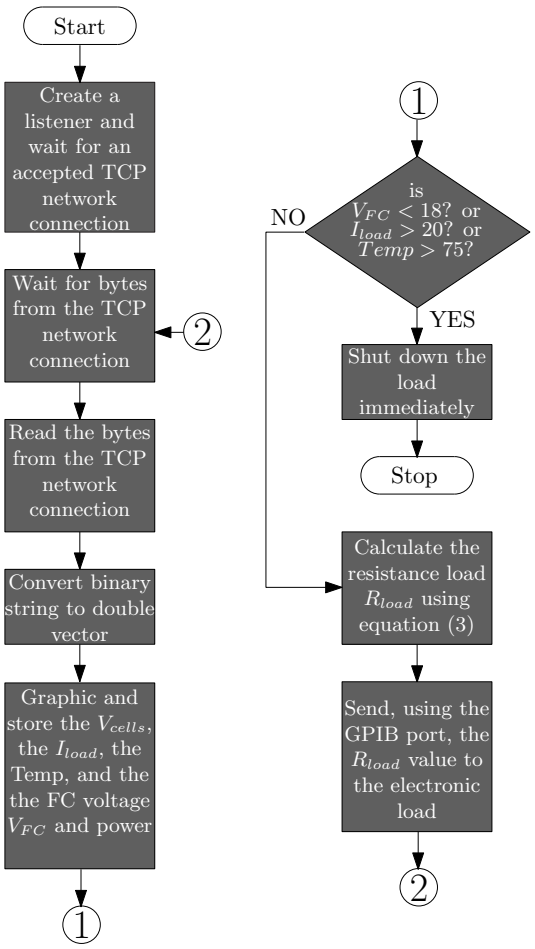

Figure 6-14: Host program flowchart diagram.

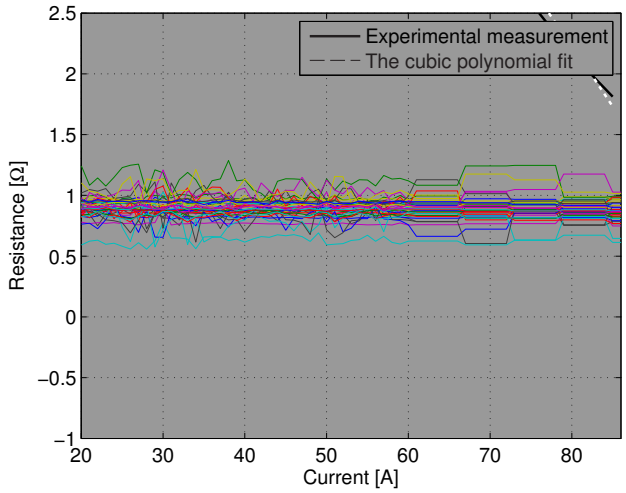

Figure 6-15: Characteristic curve of the electronic load in resistive mode.

6.5 Experimental results

Two PC3F40 PEMFCs were reported as damaged after being stored for several years without being used. An attempt was made to reactivate one of the FCs following a manual procedure, but after reaching half its maximum rated power a sudden and permanent power drop occurred. The main consequence of the manual reactivation failure was the development of the automated reactivation system shown in Fig. 6-16. A posterior reactivation attempt using the automatic system determined that a large number of the FC cells were always in an undervoltage condition associated to membrane damage. These first FC is still repair pending but we have been able to test the automatic system on the other twin FC. The experimental results have proved that the reactivation system has been able to reactivate the FC to a power-point of around 340 W, as shown in Fig. 6-17. Each trace of this figure corresponds to a different cycle of the FC reactivation. A cycle ends when any of the cells voltages is under a minimum value of 500 mV for five minutes. After this undervoltage condition appears, the load is decreased slowly to zero amperes as described in flowchart 6-13 and an alarm message is shown at the computer screen. At this point a human operator has to take the decision of either initiating a new reactivation cycle or finishing the procedure. In the experiments, the reactivation was ended when a seventh cycle (not shown) offered almost identical results than the sixth one. Fig. 6-18 presents the V-I static characteristics corresponding to the reactivation experiment, in which it can be seen how the stack voltage was regaining its performance with each of the six consecutive reactivation cycles after which an increase of more than 10 V of the FC stack's reversible potential was obtained. The six cycles depicted of the reactivation process lasted 10 hours and 25 minutes, and had a hydrogen consumption of 1433 liters at standard ambient temperature and pressure conditions (25 C, 100 kPa). The experimental results clearly verify that the PEMFC reactivation system works properly. The system's computer interface makes it easy to use and simplifies its reconfiguration for other models of PEMFC requiring reactivation.

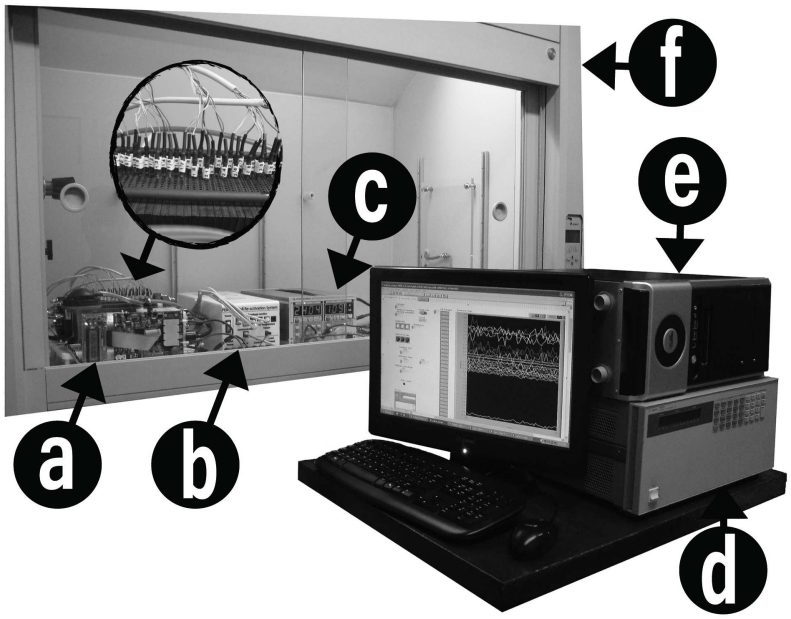

Figure 6-16: Experimental configuration using to FC reactivation: (a) PC3F40 PEMFC system, (b) PEMFC reactivation system, (c) power supply, (d) electronic load, (e) desktop computer with TCP/IP and GPIB ports, (f) fume cupboard.

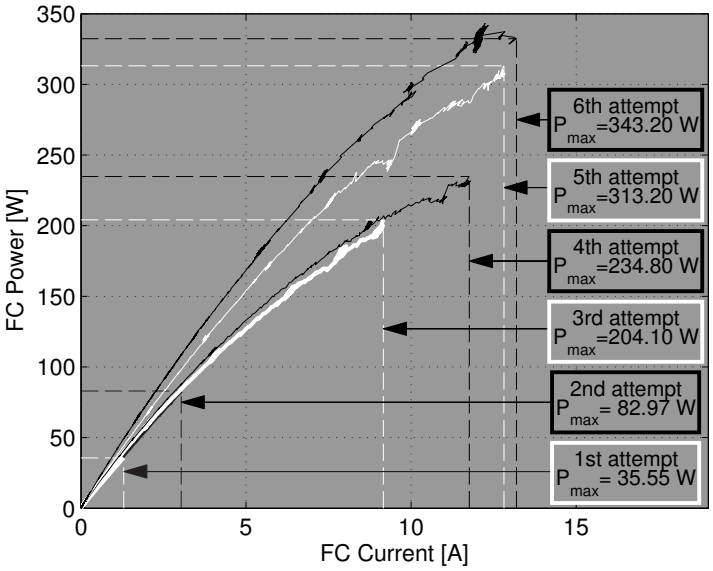

Figure 6-17: Fuel-cell power experimental characteristic.

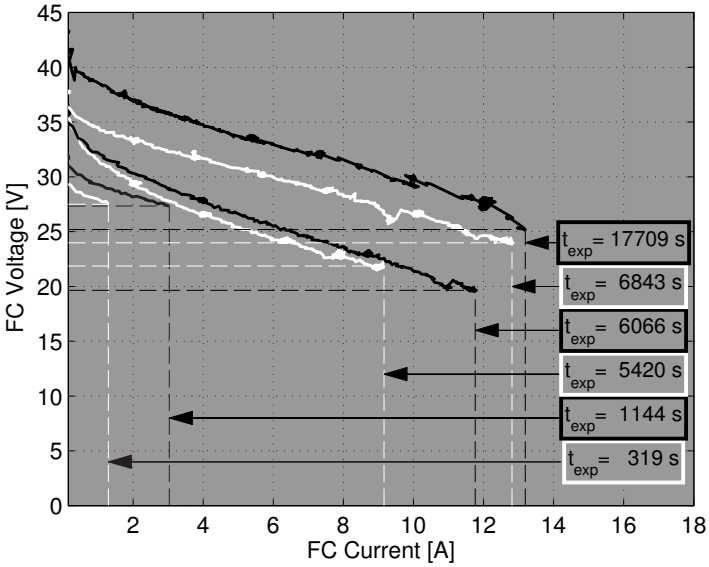

Figure 6-18: Fuel-cell V-I static experimental characteristic.

6.6 Conclusion

A new automated system for reactivating damaged FC has been developed and, using it, we have successfully reactivated a long period stored PEMFC. The proposed system implementation has allowed to monitor in real-time the main FC variables and to verify in practice the validity of the reactivation procedure for a Palcan PEMFC. Further research will address the improvement of the proposed system with an oxygen starvation detection feature that could allow the use of faster reactivation current profiles.

Chapter 7

Conclusions and Future Works

The main result of this Thesis is the design, building and testing of a new coupled-inductor buck-boost DC-DC converter structure, suitable to interconnect any pair of the elements in a PEMFC-based hybrid voltage bus: the PEMFC, the auxiliary storage device, and the load. The wide bandwidth and high efficiency performances exhibited by the converter, in addition with its simple controllability either in voltage or in current mode, allow the elements in a hybrid voltage bus to be connected in a variety of combinations, such as series, parallel or series-parallel.

The designed current controller is able to regulate either the input or the output current of the converter. It has been implemented so that if a sudden increase of the load causes the current extracted from the FC to reach a maximum level the controller switches in a fast and smooth manner from regulating the output current to regulating the input current, thus protecting the PEMFC. Similarly, it alternates from regulating the input current to limiting the load current if it increases too much, which makes the converter able to withstand even permanent short circuits.

The design and implementation of several FC emulators/simulators has allowed to test in advance the connection of the FC with the converter. Once the safety of the interconnection of the converter and its load has been assessed the real FC can be used without risking to damage it. Since the testing procedures could be very long, the use of the emulator provides savings in hydrogen consumption. Also, in some cases, the mathematical model in the emulator offers much more information on the FC variables than a real FC monitoring system.

The limitations of the available control and monitoring FC systems were also evident when the manual reactivation of a long time inactive FC resulted in its permanent damage. This motivated the design of an automated system that performed successfully in reactivating another FC of the

same model of the damaged one. To our knowledge, there is no other automated reactivation system reported in the literature, therefore this opens a new field of research that could be of great interest to facilitate the PEMFC adoption as electrical generator.

7.1 Future Works

The use of optimization techniques to determine the parameters that best fit an FC electrical circuit model is one of the tasks that are not included in the thesis but was completed. The fuel cell was modelled by an electrical circuit which includes the capacitive effects of the electrodes and the thermal effects of the stack fan. The circuit and thermal model parameters are adjusted to the experimental measurements using an evolutionary algorithm so that the obtained model reproduces the static and dynamic output voltage characteristics, and the fuel cell temperature, as a function of the load current. This is the major contribution of this work since in the specialist literature only some optimization techniques to adjust just the FC static characteristic had been applied. This work emerged because in the literature it is difficult to find all the parameters of a specific model to be used in a specified FC, in many cases different authors propose different values of them and generally none of them fits the experimental data of the real FC used. In addition, the developed model can be used by other researchers to implement different simulations and was also useful to develop a digital emulator of a PEMFC implemented by means of a power source controlled using the sbRIO (Single Board RIO) real time system from National Instruments. With this emulator it was possible to carry out critical tests and studies that would otherwise constitute a risk for the fuel cell. The developed system has been used to emulate the Ballard's 1.2 kW NEXA fuel cell, but its model can be trained to emulate other kinds of fuel cells. This work is currently under review in the journal "Revista Iberoamericana de Automática e Informática Industrial".

As a result of the above mentioned work it was observed that the model was extremely complex with a considerable computational cost during the training phase. In order to have a simpler and easier training to facilitate its implementation in real-time FC emulation systems diffusive models were investigated. These models had appropriately performed for the parameters estimation in battery applications. Additionally, several models in which the fuel cells have a fractional order behaviour have been reported, therefore the diffusive model could have a good performance in the FC parameters estimation. The tests that have been conducted confirmed the good performance of a diffusive model trained from our FC's current and voltage experimental data. Currently we are in the process of acquiring new training data to obtain a model that could reproduce the FC high frequency behaviour, up to 50 kHz. The diffusive model that will be obtained should be compared

with the experimental results already achieved by electrochemical impedance spectroscopy.

In one of the chapters of this thesis it was presented a real-time emulator of a PEMFC implemented by means of a power source controlled using the MATLAB real-time toolbox which additionally estimates the oxygen excess factor λ_{O_2}. This factor is very important because it indicates the occurrence of the dangerous phenomenon of oxygen starvation when it is smaller than one. Therefore, a low-cost real-time system that allows to estimate this important factor during FC operation and return signals that can alert to the converters connected to the FC of a dangerous behavior has been designed. The system is complete and the experimental results obtained are very good. Therefore, we are in the process of writing an article to publish this work.

With respect of the work on DC-DC converters there are 5 different lines of continuation, some of them currently ongoing:

- A detailed analysis of the buck-boost transition using the high resolution digital PWM module of a DSP to improve both the efficiency and the harmonic contents of the converter variables in this operation mode.
- The design of a small power bidirectional converter plant to test several FPGA -based digital controls.
- The adaptation of the structure to be used in a high voltage power factor correction system. The performances of Si and SiC devices will be investigated.
- The use of the developed module as the building block in the FC-based hybrid 48-V DC bus approaches currently under research.
- The modelling of the discontinuous conduction modes of the converter unidirectional implementation.

Appendix A

Fast Transitions Between Current Control Loops of the Coupled-Inductor Buck-Boost DC-DC Switching Converter

A.1 Abstract

An already published current control strategy for the coupled-inductor buck-boost converter is able to change its aim from regulating the input current to regulate the output current, and viceversa, depending on the converter operation point and the applied current references. Its two-PI-based implementation main drawback is the slow transients that occur at the control objective alternation points. Due to the magnetic coupling, the converter control-to-input and control-to-output current small signal transfer functions exhibit similar first-order-like characteristics, which has made it possible to improve the previous implementation to a single-PI based one that exhibits faster and, in some occasions, much faster transitions between input and output current regulation operation. The experiments show also that the steady-state behavior of the converter is not affected by the new control implementation.

A.2 Introduction

In distributed power generation systems, such as photovoltaic (PV) and fuel cell (FC) based power supply systems, dc-dc converters are interconnected between two voltage-like sources. The primary

task of these converters is to control the input and the output currents because, in order to assure safe and reliable operation of the FC or PV systems, their currents must have appropriate ripples and dynamics. Using the novel converter topology studied in [82] whose input and output current control loops were designed in [2], the output voltage can be regulated above and/or below its input voltage with high efficiency and wide bandwidth. We foresee that the converter can be used to transfer energy between unregulated voltage sources, limiting the input and output powers with a single and compact converter structure and with relatively simple controls like the one presented in [2]. A version of the average current control method has been used in order to regulate the currents [86], [90], and [89].

As it was already recognized in [2], the slow transition responses in the alternations between the two current-loops is the main drawback of the converter dynamic behavior. This disertation presents a procedure that allows to reduce the transition durations, which results in a dynamics improvement. In Section A.3, the buck-boost dc-dc converter with coupled-inductors is analyzed by means of the state-space averaging method [68] in order to obtain the control-to-input-current and control-to-output-current small-signal transfer functions. Based on the obtained small-signal models, the design of the control-loop compensators are studied in Section A.4. Section A.5 is dedicated to the experimental verification of both the initial and the improved control strategies. A purpose-built 800-W power stage and its two different control boards have been built and tested. Finally, the conclusions of this appendix are in Section A.6.

A.3 Analysis of the coupled inductors Buck-Boost Converter

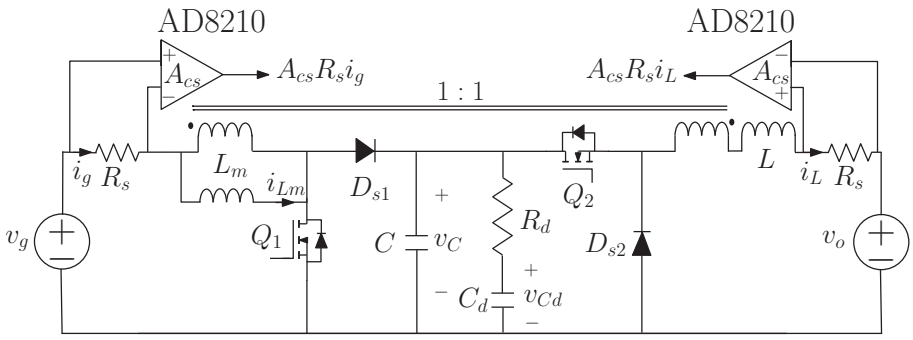

Figure A-1: Schematic circuit diagram of the buck-boost converter with magnetic coupling between inductors and damping network R_dC_d.

Let us consider the unidirectional buck-boost converter with magnetic coupling between the input and output inductors, *RC* type damping network, current sense amplifiers of A_{cs} gain, current sense resistors of R_s value, and coupled inductors turns ratio 1:1 shown in Fig. A-1. For the analysis of the converter it is assumed that the input-voltage v_g and the output-voltage v_o are voltage sources

such as fuel cells, batteries, supercapacitors and regulated DC buses. Therefore, our primary focus in the converter analysis is the control of its input and/or output current. Assuming a continuous conduction mode (CCM) of operation, no parasitic effects, and a switching frequency much higher than the converter natural frequency, the use of the state space averaging (SSA) method [68] to model the converter leads to the following set of differential equations

$$\begin{aligned}
\frac{d\bar{i}_{L_m}(t)}{dt} &= \frac{v_g(t) - \overline{v}_C(t)(1-d_1(t))}{L_m} \\
\frac{d\bar{i}_L(t)}{dt} &= \frac{\overline{v}_C(t)d_2(t) + v_g(t) - \overline{v}_C(t)(1-d_1(t)) - v_o(t)}{L} \\
\frac{d\overline{v}_C(t)}{dt} &= \frac{-\bar{i}_L(t)d_2(t) + (\bar{i}_{L_m}(t) + \bar{i}_L(t))(1-d_1(t))}{C} \\
&\quad - \frac{\overline{v}_C(t) - \overline{v}_{C_d}(t)}{CR_d} \\
\frac{d\overline{v}_{C_d}(t)}{dt} &= \frac{\overline{v}_C(t) - \overline{v}_{C_d}(t)}{C_dR_d}
\end{aligned} \tag{A.1}$$

where d_1 and d_2 are the duty cycles of the switches Q_1 and Q_2, respectively, and the overline stands for averaging during one switching period. Assuming that the converter is in steady-state with constant duty cycles $d_1(t) = D_1$ and $d_2(t) = D_2$, input-voltage $v_g(t) = V_g$, and output-voltage $v_o(t) = V_o$, the operation point of the converter is obtained as $I_{L_m} = \frac{P_g(D_2+D_1-1)}{V_gD_2}$, $I_L = \frac{P_g(1-D_1)}{V_gD_2}$, and $V_C = V_{C_d} = \frac{V_g}{1-D_1}$. Where P_g is the average input-power given by $P_g = V_gI_g = V_g(I_{Lm} + I_L)$. Linearizing (A.1) around the equilibrium point described above leads to Laplace-domain control-to-input-current and control-to-output-current transfer functions for both duty cycles $\widehat{d}_1(s)$ and $\widehat{d}_2(s)$ from the small-signal SSA model. The frequency responses of the control-to-input-current small-signal transfer function in boost mode $G_{i_gd_1}(s) \equiv \left.\frac{\widehat{i}_g(s)}{\widehat{d}_1(s)}\right|_{D_2=1}$, and in buck mode $G_{i_gd_2}(s) \equiv \left.\frac{\widehat{i}_g(s)}{\widehat{d}_2(s)}\right|_{D_1=0}$ evaluated with the components values of the Table A.1 are shown in Fig. A-2. Similarly, the frequency responses of the control-to-output-current small-signal transfer function in boost mode $G_{i_Ld_1}(s) \equiv \left.\frac{\widehat{i}_L(s)}{\widehat{d}_1(s)}\right|_{D_2=1}$ and in buck mode $G_{i_Ld_2}(s) \equiv \left.\frac{\widehat{i}_L(s)}{\widehat{d}_2(s)}\right|_{D_1=0}$ are presented in Fig. A-3. For a more detailed study of the small-signal transfer coefficients functions please refer to [2].

Table A.1: Components of buck-boost converter

Component	**Description**	**Value**
L_m	Coupled inductors	35 μH
C	Ceramic Capacitor	7 μF
L	Inductor	35 μH
R_d	Damping Resistor	1.5 Ω, 4 W
C_d	MKT Capacitor	66 μF

Each of the transfer functions are studied in their respective mode and also at the border between the two modes of operation, which is named the buck-boost mode [82, 2]. Several Bode plots

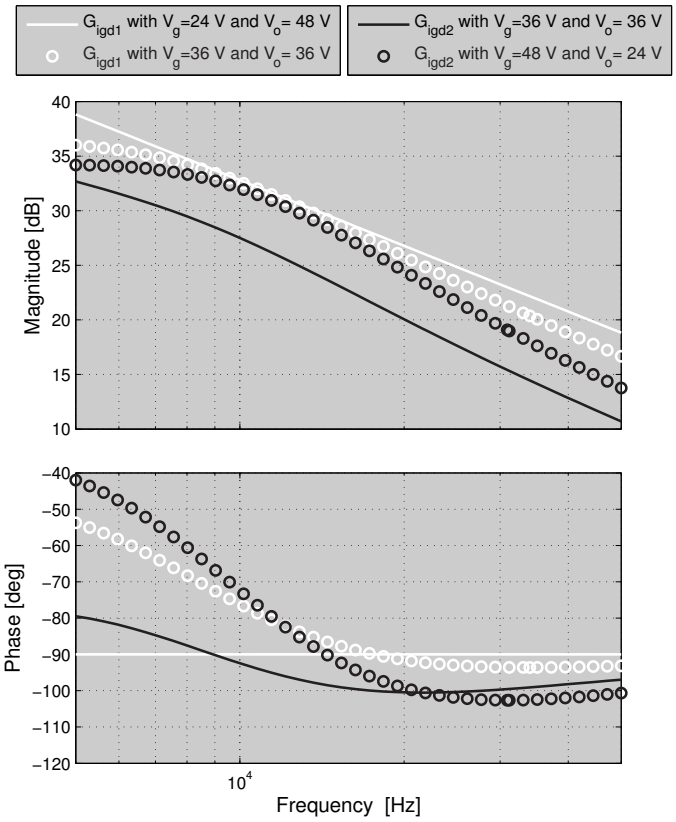

Figure A-2: Frequency responses of the small-signal control-to-input-current transfer functions $G_{i_g d_1}(s)$ and $G_{i_g d_2}(s)$ for $P_g = 384$ W and operation voltages that correspond to boost, lower-border boost, upper-border buck and buck modes.

of the frequency responses obtained from MATLAB simulations of the linear small-signal model corresponding to different operations modes are superimposed in Figs. A-2 and A-3, where the maximum plotted frequency is 50 kHz, which correspond to half of the switching frequency. Although the small-signal transfer functions $G_{i_g d_1}(s)$, $G_{i_g d_2}(s)$, $G_{i_L d_1}(s)$, and $G_{i_L d_2}(s)$ correspond to a high order system, at high frequency [2], they present roughly first-order low-pass characteristics with magnitude slopes of about -20 dB per decade and phase angles approaching $-90°$ as is illustrated in Figs. A-2 and A-3. The presence of zeros in the right half-plane is discarded because they would have caused additional large phase drops that have not been detected in the figures. Therefore, the design criteria proposed in [82] makes it possible to design wide bandwidth and high phase margin current loops for the buck-boost converter that regulate the input or/and output current in all modes of operation.

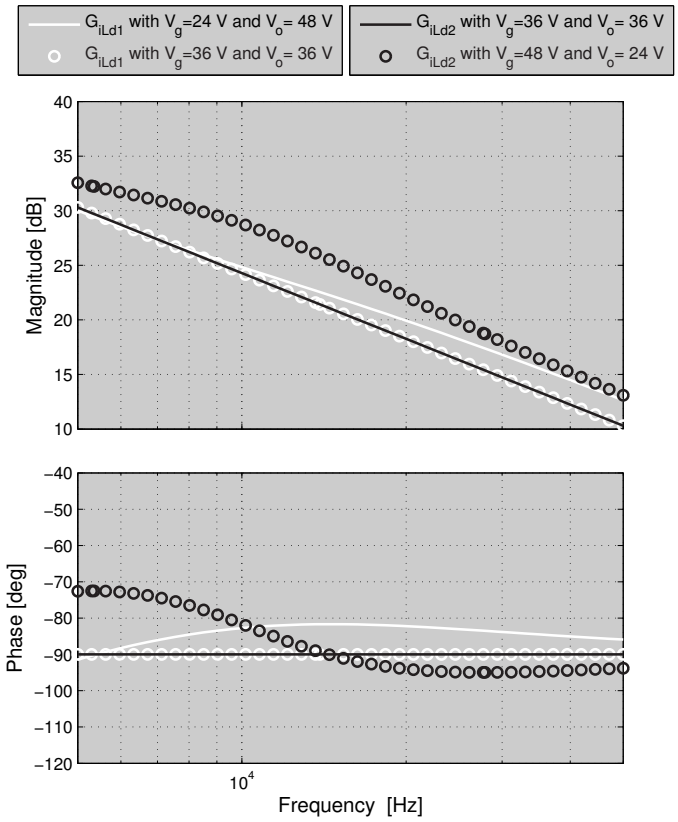

Figure A-3: Frequency responses of the small-signal control-to-output-current transfer functions $G_{i_L d_1}(s)$ and $G_{i_L d_2}(s)$ for $P_g = 384$ W and operation voltages that correspond to boost, lower-border boost, upper-border buck and buck modes.

A.4 Average Current-Mode Control of a Coupled Inductor Buck-Boost DC-DC Switching Converter

Now that the the small-signal transfer functions have been studied, the next step is to design the control loop compensators. The current loop compensator is designed using a lag network with a high frequency pole [90]. In [89], it is recommended to place the high frequency pole between one-third and one-half of the switching frequency to attenuate switching noise while in [86] it is recommended to locate this pole above half of the switching frequency. The intersection of both criteria requires the high frequency pole to be placed at half of the switching frequency. The low frequency pole of the compensator has been placed at the origin to eliminate the steady-state error [70]. The zero should be placed at least one decade below half the switching frequency according to the design guidelines proposed in [86]. Hence, the zero was placed at a tenth of the high frequency pole. Finally, the gains of both compensators were adjusted experimentally for the worst case of the frequency responses of the small-signal control-to-input/output current transfer functions of Figs. A-2 and A-3 to ensure wide bandwidth and a minimum phase margin of 45^o. The second order

compensator transfer function of the input-current loop is

$$G_{cg}(s) = K_1 \frac{(\tau_2 s + 1)}{s(\tau_1 s + 1)} \tag{A.2}$$

where the compensator parameters have been selected as follows: $\tau_1 = 3.3$ μs, $\tau_2 = 33$ μs, and $K_1 = 590$ s/A. The switching frequency f_s is 100 kHz and the corresponding switching period T_s is 10 μs. The output-current loop compensator transfer function is

$$G_{cL}(s) = K_2 \frac{(\tau_2 s + 1)}{s(\tau_1 s + 1)} \tag{A.3}$$

where $K_2 = 1298$ s/A.

In [2] a manner to combine the two current loops (A.2) and (A.3) so that, in steady-state, one of the currents is smaller than the input reference while the other, regulated by the active loop, is equal to the input reference is described. Thus, the maximum average value of each current is limited by its reference input as shown in Fig. A-4. Combining both current loops in this way is a simple technique although if there is a transition between current control loops occurs, it is slow because the PI for the loop not regulating the converter winds-up. One technique that can be used to achieve fast transitions between control loops is pre-charging the capacitors of the current-control integrators [92]. A simpler way to obtain fast transitions between control loops for this converter is to take advantage of the similarity between the transfer functions (A.2) and (A.3) to use a single PI as presented in Fig. A-5. This is an additional advantage to those already studied in previous papers of this converter [82, 2]. The new proposed control has the same behavior as the one presented in [2] but with the advantage of the possibility to perform faster transitions between control loops.

The dual PWM block presented in the Fig. A-4 is generated using the equations

$$\widehat{d}_1(t) = \begin{cases} 0 & if \quad U < 1 \\ \\ \widehat{u}(t) & if \quad U \geq 1 \end{cases} \tag{A.4}$$

$$\widehat{d}_2(t) = \begin{cases} \widehat{u}(t) & if \quad U \leq 1 \\ \\ 0 & if \quad U > 1. \end{cases} \tag{A.5}$$

where $u(t)$ is the single continuous control variable with small signal variation $\widehat{u}(t)$ and steady-state U widely described in [82, 2].

Fig. A-6 shows the final scheme of the buck-boost regulator that implemented the block diagram illustrated in Fig. A-4. Diodes D_A and D_B enable the two current loops to be combined so that,

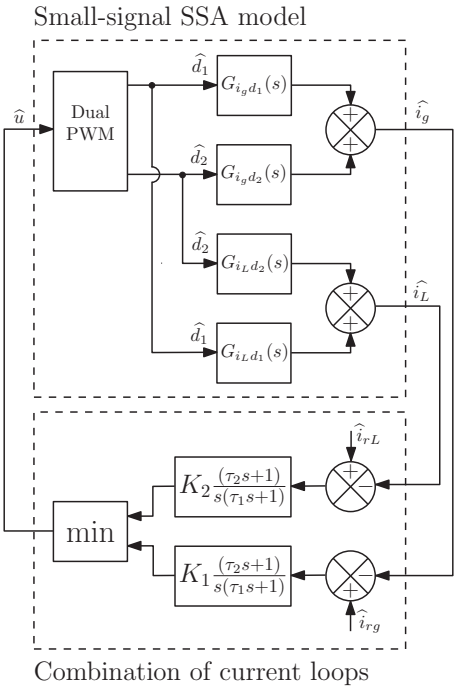

Figure A-4: Small-signal block diagram of the converter and the interaction between current loops presented in [2]. i_{rL} and i_{rg} are the small-signal variations of the output and input current references, respectively. The rest of the variables are described in the text.

in steady-state, one of the currents is smaller than the input reference while the other, regulated by the active loop, is equal to the input reference. Thus, the maximum average value of each current is limited by its reference input. The dual PWM controller integrated circuit TL1451A generates the switch activation signals $u_1(t)$ and $u_2(t)$. This circuit has two error amplifiers, an adjustable oscillator and dual common-emitter output transistor circuits. The triangular signal oscillator has been adjusted to a frequency of 100 kHz, an amplitude of $V_{pp} = 0.7$ V and a DC offset of 1.4 V. Therefore, the forward voltage drop of D_C must be approximately V_{pp} to obtain the control signals v_{c1} and v_{c2}, as illustrated in Fig. A-6. The variable resistor R_8 makes it possible to adjust the

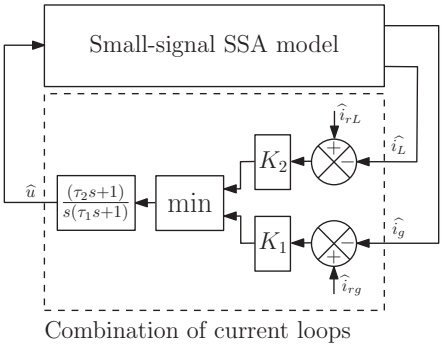

Figure A-5: Small-signal block diagram of the converter and the interaction between current loops presented in this work.

overlapping zone in the buck-boost mode [82, 2].

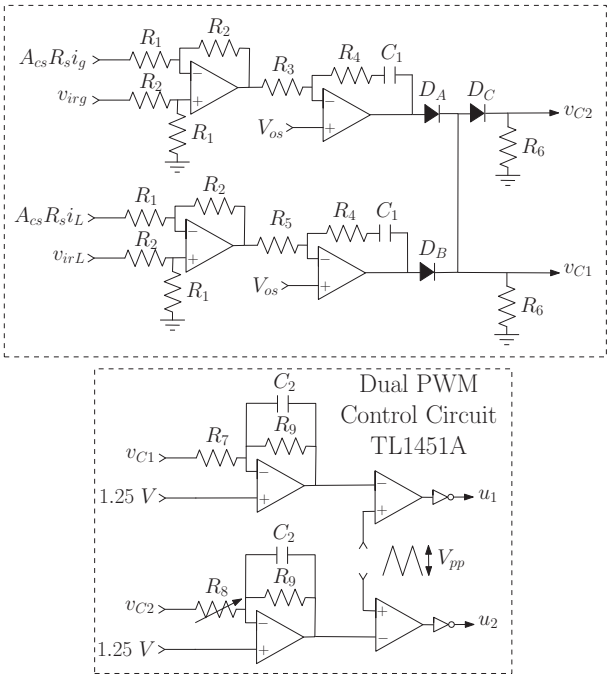

Figure A-6: Proposed simplified circuital scheme of the input and output current loop compensators of the block diagram illustrated in Fig. A-4 by the buck-boost converter presented in Fig. A-1.

The steady-state relationship between the current sensed and their references are presented in the following equations

$$\begin{aligned} V_{irg} &= V_{os} + \frac{I_g A_{cs} R_s R_2}{R_1} \\ V_{irL} &= V_{os} + \frac{I_L A_{cs} R_s R_2}{R_1}. \end{aligned} \tag{A.6}$$

Fig. A-7 presents the final scheme of the fast buck-boost regulator that implements the block diagram illustrated in Fig. A-5 using the same dual PWM generator shown in Fig. A-6. The operation of this new scheme is quite similar to the Fig. A-6 one but with the difference that it only uses one PI. The voltage drop in D_C is added to the voltage reference V_{os} to compensate for the voltage drops in D_A or D_B. In small-signal the circuit schemes of the Figs. A-6 and A-7 corresponds to the block diagrams of Figs. A-4 and A-5, respectively.

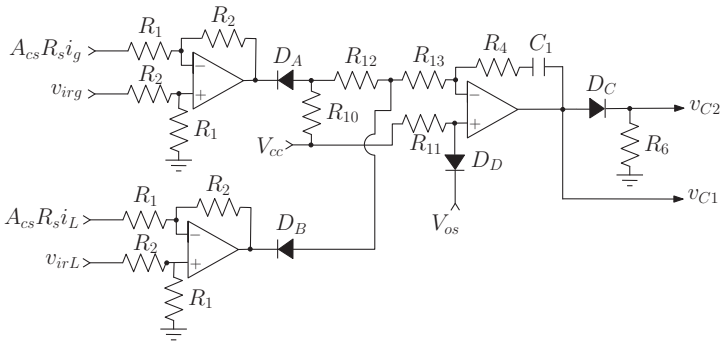

Figure A-7: Proposed simplified circuital scheme of the input and output current loop compensators of the block diagram illustrated in Fig. A-5 by the buck-boost converter presented in Fig. A-1 and using the dual PWM scheme shown in Fig. A-6.

A.5 Experimental results

To validate the controllers presented in the previous section, a prototype of the coupled-inductor buck-boost converter depicted in Fig. A-8(a) with the input and output current controllers of Figs. A-8(b) and A-8(b) has been developed and tested.

Fig. A-9 shows the experimental setup for measuring the time delays in the alternations between loops of both control schemes. In Fig. A-10, the experimental characteristic of the transitions between current loops using two PI regulators are presented, while Fig. A-11 shows the same experiment but using the fast current control with a single PI described in Figs. A-7.

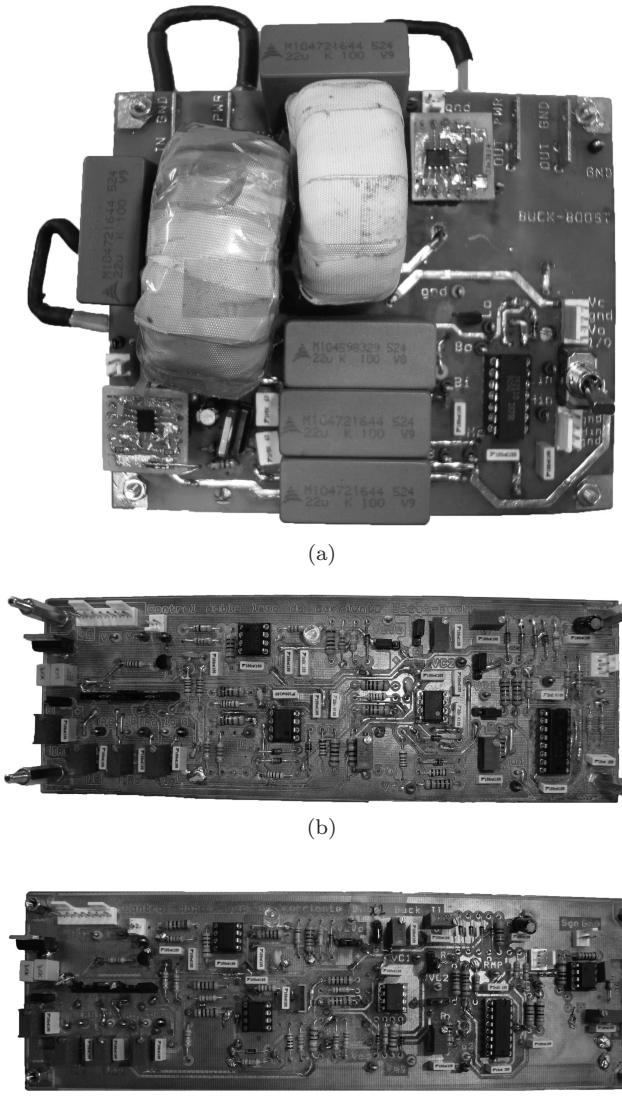

(a)

(b)

(c)

Figure A-8: Regulator prototype: (a) buck-boost power stage, (b) average current-mode control board with two PI, (c) fast average current-mode control board.

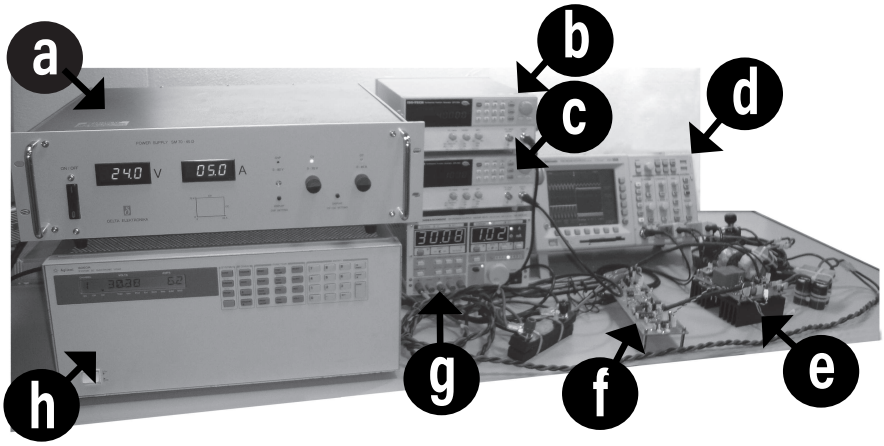

Figure A-9: Experimental configuration for testing the transitions between control loops: (a) DC power supply of the input voltage v_g, (b) input current reference signal generator, (c) output current reference signal, (d) oscilloscope, (e) buck-boost converter, (c) buck-boost current control, (g) DC power supply, (h) DC electronic load in constant voltage mode in parallel with g to emulate a voltage source-like load.

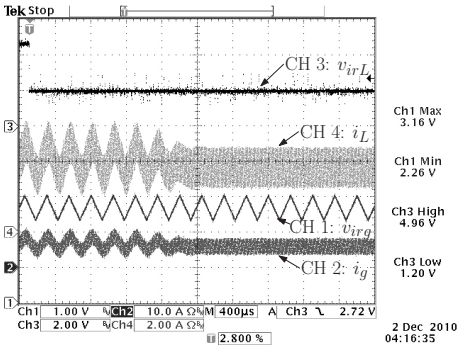

(a)

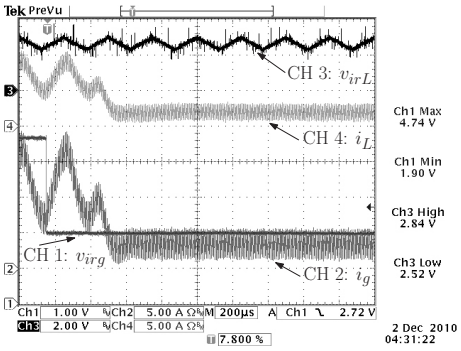

(b)

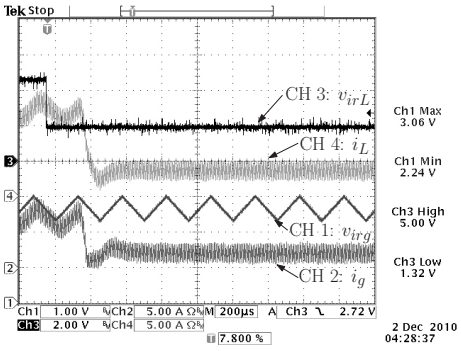

(c)

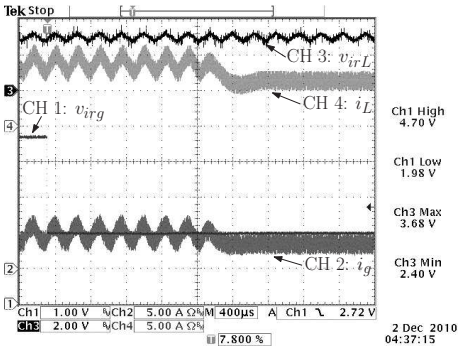

(d)

Figure A-10: Transitions between current control loops using two different input references. The first reference is a 4 kHz triangular waveform to ensure variations in the average value of one of the currents and the second reference is a 100 Hz square waveform that provides variations in the other current. Boost mode with $V_g = 32$ V, $V_o = 48$ V: (a) triangular waveform in v_{irg} and square waveform in v_{irL}, (b) square waveform in v_{irg} and triangular waveform in v_{irL}. Buck mode with $V_g = 48$ V, $V_o = 24$ V: (c) triangular waveform in v_{irg} and square waveform in v_{irL}, (d) square waveform in v_{irg} and triangular waveform in v_{irL}.

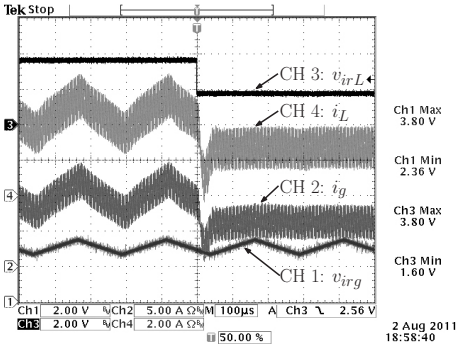

(a)

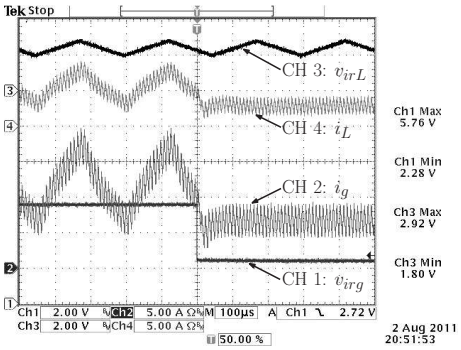

(b)

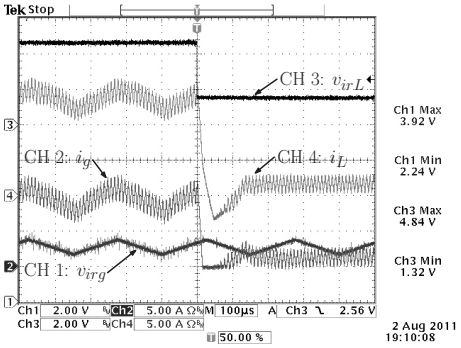

(c)

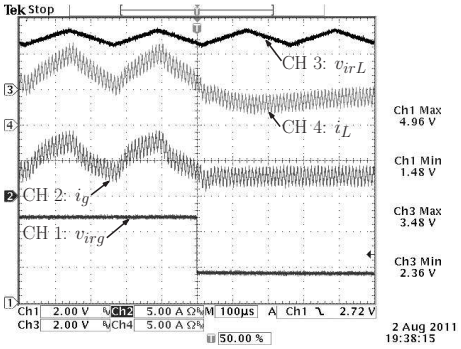

(d)

Figure A-11: Fast transitions between current control loops using two different input references. The experimental conditions, and the figures and variables plotted are the same of Fig. A-10.

The time delays of the experiments are summarized in Table A.2. The table clearly shows that the proposed control with a single PI ensures a faster transition in all operation modes in comparison with the two-PI control scheme recently published.

Table A.2: Time delay between control loops.

Operation mode	**Input-current reference waveform**	**Output-current reference waveform**	**Two PI control delay**	**Fast control delay**
boost	triangular	square	1.92 ms 192 T_s	40 μs 4 T_s
boost	square	triangular	0.44 ms 44 T_s	70 μs 7 T_s
buck	triangular	square	0.45 ms 45 T_s	160 μs 16 T_s
buck	square	triangular	2.08 ms 208 T_s	50 μs 5 T_s

A.6 Conclusion and future works

An improved version of the current control scheme for the coupled-inductor buck-boost DC-DC switching converter has been proposed and tested. With the new fast scheme, the control system is able to switch from regulating the converter input current to regulate its output current, or viceversa, in a shorter time. In the experiments, the durations of the transitions have been reduced between a factor of almost three to up to forty eight times.

Appendix B

Virtual instrument for the characterization of inductors at different operation points

B.1 Abstract

A virtual instrument for inductance characterization at different operation points is presented in this appendix. The parameters obtained from the characterization of inductors using the virtual instrument allows to make more realistic simulations and thus obtain better converter designs before making them. The reports generated by the virtual instrument of the analyzed inductor will allow to create a database to facilitate the search of the most appropriate inductor according to a desired parameter and operation point. The virtual instrument was developed using LabVIEW and this permits to control an inductance analyzer and a DC current source both of QuadTech manufacturer through GPIB communication. By controlling these two instruments, it is possible to estimate the parameters of different mathematic models of the tested inductor as a function of the DC current and the frequency operation. The analyzed inductors are components used principally for the manufacture of DC-DC converters. If the DC-DC converter control operates at constant frequency, such as those using a PWM control, it is necessary to obtain an inductor model as a function of the different operation points of the DC current at the control switching frequency. On the other hand, if the control that uses the DC-DC converter has a variable frequency like when a sliding mode control is used, it is necessary to know the inductor model as a function of the frequency and DC current of operation. In both cases the virtual instrument is a powerful tool to obtain the model that satisfies the requirements of the converter control. The experimental results presented

in this appendix and the good agreement between the experimental and simulated results presented in Chapters 2 and 3 validate the advantages of the virtual instrument.

B.2 Introduction

The use of power electronic circuits has been increasing significantly in the last decade, due to the advances in power semiconductors and also because the required electronic devices have become more sophisticated. One of the main applications of power electronics is the design and manufacture of switching converters, which have become a vital element for the transformation of AC or DC energy from renewable sources at market values.

The main drawback in the experimental validation of a converter is to build a prototype with the component values corresponding with the ones used in the previous simulations. This is because the selection of the values of the elements is a little different from those found in the laboratory, which leads to differences between the designed and the real device. Another problem is that the values of certain elements are not commercial and the designer must build the device himself, as in the case of many inductors.

Usually for the construction of an inductor the designer has a program provided by the cores manufacturer, that can estimate the number of turns and the wire size according to the full load inductance, the DC current, the ripple current, the frequency, the temperature, the selected core, and other parameters. A disadvantage of this methodology is that the value of the wire size is designed with a solid wire or single-strand wire. At high frequencies, the current tends to flow along the surface of the conductor, known as the skin effect, resulting of the increased power loss in the wire. Stranded wire with an equivalent area reduces this effect, but this other type of wire changes the inductance value to the one designed by the manufacturer's core program. Another disadvantage of this procedure is the determination of the inductance value of an inductor already manufactured and whose technical characteristics of construction are unknown. Finally, this methodology can only be used on cores provided by the manufacturer. Another alternative is to measure the inductance with a handheld LCR meter but its measurement is at a constant frequency and at very low current, when in fact the inductor is designed for a very different operation point and that is the reason why the value provided by this device differs from the operating value of the inductor. In order to characterize different already built inductors, improve the designs and make more realistic simulations of the converters, a virtual instrument to characterize inductors was designed.

The remainder of this appendix is organized as follows. Section B.3 describes the components that constitute the virtual instrument. Section B.4 provides a detailed description of the program

developed in LabVIEW to control the virtual instrument. Finally, the last two sections present the experimental results, and the conclusions of this appendix.

B.3 Components of the instrumentation system

A virtual instrument consists of an industry-standard computer or workstation equipped with powerful application software, cost-effective hardware such as plug-in boards, and driver software, which together perform the functions of traditional instruments [172]. Virtual instruments represent a fundamental shift away from traditional hardware-centered instrumentation systems towards software-centered systems that exploit the computing power, productivity, display, and connectivity capabilities of popular desktop computers and workstations [172, 173, 174].

The software is the most important component of a virtual instrument. With the right software tool, it is possible to create an appropriate user interface that permits an easy handling of the application. This software can define the acquisition control, the mathematical processing, the storage and report of the signals and display the results to the user [172]. The virtual instrument was developed with LabVIEW software. This software is based on a graphical programming environment with object-oriented programming [175]. LabVIEW allows the construction of data acquisition systems, instrumentation, control and test [176]. The hardware that conforms the virtual instrument is composed of an desktop computer, GPIB connectors, an inductance analyzer and a source of bias current as illustrated in Figure B-6.

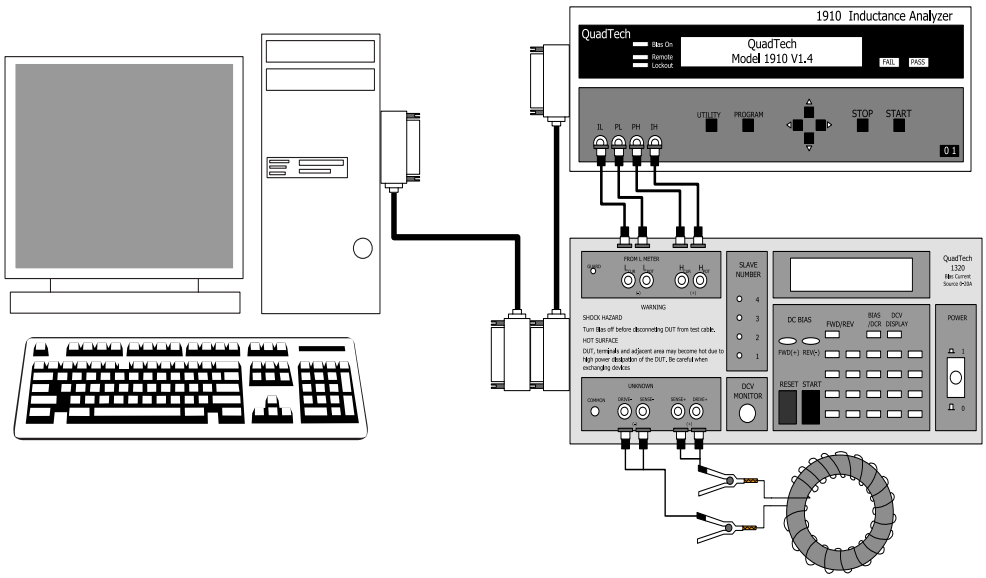

Figure B-1: Device interconnection scheme of the virtual instrument.

The original GPIB was developed in the late 1960s by Hewlett-Packard (called the HP-IB) to connect and control programmable instruments that Hewlett-Packard manufactured. With the introduction of digital controllers and programmable test equipment, it was necessary to create a communication standard with a high-speed data transfer that permits the communication between instruments and controllers from different manufacturers [177]. In 1975, the Institute of Electrical and Electronic Engineers (IEEE) published ANSI/IEEE Standard 488-1975, the IEEE Standard Digital Interface for Programmable Instrumentation, which contained the electrical, mechanical, and functional specifications of an interfacing system [178, 179]. The original IEEE 488-1975 was revised in 1978, primarily for editorial clarification and addendum [180, 181]. This bus is now used worldwide and it is known by three names: General Purpose Interface Bus (GPIB), Hewlett-Packard Interface Bus (HP-IB) and IEEE 488 Bus, because the original IEEE 488 document did not contain any guidelines for a preferred syntax or format conventions [177].

The following subsections provide a brief description of the equipments used by the virtual instrument to determinate the inductor model at different operation points.

B.3.1 Inductance Analyzer

The used inductance analyzer was the 1910 of the manufacturer QuadTech. It is designed to perform inductance and impedance measurements on coils and wire wound devices in a frequency range between 20 Hz and 1 MHz [182]. This device has the following standard interfaces: an IEEE-488.2, a RS-232 Handler and a serial printer. The analyzer has a wide range of measures as listed in Table B.1 and a good accuracy as presented in Table B.2. An impedance that is neither a pure resistance nor a pure reactance can be represented at any specific frequency by either a series or a parallel combination of resistance and reactance. Such a representation is called an equivalent circuit. The value of the primary measurement of a device depends on which equivalent circuit, series or parallel, is chosen to represent it. The equivalent circuit to model inductors that is most commonly used is a series RL network. However, the virtual instrument can analyze other equivalent circuits as a parallel RL network or any combination of impedances presented in Table B.1.

Table B.1: Parameter measurement range of the 1910 inductance analyzer

Parameter	Measurement range
Inductance (L)	0.001nH to 99.999H
Capacitance (C)	1 pF to 9.9999 F
Dissipation factor (DF)	0.00001 to 99.999
Quality factor (Q)	0.00000 to 9999.9
Admittance ($\|Y\|$), Conductance (Gp) , Susceptance (Bp)	10 nS to 9999.9 S
Impedance ($\|Z\|$), Resistance (R), Reactance (Xs), Equivalent series resistance (ESR)	0.0001 mΩ to 99.999 MΩ
Phase angle	-180.00°to +179.99°

Table B.2: Accuracy parameter measure of the 1910 inductance analyzer

Parameter	Fast speed	Medium speed	Low speed
Inductance (L)	±0.5%	±0.25%	±0.1%
Capacitance (C)	±0.5%	±0.25%	±0.1%
Dissipation factor (DF)	±0.005%	±0.0025%	±0.001%
Quality factor (Q)	±0.005%	±0.0025%	±0.001%
Admittance ($\|Y\|$), Conductance (Gp) , Susceptance (Bp)	±0.005%	±0.0025%	±0.001%
Impedance ($\|Z\|$), Resistance (R), Reactance (Xs), Equivalent series resistance (ESR)	±0.5%	±0.25%	±0.1%
Phase angle	±1.8°	±0.9°	±0.18°

B.3.2 Bias Current Source

The 1320 Bias Current Source is a programmable DC current source and DCR meter for the production and laboratory testing of inductors [183]. The 1320 Bias Current Source provides 0-20 A DC Bias and measures external resistance (DCR). A maximum of 5 units can be connected in parallel to obtain 100 A of DC Bias Current. The accuracy and resolution of the bias current output for different operation ranges are listed in Table B.1. The 1320 instrument is connected to the 1910 inductance analyzer using 4 BNC to BNC cables (1320-03). The set of 2 Binding Posts and 2 BNC terminals labeled UNKNOWN are connected to the DUT using the 1320-01 cable lead set. The DC Bias current is selectable as forward or reverse and is programmable from 20.0 A to 20.0 A. Test conditions are stored and recalled from 50 internal memory locations. The 1320 instrument also has the capability of performing up to 21 steps (tests) in any one test setup. An internal timer can be

selected on/off and a delay time from 0-100 seconds can be programmed for any test [183]. Current Output Mode is selectable as single, multiple manual or multiple automatic for multi-point current inductance testing. Standard rear panel interfaces, for remote operation or communication with other instrumentation, include an LCR Link, a Slave Link, an IEEE-488 interface and a Handler interface. Up to 30 IEEE-488 addresses are programmable.

Table B.3: Main features of the 1320 Bias Current Source.

Bias current		
Range	**Accuracy**	**Resolution**
0.000 A - 1.000 A	$\pm[1\% + 3\text{mA}]$	0.001 A
1.010 A - 5.000 A	$\pm 2\%$	0.001 A
5.050 A - 20.000 A	$\pm 3\%$	0.010 A

B.4 Virtual instrument program for the characterization of inductors

The virtual instrument program consists of a main function which is responsible for setting of the two desired parameters that will be measured by the 1910 inductance analyzer. The program uses two nested loops to make changes in the value of the current in the 1320 bias current source and the value of the frequency in the 1910 inductance analyzer. Once the inductor characterization graph has shown each of the parameters it stores all the acquired data. Fig. B-2 shows the block diagram of the main function.

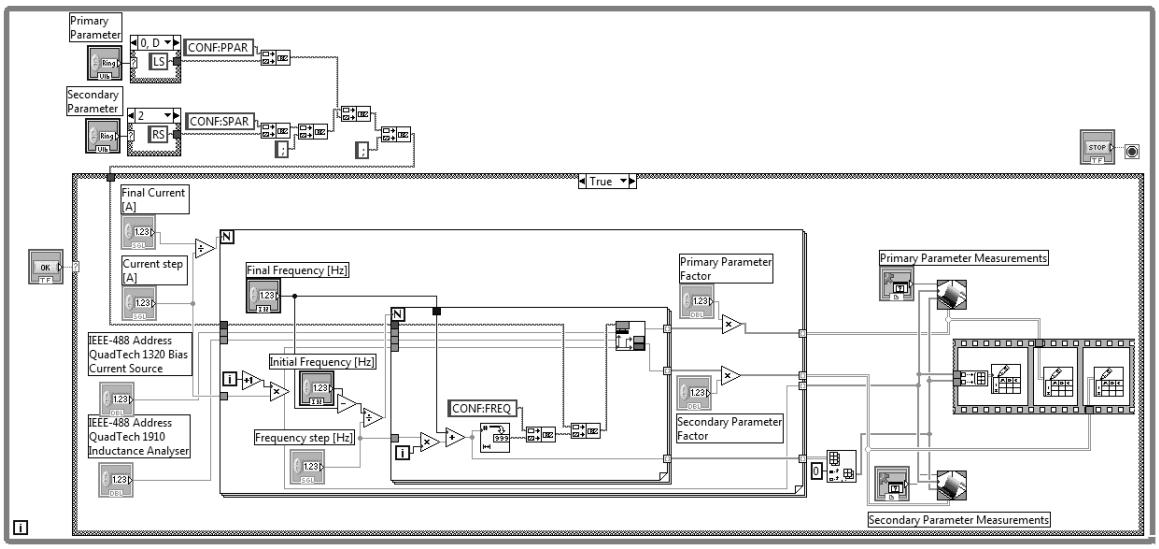

Figure B-2: Block diagram of the main function of the virtual instrument.

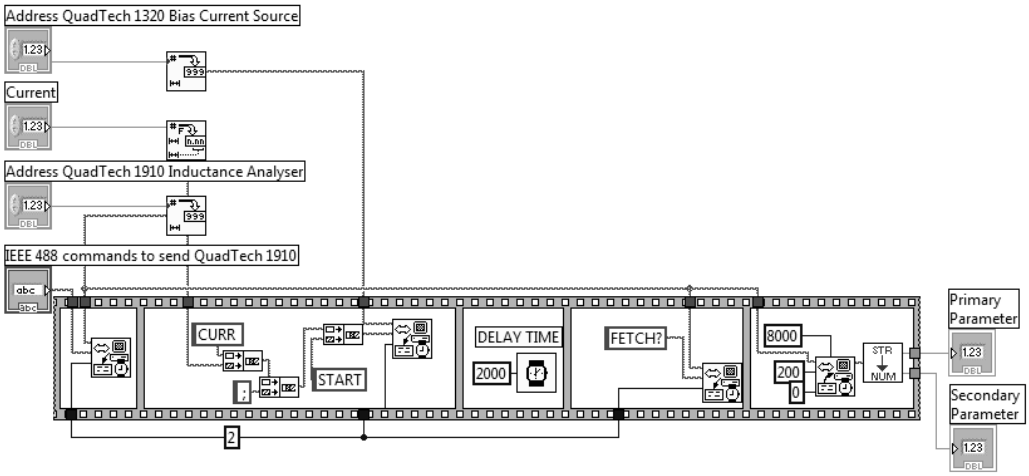

Figure B-3: Block diagram of the subfunction responsible for reading and writing GPIB port presented in Fig. B-2.

Figure B-2 illustrates a subfunction detailed in Fig. B-3 that is called in each iteration of the nested loop and it is responsible for communication between the virtual instrument and the controlled equipment. This subfunction performs a sequence to ensure proper functioning of the equipment to be controlled. The first sequence sends to the inductance analyzer the parameters of the equivalent circuit to be measured and the range of frequency to characterize the inductor. The following sequence sends the DC current value and the activating signal to the 1320 bias current source connected to the inductor. The next step is a delay sequence to warranty that the inductance analyzer acquires the measurements in the steady state current value and so avoid the transient current. The last sequence, waits for the inductance analyzer to sent the measurements which will be converted from string to number format using the subfunction illustrated in Fig. B-4. Finally, the graphical user interface of the virtual instrument for the characterization of inductors developed in LabVIEW is illustrated in Fig. B-5.

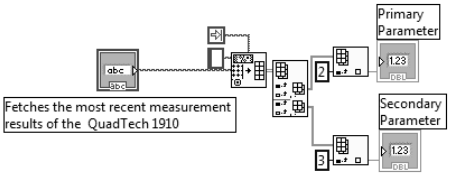

Figure B-4: Block diagram of the subfunction that converts the measurements sent by the analyzer inductances from a text format to a number format.

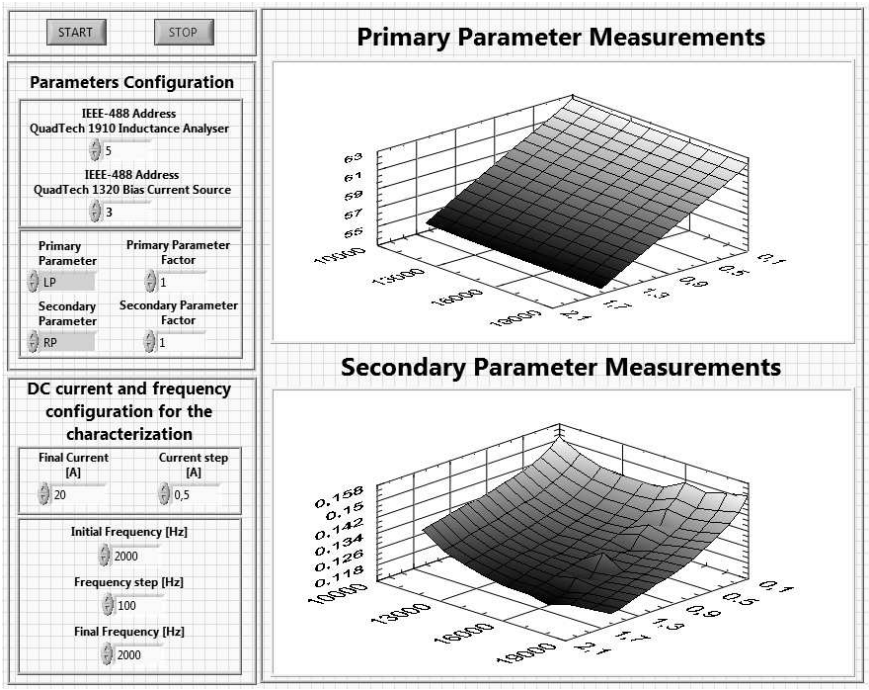

Figure B-5: Graphical user interface of the virtual instrument for the characterization of inductors.

B.5 Experimental results

Fig. B-6 shows the experimental configuration for the measurement of the inductor characteristic at different operation points.
The first test used the 77206-A7 core manufacturer Magnetics and for the design of the inductor the program named *Magnetics Inductor Design Using Powder Cores* provided by the same manufacturer was applied. The inductor was designed to operate at a frequency of 20 kHz, a current of 4.5 A and an inductance at full load of 33 μH. For the input parameters, the Magnetics program established that the inductor should be built with 29 turns of a single-strand wire of an equal area of 18 AWG (American Wire Gauge) as depicted in Figure B-7.

For the inductor built using the virtual instrument the series RL network by different operation points of current and frequency were determined. The current was varying from 0.5 A in increments of 0.5 A to 9 A, while the frequency was differing from 10 kHz to 29 kHz in increments of 1 kHz. Fig. B-8(a) shows the series inductance and Fig. B-8(b) presents the series resistance of the analyzed inductor. The virtual instrument can also produce various 2D curves that result from fixing one of the parameters, current or frequency, and varying the other parameter at all operation points. From Fig. B-8(a), that analyzes the characteristic of the inductor at a frequency of 20 kHz, Figure B-8(c)is obtained.

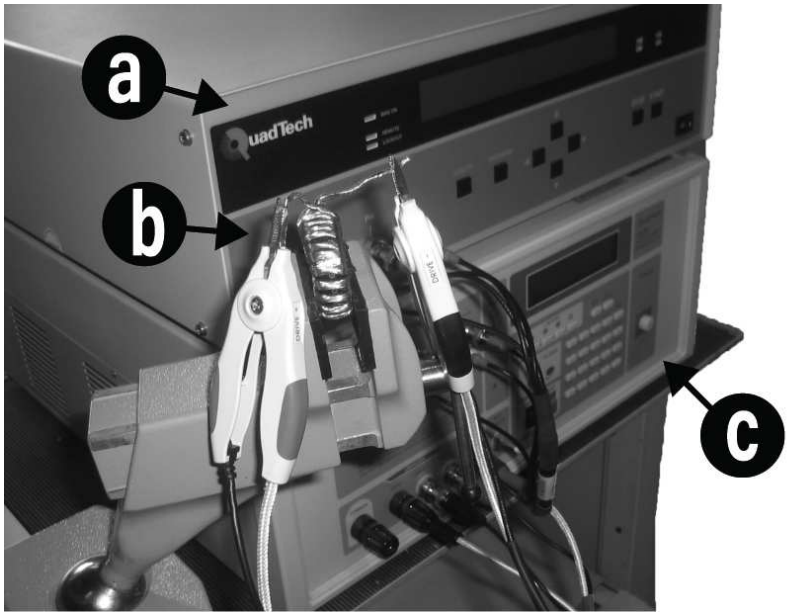

Figure B-6: Experimental configuration of the virtual instrument for the characterization of inductors: (a) 1910 inductance analyzer, (b) inductor being tested, (c) 1320 bias current source.

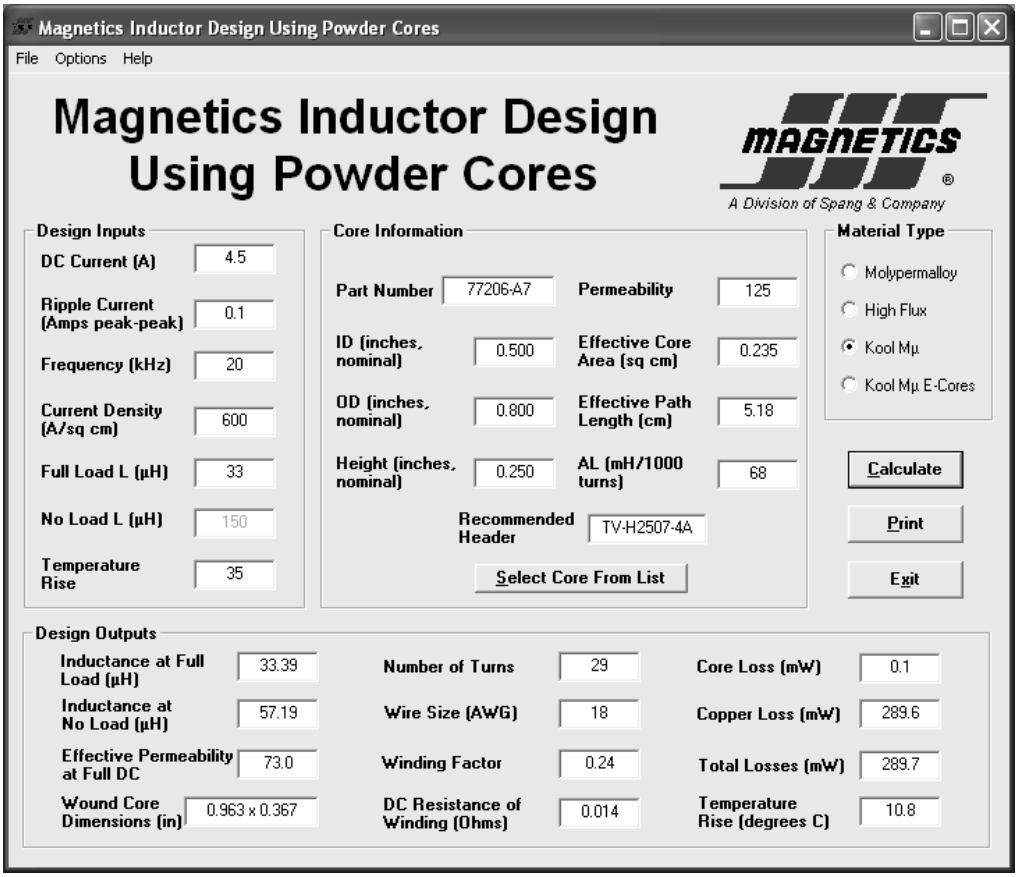

Figure B-7: Result of magnetics program for the design of the 33 μH inductor.

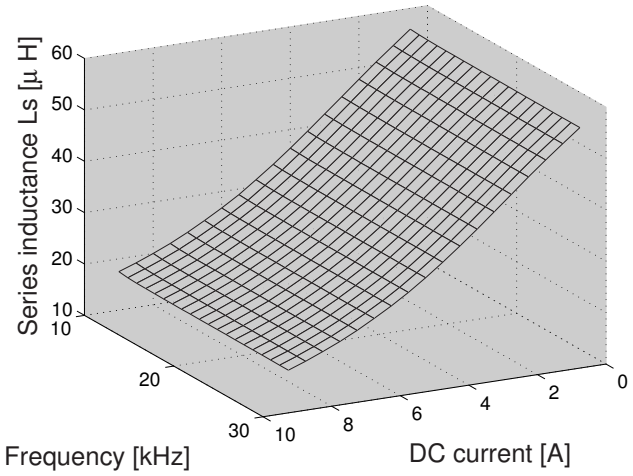

(a)

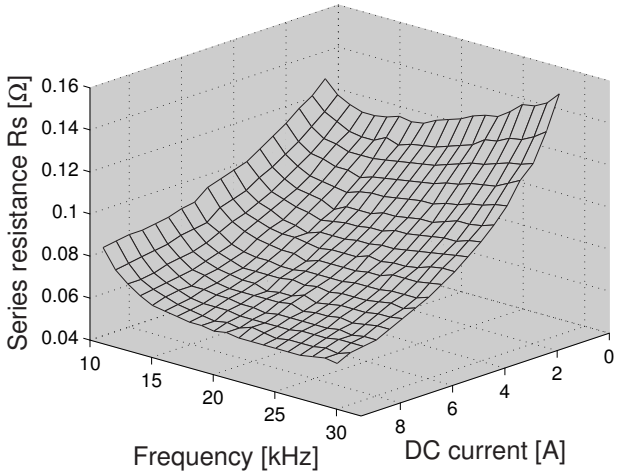

(b)

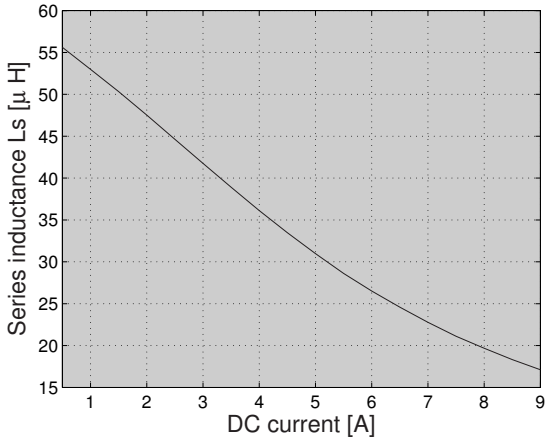

(c)

Figure B-8: Experimental results of the characterization of the 33 μH inductor using a circuit model consisting of a RL network: (a) series inductance, (b) series resistance, (c) series inductance by a constant frequency of 20 kHz.

Fig. B-8(a) shows that for a current of 4.5 A the inductance value is of 33.48 μH. This value is very close to that estimated by the Magnetics program of 33 μH in Fig. B-7, and therefore has a small relative error of 1.43%. The experimental results obtained by the virtual instrument and presented in Fig. B-8 behave as expected, since the series inductance should decrease with increasing current, and series resistance should increase with operation frequency.

A very common practice to make inductors is to use stranded wire to reduce the impact of the skin effect. Fig. B-9 shows a design of the inductor made with the Magnetics program, which determines that for an inductance of 120 μH at a full load of 12 A,it is required for the 77083-A7 core to give 57 turns with a conductor single-strand wire of an area equal to 14 AWG. Instead, the inductor was made using stranded wire with an equivalent size of 14 AWG. The current was varying from 0.5 A in increments of 0.5 A up to 20 A, while the frequency was varying from 10 kHz to 29 kHz in increments of 1 kHz. Fig. B-10(a) shows the series inductance and Fig. B-10(b) presents the series resistance of the analyzed inductor. The virtual instrument can also produce various 2D curves which result from leaving one of the parameters fixed, current or frequency, and varying the other parameter at all operation points. From Fig. B-10(a), which analyzes the characteristic of the inductor at a frequency of 20 kHz, Fig. B-10(c)is obtained. From this figure an inductance value of 165.6 μH was obtained by a current of 12 A. This value differs from the estimated by the Magnetics program of 120 μH in Fig. B-9, and the relative error is therefore significant: 27.54 %. In conclusion, the Magnetics program requires a single-strand wire for the construction of the inductor and substantial differences are obtained with stranded wire. And that is why the virtual instrument becomes a powerful tool for manufacturing and modelling inductors.

The last test analyzes the PE-51 511 toroidal inductor to verify the data provided by the Pulse manufacturer. Figs. B-11(a) and B-11(b) show the RL network series parameters obtained by the virtual instrument for the PE-51511 toroidal inductor. According to the catalog specification, this inductor has an inductance of 43 μH for a current of 10 A and an operating frequency ranging from 20 kHz to 50 kHz, but as shown in Figure B-11(c) the inductance values do not match with the values given by the manufacturer. Once again, it has been shown how important it is to characterize elements well so that the virtual instrument that designs simulations can more closely mirror experimental results.

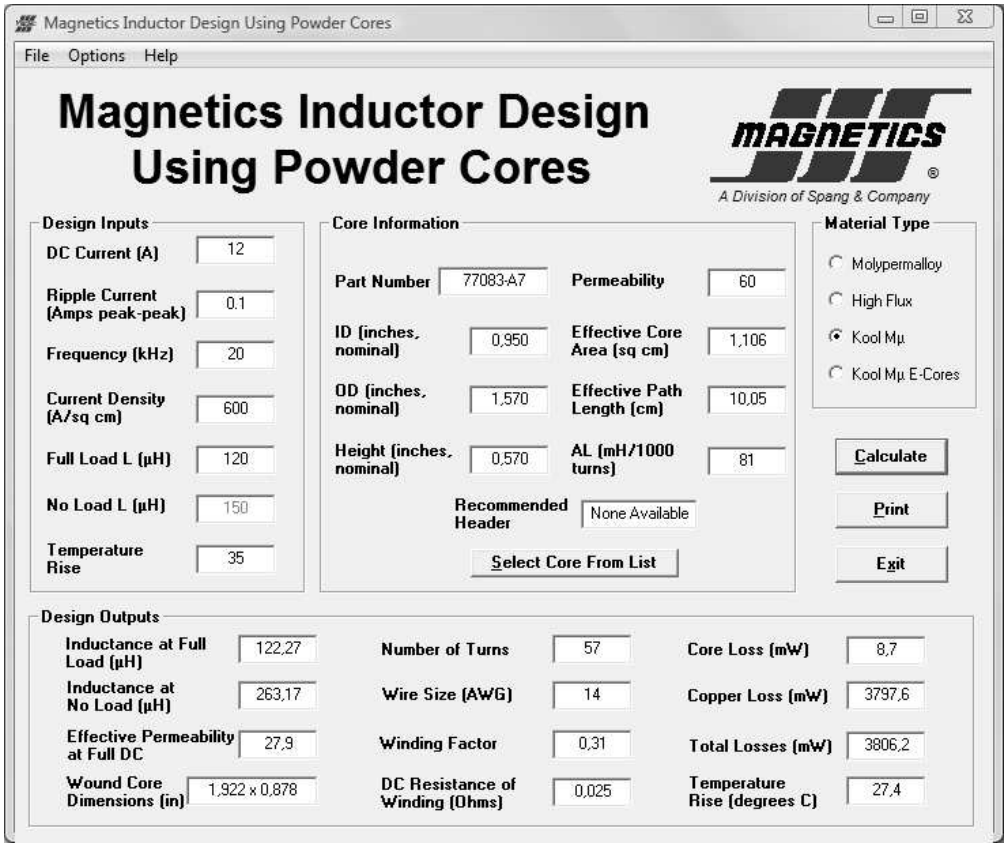

Figure B-9: Result of magnetics program for the design of the 120 μH inductor.

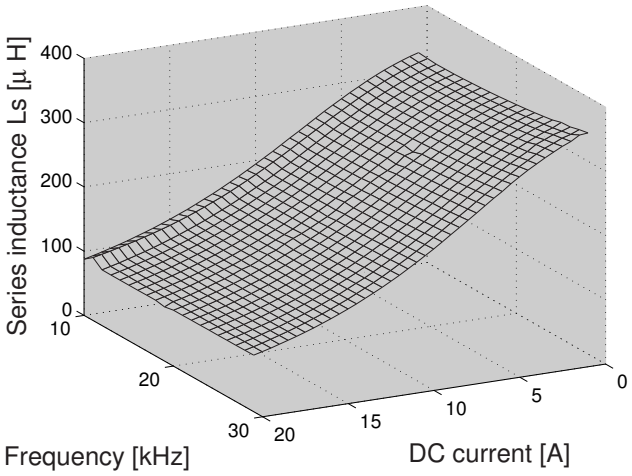

(a)

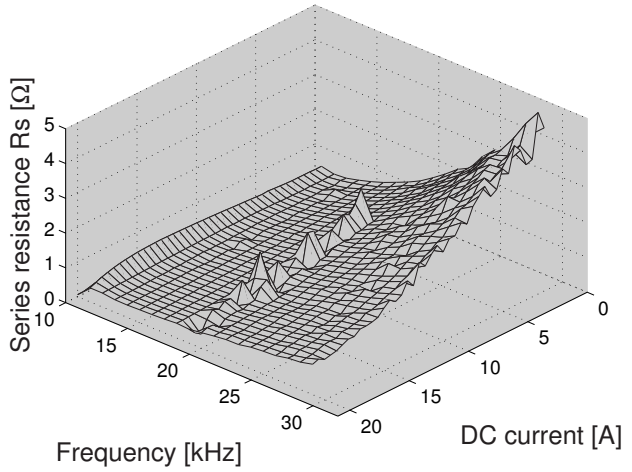

(b)

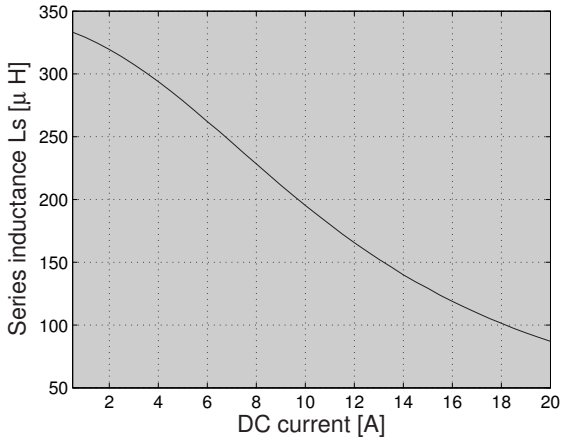

(c)

Figure B-10: Experimental results of the characterization of the 120 μH inductor using a circuit model consisting of RL network: (a) series inductance, (b) series resistance, (c) series inductance at a constant frequency of 20 kHz.

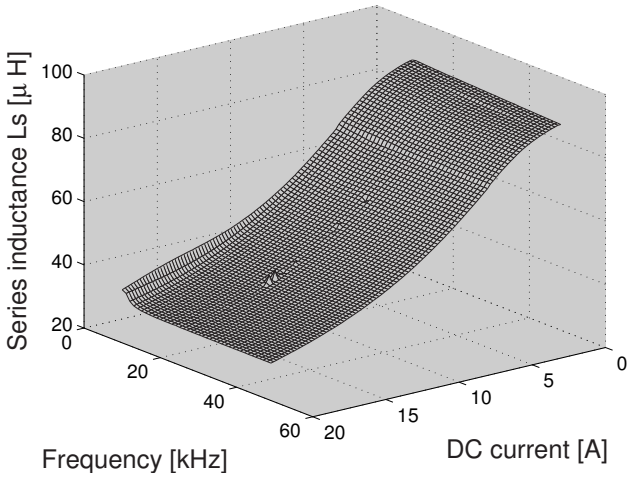

(a)

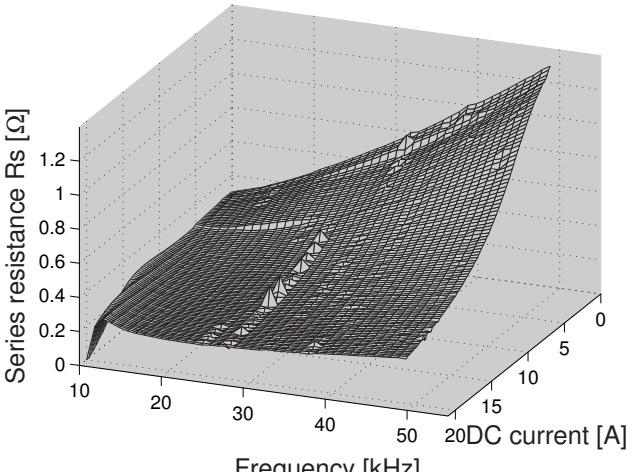

(b)

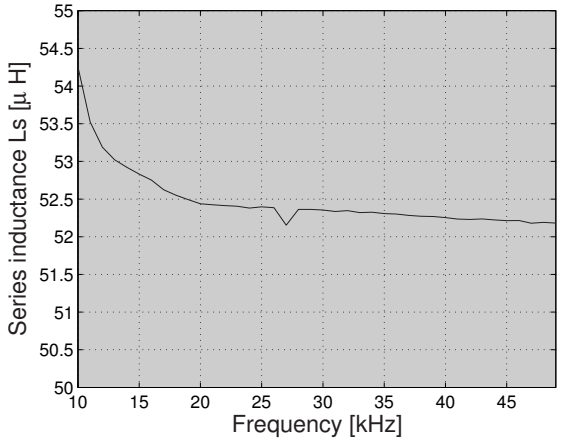

(c)

Figure B-11: Experimental results of the characterization of the PE-51 511 toroidal inductor from the Pulse manufacturer: (a)series inductance, (b) series resistance, (c)series inductance at a constant current of 10 A.

B.6 Conclusions

The virtual instrument presented in this appendix models various inductors at different operation points in an automatic and simple form. The developed virtual instrument made it possible to create a database for different inductors that have already been constructed and thus be able to select the most appropriate inductor according to the operation point. The inductor characteristic can make better simulations and designs of the converter's components.

Bibliography

[1] "The fuel cell today industry review 2011," Fuel Cell Today, Tech. Rep., 2011.

[2] C. Restrepo, J. Calvente, A. Romero, E. Vidal-Idiarte, and R. Giral, "Current mode control of a coupled-inductor buck-boost dc-dc switching converter," *IEEE Trans. Power Electron.*, vol. PP, no. 99, p. 1, 2011.

[3] M. Balat, "Potential importance of hydrogen as a future solution to environmental and transportation problems," *International Journal of Hydrogen Energy*, vol. 33, no. 15, pp. 4013 – 4029, 2008.

[4] U. E. protection agency, "Nitrous oxide," http://www.epa.gov/nitrousoxide/scientific.html, Tech. Rep., 2012.

[5] N. Lutsey, "A technical analysis of model year 2011 us automobile efficiency," *Transportation Research Part D: Transport and Environment*, vol. 17, no. 5, pp. 361 – 369, 2012.

[6] P. McGuiness and U. Pirnat, "Four steps to the hydrogen car, planet earth 2011 - global warming challenges and opportunities for policy and practice, prof. elias carayannis (ed.)."

[7] M. Conte, F. Di Mario, A. Iacobazzi, A. Mattucci, A. Moreno, and M. Ronchetti, "Hydrogen as future energy carrier: The enea point of view on technology and application prospects," *Energies*, vol. 2, no. 1, pp. 150–179, 2009. [Online]. Available: http://www.mdpi.com/1996-1073/2/1/150/

[8] C. of the Desert, "Hydrogen fuel cell engines and related technologies, module 1: Hydrogen properties," http://*www*1.*eere.energy.gov/hydrogenandfuelcells/tech*$_v$*alidation/pdfs/fcm*01*r*0.*pdf*, Tech. Rep., December 2001.

[9] H. Ozcan, "Hydrogen enrichment effects on the second law analysis of a lean burn natural gas engine," *International Journal of Hydrogen Energy*, vol. 35, no. 3, pp. 1443 – 1452, 2010.

[10] R. C. Bowman and N. Stetson, *On-Board Hydrogen Storage Systems Projected Performance and Cost Parameters*, DOE Hydrogen and Fuel Cells Program Record, 2010.

[11] A. Zttel, "Materials for hydrogen storage," *Materials Today*, vol. 6, no. 9, pp. 24 – 33, 2003. [Online]. Available: http://www.sciencedirect.com/science/article/pii/S1369702103009222

[12] S. Sherif, N. Zeytinoglu, and T. Veziroglu, "Liquid hydrogen: Potential, problems, and a proposed research program."

[13] B. P. S. Inc., *Introduction to Fuel Cell Technology*, Ballard Power Systems Inc., 2002.

[14] B. Sakintuna, F. Lamari-Darkrim, and M. Hirscher, "Metal hydride materials for solid hydrogen storage: A review," *International Journal of Hydrogen Energy*, vol. 32, no. 9, pp. 1121 – 1140, 2007.

[15] J. Zheng, X. Liu, P. Xu, P. Liu, Y. Zhao, and J. Yang, "Development of high pressure gaseous hydrogen storage technologies," *International Journal of Hydrogen Energy*, vol. 37, no. 1, pp. 1048 – 1057, 2012.

[16] R. Ahluwalia and J. Peng, "Automotive hydrogen storage system using cryo-adsorption on activated carbon," *International Journal of Hydrogen Energy*, vol. 34, no. 13, pp. 5476 – 5487, 2009.

[17] R. Ahluwalia, T. Hua, and J. Peng, "On-board and off-board performance of hydrogen storage options for light-duty vehicles," *International Journal of Hydrogen Energy*, vol. 37, no. 3, pp. 2891 – 2910, 2012.

[18] T. Wallner, H. Lohse-Busch, S. Gurski, M. Duoba, W. Thiel, D. Martin, and T. Korn, "Fuel economy and emissions evaluation of bmw hydrogen 7 mono-fuel demonstration vehicles," *International Journal of Hydrogen Energy*, vol. 33, no. 24, pp. 7607 – 7618, 2008.

[19] J. Andjar and F. Segura, "Fuel cells: History and updating. a walk along two centuries," *Renewable and Sustainable Energy Reviews*, vol. 13, no. 9, pp. 2309 – 2322, 2009.

[20] B. G. Pollet, I. Staffell, and J. L. Shang, "Current status of hybrid, battery and fuel cell electric vehicles: from electrochemistry to market prospects," *Electrochimica Acta*, no. 0, pp. –, 2012.

[21] K. Mazloomi and C. Gomes, "Hydrogen as an energy carrier: Prospects and challenges," *Renewable and Sustainable Energy Reviews*, vol. 16, no. 5, pp. 3024 – 3033, 2012. [Online]. Available: http://www.sciencedirect.com/science/article/pii/S1364032112001220

[22] D. Haeseldonckx and W. Dhaeseleer, "The use of the natural-gas pipeline infrastructure for hydrogen transport in a changing market structure," *International Journal of Hydrogen Energy*, vol. 32, no. 1011, pp. 1381 – 1386, 2007.

[23] "Hydrogen embrittlement of high strength pipeline steels," *Corrosion Science*, vol. 48, no. 12, pp. 4378 – 4385, 2006.

[24] N. Eliaz, A. Shachar, B. Tal, and D. Eliezer, "Characteristics of hydrogen embrittlement, stress corrosion cracking and tempered martensite embrittlement in high-strength steels," *Engineering Failure Analysis*, vol. 9, no. 2, pp. 167 – 184, 2002.

[25] H. F. Clarity, "Honda fcx clarity official website," http://automobiles.honda.com/fcx-clarity/home-energy-station.aspx, Tech. Rep., 2011.

[26] S. Y. Park, J. W. Kim, and D. H. Lee, "Development of a market penetration forecasting model for hydrogen fuel cell vehicles considering infrastructure and cost reduction effects," *Energy Policy*, vol. 39, no. 6, pp. 3307 – 3315, 2011.

[27] E. Endo, "Market penetration analysis of fuel cell vehicles in japan by using the energy system model markal," *International Journal of Hydrogen Energy*, vol. 32, no. 1011, pp. 1347 – 1354, 2007, ¡ce:title¿EHEC2005¡/ce:title¿.

[28] D. Keles, M. Wietschel, D. Mst, and O. Rentz, "Market penetration of fuel cell vehicles analysis based on agent behaviour," *International Journal of Hydrogen Energy*, vol. 33, no. 16, pp. 4444 – 4455, 2008.

[29] A. Contreras, E. Guervs, and F. Posso, "Market penetration analysis of the use of hydrogen in the road transport sector of the madrid region, using markal," *International Journal of Hydrogen Energy*, vol. 34, no. 1, pp. 13 – 20, 2009.

[30] E. Rosenberg, A. Fidje, K. A. Espegren, C. Stiller, A. M. Svensson, and S. Mller-Holst, "Market penetration analysis of hydrogen vehicles in norwegian passenger transport towards 2050," *International Journal of Hydrogen Energy*, vol. 35, no. 14, pp. 7267 – 7279, 2010.

[31] F. K. A. Carrette, L. and U. Stimming, "Fuel cells: Principles, types, fuels, and applications," *ChemPhysChem*.

[32] J. Larminie and A. Dicks, *Fuel Cell Systems Explained*, 2nd ed. Publisher Wiley, 2003.

[33] J. Correa, F. Farret, L. Canha, and M. Simoes, "An electrochemical-based fuel-cell model suitable for electrical engineering automation approach," *IEEE Trans. Ind. Electron.*, vol. 51, no. 5, pp. 1103 – 1112, oct. 2004.

[34] J. Pukrushpan, A. Stefanopoulou, and H. Peng, "Control of fuel cell breathing," *IEEE Control Syst. Mag.*, vol. 24, no. 2, pp. 30 – 46, apr 2004.

[35] H. P. Jay T. Pukrushpan, Anna G. Stefanopoulou, *Control of fuel cell power systems: principles, modeling, analysis, and feedback design*, 1st ed. Springer, 2004.

[36] F. Segura, J. Andujar, and E. Duran, "Analog current control techniques for power control in PEM fuel-cell hybrid systems: A critical review and a practical application," *IEEE Trans. Ind. Electron.*, vol. 58, no. 4, pp. 1171 –1184, april 2011.

[37] M. Vasallo, J. Andujar, C. Garcia, and J. Brey, "A methodology for sizing backup fuel-cell/battery hybrid power systems," *IEEE Trans. Ind. Electron.*, vol. 57, no. 6, pp. 1964 –1975, june 2010.

[38] A. Shahin, M. Hinaje, J.-P. Martin, S. Pierfederici, S. Rael, and B. Davat, "High voltage ratio DC-DC converter for fuel-cell applications," *IEEE Trans. Ind. Electron.*, vol. 57, no. 12, pp. 3944 –3955, dec. 2010.

[39] X. Zhu, X. Li, G. Shen, and D. Xu, "Design of the dynamic power compensation for PEMFC distributed power system," *IEEE Trans. Ind. Electron.*, vol. 57, no. 6, pp. 1935 –1944, june 2010.

[40] P. Rodatz, G. Paganelli, A. Sciarretta, and L. Guzzella, "Optimal power management of an experimental fuel cell/supercapacitor-powered hybrid vehicle," *Control Engineering Practice*, vol. 13, no. 1, pp. 41 – 53, 2005.

[41] P. Corbo, F. Corcione, F. Migliardini, and O. Veneri, "Experimental assessment of energy-management strategies in fuel-cell propulsion systems," *J. of Power Sources*, vol. 157, no. 2, pp. 799 – 808, 2006.

[42] P. Thounthong, S. Rael, B. Davat, and I. Sadli, "A control strategy of fuel cell/battery hybrid power source for electric vehicle applications," in *Power Electronics Specialists Conference, 2006. PESC '06. 37th IEEE*, june 2006, pp. 1 –7.

[43] C. Ramos-Paja, C. Bordons, A. Romero, R. Giral, and L. Martinez-Salamero, "Minimum fuel consumption strategy for PEM fuel cells," *IEEE Trans. Ind. Electron.*, vol. 56, no. 3, pp. 685 –696, 2009.

[44] D. Biel, F. Guinjoan, E. Fossas, and J. Chavarria, "Sliding-mode control design of a boost-buck switching converter for AC signal generation," *IEEE Trans. Circuits Syst. I, Reg. Papers*, vol. 51, no. 8, pp. 1539 – 1551, Aug. 2004.

[45] J. Chen, D. Maksimovic, and R. Erickson, "Analysis and design of a low-stress buck-boost converter in universal-input PFC applications," *IEEE Trans. Power Electron.*, vol. 21, no. 2, pp. 320 – 329, Mar. 2006.

[46] T. Crocker and N. Cooper, "Fast and furious [electric dreams]," *Power Engineer*, vol. 18, no. 4, pp. 39 –41, Aug. 2004.

[47] M. Gaboriault and A. Notman, "A high efficiency, noninverting, buck-boost DC-DC converter," in *Proc. 19th IEEE Appl. Power Electron. Conf. Expo., APEC*, vol. 3, 2004, pp. 1411–1415.

[48] P.-C. Huang, W.-Q. Wu, H.-H. Ho, and K.-H. Chen, "Hybrid buck-boost feedforward and reduced average inductor current techniques in fast line transient and high-efficiency buck-boost converter," *IEEE Trans. Power Electron.*, vol. 25, no. 3, pp. 719–730, Mar. 2010.

[49] B. Sahu and G. Rincon-Mora, "A low voltage, dynamic, noninverting, synchronous buck-boost converter for portable applications," *IEEE Trans. Power Electron.*, vol. 19, no. 2, pp. 443–452, Mar. 2004.

[50] Y.-J. Lee, A. Khaligh, and A. Emadi, "A compensation technique for smooth transitions in a noninverting buck-boost converter," *IEEE Trans. Power Electron.*, vol. 24, no. 4, pp. 1002–1015, Apr. 2009.

[51] Y.-J. Lee, A. Khaligh, A. Chakraborty, and A. Emadi, "Digital combination of buck and boost converters to control a positive buck-boost converter and improve the output transients," *IEEE Trans. Power Electron.*, vol. 24, no. 5, pp. 1267–1279, May. 2009.

[52] E. Schaltz, P. Rasmussen, and A. Khaligh, "Non-inverting buck-boost converter for fuel cell applications," in *Proc. 34th Annu. Conf. IEEE Ind. Electron. Soc., IECON*, Nov. 2008, pp. 855–860.

[53] J.-K. Shiau, C.-J. Cheng, and C.-E. Tseng, "Stability analysis of a non-inverting synchronous buck-boost power converter for a solar power management system," in *Proc. 1st IEEE Int. Conf. Sustainable Energy Technol., ICSET*, Nov. 2008, pp. 263–268.

[54] O. Mourra, A. Fernandez, and F. Tonicello, "Buck boost regulator (B^2R) for spacecraft solar array power conversion," in *Proc. 25th IEEE Appl. Power Electron. Conf. Expo., APEC*, Feb. 2010, pp. 1313–1319.

[55] S. Waffler and J. Kolar, "A novel low-loss modulation strategy for high-power bidirectional buck + boost converters," *IEEE Trans. Power Electron.*, vol. 24, no. 6, pp. 1589 –1599, Jun. 2009.

[56] X. Ren, X. Ruan, H. Qian, M. Li, and Q. Chen, "Three-mode dual-frequency two-edge modulation scheme for four-switch buck-boost converter," *IEEE Trans. Power Electron.*, vol. 24, no. 2, pp. 499–509, Feb. 2009.

[57] R. W. Erickson and D. Maksimovic, *Fundamentals of Power Electronics*, 2nd ed. Kluwer Academic Publishers, 2001.

[58] J. Chen, D. Maksimovic, and R. Erickson, "Buck-boost PWM converters having two independently controlled switches," in *Proc. 32nd IEEE Annu. Power Electron. Specialists Conf., PESC*, vol. 2, 2001, pp. 736–741.

[59] K. Hwu and Y. Yau, "Two types of KY buck-boost converters," *IEEE Trans. Ind. Electron.*, vol. 56, no. 8, pp. 2970–2980, Aug. 2009.

[60] S. Kapat, A. Patra, and S. Banerjee, "A current-controlled tristate boost converter with improved performance through RHP zero elimination," *IEEE Trans. Power Electron.*, vol. 24, no. 3, pp. 776–786, Mar. 2009.

[61] J. Calvente, L. Martinez-Salamero, H. Valderrama, and E. Vidal-Idiarte, "Using magnetic coupling to eliminate right half-plane zeros in boost converters," *IEEE Power Electron Lett.*, vol. 2, no. 2, pp. 58–62, Jun. 2004.

[62] J. Calvente, L. Martinez-Salamero, P. Garces, and A. Romero, "Zero dynamics-based design of damping networks for switching converters," *IEEE Trans. Aerosp. Electron. Syst.*, vol. 39, no. 4, pp. 1292–1303, Oct. 2003.

[63] R. Erickson, "Optimal single resistors damping of input filters," in *Proc. 14th IEEE Appl. Power Electron. Conf. Expo., APEC*, vol. 2, Mar. 1999, pp. 1073–1079.

[64] E. Sanchis-Kilders, A. Ferreres, E. Maset, J. Ejea, V. Esteve, J. Jordan, A. Garrigos, and J. Calvente, "Soft switching bidirectional converter for battery discharging-charging," in *Proc. 21st IEEE Appl. Power Electron. Conf. Expo., APEC*, Mar. 2006, pp. 603–609.

[65] E. Sanchis-Kilders, A. Ferreres, E. Maset, J. Ejea, V. Esteve, J. Jordan, J. Calvente, and A. Garrigos, "Bidirectional high-power high-efficiency non-isolated step-up dc-dc converter," in *Proc. 37th IEEE Annu. Power Electron. Specialists Conf., PESC*, Jun. 2006, pp. 1–7.

[66] E. Sanchis, E. Maset, A. Ferreres, J. B. Ejea, J. Calvente, A. Garrigos, V. Esteve, J. Jordan, and B. J. M., "Bidirectional high-efficiency non-isolated step-up battery regulator," *IEEE Trans. Aerosp. Electron. Syst.*, To be published.

[67] J. Calvente, L. Martinez-Salamero, P. Garces, R. Leyva, and A. Capel, "Dynamic optimization of bidirectional topologies for battery charge/discharge in satellites," in *Proc. 32nd IEEE Annu. Power Electron. Specialists Conf., PESC*, vol. 4, 2001, pp. 1994–1999.

[68] R. Middlebrook and S. Ćuk, "A general unified approach to modeling switching-converter power stages," in *Rec. IEEE Power Electron. Specialists Conf.*, Jun. 1976, pp. 18–34.

[69] E. Van Dijk, J. Spruijt, D. O'Sullivan, and J. Klaassens, "Pwm-switch modeling of dc-dc converters," *IEEE Trans. Power Electron.*, vol. 10, no. 6, pp. 659 – 665, Nov. 1995.

[70] T. Instruments, "Designing with the TL5001 PWM controller," Texas Instruments, Aplication Report SLVA034A, 1995.

[71] R. Paul and D. Maksimovic, "Analysis of PWM nonlinearity in non-inverting buck-boost power converters," in *Proc. 39th IEEE Annu. Power Electron. Specialists Conf., PESC*, Jun. 2008, pp. 3741–3747.

[72] S. Park and T. Jahns, "A self-boost charge pump topology for a gate drive high-side power supply," in *Proc. 19th IEEE Appl. Power Electron. Conf. Expo., APEC*, vol. 1, Feb. 2003, pp. 126–131.

[73] M. Sokolov and D. Shmilovitz, "A modified MPPT scheme for accelerated convergence," *Energy Conversion, IEEE Transactions on*, vol. 23, no. 4, pp. 1105 –1107, 2008.

[74] J. Agorreta, L. Reinaldos, R. Gonzalez, M. Borrega, J. Balda, and L. Marroyo, "Fuzzy switching technique applied to PWM boost converter operating in mixed conduction mode for PV systems," *IEEE Trans. Ind. Electro.*, vol. 56, no. 11, pp. 4363 –4373, 2009.

[75] I. T. Papaioannou, M. C. Alexiadis, C. S. Demoulias, D. P. Labridis, and P. S. Dokopoulos, "Modeling and field measurements of photovoltaic units connected to LV grid. Study of penetration scenarios," *IEEE Trans. Power Del.*, vol. 26, no. 2, pp. 979 –987, 2011.

[76] P. Thounthong, S. Pierfederici, J.-P. Martin, M. Hinaje, and B. Davat, "Modeling and control of fuel cell/supercapacitor hybrid source based on differential flatness control," *IEEE Trans. Veh. Technol.*, vol. 59, no. 6, pp. 2700 –2710, 2010.

[77] D. Sha, Z. Guo, and X. Liao, "Cross-feedback output-current-sharing control for input-series-output-parallel modular DC-DC converters," *IEEE Trans. Power Electron.*, vol. 25, no. 11, pp. 2762 –2771, 2010.

[78] D. Lamar, J. Zuniga, A. Alonso, M. Gonzalez, and M. Alvarez, "A very simple control strategy for power factor correctors driving high-brightness LEDs," *IEEE Trans. Power Electron.*, vol. 24, no. 8, pp. 2032 –2042, 2009.

[79] W.-K. Lun, K. Loo, S.-C. Tan, Y. Lai, and C. Tse, "Bilevel current driving technique for LEDs," *IEEE Trans. Power Electron.*, vol. 24, no. 12, pp. 2920 –2932, 2009.

[80] C. Ramos-Paja, A. Romero, R. Giral, J. Calvente, and L. Martinez-Salamero, "Mathematical analysis of hybrid topologies efficiency for PEM fuel cell power systems design," *Int. J. of Electr. Power & Energy Syst.*, vol. 32, no. 9, pp. 1049 – 1061, 2010.

[81] X. Yu, M. Starke, L. Tolbert, and B. Ozpineci, "Fuel cell power conditioning for electric power applications: a summary," *IET Electr. Power Appl.*, vol. 1, no. 5, pp. 643 –656, 2007.

[82] C. Restrepo, J. Calvente, A. Cid, A. El Aroudi, and R. Giral, "A non-inverting buck-boost DC-DC switching converter with high efficiency and wide bandwidth," *IEEE Trans. Power Electron.*, vol. 26, no. 9, pp. 2490 –2503, sept. 2011.

[83] L. Dixon, "Average current mode control of switching power supplies," Unitrode Power Supply Design Seminar, Tech. Rep., 1988.

[84] D. O'Sullivan, H. Spruyt, and A. Crausaz, "PWM conductance control," in *Proc. 19th IEEE Annu. Power Electron. Specialists Conf., PESC*, 1988, pp. 351 –359 vol.1.

[85] Y.-S. Jung, J.-Y. Lee, and M.-J. Youn, "A new small signal modeling of average current mode control," in *Proc. 29th IEEE Annu. Power Electron. Specialists Conf., PESC*, vol. 2, May 1998, pp. 1118 –1124 vol.2.

[86] W. Tang, F. Lee, and R. Ridley, "Small-signal modeling of average current-mode control," *IEEE Trans. Power Electron.*, vol. 8, no. 2, pp. 112 –119, apr 1993.

[87] J. B. Ejea, A. Ferreres, E. Sanchis-Kilders, E. Maset, V. Esteve, J. Jordan, and A. Garrigos, "Optimized topology for high efficiency battery discharge regulator," *IEEE Trans. Aerosp. Electron. Syst.*, vol. 44, no. 4, pp. 1511 –1521, 2008.

[88] P. Villegas, J. Sebastian, M. Hernando, F. Nuno, and J. Martinez, "Average current mode control of series-switching post-regulators used in power factor correctors," *IEEE Trans. Power Electron.*, vol. 15, no. 5, pp. 813 –819, Sept. 2000.

[89] P. Cooke, "Modeling average current mode control [of power convertors]," in *Proc. 15th IEEE Appl. Power Electron. Conf. Expo., APEC*, 2000.

[90] J. Sun and R. Bass, "Modeling and practical design issues for average current control," in *Proc. 14th IEEE Appl. Power Electron. Conf. Expo., APEC*, vol. 2, Mar. 1999, pp. 980 –986 vol.2.

[91] J. Park, J. Fan, X. Wang, and A. Huang, "A sample-data model for double edge current programmed mode control (DECPM) in high-frequency and wide-range DC-DC converters," *IEEE Trans. Power Electron.*, vol. 25, no. 4, pp. 1023 –1033, 2010.

[92] D. Dening, "A buck-or-boost converter module with embedded inductor and fast current limit," *IEEE Trans. Power Electron.*, 2009.

[93] J. Correa, F. Farret, J. Gomes, and M. Simoes, "Simulation of fuel-cell stacks using a computer-controlled power rectifier with the purposes of actual high-power injection applications," *IEEE Trans. Ind. Appl.*, vol. 39, no. 4, pp. 1136 – 1142, july-aug. 2003.

[94] T.-W. Lee, S.-H. Kim, Y.-H. Yoon, S.-J. Jang, and C.-Y. Won, "A 3 kw fuel cell generation system using the fuel cell simulator," in *Proc. IEEE Int. Symp. Ind. Electron., ISIE*, vol. 2, may 2004, pp. 833 – 837 vol. 2.

[95] P. Acharya, P. Enjeti, and I. Pitel, "An advanced fuel cell simulator," in *Proc. 19th IEEE Appl. Power Electron. Conf. Expo., APEC*, vol. 3, 2004, pp. 1554 – 1558 Vol.3.

[96] M. Ordonez, M. Iqbal, and J. Quaicoe, "Development of a fuel cell simulator based on an experimentally derived model," pp. 1449 –1452, may 2005.

[97] ——, "A novel fuel cell simulator," in *Proc. 36th IEEE Annu. Power Electron. Specialists Conf., PESC*, june 2005, pp. 178 –184.

[98] A. Samosir, M. Anwari, and A. Yatim, "A simple pem fuel cell emulator using electrical circuit model," in *Proc. Int. Power Electron. Conf., IPEC*, oct. 2010, pp. 881 –885.

[99] C. Wang, M. Nehrir, and S. Shaw, "Dynamic models and model validation for pem fuel cells using electrical circuits," *IEEE Trans. Energy Convers.*, vol. 20, no. 2, pp. 442 – 451, june 2005.

[100] J. C. Amphlett, R. M. Baumert, R. F. Mann, B. A. Peppley, P. R. Roberge, and T. J. Harris, "Performance modeling of the ballard mark iv solid polymer electrolyte fuel cell," *J. of The Electrochemical Soc.*, vol. 142, no. 1, pp. 1–8, 1995.

[101] A. Rowe and X. Li, "Mathematical modeling of proton exchange membrane fuel cells," *J. of Power Sources*, vol. 102, no. 1-2, pp. 82 – 96, 2001.

[102] C. Wang and M. Nehrir, "A physically based dynamic model for solid oxide fuel cells," *IEEE Trans. Energy Convers.*, vol. 22, no. 4, pp. 887 –897, dec. 2007.

[103] J. Larminie and A. Dicks, *Fuel Cell Handbook*, 5th ed. EG&GServices, Parsons Inc., DEO of Fossil Energy, National Energy Technology Lab, 2000.

[104] J. Amphlett, R. Mann, B. Peppley, P. Roberge, and A. Rodrigues, "A model predicting transient responses of proton exchange membrane fuel cells," *J. of Power Sources*, vol. 61, no. 1-2, pp. 183 – 188, 1996.

[105] G. N. Hatsopoulos and J. H. Keenan, *Principles of General Thermodynamics*. New York:Wiley, 1965.

[106] J. Larminie and A. Dicks, *Fuel Cell Systems Explained*. New York:Wiley, 2001.

[107] ——, *Instrumentation Newsletter*. National Instruments Corporation, 2007, vol. 19, no. 4.

[108] P. Bevington and D. K. Robinson, *Data Reduction and Error Analysis for the Physical Sciences*. McGraw-Hill Education, 2002.

[109] R. A. G. R. M.-S. L. Ramos, C. and C. Sanchez, "Switching and linear power stages evaluation for pem fuel cell emulation," *Int. J. of Circuit Theory and Appl.*, vol. 39, no. 4, pp. 1136–1142, July-Aug. 2010.

[110] Z. Liu, L. Yang, Z. Mao, W. Zhuge, Y. Zhang, and L. Wang, "Behavior of PEMFC in starvation," *J. of Power Sources*, vol. 157, no. 1, pp. 166 – 176, 2006.

[111] P. Thounthong and P. Sethakul, "Analysis of a fuel starvation phenomenon of a pem fuel cell," in *Power Convers. Conf., PCC*, April 2007, pp. 731–738.

[112] W. Schmittinger and A. Vahidi, "A review of the main parameters influencing long-term performance and durability of pem fuel cells," *J. of Power Sources*, vol. 180, no. 1, pp. 1 – 14, 2008.

[113] C. Restrepo, C. Torres, J. Calvente, R. Giral, and R. Leyva, "Simulator of a pem fuel-cell stack based on a dynamic model," in *Proc. 35th Annu. Conf. IEEE Ind. Electron. Soc., IECON*, 3-5 2009, pp. 2796 –2801.

[114] C. Ramos-Paja, R. Giral, L. Martinez-Salamero, J. Romano, A. Romero, and G. Spagnuolo, "A PEM fuel-cell model featuring oxygen-excess-ratio estimation and power-electronics interaction," *IEEE Trans. Ind. Electron.*, vol. 57, no. 6, pp. 1914 – 1924, june 2010.

[115] L. Palma, M. Todorovic, and P. Enjeti, "Analysis of common-mode voltage in utility-interactive fuel cell power conditioners," *IEEE Trans. Ind. Electron.*, vol. 56, no. 1, pp. 20–27, 2009.

[116] M. Todorovic, J. Palma, and P. Enjeti, "Design of a wide input range dcdc converter with a robust power control scheme suitable for fuel cell power conversion," *IEEE Trans. Ind. Electron.*, vol. 55, no. 3, pp. 1247–1255, 2008.

[117] M. Zhu and F. L. Luo, "Transient analysis of multi-state dcdc converters using system energy characteristics," *Int. J. of Circuit Theory and Appl.*, vol. 36, no. 3, p. 327344, 2008.

[118] H. Chiu, C. Yao, and Y. Lo, "A DC/DC converter topology for renewable energy systems," *Int. J. of Circuit Theory and Appl.*, vol. 37, no. 3, pp. 485–495, 2009.

[119] N. Genc and I. Iskender, "Steady-state analysis of a novel ZVT interleaved boost converter," *Int. J. of Circuit Theory and Appl.*, 2010.

[120] "Design and experimental validation of a constrained mpc for the air feed of a fuel cell," *Contr. Eng. Practice*, vol. 17, no. 8, pp. 874 – 885, 2009.

[121] J. Pukrushpan, A. Stefanopoulou, and H. Peng, "Control of fuel cell breathing," *IEEE Control Syst. Mag.*, vol. 24, pp. 30 – 46, 2004.

[122] A. Hernandez, D. Hissel, and R. Outbib, "Fuel cell fault diagnosis: A stochastic approach," *Proc. IEEE Int. Symp. Ind. Electron., ISIE*, vol. 6, pp. 1984–1989, 2006.

[123] C. Bordons, A. Arce, and A. J. del Real, "Constrained predictive control strategies for pem fuel cells," *American Control Conf.*, pp. 2486–2491, 2006.

[124] S. Jemei, D. Hissel, M.-C. Pera, and J. Kauffmann, "A new modeling approach of embedded fuel-cell power generators based on artificial neural network," *IEEE Trans. Ind. Electron.*, vol. 55, no. 1, pp. 437–447, 2008.

[125] C. A. Ramos-Paja, C. Bordons, A. Romero, R. Giral, and L. Martinez-Salamero, "Minimum fuel consumption strategy for pem fuel cells," *IEEE Trans. Ind. Electron.*, vol. 56, no. 3, pp. 685–696, march 2009.

[126] E. F. Camacho and C. Bordons, *Model Predictive Control (2nd edition)*. Springer, 2007.

[127] A. J. del Real, A. Arce, and C. Bordons, "Development and experimental validation of a pem fuel cell dynamic model," *J. of Power Sources*, vol. 173, no. 1, pp. 310–324, 2007.

[128] J. T. Pukrushpan, A. G. Stefanopoulou, and H. Peng, *Control of Fuel Cell Power Systems: Principles, Modeling, Analysis and Feedback Design.* Springer-Verlag London, 2004.

[129] C. Ramos, A. Romero, and R. Giral, *Fuel cell modeling and control: A power electronics approach*, 1st ed. LAP Lambert Academic, 2010.

[130] I.-S. Kim, "Robust state estimator design for a solar battery charging system," *Int. J. of Electron.*, vol. 96, no. 3, pp. 229 – 247, 2009.

[131] A. D. Cheok, T. S. Chong, and W. Zhongfang, "Real-time computer-based torque measurement of switched reluctance motors," *Int. J. of Electron.*, vol. 89, no. 9, pp. 693 – 715, 2002.

[132] F. Uriarte and K. Butler-Purry, "Real-time simulation using pc-based kernels," in *Power Syst. Conf. and Exposition, 2006. PSCE '06. 2006 IEEE PES*, 29 2006-Nov. 1 2006, pp. 1991–1995.

[133] MathWorks, *Real-Time Windows Target User's Guide - Version 3. For Use with MATLAB and SIMULINK*, The MathWorks, Inc., Natick, MA, 2009.

[134] G. K. Andersen, C. K. Klumpner, B. Sren, and F. Blaabjerg, "A new power converter for fuel cells with high system efficiency," *Int. J. of Electron.*, vol. 90, no. 11, pp. 737 – 750, 2003.

[135] Y. Huang and C. K. Tse, "Circuit theory of paralleling switching converters," *Int. J. of Circuit Theory and Appl.*, vol. 37, no. 1, p. 109135, 2009.

[136] S. A. G. R. V.-J. Ramos, C. and R. Rios, "Design, modeling, control and implementation of a fuel cell generation system," *Revista Facultad de Ingeniera, Universidad de Antioquia, Colombia*, no. 59, pp. 9–22, Jun. 2011.

[137] H. A. Guesmi, K. and J. Zaytoon, "Control of nonlinear phenomena in DCDC converters: Fuzzy logic approach," *Int. J. of Circuit Theory and Appl.*, vol. 36, no. 7, p. 857874, 2008.

[138] X. Kong and A. Khambadkone, "Modeling of a PEM Fuel-Cell stack for dynamic and steady-state operation using ANN-based submodels," *IEEE Trans. Ind. Electron.*, vol. 56, no. 12, pp. 4903 –4914, dec. 2009.

[139] J.-H. Jung, S. Ahmed, and P. Enjeti, "PEM Fuel-Cell stack model development for real-time simulation applications," *IEEE Trans. Ind. Electron.*, vol. 58, no. 9, pp. 4217 –4231, sept. 2011.

[140] E.-H. Aglzim, A. Rouane, and R. El-Moznine, "An electronic measurement instrumentation of the impedance of a loaded fuel cell or battery," *Sensors*, vol. 7, no. 10, pp. 2363–2377, 2007. [Online]. Available: http://www.mdpi.com/1424-8220/7/10/2363/

[141] M. Ordonez, M. Sonnaillon, J. Quaicoe, and M. Iqbal, "An embedded frequency response analyzer for fuel cell monitoring and characterization," *IEEE Trans. Ind. Electron.*, vol. 57, no. 6, pp. 1925 –1934, june 2010.

[142] P. Pei, X. Yuan, J. Gou, and P. Li, "Dynamic response during pem fuel cell loading-up," *Materials*, vol. 2, no. 3, pp. 734–748, 2009. [Online]. Available: http://www.mdpi.com/1996-1944/2/3/734/

[143] L. Gauchia and J. Sanz, "A per-unit hardware-in-the-loop simulation of a fuel cell/battery hybrid energy system," *IEEE Trans. Ind. Electron.*, vol. 57, no. 4, pp. 1186 –1194, april 2010.

[144] A. Dhirde, N. Dale, H. Salehfar, M. Mann, and T. Han, "Equivalent electric circuit modeling and performance analysis of a pem fuel cell stack using impedance spectroscopy," *IEEE Trans. Energy Convers.*, vol. 25, no. 3, pp. 778 –786, sept. 2010.

[145] D.-S. Chan and K.-L. Hsueh, "A transient model for fuel cell cathode-water propagation behavior inside a cathode after a step potential," *Energies*, vol. 3, no. 5, pp. 920–939, 2010. [Online]. Available: http://www.mdpi.com/1996-1073/3/5/920/

[146] G. Fontes, C. Turpin, and S. Astier, "A large-signal and dynamic circuit model of a H_2/O_2 PEM Fuel Cell: Description, parameter identification, and exploitation," *IEEE Trans. Ind. Electron.*, vol. 57, no. 6, pp. 1874 –1881, june 2010.

[147] Q. Li, W. Chen, Y. Wang, S. Liu, and J. Jia, "Parameter identification for pem fuel-cell mechanism model based on effective informed adaptive particle swarm optimization," *IEEE Trans. Ind. Electron.*, vol. 58, no. 6, pp. 2410 –2419, june 2011.

[148] A. Forrai, H. Funato, Y. Yanagita, and Y. Kato, "Fuel-cell parameter estimation and diagnostics," *IEEE Trans. Energy Convers.*, vol. 20, no. 3, pp. 668 – 675, sept. 2005.

[149] A. Rathore, A. Bhat, and R. Oruganti, "Analysis, design and experimental results of wide range ZVS active-clamped L-L type current-fed DC/DC converter for Fuel Cells to utility interface," *IEEE Trans. Ind. Electron.*, vol. PP, no. 99, p. 1, jan 2011.

[150] D. Vinnikov and I. Roasto, "Quasi-z-source-based isolated dc/dc converters for distributed power generation," *IEEE Trans. Ind. Electron.*, vol. 58, no. 1, pp. 192 –201, jan. 2011.

[151] J.-Y. Lee, Y.-S. Jeong, and B.-M. Han, "An isolated dc/dc converter using high-frequency unregulated *llc* resonant converter for fuel cell applications," *IEEE Trans. Ind. Electron.*, vol. 58, no. 7, pp. 2926 –2934, july 2011.

[152] R.-J. Wai and C.-Y. Lin, "Dual active low-frequency ripple control for clean-energy power-conditioning mechanism," *IEEE Trans. Ind. Electron.*, vol. 58, no. 11, pp. 5172 –5185, nov. 2011.

[153] B. Yuan, X. Yang, D. Li, J. Duan, Z. Zhai, and X. Zeng, "Analysis and design of a high step-up current fed multi-resonant dc-dc converter with low circulating energy and zero-current switching for all active switches," *IEEE Trans. Ind. Electron.*, vol. PP, no. 99, p. 1, 2011.

[154] C.-S. Leu and M.-H. Li, "A novel current-fed boost converter with ripple reduction for high-voltage conversion applications," *IEEE Trans. Ind. Electron.*, vol. 57, no. 6, pp. 2018 –2023, june 2010.

[155] M. Grötsch, M. Mangold, and A. Kienle, "Analysis of the coupling behavior of pem fuel cells and dc-dc converters," *Energies*, vol. 2, no. 1, pp. 71–96, 2009. [Online]. Available: http://www.mdpi.com/1996-1073/2/1/71/

[156] C. Restrepo, C. Ramos-Paja, R. Giral, J. Calvente, and A. Romero, "Fuel cell emulator for oxygen excess ratio estimation on power electronics applications."

[157] F. Pinto and A. Vega-Leal, "A test of HIL COTS technology for fuel cell systems emulation," *IEEE Trans. Ind. Electron.*, vol. 57, no. 4, pp. 1237 –1244, april 2010.

[158] S.-Y. Choe, J.-W. Ahn, J.-G. Lee, and S.-H. Baek, "Dynamic simulator for a pem fuel cell system with a pwm dc/dc converter," *IEEE Trans. Energy Convers.*, vol. 23, no. 2, pp. 669 –680, june 2008.

[159] F. Gao, B. Blunier, M. Simo andes, and A. Miraoui, "Pem fuel cell stack modeling for real-time emulation in hardware-in-the-loop applications," *IEEE Trans. Energy Convers.*, vol. 26, no. 1, pp. 184 –194, march 2011.

[160] F. Marignetti, M. Minutillo, A. Perna, and E. Jannelli, "Assessment of Fuel Cell performance under different air stoichiometries and fuel composition," *IEEE Trans. Ind. Electron.*, vol. 58, no. 6, pp. 2420 –2426, june 2011.

[161] A. Arce, A. del Real, C. Bordons, and D. Ramirez, "Real-time implementation of a constrained MPC for efficient airflow control in a PEM Fuel Cell," *IEEE Trans. Ind. Electron.*, vol. 57, no. 6, pp. 1892 –1905, june 2010.

[162] K.-W. Suh and A. Stefanopoulou, "Performance limitations of air flow control in power-autonomous fuel cell systems," *Control Systems Technology, IEEE Transactions on*, vol. 15, no. 3, pp. 465 –473, may 2007.

[163] R. Talj, D. Hissel, R. Ortega, M. Becherif, and M. Hilairet, "Experimental validation of a pem fuel-cell reduced-order model and a moto-compressor higher order sliding-mode control," *IEEE Trans. Ind. Electron.*, vol. 57, no. 6, pp. 1906 –1913, june 2010.

[164] B. P. S. Inc., *Nexa (310-0027) Power Module Users Manual, MAN5100078*, Ballard Power Systems Inc., 2003.

[165] S. I. Gregory Muchnic, G. N. Uriel M. Oko, and A. N. Christopher S. Dannehy, "Fuel cell stack rejuvenation," US Patent US 6 558 824, 05 06, 2003.

[166] K. C. Adams, William A., D. C. Gardner, Christopher L., E. C. Dunn, James H., and O. C. Vered, Ron, "Fuel cell health management system," US Patent Application US 2003/0 211 372 A1, 11 13, 2003.

[167] A. Adams, William, L. Gardner, Christopher, H. Dunn, James, and R. Vered, "Fuel cell health management system," WO Patent Application WO 2003/083 975 A2, 10 09, 2003.

[168] W. A. Adams, C. L. Gardner, J. H. Dunn, and R. Vered, "Method and apparatus for rejuvenating fuel cells," US Patent US 7 038 424, 05 02, 2006.

[169] P. F. C. Ltd, *Palcan Fuel Cells Sales Agreement*, Palcan Fuel Cells Ltd.

[170] N. I. Corporation, *NI sbRIO-961x/963x/964x and NI sbRIO-9612XT/9632XT/9642XT USER GUIDE*, National Instruments Corporation.

[171] A. Technologies, *Operating Manual, Electronic Load Mainframes Models 6050A and 6051A*, Agilent Technologies, 1997.

[172] "Virtual instrumentation," http://zone.ni.com/devzone/cda/tut/p/id/4752, National Instruments, Tech. Rep.

[173] Austin, *LabVIEW 7 Express, User Manual.* National Instruments, 2003.

[174] B. Robert H, *Learning with LabVIEW 7 Express.* Pearson Education, Inc, 2004.

[175] J. Travis, *LabVIEW for everyone.* Prentice-Hall, Inc, 2002.

[176] G. W. Johnson and R. Jennings, *LabVIEW graphical programming.* McGraw-Hill, 2001.

[177] "Virtual instrumentation," http://zone.ni.com/devzone/cda/tut/p/id/3419, National Instruments, Tech. Rep.

[178] "IEEE standard digital interface for programmable instrumentation," *ANSI/IEEE Std 488.1-1987*, pp. –, 16 Jun 1988.

[179] "IEEE standard for higher performance protocol for the standard digital interface for programmable instrumentation," *IEEE Std 488.1-2003*, pp. –, 2003.

[180] "IEEE standard codes, formats, protocols, and common commands. for use with ansi/ieee std 488.1-1987 ieee standard digital interface for programmable instrumentation," *ANSI/IEEE Std 488.2-1987*, pp. –, 22 Apr 1988.

[181] "IEEE standard codes, formats, protocols, and common commands for use with ieee std 488.1-1987, ieee standard digital interface for programmable instrumentation," *IEEE Std 488.2-1992*, pp. –, 28 Dec 1992.

[182] QuadTech, *1910 Inductance Analyzer, Instruction Manual*, 2000.

[183] ——, *1320 Bias Current Source, Instruction Manual*, 1999.